Thermo-Hydro-Mechanical Behavior of Conductive Fractures using a Hybrid Finite Difference – Displacement Discontinuity Method

by

Mohammadreza Jalali

A thesis
presented to the University of Waterloo
in fulfillment of the
thesis requirement for the degree of
Doctor of Philosophy
in
Earth Sciences

Waterloo, Ontario, Canada, 2013

Author's Declaration

I hereby declare that I am the sole author of this thesis. This is a true copy of the thesis, including any required final revisions, as accepted by my examiners.

I understand that my thesis may be made electronically available to the public.

Abstract

Large amounts of hydrocarbon reserves are trapped in fractured reservoirs where fluid flux is far more rapid along fractures than through the porous matrix, even though the volume of the pore space may be a hundred times greater than the volume of the fractures. These are considered extremely challenging in terms of accurate recovery prediction because of their complexity and heterogeneity. Conventional reservoir simulators are generally not suited to naturally fractured reservoirs' production history simulation, especially when production processes are associated with large pressure and temperature changes that lead to large redistribution of effective stresses, causing natural fracture aperture alterations. In this case, all the effective processes, i.e. hydraulic, thermal and geomechanical, should be considered simultaneously to explain and evaluate the behavior of stress-sensitive reservoirs over the production period. This is called thermo-hydro-mechanical (THM) coupling.

In this study, a fully coupled thermo-hydro-mechanical approach is developed to simulate the physical behavior of fractures in a plane strain thermo-poroelastic medium. A hybrid numerical method, which implements both the finite difference method (FDM) and the displacement discontinuity method (DDM), is established to study the pressure, temperature, deformation and stress variations of fractures and surrounding rocks during production processes. This method is straightforward and can be implemented in conventional reservoir simulators to update fracture conductivity as it uses the same grid block as the reservoir grids and requires only discretization of fractures.

The hybrid model is then verified with couple of analytical solutions for the fracture aperture variation under different conditions. This model is implemented for some examples to present the behavior of fracture network as well as its surrounding rock under thermal injection and production. The results of this work clearly show the importance of rate, aspect ratio (i.e. geometry) and the coupling effects among fracture flow rate and aperture changes arising from coupled stress, pressure and temperature changes. The outcomes of this approach can be used to study the behavior of hydraulic injection for induced fracturing and promoting of shearing such as hydraulic fracturing of shale gas or shale oil reservoirs as well as massive waste disposal in the porous carbonate rocks. Furthermore, implementation of this technique should be able to lead to a better understanding of induced seismicity in injection projects of all kinds, whether it is for waste water disposal, or for the extraction of geothermal energy.

Acknowledgements

This research project would not have been possible without the support of many people. I wish to express my sincere appreciation to my supervisor, Dr. Maurice B. Dusseault, who patiently provided the vision, encouragement and advice necessary for me to proceed through the doctoral program and complete my dissertation. Deepest gratitude is also due to the members of the supervisory committee, Dr. Leo Rothenburg, Dr. Edward Sudicky and Dr. Steve G. Evans for their guidance, assistance and inspiring discussions. Dr. Roberto Aguilera graciously agreed to be the external examiner, and his feedback in the final stages of this work was invaluable.

I would like to thank the Schlumberger's Regional Technology Center (RTC) in Calgary especially Carlos Emilio Perez Damas, Dr. Jose A. Rivero, Dr. David Law and David Bexte who rendered their help during the period of my internship. The associated experience broadened my perspective on the practical aspects in the industry.

I would also like to convey thanks to University of Waterloo, Natural Sciences and Engineering Council (NSERC) of Canada, and the Schlumberger Company for financial support.

Many friends have helped me stay sane through these difficult years. Their support and care helped me overcome setbacks and stay focused on my graduate study. I greatly value their friendship and I deeply appreciate their belief in me.

Last, but not least, I would like to express my love and gratitude to my beloved family; for their understanding and endless love, through the duration of my studies. Without their encouragement, I would not have finished the degree.

Dedication

This thesis is dedicated to my beloved parents, sister and brother whose love and support sustained me through.

Table of Contents

List of Figures

List of Tables

Nomenclature

A	[m^2]	Surface area
b	[$kg/m.s^2$]	solid body force
B	[-]	Skempton's pore pressure coefficient
c_f	[1/MPa]	Fluid compressibility
c^f	[m^2/s]	Hydraulic diffusivity
c^T	[m^2/s]	Thermal diffusivity
C	[J/kg.°C]	Specific heat
d	[m]	Characteristic length
D_n	[m]	Normal displacement discontinuity
$D_{n\,max}$	[m]	Fracture maximum closure
D_s	[m]	Shear displacement discontinuity
E	[MPa]	Young's modulus
G	[MPa]	Shear modulus
h	[J/m^2.°C.s]	Heat transfer coefficient
$H(t)$	[-]	Heaviside step function
JCS	[MPa]	Joint compressive strength
JRC	[-]	Joint roughness coefficient
k	[m^2]	Intrinsic permeability
k_T	[J/m.s.°C]	Thermal conductivity
K_b	[MPa]	Bulk's modulus
K_n	[MPa/m]	Fracture normal stiffness
K_s	[MPa/m]	Fracture shear stiffness
m	[-]	Fluid content
M	[MPa]	Biot's modulus
n	[-]	Unit normal vector
N	[-]	Number of fracture segments
p	[MPa]	Pressure

q^f	[m/s]	Fluid flux (Darcy's velocity)
Q^f	[m^3/s]	Volumetric fluid flow rate
Q_{fs}	[m/s]	Fluid source strength
q^h	[J/m^2.s]	Heat flux
Q^h	[J/s]	Volumetric heat flow rate
Q_{hs}	[J/s]	Heat source strength
Re	[-]	Reynolds number
S	[1/MPa]	Storage coefficient
t	[s]	Time
T	[°C]	Temperature
u	[m]	Solid displacement
UCS	[MPa]	Unconfined Compressive Strength
V	[m^3]	Volume
w	[m]	Fracture aperture
α	[-]	Biot's effective stress coefficient
β	[1/°C]	Volumetric thermal expansion coefficient
β_m	[1/°C]	Hydro-thermal coupling coefficient
β_o	[1/°C]	Hydro-thermal coupling coefficient
δ_{ij}		Kronecker delta
ε_{ij}	[-]	Solid strain
ε_{vol}	[-]	Volumetric strain
ϕ	[-]	Porosity
ϕ_f	[-]	Friction angle
ϕ_r	[-]	residual friction angle
η	[-]	Hydro-mechanical coefficient
κ_p	[m^2/Pa.s]	fluid mobility
λ	[MPa]	Lame's first parameter
λ_1	[-]	Thermo-mechanical coefficient

μ	[Pa.s]	Fluid dynamic viscosity
ν	[-]	Poisson's ratio
ν_u	[-]	Undrained Poisson's ratio
ρ_f	[kg/m^3]	Fluid density
ς	[J/kg.°C]	Specific entropy
σ_{ij}	[MPa]	Total stress
σ'_{ij}	[MPa]	Effective stress
τ	[s]	Time step difference
ϑ		Heat capacity ratio
Υ	[MPa/°C]	Hydro-thermal coupling coefficient
ψ	[-]	Dilation angle

Subscripts

b	bulk
cond	conduction
conv	convection
f	fluid
fr	fracture
i	influenced fracture element
int	interface
inj	injection
j	influencing element
max	maximum
mob	mobilized
prod	production
r	residual
s	solid
0	reference

Superscripts

dn	normal displacement discontinuity
ds	shear displacement discontinuity
f	hydraulic
fs	fluid source
hs	heat source
T	thermal
τ	time duration
$\tilde{}$	relative displacement

List of abbreviations

BEM	Boundary Element Method
DDM	Displacement Discontinuity Method
DEM	Discrete Element Method
DFN	Discrete Fracture Network
FDM	Finite Difference Method
FEM	Finite Element Method
HM	Hydro-Mechanical
NFR	Naturally Fractured Reservoirs
PDE	Partial Differential Equation
THM	Thermo-Hydro-Mechanical
TM	Thermo-Mechanical

Chapter 1
Introduction

1.1 Petroleum Geomechanics

In the last three decades, there has been an increasing emphasis on the importance of geomechanics in petroleum engineering. In reservoir management, geomechanics plays a role as a multidisciplinary aspect among the various other engineering specialties (geology, thermodynamics, and fluid flow). In fact, the term "geomechanics" is often applied very broadly to describe a wide range of reservoir phenomena. Some of the reservoir engineering challenges involving geomechanics include (Figure 1.1):

- Wellbore stability during drilling and open hole completion
- Reservoir compaction and surface subsidence
- Sand production
- Behavior of naturally fractured reservoirs
- Integrity of completions during production (casing failures)
- Hydraulic fracturing
- Thermal fracturing with cold fluids
- Coal bed methane production
- Drilling cuttings reinjection

Numerical modelling of such processes is complex, first because of the complexity of the physics involved, and second because of the structurally complicated geometry of the reservoir and cap rock. This kind of modelling has been historically carried out in three separate areas:

- Reservoir simulation which consists of multiphase flow modeling and heat transfer in a porous medium;
- Geomechanical modelling that computes the deformation of the rocks as a consequence of the hydrocarbon exploitation activities such as production, injection, thermal recovery and so on; and,
- Fracture mechanics and fractured media behaviour which are important in stress-sensitive reservoirs such as naturally fractured reservoirs and in cases dealing with fracture propagation and geometry [Settari and Walters, 2001]

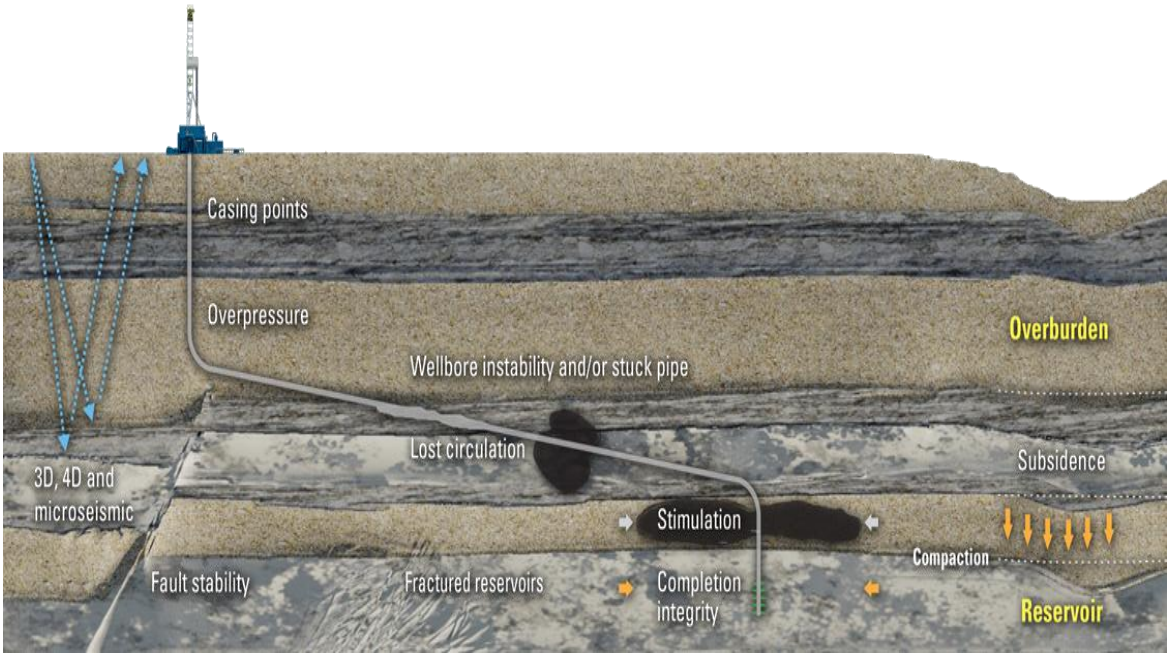

Figure 1.1. Reservoir engineering problems involving geomechanics [reproduced from www.slb.com].

Rapid progress in computer technology in recent years has allowed the tackling of numerically more challenging problems associated with non-linear materials and multiphase flow as well as the simulation of fractured rock mass behaviour. Because of the complexity of the solutions for multiphase flow and geomechanics models themselves, the solution of the coupled problem is even more complicated and needs further study to improve accuracy, convergence, and computing efficiency. In particular, researchers have been debating which coupling approach is best for computing fluid-solid interactions, and for which cases. The term 'interaction' is understood here as the mechanical force effect rather than the effect of any associated chemical reactions [Tran et al., 2002].

1.2 Naturally Fractured Reservoirs

A significant amount of oil and gas reserves - more than 60% of the world's proved conventional oil reserves as well as 50% of the world's proved gas reserves[1] - are found in carbonate rocks which are mostly naturally fractured (Figure 1.2). Fractures are planar discontinuities which occur in different scales from microscopic to macroscopic and kilometer sized features and are due to deformation or digenesis.

As a definition, Narr et al. (2006) proposed that "all reservoirs should be considered fractured until proven otherwise…", but this seems extreme in the case of high permeability unconsolidated sandstones where, if fractures exist, their impact on flow is negligible.

Nelson (2001) proposed the following classification for naturally fractured reservoirs based on the positive effect of fractures on reservoir transport properties (Figure 1.3):

[1] Schlumberger Market Analysis, 2007

Type I - Fractures provide the essential porosity (i.e. storage capacity) and flow capacity in a reservoir where matrix porosity and permeability are low. In this type of reservoir, fracture characteristics are the dominant parameters for reservoir evaluation and few producing wells are required to deplete the reservoir.

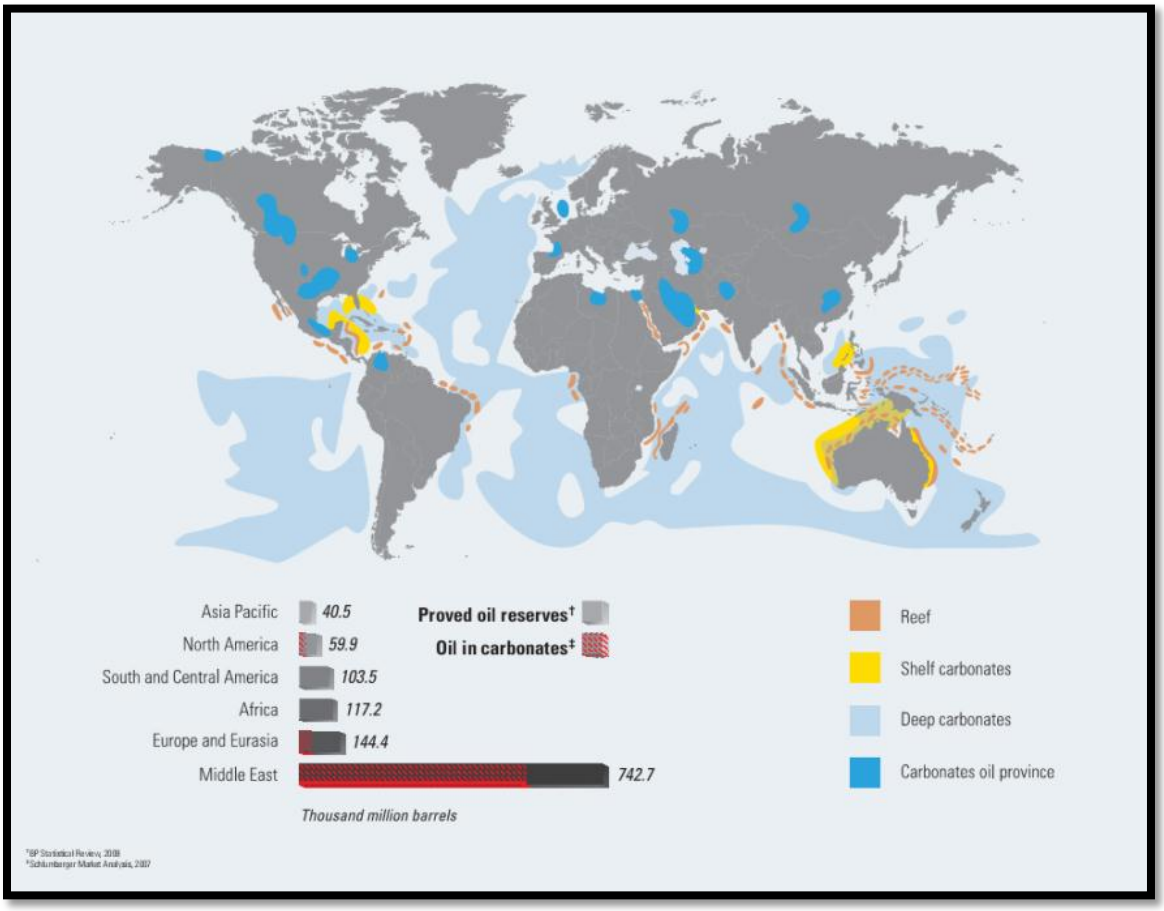

Figure 1.2. World distribution of carbonate reservoirs [reproduced from BP Statistical Review, 2008 & Schlumberger Market Analysis, 2007]

Type II - Rock matrix has higher porosity whereas fractures provide the essential flow capacity in a reservoir. In this case, cross-flow between fractures and matrix and rate control are the key parameters, with production rate controlled by fractures. Monitoring fracture behavior is

important during water flooding processes and to assess the effect of large drawdowns which may lead to greater fracture closure and flow reduction.

Type III - The fractured reservoir is already economically producible (high porosity and permeability in the matrix) and the fractures provide an assist and tend to define the reservoir's flow property anisotropy.

Type IV – Fractures, perhaps partially filled with cementing agents, act as baffles and barriers to flow in an already producible reservoir and reduce the drainage and sweep efficiency.

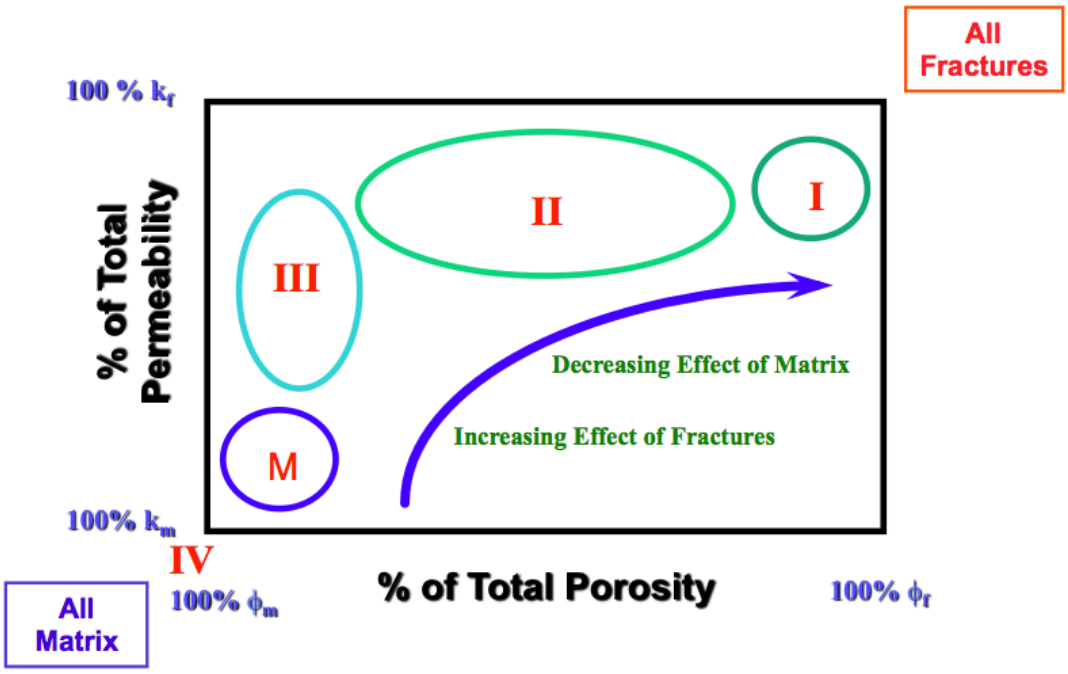

Figure 1.3. Naturally fractured reservoir classification [reproduced from Nelson, 2001]

Characterization of naturally fractured reservoirs (NFRs) is important for reservoir management because fractures behave differently than the rock matrix. In a fractured reservoir, for example, easily accessible fluids are stored in fractures, leading to rapid recovery at the early stage of exploitation, followed by a precipitous decline in production. Also, fracture behavior dominates

production and injection activities, and fracture flux is affected strongly by changes in pore pressure, temperature, saturation, as well as effective stress.

Fracture connectivity and conductivity is perhaps the most important flow properties of naturally fractured reservoirs. Conductivity is a strong function of fracture aperture ($k \propto w^2$) and the aperture is highly sensitive to the effective stress across the fracture as well as pore pressure, temperature and saturation. Pore pressure changes (Δp) arise as a result of production or injection of fluids from various wells, and temperature changes (ΔT) arise from injection of fluids that may be colder or hotter than the reservoir temperature. During enhanced oil recovery using steam injection, for example, fluid temperatures may be 250-300°C greater than the initial reservoir temperature. ΔT leads to thermoelastic strains, which in turn cause effective stress changes ($\Delta \sigma'$). The magnitude of the stresses induced by large ΔT values is huge, far higher than the initial in situ effective stresses at the typical depths involved (300-800 m in Alberta).

This stress-dependent permeability effect may dominate the flow behaviour in fractured reservoirs. It is also important in unconsolidated reservoirs with high matrix porosity and permeability, as well as consolidated reservoirs with low matrix permeability and porosity which require a dynamic model of permeability changes for better reservoir characterization [Davies and Davies, 2001]. Unless these changes are understood and analyzed, predictive modeling based on physical processes is not possible (excepting curve-fitting to history, which is not fully physical modeling). These effects are usually ignored or simplified (i.e. linear behavior) in conventional oil reservoirs, an assumption that may be sufficient in some cases (e.g. a dense un-

fractured quartzite reservoir), but is not appropriate for NFR's. Hence, coupled Δp, ΔT and $\Delta \sigma'$ effects must be considered for fractured reservoirs.

1.3 THM Coupling in Naturally Fractured Reservoirs

The word coupling refers to combined analysis of interacting physical processes that have in the past been treated separately. For example, in the case of fluid flow in fractured media, input of hot or cold fluids changes the stresses, altering the fracture apertures, which affects the conductivity and thus the flow rate and temperature changes. This type of feed-back loop is characteristic of coupled processes.

Conventional non-coupled reservoir simulators calibrated empirically through history-matching are not appropriate for modeling the simultaneous interaction among effective stress, pressure and temperature in a reservoir, as they consider pore compressibility as the only geomechanical parameter for simulation and assume permeability and porosity as static or pressure-dependent variables. These assumptions are insufficient because fracture conductivity is a strong function of effective stress and temperature as well as pressure. Parameter impacts on both reservoir characterization and simulation processes should be considered via a thermo-hydro-mechanically (THM) coupled approach for simulations that are more physically correct and thus more likely to be properly calibrated (Figure 1.4).

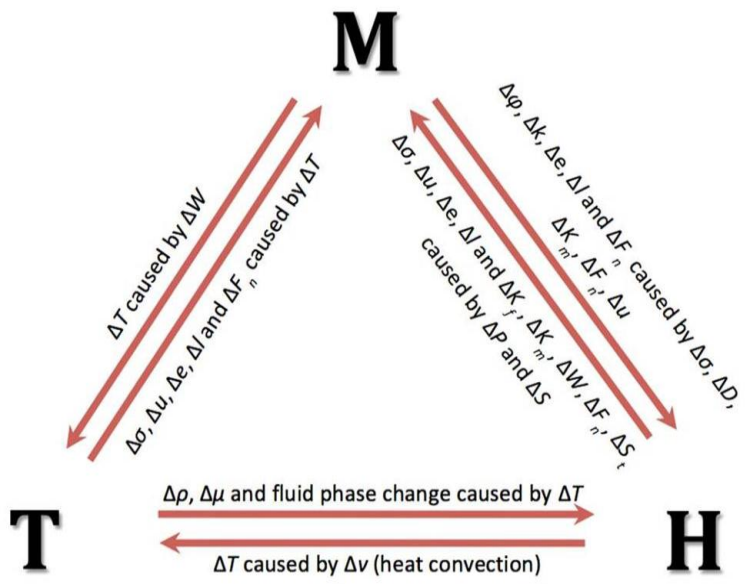

M	σ	stress
	W	Mechanical work
	K_m	Deformability
	S_t	Strength
	D	Rock damage
	u	Relative displacement
	l	Size
	F_n	Connectivity
	K_f	Fracture`s stiffness
H	P	Fluid pressure
	v	Velocity
	S	Saturation
	ρ	Density
	μ	Viscosity
	e	Hydraulic aperture
	φ	Porosity
	k	permeability
T	T	temperature

Figure 1.4. Basic mechanisms of coupled THM processes in fractured reservoirs [Lanru and Xiating, 2003]

The level of Δσ′-Δp-ΔT coupling can be classified into three different categories: (i) explicit, (ii) iterative, and (iii) fully-coupled. The most robust method is the fully-coupled approach, where the momentum conservation, fluid mass conservation, and energy conservation governing equations are solved simultaneously. To our knowledge, there is no commercial fully-coupled simulator yet and most of the effort has been toward iterative coupling between existing fluid flow and geomechanical simulators, where coupling parameters are sent back and forth between the simulators until convergence. This approach does not require so much code development and will produce the same results as a fully coupled approach if both use sufficiently tight convergence tolerances for iterations [Settari and Walters, 2001]. Some of the advantages and disadvantages of different coupling approaches are presented in Table 1.1.

Table 1.1. Advantages and disadvantages of coupling techniques [Jalali and Dusseault, 2011]

Approach	Advantage	Disadvantage
Explicit Coupling	▪ Effective and time-saving for subsidence problems ▪ Flexible and straightforward	▪ One-way coupling for geomechanics ▪ Stability and accuracy
Iterative Coupling	▪ Flexible in the case of numerical methods ▪ It is possible to couple conventional reservoir simulators (e.g. ECLIPSE, TOUGH2, STARS) with geomechanical modules (e.g. FLAC, UDEC, VISAGE) .	▪ Require large number of iterations (1st order convergence) ▪ Relatively small jumps in pore volume can be handled
Full Coupling	▪ The most stable approach ▪ Preserves 2nd order convergence ▪ Reliable and a benchmark for other coupling methods	▪ Difficult to couple existing modules and softwares ▪ Require more code development ▪ Slower than other coupling techniques

1.4 Hybrid Numerical Models

The main idea of any numerical method is to replace the problem with an approximate problem which is more easily solved, with the solution as close as possible to the true solution. A variety of numerical methods have been used to model THM coupled problems. Among them, hybrid models, which are defined as a combination of different numerical methods, are quite popular among modelers as they benefit from all numerical methods that are involved. However, the computational load is heavy and displacement continuity and stress equilibrium at the interfaces are concerns.

1.5 Goals of the Thesis

Moving toward an approach which could clarify the physics of thermo-hydro-mechanical processes in naturally fractured reservoirs is the main goal of this study. In this case, the ideal approach would be explicit representation of fractures in a fractured reservoir, especially in the

sensitive areas such as near the wellbore, and then calculation of the effect of pressure, temperature, and deformation on fracture properties (i.e. aperture) to update the reservoir properties such as matrix and fracture porosity and conductivity. As mentioned before, there is no commercial fully coupled simulator in the industry that can consider the behavior of fractures explicitly under thermal injection and production. Furthermore, for realistic simulation, it is necessary to consider the opening, shearing and dilation of natural fractures during injection and production activity.

To reach this goal, a coupling approach between fluid-flow and geomechanics in a non-isothermal continuum will be considered in order to model the influence of production activities such as fluid production, injection, or thermal recovery, on fractures within a linear poroelastic, isotropic and homogeneous medium. For this purpose, a finite difference method (FDM) is combined with a displacement discontinuity method (DDM), which is an indirect boundary element method, to model the influence of reservoir activities.

In the following chapters, thermo-poroelasticity, its governing equations and the required conservation equations are reviewed in Chapter 2; a brief review of different numerical methods for fracture reservoir modeling followed by a description of displacement discontinuity method are presented in Chapter 3; combination of the finite difference method with a thermo-poroelastic displacement discontinuity method is introduced in Chapter 4; several analytical verifications and a comparison between poroelastic, thermoelastic and thermo-poroelastic behavior of a single fracture are presented in Chapter 5; several applications of this method are

described and demonstrated in Chapter 6; and conclusions and recommendations are made in Chapter 7.

Chapter 2
Thermo-poroelasticity

The coupled response of geomaterials to man-made perturbations (e.g. cold water injection, steam injection, and hydraulic fracturing) cannot be predicted by considering each process separately, although this is part of the process of understanding coupling. A THM model is needed to study the two-way interactions among temperature (T), pressure (H) and deformation (M), a problem rendered far more complex when fractures are included because many ambiguities remain associated with the thermal, hydraulic and mechanical response of fractures under coupled circumstances. THM coupling is defined via the fundamental coupling principles of thermo-poroelasticity which can be defined as the combination of two-way coupling of thermoelasticity (TM) and poroelasticity (HM).

Thermo-poroelasticity describes the coupling of pore pressure, temperature, stress and deformation in a deformable, fluid-saturated porous medium via combining the energy conservation equation with Fourier's law, the fluid mass conservation equation with Darcy's law and the linear momentum conservation equation with Hooke's law. In order to represent a thermo-poroelasticity model, four sets of governing equations should be defined as below:

- Constitutive equations
- Force equilibrium equations
- Fluid diffusion equations
- Heat entropy balance

It is worthwhile to describe some definitions about porous media here. Based on Coussy (2004), a fluid-saturated porous media consists of a matrix and a porous space, with the latter usually interconnected and filled by a fluid (effective porosity). The matrix is composed of solid material as well as some occluded porosity which is not an effective porosity and it may be saturated with fluid. In another approach, a porous medium is a combination of two continua, i.e. the skeleton continuum and the fluid continuum (Figure 2.1). The skeleton is composed of the matrix and connected porous space without any fluid, whereas the fluid continuum contains saturated porous space with fluid without any matrix.

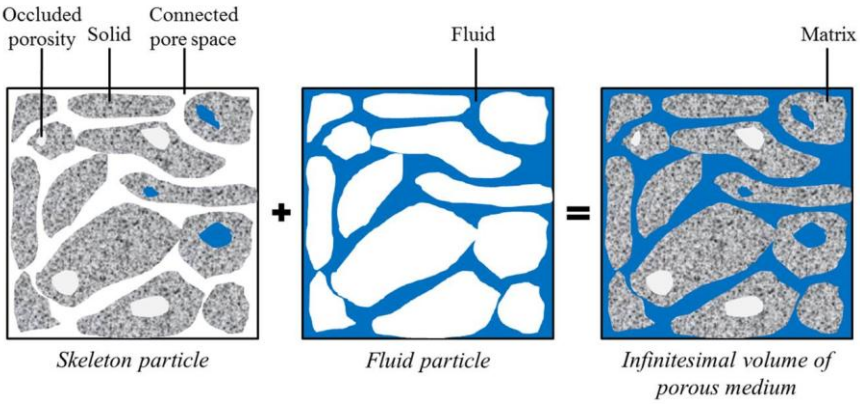

Figure 2.1. Porous medium as the superposition of skeleton particle and fluid particle in an infinitesimal volume [reproduced from Coussy, 2004].

2.1 Literature Review

In the beginning of 18th century, Gough introduced thermoelasticity through the concept of material temperature changes due to stretching and Weber (1830) formularized the thermoelastic effect. Schiffman (1971) introduced heat transfer into Biot's poroelastic concepts, and the governing equation of thermoelastic consolidation was provided by Booker and Savvidou (1985). They considered only conductive flux, not convection, which is the mechanism of heat

transfer via fluid flow. In 1978, Aktan and Farouq Ali worked on induced thermal stresses due to hot water injection and introduced the thermoelastic stress-strain relationship. Hojka et al. (1993) solved the convection and conduction-coupling problem for a plane strain borehole in analytical form. They showed the stress and temperature distributions around the borehole for some steady-state flow cases without heat loss to bounding strata.

The fundamentals of poroelasticity are based on the original concept of effective stress and one-dimensional consolidation for incompressible solid grains formulated by Terzaghi in 1925. Thereafter, Biot (1941) investigated the coupling between stresses and pore pressure in a porous medium and developed a generalized three-dimensional theory of consolidation with the basic principles of continuum mechanics including mineral compressibility, the "Theory of Poroelasticity" [Geertsma, 1966]. Biot's theory and published applications are oriented more toward rock mechanics than fluid flow so it is less compatible with conventional fluid-flow models (without geomechanics consideration) in terms of concept understanding, physical interpretation of parameters (e.g., rock compressibilities), and computer code implementation.

Skempton (1954) derived a relationship between the total stress and fluid pore pressure under undrained initial loading through the so-called Skempton pore pressure parameters A and B. Geertsma (1957) gave a better insight to the relationship among pressure, stress and volume, clarifying the concept of compressibility in a porous medium and van der Knaap (1959) extended his work to nonlinear elastic geomaterials such as dense but uncemented sands. Geertsma (1966) applied Biot's theory to subsidence problems in petroleum engineering, perhaps the first loosely coupled flow-geomechanics analysis published.

Nur and Byerlee (1971) proved that the effective stress law proposed by Biot is more general and physically sensible than that proposed by Terzaghi, although Terzaghi understood clearly the limitations of the assumptions he had to make in the 1920's to solve practical engineering problems in clay consolidation (one-dimensional analysis, ignoring fluid and mineral grain compressibility, etc.). In other developments relevant to coupled flow-stress problems, Ghaboussi and Wilson (1973) introduced fluid compressibility into classic soil mechanics consolidation theory, and Rice and Cleary (1976) showed how to solve poroelasticity problems by assuming pore pressure and stress as primary variables instead of displacements as employed by Biot.

2.2 Equations of State and Constitutive Equations

As mentioned before, three physical laws known as equations of state as well as constitutive equations for stress, pressure and temperature are required to describe the physical behavior of a thermo-hydro-mechanical model. In this section a brief review of Hooke's law, Darcy's law and Fourier's law is given as well as the constitutive equations for calculating the total stress, fluid content and specific entropy variation in porous media.

2.2.1 Hooke's law

In reality, the stress-strain behavior of rocks is quite complicated and some assumptions and simplifications are usually considered to estimate the behavior of rocks with reasonable simplicity. The most commonly used assumption for the stress-strain relationship of rocks is *linear elasticity* that considers the strain tensor as a linear function of stress tensor. This is a reasonable assumption for the rock behavior under (small) incremental stress changes. Also it is

assumed that the stress is not dependent on the rate of strain changes and the history of strains. Considering stress and strain as second order tensors with six components each in three-dimensional coordinates, the stress-strain relationship for a linear isotropic elasticity, which is known as *Hooke's law*, can be written as:

$$\boldsymbol{\sigma}_{ij} = 2G\boldsymbol{\varepsilon}_{ij} + \lambda\varepsilon_{\text{vol}}\delta_{ij} \qquad i, j = 1,2,3 \tag{2.1}$$

where $\boldsymbol{\sigma}_{ij}$ and ε_{ij} are total stress and linearized strain tensors, G is shear modulus, λ is Lamé's first parameter, ε_{vol} is the volumetric strain ($\varepsilon_{\text{vol}}=\boldsymbol{\varepsilon}_x+\boldsymbol{\varepsilon}_y+\boldsymbol{\varepsilon}_z$) and δ_{ij} is the Kronecker delta that is defined as:

$$\delta_{ij} = \begin{cases} 0 & \text{for } i \neq j \\ 1 & \text{for } i = j \end{cases}$$

The two indices for stress and strain correspond to the three principle directions (i.e. x, y and z or 1, 2 and 3) and are used to describe these tensors of which the first index describes the plane on which the stress or strain acts, whereas the second index shows the direction of the stress or strain. $\boldsymbol{\sigma}_{12}$, for example, corresponds to the total stress acting on the x-plane toward the y-direction.

2.2.2 Darcy's law

Viscous single phase fluid flow in porous media is usually described by Darcy's law, which relates the fluid volume flow rate to pore pressure gradient ignoring the gravity effect, as below:

$$\mathbf{Q}^{\text{f}} = \mathbf{q}^{\text{f}} A = -\frac{\mathbf{k}}{\mu} A\nabla p \tag{2.2}$$

where $\mathbf{Q}^{\mathrm{f}}$ and $\mathbf{v}^{\mathrm{f}}$ are volumetric fluid flow rate and fluid flux vector (known as Darcy's velocity) per unit time flowing through a surface, respectively. A is the surface through which the fluid flows, μ is the fluid dynamic viscosity, $\mathbf{k}$ is the second rank intrinsic permeability tensor and ∇p is the pore pressure gradient. The permeability tensor is usually symmetric (i.e. $k_{xy}=k_{yx}$).

Darcy's low is valid for laminar and viscous flow in a continuum. In laminar flow, velocity is proportional to the first power of the hydraulic gradient (Poiseuille's law), and this criterion can be quantified using the Reynolds number that gives a measure of the ratio of inertial forces to viscous forces and is defined as

$$\mathrm{Re} = \frac{\rho_{\mathrm{f}} \left|\mathbf{q}^{\mathrm{f}}\right| d}{\mu} \tag{2.3}$$

Here ρ_{f} is the fluid density, $|\mathbf{q}^{\mathrm{f}}|$ is the magnitude of Darcy's velocity and d is the characteristic length. Based on experimental data, flow regimes with Re less than 1 can be considered as Darcian flow, which is the assumed case for porous media flow [Bear, 1988].

2.2.3 Fourier's law

Fourier in 1822 formulated an empirical relationship between the heat conduction rate and temperature gradient in the direction of heat flow by introducing the thermal conductivity as below:

$$\mathbf{Q}^{\mathrm{h}} = \mathbf{q}^{\mathrm{h}} A = -\mathbf{k}_{\mathrm{T}} A \nabla T \tag{2.4}$$

where $\mathbf{Q}^{\mathrm{h}}$ and $\mathbf{v}^{\mathrm{h}}$ are the volumetric heat flow rate and heat flux vector per unit time, respectively, $\mathbf{k}_{\mathrm{T}}$ is the second rank thermal conductivity tensor and ∇T is the temperature gradient. The thermal conductivity tensor is also symmetric (i.e. $k_{\mathrm{T}\,xy}=k_{\mathrm{T}\,yx}$).

Thermal conductivity of a porous medium depends on temperature, pressure, pore fluids composition, mineralogy and geometric microstructure [MacGillivray et al., 1996]. In a fluid-saturated porous medium containing solid and fluid phases with an identical temperature, an equivalent thermal conductivity can be defined for the whole medium. The equivalent thermal conductivity tensor $\mathbf{k}_{T\,b}$ is composed of the isotropic thermal conductivity of the porous medium term neglecting the fluid flow ($k_{T\,b} = (1-\phi)k_{T\,s} + \phi k_{T\,f}$), and a macro-conductivity term which arises due to the fluid velocity heterogeneity [Castelletto, 2010]. Here the subscripts b, s, and f correspond to bulk, solid and fluid, respectively.

2.2.4 Constitutive Equations

Three constitutive equations are required to describe an isotropic and homogeneous saturated elastic porous material under small strain and laminar fluid flow conditions. This is done by combining the isothermal hydromechanical governing equations introduced by Biot [1941] with a non-isothermal term considering the thermal expansion due to temperature changes. Three conjugate pairs (six variables in total) are implemented to describe a thermo-poroelastic system, which are

- Total stress $\boldsymbol{\sigma}$ and linearized strain $\boldsymbol{\varepsilon}$;
- Pore pressure p and fluid content m;
- Temperature T and specific entropy ς.

The fluid content is defined as fluid volume per unit volume of the porous medium [Rice and Cleary, 1976] and the specific entropy is the entropy of the porous medium per unit volume [McTigue, 1986]. These conjugate pairs are scalar variables except for the total stress and strain

which are both second rank tensors with six independent components each. The classical continuum mechanics sign convention is considered for stresses, i.e. tensile stress is positive whereas compressive stress is negative. For strains, elongation is positive whereas shortening is negative. Pore pressure compression is considered as positive in this study for consistency.

Considering strain, pore pressure and temperature as independent variables, total stress, fluid mass content and specific entropy variation, which are assumed as dependent variables, can be rewritten as [Coussy, 2004]:

$$\Delta\sigma_{ij} = 2G\varepsilon_{ij} + \lambda\varepsilon_{\mathrm{vol}}\delta_{ij} - \alpha\Delta p\delta_{ij} - K_{\mathrm{b}}\beta_{\mathrm{s}}\Delta T\delta_{ij} \tag{2.5a}$$

$$\Delta m = \alpha\varepsilon_{\mathrm{vol}} + \frac{\alpha}{BK_{\mathrm{b}}}\Delta p + \phi_0(\beta_{\mathrm{f}} - \beta_{\mathrm{s}})\Delta T \tag{2.5b}$$

$$\Delta\varsigma = K_{\mathrm{b}}\beta_{\mathrm{s}}\varepsilon_{\mathrm{vol}} - \phi_0(\beta_{\mathrm{f}} - \beta_{\mathrm{s}})\Delta p - \frac{1}{T_0}\left[\phi_0 C_{\mathrm{f}} + (\alpha - \phi_0)C_{\mathrm{s}}\right]\Delta T \tag{2.5c}$$

In (2.5), K_{b} is the skeleton bulk modulus, α (=1-K_{b}/K_{s}) is Biot's effective stress coefficient, B is the Skempton's pore pressure coefficient, ϕ_0 is the initial porosity, β_{s} and β_{f} are the volumetric thermal expansion coefficients of solid and fluid, T_0 is the absolute temperature and C_{f} and C_{s} are the fluid and rock specific heat, respectively.

Some assumptions were considered in the derivation of the constitutive equations. In Eq. 2.5a, it was assumed that temperature variations do not change the porosity (ϕ_0), so the volumetric skeleton thermal expansion coefficient was replaced by the solid thermal expansion coefficient. In Eq. 2.5b, the last term on the right-hand side reflects changes in the fluid content due to temperature changes at constant volumetric strain and pressure, which required considering pore

and fluid thermal expansion coefficients. Applying the constant porosity assumption in this term, the solid thermal expansion coefficient can be used. Finally the last term in Eq. 2.5c corresponds to the volumetric specific heat that can be defined as a combination of both solid and fluid volumetric specific heat [Palciauskas and Domenico, 1982; McTigue, 1986; Coussy, 2004; Ghassemi and Zhang, 2004].

2.3 Balance Laws

Three conservation governing equations which govern the hydromechanical system in a non-isothermal condition will be described in this section. These equations are the force equilibrium equation for stress and deformation, the fluid diffusion equation for pore pressure and the heat entropy balance to estimate temperature propagation.

2.3.1 Linear Momentum Conservation Equation

The force-equilibrium equation for a porous medium arises as a direct result of the linear momentum conservation equation which states that the linear momentum variation of an arbitrary portion of a continuum over time is equal to the resultant force acting on that considered portion (i.e. tractions and body forces) in the following form:

$$\frac{d}{dt}\int_V \rho v_i dV = \int_S \sigma_{ij} n_j dS + \int_V \rho b_i dV \tag{2.6}$$

Assuming a quasi-static condition (no inertial forces) and using the surface integral conversion into the volume integral, the static force-equilibrium equation can be written as:

$$\sigma_{ij,j} + \rho b_i = 0 \tag{2.7}$$

In Eqs. 2.6 and 2.7, S and V are the surface area and volume of the control volume, respectively, n_i is the unit vector in i-direction, ρ is the bulk density of medium ($\rho = \phi\rho_f + (1 - \phi)\rho_s$), v_i is the velocity vector in the i-direction and b_i is the solid body force. It should be noted that Einstein tensorial notation has been adopted in these formulations.

Applying the constitutive equation (2.5a) into Eq. 2.7 while neglecting body forces yields:

$$2G\varepsilon_{ij.j} + \lambda\varepsilon_{\mathrm{vol},i} - \alpha p_{,i} - K_b\beta_s T_{,i} = 0 \tag{2.8}$$

Using the relationship between strains and displacements ($\varepsilon_{ij}=1/2(u_{i,j}+u_{j,i})$), Eq. 2.8 leads to Navier-type force equilibrium equations:

$$Gu_{i,jj} + (\lambda + G)u_{j,ji} - \alpha p_{,i} - \beta_s K_b T_{,i} = 0 \tag{2.9}$$

2.3.2 Fluid Mass Conservation Equation

Conservation of fluid mass for a control volume without any chemical reaction stipulates that the fluid mass variation over time in a control volume is equal to the net mass flow through the control surface, which has the following form:

$$\frac{\partial \rho_f \zeta}{\partial t} = -\nabla.\left(\rho_f \mathbf{q}^f\right) \pm \rho_f q_s^f \tag{2.10}$$

The first term on the left hand side is the fluid mass content ($\rho_f.\zeta$) variation over time, whereas the first term on the right hand side is the net mass flow and the second term is the source/sink mass flow rate ($\rho_f.q^f_s$), for which a positive sign corresponds to injection into the control volume and a negative sign is associated with fluid withdrawal from the control volume.

Applying the constitutive equation for the fluid content (Eq. 2.5b) and Darcy's law for the fluid flux vector (Eq. 2.2) while assuming a constant fluid density over time leads to

$$\alpha\varepsilon_{\mathrm{vol},t} + \frac{1}{M}\,p_{,t} + \phi_0(\beta_\mathrm{f} - \beta_\mathrm{s})T_{,t} = \boldsymbol{\kappa}_\mathrm{p}\,p_{,ii} \pm q_\mathrm{s}^\mathrm{f} \tag{2.11}$$

where $\boldsymbol{\kappa}_\mathrm{p}$ (=$\mathbf{k}/\mu$) is the mobility tensor and M is the Biot's modulus (Biot denotes it by Q) which is a measure of the amount of fluid that can be forced into the rock under constant rock volume and temperature [Biot, 1941]. In an isothermal continuum with a rigid and undeformable rock, Eq. 2.11 reduces to the typical diffusion equation in hydrology and petroleum engineering as:

$$p_{,t} = \frac{k}{\mu\phi c_\mathrm{f}}\,p_{,ii} \pm q_\mathrm{s}^\mathrm{f} \tag{2.12}$$

where c_f is the fluid compressibility and $c^\mathrm{f} = k/\mu\phi c_\mathrm{f}$ is the hydraulic diffusivity.

2.3.3 Energy Conservation Equation

In writing the energy conservation equation, the porous medium is assumed to be an open system, i.e. the control volume may exchange fluid mass with the outside through deformation [Berchenko, 1998]. Also it is assumed that viscous dissipation, radiative effects and work (energy loss) due to pressure changes are negligible [Bejan and Kraus, 2003]. Considering no heat transfer between solid and fluid phases (i.e. parallel heat conduction), heat transfer in solid and fluid phases can be written as

$$(1-\phi)\rho_\mathrm{s}C_\mathrm{s}\frac{\partial T_\mathrm{s}}{\partial t} = (1-\phi)\nabla.(k_{\mathrm{T\,s}}\nabla T_\mathrm{s}) + (1-\phi)q_\mathrm{g}^\mathrm{h} + h(T_\mathrm{f} - T_\mathrm{s}) \tag{2.13}$$

$$\phi\rho_\mathrm{f}C_\mathrm{f}\frac{\partial T_\mathrm{f}}{\partial t} + \rho_\mathrm{f}C_\mathrm{f}\mathbf{q}^\mathrm{f}\nabla T_\mathrm{f} = \phi\nabla.(k_{\mathrm{T\,f}}\nabla T_\mathrm{f}) + \phi q_\mathrm{g}^\mathrm{h} + h(T_\mathrm{s} - T_\mathrm{f}) \tag{2.14}$$

Here, C_s and C_f are the solid specific heat and fluid specific heat at constant fluid pressure, respectively, q^h_g is the rate of heat generation per unit volume and h is the heat transfer coefficient between solid and fluid phases. As shown in Eq. 2.14, a convective term (which contains fluid velocity) is required for the fluid heat transfer calculation. In a steady-state heat transfer case, solid and fluid temperatures in each control volume at a specific time are identical, but in the case of transient heat flow, the solid temperature lags behind the fluid temperature (Figure 2.2) [Hojka et al., 1993]. However, it is acceptable for most cases such as the current study to assume that solid and fluid phases are in local equilibrium (i.e. $T_s = T_f = T$). In this case, Eqs 2.13 and 2.14 can be added together as

$$\rho_b C_b \frac{\partial T}{\partial t} + \rho_f C_f \mathbf{q}^f \nabla T = \nabla.(k_{T\,b} \nabla T) + q^h_g \tag{2.15}$$

where [Bejan and Kraus, 2003]

$$\rho_b C_b = (1-\phi)\rho_s C_s + \phi \rho_f C_f \tag{2.16}$$

$$k_{T\,b} = (1-\phi)k_{T\,s} + \phi k_{T\,f} \tag{2.17}$$

$$q^h_{g\,b} = (1-\phi)q^h_{g\,s} + \phi q^h_{g\,f} \tag{2.18}$$

By introducing the heat capacity ratio ($\vartheta = \rho_b C_b / \rho_f C_f$), Eq. 2.15 can be written as

$$\vartheta \frac{\partial T}{\partial t} + \mathbf{q}_f.\nabla T = \nabla.(c^T \nabla T) + \frac{q^h_{g\,b}}{\rho_f C_f} \tag{2.19}$$

where $c^T = k_{T\,b}/\rho_f C_f$ is the thermal diffusivity of the saturated porous medium.

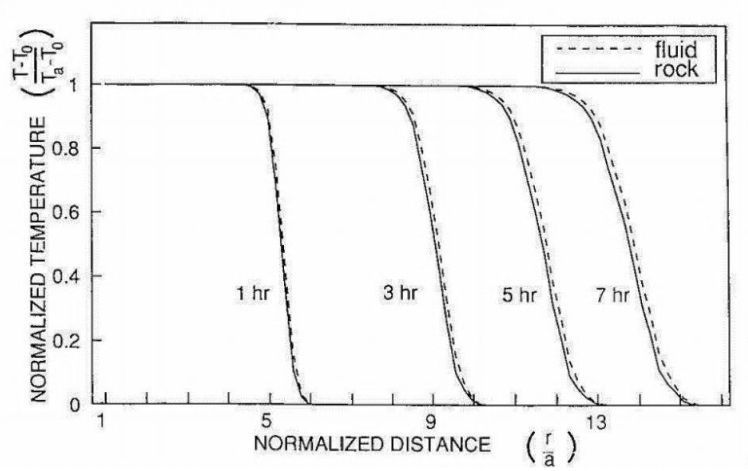

Figure 2.2. Steady state and transient heat transfer around a borehole during hot fluid injection [reproduced from Hojka et al., 1993]

2.4 Chapter Summary

This chapter described the fundamental governing equations of thermo-hydromechanical coupling of a non-isothermal fully saturated poroelastic medium. For this purpose a brief review of the physical laws and constitutive equations was given, followed by the development of the three conservation partial differential equations (Eqs. 2.9, 2.11, and 2.19) that require solving together in a fully coupled approach.

Chapter 3

Displacement Discontinuity Method

3.1 Numerical Methods for Fractured Reservoirs Modeling

The main idea of any numerical method is to replace the problem with an approximate problem which is easier to solve with the solution being as close as possible to the original (or "real") solution. A variety of numerical methods has been used to model THM coupled problems (Figure 3.1).

In numerical methods, a continuum is usually subdivided into a finite number of domains (elements, block-averaged nodes …) with finite degrees of freedom and simplified mathematical behaviour. To solve the discretized problem numerically, the following criteria should be satisfied:

- The physical statement of the problem must be expressed by the appropriate governing partial differential equations for the physics being considered, and,
- The continuity condition at interfaces between adjacent elements must be satisfied.

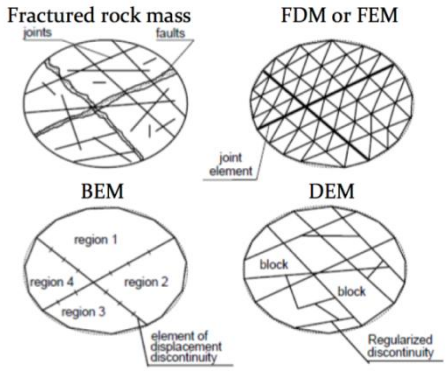

Figure 3.1. Fractured rock mass representation using different numerical methods [reproduced from Jing, 2003]

In the case of fractured reservoir modeling, two different approaches have been used in the literature, continuous and discontinuous (discrete) methods. In the following, some of the numerical techniques used in each category are described. Among these methods, the displacement discontinuity method, which is an indirect boundary element approach, has been chosen to simulate the fracture behavior, and is therefore described in greater detail than other methods.

3.1.1 Continuous Methods

3.1.1.1 Finite Difference Method (FDM)

The Finite Difference Method (FDM) is based on finding an approximate solution for partial differential equations (PDEs) using a finite number of points (i.e. grid points, mesh points or net points). In this case, each derivative is replaced with an approximate differential formula based on the Taylor's series expansion and then the PDE is converted to a set of algebraic system equations which relate the values of unknown variables (i.e. pressure, temperature, displacement) at each grid point [Aziz & Settari, 1979]. The solution of this algebraic system of equations by considering the applied boundary conditions of the problem will satisfy the governing PDEs as well as the specified boundary conditions.

Fractures cannot be modeled explicitly in FDM, as it requires continuity of the governing equations between neighboring grid points. However it is possible to introduce weakness zones with a certain specified thickness that cannot permit opening and must remain attached to the neighboring nodes [Jing, 2003]. Also, Caillabet et al. (2000) and Granet et al. (2001) implemented special elements, known as *fracture elements*, to model fluid flow (Figure 3.2). In

their approach, fracture thickness is taken into account for the fluid flow calculation but not in the geometrical representation of the problem, as the fracture thickness is negligible compared to the matrix block size.

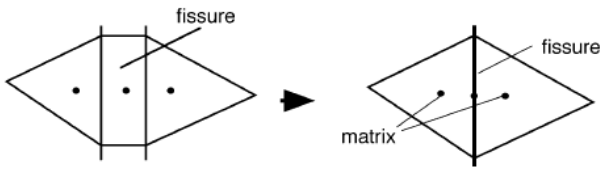

Figure 3.2. Real and geometrical fracture element representation [reproduced from Granet *et al.*, 2001]

3.1.1.2 Finite Element Method (FEM)

The Finite Element Method (FEM) is based on a piecewise representation of the solution in terms of specified basis functions. FEM consists of three fundamental steps, which are: domain discretization, local approximation, and global matrix assembly and solution. The problem's domain is discretized into a finite number of subdomains (finite elements) with a regular shape and fixed number of nodes. The field variables are then written as a trial function of its nodal value in a polynomial form (i.e. weak form). Appropriate test functions are multiplied by the weak form of the governing equations, and then integrated over each element. The results are then assembled into a global matrix, and by solving the linear system of equations, the value of the field variables at each integration point is determined.

Much work has been done during the last 40 years to represent rock fractures in the FEM method because of its generality and ability to accommodate non-linear properties and relationships (e.g. $k = f(\sigma')$ or $E = f(\sigma')$). Goodman et al. (1968) proposed a zero thickness *joint element* in which the normal and shear stresses and the deformations normal to and along the fractures are related

through constant normal and shear stiffness values (K_n and K_s). The zero thickness assumption (i.e. large aspect ratio) may lead to some numerical ill-conditioning in the global matrix.

Zienkiewicz et al. (1970) introduced a six-point small thickness fracture element by adding two more nodes in the middle of the element. Adding more nodes allows the element to be curved, increasing the efficiency of FEM to model problems with complex geometries. Ghaboussi and Wilson (1973) implemented aspects of plastic behaviour in a finite thickness FEM fracture element and Desai et al. (1984) proposed a *thin-layer* element that used a special constitutive law for contact and frictional sliding. Buczkowski and Kleiber (1997) implemented an interface element model for contact mechanics applications with an orthotropic friction based on the theory of plasticity (Figure 3.3). Nevertheless, these methods cannot be used to model large-scale fracture opening, sliding and complete detachment (opening) because of the basic continuum assumption of FEM.

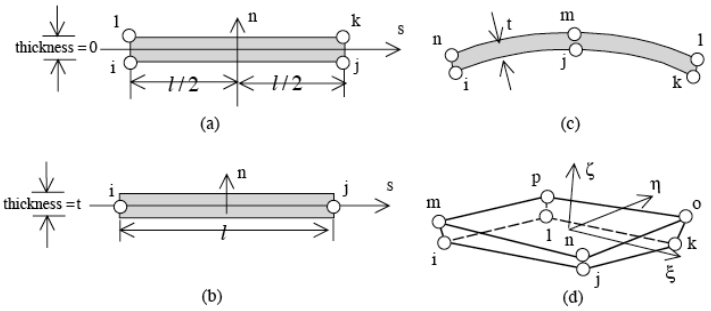

Figure 3.3. FEM fracture elements by (a) Goodman *et al*. (1968), (b) Ghaboussi and Wilson (1973), (c) Zienkiewicz *et al*. (1970) and (d) Buczkowski and Kleiber (1997) [reproduced from Jing, 2003]

3.1.1.3 Boundary Element Method (BEM)

Unlike finite difference and finite element methods, which require discretizing the whole region of the problem, in the Boundary Element Method (BEM) only the boundary of the region is

discretized. A known or calculated solution of a simple singular problem is used to build up the numerical solution for the whole mass by satisfying the boundary condition at each boundary element. BEM solutions can be summarized as:

1. Boundary discretization with a finite number of elements,

2. Approximation of the local solution at boundary elements via shape functions,

3. Evaluation of boundary influence coefficients,

4. Application of boundary conditions and solution of the linear system of algebraic equations,

5. Evaluation of field variables inside the domain at a specified number of points.

BEM methods can be classified into direct and indirect methods. In the direct formulation, calculated deformation and stresses have a clear physical meaning, whereas there is no explicit physical meaning for the displacements and tractions in the indirect formulation, they are expressed as fictitious source densities [Jing, 2003].

In direct BEM, fractures are modeled by assuming two opposite surfaces along the fracture plane, expect at the fracture tips where special tip elements have to be used to address mathematical singularities such as those associates with a sharp fracture tip. An alternative for fracture modeling is the Displacement Discontinuity Method (DDM), which is an indirect method. This method was first proposed by Salamon (1963, 1968) for tabular mine simulation and further developed by Crouch and Starfield (1983). It is based on integrating the analytical solution of a constant displacement discontinuity (DD) over a finite line segment embedded

within an infinite or semi-infinite elastic solid that can be orthotropic in properties, with the orthotropy oriented with the DD line segment.

3.1.2 Discontinuous Methods

3.1.2.1 Discrete Element Method (DEM)

In the Discrete Element Method (DEM) two types of mechanical behavior are considered: those of the discontinuities (the contacts) and those of the solid materials (the blocks or matrix). The analysis domain is treated as a combination of rigid or deformable (using FDM or FEM) matrix blocks and the contacts among them which are identified and updated during the simulation. As a result, the main difference between DEM and continuum methods is that in DEM the pattern of the contacts changes continuously, whereas in continuum methods the pattern is fixed [Jing, 2003].

Cundall and Hart (1989) identified five main classes of DEM codes:

- *Distinct Element Programs* assume rigid or deformable matrix blocks as well as deformable contacts among blocks. Time-marching is done explicitly in each time step to calculate the motion in the model to define the new set of contacts between blocks. Some of the representative codes are UDEC, 3DEC, PFC [ITASCA solution] and DIBS [Walton, 1980].
- *Modal Methods* use a modal superposition to deal with deformable blocks, which is suitable for loosely packed discontinua and dense packing simulation. Hocking et al. (1985) implemented this method in their code, CICE.

- *Discontinuous Deformation Analysis (DDA)* is similar to DEM for the block and contact deformation, except it assumes an iterative scheme of time-marching as well as superposition of strain modes. A representative code is DDA by Shi (1989).
- *Momentum-exchange Methods* assume rigid contacts and matrix blocks. During a collision, momentum is exchanged between two contacting bodies, and it also is possible to model frictional sliding [Hahn, 1988]
- *Limiting Equilibrium Methods* consider a rigid system of blocks and use vector analysis to evaluate the movement of blocks in the fractured system. Some examples include work done by Goodman and Shi (1985) and Warburton (1981).

3.1.2.2 Discrete Fracture Network (DFN) Method

Discrete Fracture Network (DFN) approaches consider fluid flow and transport phenomena in a discrete connected fractured media. The two key factors in DFN models are fracture geometry and transmissivity. DFN is a strong approach for fluid flow and transport simulation in areas which thermal and mechanical processes are not significant, such as in shallow fractured aquifers. It is difficult to model heat flow and mechanical deformation using DFN, so these phenomena must be analyzed and approximated with another parallel method. Most applications of DFN models focus on fracture conductivity characterization, fracture influence on flow, and near-field studies such as around a wellbore or tunnel [Jing, 2003].

Advantages and disadvantages of possible numerical methods which can be implemented to simulate fractured reservoirs have been summarized in Table 3.1.

Table 3.1. Advantages and disadvantages of possible numerical methods for coupled simulation of naturally fractured reservoirs

Numerical Method		Advantages	Disadvantages
Continuous	FDM	• Easy to formulate. • No local trial (interpolation) functions required to approximate PDEs. • The most direct and intuitive technique.	• Cannot handle complex geometries, material inhomogeneities. • Neumann boundary condition can be only approximated, not exactly enforced. • Inflexible in dealing with explicit fractures, due to the necessity of continuity of functions between neighboring grid points.
	FEM	• Flexible in handling material inhomogeneity and anisotropy. • No coordinate transformation is required for complex geometries. • Can handle complex boundary conditions. • Suitable for dynamic problems. • Neumann boundary conditions are enforced exactly.	• Large-scale opening, sliding and complete detachment are not permitted due to continuum assumptions. • Numerical ill-conditioning will occur due to large aspect ratios of fracture elements in the explicit representation of a large number of fractures. • Cannot be used for fracture growth, however there are some special algorithms to overcome this problem, e.g., enriched FEM.
	BEM	• Discretization of the boundary only (reduction of model dimension by one). • Simplified pre-processing. • Improved accuracy in stress concentration problems. • Simple and accurate modeling of problems involving infinite and semi-infinite domains. • Simplified treatment of symmetrical problems (no discretization needed in the plane of symmetry).	• Non-symmetric, fully populated system of equations in collocation BEM. • Treatment of inhomogeneous and non-linear problems is extremely difficult. • Requires the knowledge of a suitable fundamental solution, hence usually an elastic solution. • Practical application relatively recent, not as well-known as FEM among users.
Discontinuous	DEM	• Explicit representation of fractures. • Flexible to handle large amount of fractures.	• Lack of knowledge of the geometry of fractures. • Large amount of computation required. • Matrix-fracture flow interaction cannot handled adequately.
	DFN	• Requires fewer degrees of freedom in comparison with FEM. • Suitable for generic quantitative studies of fracture impacts.	• Lack of knowledge of the geometry of fractures and hydraulic properties of fractures. • Large amount of computation required. • Can't handle heat flow and mechanical process.
Hybrid Methods		• Benefits from both continuous and discrete methods.	• Large amount of computation required. • Displacement continuity and stress equilibrium at the interface is a big concern.

3.2 Elastic Displacement Discontinuity Method

The displacement discontinuity method is an indirect boundary element method developed by Crouch & Starfield in 1983 (based upon the original formulation by Salamon in the 1960's)

which uses the analytical solution for the displacement field arising from a finite line segment in an infinite body subjected to a constant displacement discontinuity. This method was developed for thin planar underground excavations, and then used for modeling faults, fractures and tabular reservoirs, as well as other cases with a large aspect ratio.

From a physical point of view, the displacement discontinuity can be envisioned as a line fracture where the opposing fracture surfaces have been displaced in different directions relative to each other (shear or normal displacement). This relative displacement may have any specified distribution along the fracture such as constant, linear, and quadratic; in this study a constant relative displacement is considered over the fractures (i.e. the displacement discontinuities).

As a numerical method, in this approach the fracture is discretized into N boundary elements with displacement discontinuities. Based on the analytical solution of a single and constant displacement discontinuity, a numerical solution can be derived using the superposition of the effects of all the N boundary elements.

In a two-dimensional infinite elastic solid with a finite line segment fracture, displacement discontinuities in the x and y directions are defined as the displacement difference between two sides of the fracture segment. Assuming a line fracture elongated from $-a$ to $+a$ along the x-axis (y=0), two surfaces can be distinguished in positive ($y=0^+$) and negative ($y=0^-$) sides. Based on this assumption, x- and y-displacements undergo a constant change crossing from one side to another which are described as D_x and D_y as below (Figure 3.4):

$$\begin{aligned} D_x &= u_x(x,0^-) - u_x(x,0^+) \\ D_y &= u_y(x,0^-) - u_y(x,0^+) \end{aligned} \tag{3.1}$$

Based on Eq. 3.1, D_x and D_y are positive as illustrated in Figure 3.4; i.e., positive D_y is associated with fracture closure and a negative value with fracture opening. It is assumed that the fracture has a finite thickness (aperture), small with respect to its length, to avoid overlapping the two surfaces for a positive value of D_y.

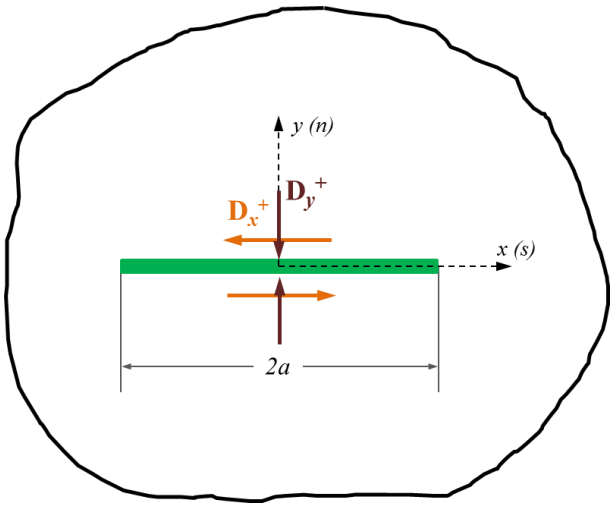

Figure 3.4. Constant displacement discontinuity components D_x and D_y [reproduced from Crouch and Starfield, 1983]

For deformation and stress in the infinite elastic solid as a function of constant displacement discontinuities and the geometry of fracture, Crouch proposed [Crouch, 1976]:

$$\begin{aligned} u_x &= D_x\left[2(1-\nu)f_{,y} - yf_{,xx}\right] + D_y\left[-(1-2\nu)f_{,x} - yf_{,xy}\right] \\ u_y &= D_x\left[(1-2\nu)f_{,x} - yf_{,xy}\right] + D_y\left[2(1-\nu)f_{,y} - yf_{,yy}\right] \end{aligned} \tag{3.2}$$

$$\begin{aligned} \sigma_{xx} &= 2GD_x\left[2f_{,xy} + yf_{,xyy}\right] + 2GD_y\left[f_{,yy} + yf_{,yyy}\right] \\ \sigma_{yy} &= 2GD_x\left[-yf_{,xyy}\right] + 2GD_y\left[f_{,yy} - yf_{,yyy}\right] \\ \sigma_{xy} &= 2GD_x\left[f_{,yy} + yf_{,yyy}\right] + 2GD_y\left[-yf_{,xyy}\right] \end{aligned} \tag{3.3}$$

The function $f(x,y)$ in Eqs. 3.2 and 3.3 is the integral solution of Kelvin's problem for plane strain conditions:

$$f(x,y) = \frac{-1}{4p(1-n)}\left[y\left(\arctan\frac{y}{x-a} - \arctan\frac{y}{x+a} \right) \right.$$
$$\left. -(x-a)\ln\sqrt{\left[(x-a)^2+y^2\right]} + (x+a)\ln\sqrt{\left[(x+a)^2+y^2\right]} \right] \tag{3.4}$$

The derivatives of function $f(x,y)$ which has been used in Eqs. 3.2 and 3.3 are

$$f_{,x} = \frac{\partial f}{\partial x} = \frac{1}{4\pi(1-\nu)}\left[\ln\sqrt{(x-a)^2+y^2} - \ln\sqrt{(x+a)^2+y^2} \right]$$
$$f_{,y} = \frac{\partial f}{\partial y} = \frac{-1}{4\pi(1-\nu)}\left[\arctan\frac{y}{x-a} - \arctan\frac{y}{x+a} \right]$$
$$f_{,xy} = \frac{\partial^2 f}{\partial x \partial y} = \frac{1}{4\pi(1-\nu)}\left[\frac{y}{(x-a)^2+y^2} - \frac{y}{(x+a)^2+y^2} \right]$$
$$f_{,xx} = -f_{,yy} = \frac{\partial^2 f}{\partial x^2} = \frac{1}{4\pi(1-\nu)}\left[\frac{x-a}{(x-a)^2+y^2} - \frac{x+a}{(x+a)^2+y^2} \right] \tag{3.5}$$
$$f_{,xyy} = -f_{,xxx} = \frac{1}{4\pi(1-\nu)}\left[\frac{(x-a)^2-y^2}{\left\{(x-a)^2+y^2\right\}^2} - \frac{(x+a)^2-y^2}{\left\{(x+a)^2+y^2\right\}^2} \right]$$
$$f_{,yyy} = -f_{,xxy} = \frac{y}{2\pi(1-\nu)}\left[\frac{x-a}{\left\{(x-a)^2+y^2\right\}^2} - \frac{x+a}{\left\{(x+a)^2+y^2\right\}^2} \right]$$

Displacement and stress are continuous everywhere in the infinite body. The only case that requires explicit evaluation is along the line $y = 0$. Based on the above equations, displacement is continuous for $|x| > a$ on $y = 0$, but have a constant discontinuity (D_x and D_y) for $|x| < a$. Stress is singular and discontinuous at $x = \pm a$, but are continuous everywhere else along $y = 0$. Also based on Eqs. 3.3, the normal stress (σ_{xx} and σ_{yy}) on $y = 0$ is dependent only on D_y whereas the shear stress σ_{xy} is dependent only on D_x. The fundamental solutions for a constant D_n and Ds in an elastic medium are presented in 0 A.

This method is suitable for modeling of isotropic and homogeneous impermeable fractured rocks in the case where there is no appreciable leak-off off the fluids flowing along the fractures into the matrix blocks.

3.3 Poroelastic Displacement Discontinuity Method

Carvalho (1990) proposed the fundamental solution of induced stress and pore pressure for a two-dimensional infinite porous media based on the theory of poroelasticity. This concept was developed more by other authors such as Tao et al. (2011). In this case, the effect of fluid pressure changes can be added to the elastic DDM solution to come up with the fundamental solutions for pore pressure, stress and displacement. The effect of fluid flow changes is considered in the formulation via introducing a fluid source strength term defined as the interface flow rate along the fracture (Figure 3.5), i.e.

$$\begin{aligned} D_{\mathrm{x}} &= u_{\mathrm{x}}(x,0^{-}) - u_{\mathrm{x}}(x,0^{+}) \\ D_{\mathrm{y}} &= u_{\mathrm{y}}(x,0^{-}) - u_{\mathrm{y}}(x,0^{+}) \\ Q_{\mathrm{fs}} &= q^{\mathrm{f}}_{\mathrm{int}} \end{aligned} \tag{3.6}$$

where Q_{fs} is the strength of fluid source, $q^{\mathrm{f}}_{\mathrm{int}}$ in the interface fluid flow rate per unit length and width of fracture. It should be noted that Q_{fs} is positive when there is a fluid flow from the fracture into the matrix (fluid leak-off).

As mentioned in Chapter 2, the governing equations 2.9 and 2.11 must be solved simultaneously (a fully coupled solution) to estimate pore pressure, stress and displacement in the domain under consideration. This can be done numerically using the definition of discontinuities in Eq. 3.6 and applying the initial conditions as well as inner and outer fracture boundary conditions as below:

Initial conditions

$$p(x,y,0) = p_0$$
$$u_x(x,y,0) = 0,\ u_y(x,y,0) = 0 \qquad (3.7)$$
$$\sigma_{xx}(x,y,0) = \sigma_{xx\ ini},\ \sigma_{yy}(x,y,0) = \sigma_{yy\ ini},\ \sigma_{xy}(x,y,0) = \sigma_{xy\ ini}$$

Boundary conditions

$$\text{Inner B.C.:}\quad \begin{aligned} & u_x(x,0^-,t) - u_x(x,0^+,t) = D_s \\ & u_y(x,0^-,t) - u_y(x,0^+,t) = D_n \qquad \text{for} \quad |x| \le a \\ & q_{int}^f = Q_{fs} \end{aligned} \qquad (3.8)$$

$$\text{Outer B.C.:}\quad \begin{aligned} & p(x,y,0) = p_0 \\ & u_x(x,y,0) = 0,\ u_y(x,y,0) = 0 \qquad \text{for} \quad \sqrt{x^2+y^2} \to \infty \\ & \sigma_{xx}(x,y,0) = \sigma_{xx\ ini},\ \sigma_{yy}(x,y,0) = \sigma_{yy\ ini},\ \sigma_{xy}(x,y,0) = \sigma_{xy\ ini} \end{aligned} \qquad (3.9)$$

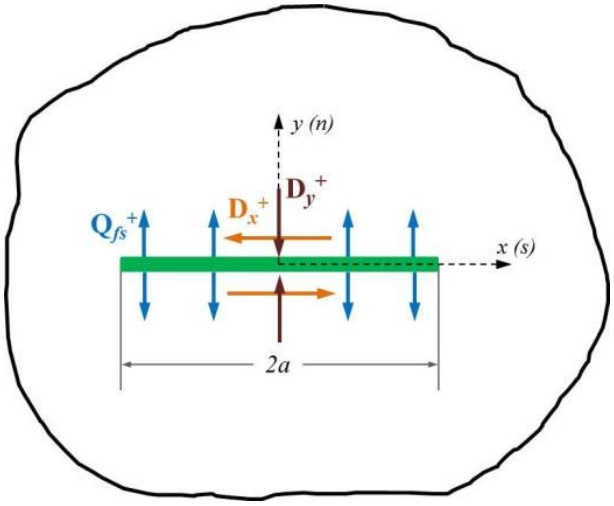

Figure 3.5. Constant displacement discontinuities and fluid source strength components [modified after Crouch and Starfield, 1983]

In these equations, p_0 is the initial pore pressure, D_n and D_s are the normal and shear displacement discontinuities (D_y and D_x in Eq. 3.6), and the 'ini' subscript specifies that it is an initial value. The inner boundary conditions in these equations correspond to the applied

constraint in the fracture, whereas the outer boundary conditions are defined by the in-situ conditions far from the fracture surfaces in the unaffected zone (the "far-field" conditions).

To solve the poroelastic governing equations, Carvalho (1990) proposed the superposition of induced displacement, stress and pore pressure calculated using two separate boundary conditions as follows:

- Constant fluid source strength without any displacement discontinuities, i.e.

$$q_{\text{int}}^{\text{f}} = Q_{\text{fs}},\ u_{\text{x}}(x,0^{-},t) - u_{\text{x}}(x,0^{+},t) = 0,\ u_{\text{y}}(x,0^{-},t) - u_{\text{y}}(x,0^{+},t) = 0$$

- Constant displacement discontinuities without any fluid source, i.e.

$$u_{\text{x}}(x,0^{-},t) - u_{\text{x}}(x,0^{+},t) = D_{\text{s}},\ u_{\text{y}}(x,0^{-},t) - u_{\text{y}}(x,0^{+},t) = D_{\text{n}},\ q_{\text{int}}^{\text{f}} = 0$$

The fundamental solutions for constant Q_{fs}, D_{n} and D_{s} over an element segment are given in 0, respectively. Knowing these fundamental solutions, the pore pressure, displacement and stress at any point (x,y) can be estimated with the functions defined below:

Induced pore pressure

$$p(x,y,t) = p^{\text{dn}}(x,y,t)D_{\text{n}} + p^{\text{ds}}(x,y,t)D_{\text{s}} + p^{\text{qf}}(x,y,t)Q_{\text{fs}} \tag{3.10}$$

Induced displacement

$$\begin{aligned} u_{\text{x}}(x,y,t) &= u_{\text{x}}^{\text{dn}}(x,y,t)D_{\text{n}} + u_{\text{x}}^{\text{ds}}(x,y,t)D_{\text{s}} + u_{\text{x}}^{\text{qf}}(x,y,t)Q_{\text{fs}} \\ u_{\text{y}}(x,y,t) &= u_{\text{y}}^{\text{dn}}(x,y,t)D_{\text{n}} + u_{\text{y}}^{\text{ds}}(x,y,t)D_{\text{s}} + u_{\text{y}}^{\text{qf}}(x,y,t)Q_{\text{fs}} \end{aligned} \tag{3.11}$$

Induced stress

$$\begin{aligned}
\sigma_{xx}(x,y,t) &= \sigma_{xx}^{dn}(x,y,t)D_n + \sigma_{xx}^{ds}(x,y,t)D_s + \sigma_{xx}^{qf}(x,y,t)Q_{fs} \\
\sigma_{yy}(x,y,t) &= \sigma_{yy}^{dn}(x,y,t)D_n + \sigma_{yy}^{ds}(x,y,t)D_s + \sigma_{yy}^{qf}(x,y,t)Q_{fs} \\
\sigma_{xy}(x,y,t) &= \sigma_{xy}^{dn}(x,y,t)D_n + \sigma_{xy}^{ds}(x,y,t)D_s + \sigma_{xy}^{qf}(x,y,t)Q_{fs}
\end{aligned} \tag{3.12}$$

3.4 Thermo-poroelastic Displacement Discontinuity Method

A heat conduction singular solution was added to the poroelastic displacement discontinuity method to construct a thermo-poroelastic approach by Berchenko (1998). Later on, this concept was further developed by different authors such as Ghassemi and Zhang (2004). The same approach, which was implemented in the case of adding a fluid source to the classic elastic DD solution, is adopted here to address the simulation of temperature variations in the medium. In this case a heat source strength term is added to the poroelastic DD solutions to specify the amount of heat exchange between the fracture and the surrounding rock, as indicated below (Figure 3.6):

$$\begin{aligned}
D_x &= u_x(x,0^-) - u_x(x,0^+) \\
D_y &= u_y(x,0^-) - u_y(x,0^+) \\
Q_{fs} &= q_{int}^{f} \\
Q_{hs} &= q_{int}^{h}
\end{aligned} \tag{3.13}$$

where Q_{hs} is the strength of heat source and q^{h}_{int} is the interface heat flow rate per unit width and length of fracture. It is assumed that the interface heat flow rate is positive when there is a heat flow from the fracture into the matrix, i.e. when the fracture fluid is warmer than the adjacent rock.

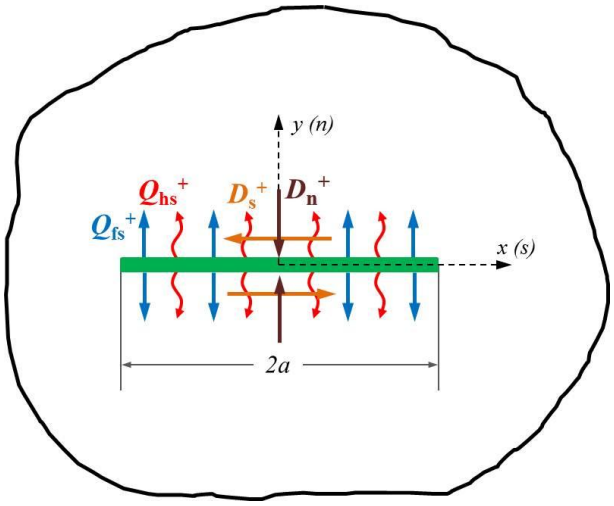

Figure 3.6. Constant displacement discontinuities and fluid and heat source strength components [modified after Crouch and Starfield, 1983]

The fundamental solution for the heat source strength is based on the heat conservation equation (Eq. 2.15) without the heat convection term (second term on the left hand side). It can be seen that temperature is not fully coupled to stress and pressure changes, as there are no geomechanical and hydraulic terms in Eq. 2.15. In the case of geomechanical coupling, the effect of volumetric strain on temperature variation is usually negligible, however the effect of temperature on stress and deformation changes is considered. For the fluid-heat coupling, convective heat transfer is not considered in the fundamental solution, whereas the heat variation effect on fluid flow in considered. It will be seen later that heat convection mechanism is only considered in the fracture network. This is a reasonable assumption for impermeable or low-permeability rocks with highly conductive fractures, such that the fluid velocity in fractures is much higher (100-1000 order) than the rock matrix.

Similar to Carvalho's work (Ibid.), the temperature effect is superimposed with the poroelastic boundary conditions as below:

- Constant heat source strength without any displacement discontinuities and fluid source:

$$q_{\text{int}}^{\text{h}} = Q_{\text{hs}},\ u_{\text{x}}(x,0^{-},t) - u_{\text{x}}(x,0^{+},t) = 0,\ u_{\text{y}}(x,0^{-},t) - u_{\text{y}}(x,0^{+},t) = 0,\ q_{\text{int}}^{\text{f}} = 0$$

- Constant fluid source strength without any displacement discontinuities and heat source:

$$q_{\text{int}}^{\text{f}} = Q_{\text{fs}},\ u_{\text{x}}(x,0^{-},t) - u_{\text{x}}(x,0^{+},t) = 0,\ u_{\text{y}}(x,0^{-},t) - u_{\text{y}}(x,0^{+},t) = 0,\ q_{\text{int}}^{\text{h}} = 0$$

- Constant displacement discontinuities without any fluid and heat sources:

$$u_{\text{x}}(x,0^{-},t) - u_{\text{x}}(x,0^{+},t) = D_{\text{s}},\ u_{\text{y}}(x,0^{-},t) - u_{\text{y}}(x,0^{+},t) = D_{\text{n}},\ q_{\text{int}}^{\text{f}} = 0,\ q_{\text{int}}^{\text{h}} = 0$$

The fundamental solutions for the constant heat source strength Q_{hs} over an element segment are given in Appendix D. Now it is possible to write the final form of the induced pressure, temperature, displacements and stresses as the superposition of all the displacement discontinuities and sources as below:

Induced temperature

$$T(x,y,t) = T^{\text{qh}}(x,y,t)Q_{\text{hs}} \tag{3.14}$$

Induced pore pressure

$$p(x,y,t) = p^{\text{dn}}(x,y,t)D_{\text{n}} + p^{\text{ds}}(x,y,t)D_{\text{s}} + p^{\text{qf}}(x,y,t)Q_{\text{fs}} + p^{\text{qh}}(x,y,t)Q_{\text{hs}} \tag{3.15}$$

Induced displacement

$$\begin{aligned} u_{\text{x}}(x,y,t) &= u_{\text{x}}^{\text{dn}}(x,y,t)D_{\text{n}} + u_{\text{x}}^{\text{ds}}(x,y,t)D_{\text{s}} + u_{\text{x}}^{\text{qf}}(x,y,t)Q_{\text{fs}} + u_{\text{x}}^{\text{qh}}(x,y,t)Q_{\text{hs}} \\ u_{\text{y}}(x,y,t) &= u_{\text{y}}^{\text{dn}}(x,y,t)D_{\text{n}} + u_{\text{y}}^{\text{ds}}(x,y,t)D_{\text{s}} + u_{\text{y}}^{\text{qf}}(x,y,t)Q_{\text{fs}} + u_{\text{y}}^{\text{qh}}(x,y,t)Q_{\text{hs}} \end{aligned} \tag{3.16}$$

Induced stress

$$\begin{aligned} \sigma_{\text{xx}}(x,y,t) &= \sigma_{\text{xx}}^{\text{dn}}(x,y,t)D_{\text{n}} + \sigma_{\text{xx}}^{\text{ds}}(x,y,t)D_{\text{s}} + \sigma_{\text{xx}}^{\text{qf}}(x,y,t)Q_{\text{fs}} + \sigma_{\text{xx}}^{\text{qh}}(x,y,t)Q_{\text{hs}} \\ \sigma_{\text{yy}}(x,y,t) &= \sigma_{\text{yy}}^{\text{dn}}(x,y,t)D_{\text{n}} + \sigma_{\text{yy}}^{\text{ds}}(x,y,t)D_{\text{s}} + \sigma_{\text{yy}}^{\text{qf}}(x,y,t)Q_{\text{fs}} + \sigma_{\text{yy}}^{\text{qh}}(x,y,t)Q_{\text{hs}} \\ \sigma_{\text{xy}}(x,y,t) &= \sigma_{\text{xy}}^{\text{dn}}(x,y,t)D_{\text{n}} + \sigma_{\text{xy}}^{\text{ds}}(x,y,t)D_{\text{s}} + \sigma_{\text{xy}}^{\text{qf}}(x,y,t)Q_{\text{fs}} + \sigma_{\text{xy}}^{\text{qh}}(x,y,t)Q_{\text{hs}} \end{aligned} \tag{3.17}$$

3.5 Chapter Summary

In this chapter, a brief review on the existing numerical methods for solving the thermo-hydromechanical governing equations was given. Some of the advantages and disadvantages of each method were summarized. Among all these methods, a hybrid FDM-DDM method was selected for this study which appears to be most suitable for discrete fractures in an infinite poroelastic medium. Displacement discontinuity method is an indirect boundary element method which accounts for the presence of fractures by introducing displacement discontinuities and fluid and heat sources in the fracture. The fundamental solutions required to estimate these discontinuities and sources in each fracture segment were presented. Pressure, temperature, stress and displacement at any arbitrary point in the medium (except the fracture tips) can be estimated using the superposition of the effect of all these discontinuities, fluid and heat sources.

Chapter 4
Thermo-Hydro-Mechanical Coupling using Hybrid FDM-DDM Model

4.1 Introduction

Hybrid numerical methods are defined as the combination of different numerical methods in a way that hopefully reaps the benefits from all the combined methods, but at the price of an increment in computational time. It is common to couple a continuous method (e.g. finite difference method, finite element method) with a discontinuous method (e.g. discrete element method, displacement discontinuity method) to model the presence of discontinuities (e.g. fractures or openings) in a continuous medium.

In this study, the finite different method (FDM) is coupled with the displacement discontinuity method (DDM). DDM is an indirect boundary element method as it involves discretization only of the boundary of the fractures, which is a suitable approach for infinite or semi-infinite problems. FDM is implemented to simulate the fluid and heat transfer in the fracture, which is applied as the internal boundary condition to DDM to estimate the pore pressure, temperature, displacement and stress in the rock matrix blocks adjacent to the fractures. The whole concept of this hybrid model is summarized in Figure 4.1.

The superposition of the displacement discontinuity method as well as the time marching scheme chosen is described in this section. A brief review of relevant fracture mechanics is undertaken to clarify the stress-displacement relationships of fractures under opening and closure. The fluid and heat flow formulation in the fracture is presented and the finite difference form of these

equations is described. Finally the displacement discontinuity equations, fracture mechanics laws and fluid and heat flow finite difference schemes are integrated to form a system of equations.

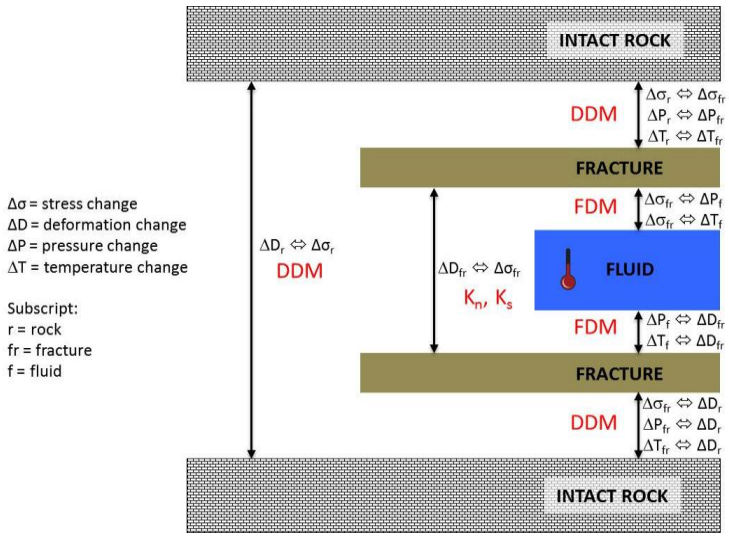

Figure 4.1. Fluid-rock interaction in a fractured thermo-poroelastic media [modified after Asgian, 1988]

4.2 Two-Dimensional Constant Displacement Discontinuity Solution for Multiple Fracture Segments in a Thermo-poroelastic Medium

4.2.1 Influence Coefficients

The fundamental solutions for pressure, temperature, displacement and stress for a fracture segment were presented in Chapter 3. In this section, those fundamental solutions are generalized for multiple fracture segments and a time marching scheme is added to the DDM formulations.

In the DDM approach, a fracture can be discretized into *N* fracture segments, and any segment has four degrees of freedom in a thermo-poroelastic medium, i.e. normal and shear displacement

discontinuities, heat source strength and fluid source strength. Induced pressure, temperature, displacement and stress at any point z at specific time t in the medium (including the fracture segments) can be estimated as a linear combination of all the fracture segments' discontinuities and strengths as specified below

$$T(x_z, y_z, t) = \sum_{j=1}^{N} T_j^{\mathrm{qh}}(\tilde{x}, \tilde{y}, t) Q_{\mathrm{hs}\,j} \tag{4.1}$$

$$p(x_z, y_z, t) = \sum_{j=1}^{N} p_j^{\mathrm{dn}}(\tilde{x}, \tilde{y}, t) D_{\mathrm{n}\,j} + \sum_{j=1}^{N} p_j^{\mathrm{ds}}(\tilde{x}, \tilde{y}, t) D_{\mathrm{s}\,j} + \sum_{j=1}^{N} p_j^{\mathrm{qf}}(\tilde{x}, \tilde{y}, t) Q_{\mathrm{fs}\,j} + \sum_{j=1}^{N} p_j^{\mathrm{qh}}(\tilde{x}, \tilde{y}, t) Q_{\mathrm{hs}\,j} \tag{4.2}$$

$$\begin{aligned} u_{\mathrm{x}}(x_z, y_z, t) &= \sum_{j=1}^{N} u_{\mathrm{x}\,j}^{\mathrm{dn}}(\tilde{x}, \tilde{y}, t) D_{\mathrm{n}\,j} + \sum_{j=1}^{N} u_{\mathrm{x}\,j}^{\mathrm{ds}}(\tilde{x}, \tilde{y}, t) D_{\mathrm{s}\,j} + \sum_{j=1}^{N} u_{\mathrm{x}\,j}^{\mathrm{qf}}(\tilde{x}, \tilde{y}, t) Q_{\mathrm{fs}\,j} + \sum_{j=1}^{N} u_{\mathrm{x}\,j}^{\mathrm{qh}}(\tilde{x}, \tilde{y}, t) Q_{\mathrm{hs}\,j} \\ u_{\mathrm{y}}(x_z, y_z, t) &= \sum_{j=1}^{N} u_{\mathrm{y}\,j}^{\mathrm{dn}}(\tilde{x}, \tilde{y}, t) D_{\mathrm{n}\,j} + \sum_{j=1}^{N} u_{\mathrm{y}\,j}^{\mathrm{ds}}(\tilde{x}, \tilde{y}, t) D_{\mathrm{s}\,j} + \sum_{j=1}^{N} u_{\mathrm{y}\,j}^{\mathrm{qf}}(\tilde{x}, \tilde{y}, t) Q_{\mathrm{fs}\,j} + \sum_{j=1}^{N} u_{\mathrm{y}\,j}^{\mathrm{qh}}(\tilde{x}, \tilde{y}, t) Q_{\mathrm{hs}\,j} \end{aligned} \tag{4.3}$$

$$\begin{aligned} \sigma_{\mathrm{xx}}(x_z, y_z, t) &= \sum_{j=1}^{N} \sigma_{\mathrm{xx}\,j}^{\mathrm{dn}}(\tilde{x}, \tilde{y}, t) D_{\mathrm{n}\,j} + \sum_{j=1}^{N} \sigma_{\mathrm{xx}\,j}^{\mathrm{ds}}(\tilde{x}, \tilde{y}, t) D_{\mathrm{s}\,j} + \sum_{j=1}^{N} \sigma_{\mathrm{xx}\,j}^{\mathrm{qf}}(\tilde{x}, \tilde{y}, t) Q_{\mathrm{fs}\,j} + \sum_{j=1}^{N} \sigma_{\mathrm{xx}\,j}^{\mathrm{qh}}(\tilde{x}, \tilde{y}, t) Q_{\mathrm{hs}\,j} \\ \sigma_{\mathrm{yy}}(x_z, y_z, t) &= \sum_{j=1}^{N} \sigma_{\mathrm{yy}\,j}^{\mathrm{dn}}(\tilde{x}, \tilde{y}, t) D_{\mathrm{n}\,j} + \sum_{j=1}^{N} \sigma_{\mathrm{yy}\,j}^{\mathrm{ds}}(\tilde{x}, \tilde{y}, t) D_{\mathrm{s}\,j} + \sum_{j=1}^{N} \sigma_{\mathrm{yy}\,j}^{\mathrm{qf}}(\tilde{x}, \tilde{y}, t) Q_{\mathrm{fs}\,j} + \sum_{j=1}^{N} \sigma_{\mathrm{yy}\,j}^{\mathrm{qh}}(\tilde{x}, \tilde{y}, t) Q_{\mathrm{hs}\,j} \\ \sigma_{\mathrm{xy}}(x_z, y_z, t) &= \sum_{j=1}^{N} \sigma_{\mathrm{xy}\,j}^{\mathrm{dn}}(\tilde{x}, \tilde{y}, t) D_{\mathrm{n}\,j} + \sum_{j=1}^{N} \sigma_{\mathrm{xy}\,j}^{\mathrm{ds}}(\tilde{x}, \tilde{y}, t) D_{\mathrm{s}\,j} + \sum_{j=1}^{N} \sigma_{\mathrm{xy}\,j}^{\mathrm{qf}}(\tilde{x}, \tilde{y}, t) Q_{\mathrm{fs}\,j} + \sum_{j=1}^{N} \sigma_{\mathrm{xy}\,j}^{\mathrm{qh}}(\tilde{x}, \tilde{y}, t) Q_{\mathrm{hs}\,j} \end{aligned} \tag{4.4}$$

Here, x_z and y_z are the coordinates of the field point z in local coordinates of (x_j,y_j), $\tilde{x}$ and $\tilde{y}$ are the distances to the midpoint of the influencing fracture segment j (for the case of constant DD) and the field point z, in the x- and y-directions, respectively.

One must know the values of the discontinuities and source strengths prior to the estimation of pressure, temperature, displacement and stress in the medium. To achieve this, Eqs. 4.1-4.4 can be written for the fracture segments for which the values of stress, displacement, pressure and temperature changes can be estimated (using fracture mechanics laws as well as fluid and heat

flow finite difference equations). The normal and shear stresses plus induced pressure and temperature in the i^{th} fracture segment with the orientation of β_i with respect to the x-axis can be expressed as the superposition of the effect of all fracture segments' discontinuities and strengths as following (Figure 4.2):

$$\begin{aligned}
\sigma_{\mathrm{s}\,i} &= \sum_{j=1}^{N} A_{ij} D_{\mathrm{s}\,j} + \sum_{j=1}^{N} B_{ij} D_{\mathrm{n}\,j} + \sum_{j=1}^{N} C_{ij} Q_{\mathrm{fs}\,j} + \sum_{j=1}^{N} E_{ij} Q_{\mathrm{hs}\,j} \\
\sigma_{\mathrm{n}\,i} &= \sum_{j=1}^{N} F_{ij} D_{\mathrm{s}\,j} + \sum_{j=1}^{N} H_{ij} D_{\mathrm{n}\,j} + \sum_{j=1}^{N} L_{ij} Q_{\mathrm{fs}\,j} + \sum_{j=1}^{N} M_{ij} Q_{\mathrm{hs}\,j} \\
p_i &= \sum_{j=1}^{N} N_{ij} D_{\mathrm{s}\,j} + \sum_{j=1}^{N} O_{ij} D_{\mathrm{n}\,j} + \sum_{j=1}^{N} R_{ij} Q_{\mathrm{fs}\,j} + \sum_{j=1}^{N} S_{ij} Q_{\mathrm{hs}\,j} \\
T_i &= \sum_{j=1}^{N} U_{ij} Q_{\mathrm{hs}\,j}
\end{aligned} \tag{4.5}$$

where A_{ij}, B_{ij}, C_{ij}, E_{ij}, F_{ij}, H_{ij}, L_{ij}, M_{ij}, N_{ij}, O_{ij}, R_{ij}, S_{ij}, U_{ij} are the influence coefficients of the influencing fracture segment j on the influenced fracture segment i [Carvalho, 1990; Berchenko, 1998; Ghassemi and Zhang, 2004; Tao, 2010].

These influence coefficients in Eq.4.5 are related to the fundamental solutions for discontinuities and strengths. In the case of fluid and heat source strengths, the related influence coefficients are identical to the fundamental solutions as the pressure and temperature are scalar parameters and their values do not change in different directions and coordinate systems. This is not the case for influence coefficients related to the stress and displacements. As the fundamental solutions are calculated in the local coordinates of the influencing segment (j), it is required to do some stress transformation from the local coordinates (x_j,y_j) to the other local coordinates (x_i,y_i). The required formulation for coordinate transformation can be found in Appendix E.

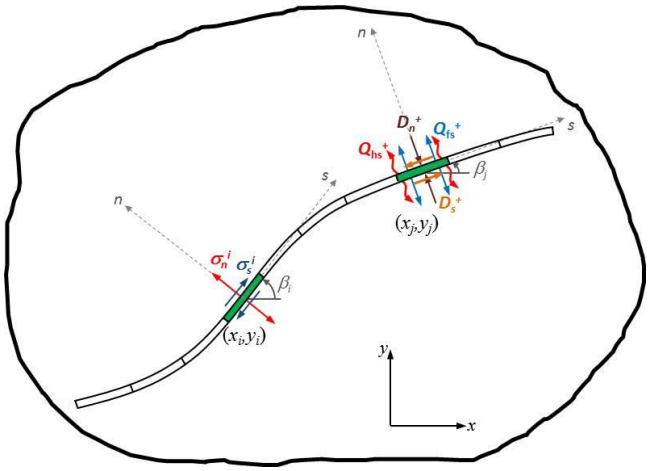

Figure 4.2. Influence of the j^{th} fracture element on the i^{th} fracture element in a thermo-poroelastic medium

Based on the discussion above, the influenced coefficient can be written as the fundamental solution as below:

$$
\begin{aligned}
A_{ij}(\tilde{x},\tilde{y},t) &= \left(\sigma^{ds}_{yy\ j}(\tilde{x},\tilde{y},t)-\sigma^{ds}_{xx\ j}(\tilde{x},\tilde{y},t)\right)\sin\gamma_{ij}\cos\gamma_{ij}+\sigma^{ds}_{xy\ j}(\tilde{x},\tilde{y},t)\left(\cos^2\gamma_{ij}-\sin^2\gamma_{ij}\right)\\
B_{ij}(\tilde{x},\tilde{y},t) &= \left(\sigma^{dn}_{yy\ j}(\tilde{x},\tilde{y},t)-\sigma^{dn}_{xx\ j}(\tilde{x},\tilde{y},t)\right)\sin\gamma_{ij}\cos\gamma_{ij}+\sigma^{dn}_{xy\ j}(\tilde{x},\tilde{y},t)\left(\cos^2\gamma_{ij}-\sin^2\gamma_{ij}\right)\\
C_{ij}(\tilde{x},\tilde{y},t) &= \left(\sigma^{qf}_{yy\ j}(\tilde{x},\tilde{y},t)-\sigma^{qf}_{xx\ j}(\tilde{x},\tilde{y},t)\right)\sin\gamma_{ij}\cos\gamma_{ij}+\sigma^{qf}_{xy\ j}(\tilde{x},\tilde{y},t)\left(\cos^2\gamma_{ij}-\sin^2\gamma_{ij}\right)\\
E_{ij}(\tilde{x},\tilde{y},t) &= \left(\sigma^{qh}_{yy\ j}(\tilde{x},\tilde{y},t)-\sigma^{qh}_{xx\ j}(\tilde{x},\tilde{y},t)\right)\sin\gamma_{ij}\cos\gamma_{ij}+\sigma^{qh}_{xy\ j}(\tilde{x},\tilde{y},t)\left(\cos^2\gamma_{ij}-\sin^2\gamma_{ij}\right)
\end{aligned}
$$

$$
\begin{aligned}
F_{ij}(\tilde{x},\tilde{y},t) &= \sigma^{ds}_{xx\ j}(\tilde{x},\tilde{y},t)\sin^2\gamma_{ij}+2\sigma^{ds}_{xy\ j}(\tilde{x},\tilde{y},t)\sin\gamma_{ij}\cos\gamma_{ij}+\sigma^{ds}_{yy\ j}(\tilde{x},\tilde{y},t)\cos^2\gamma_{ij}\\
H_{ij}(\tilde{x},\tilde{y},t) &= \sigma^{dn}_{xx\ j}(\tilde{x},\tilde{y},t)\sin^2\gamma_{ij}+2\sigma^{dn}_{xy\ j}(\tilde{x},\tilde{y},t)\sin\gamma_{ij}\cos\gamma_{ij}+\sigma^{dn}_{yy\ j}(\tilde{x},\tilde{y},t)\cos^2\gamma_{ij}\\
L_{ij}(\tilde{x},\tilde{y},t) &= \sigma^{qf}_{xx\ j}(\tilde{x},\tilde{y},t)\sin^2\gamma_{ij}+2\sigma^{qf}_{xy\ j}(\tilde{x},\tilde{y},t)\sin\gamma_{ij}\cos\gamma_{ij}+\sigma^{qf}_{yy\ j}(\tilde{x},\tilde{y},t)\cos^2\gamma_{ij}\\
M_{ij}(\tilde{x},\tilde{y},t) &= \sigma^{qh}_{xx\ j}(\tilde{x},\tilde{y},t)\sin^2\gamma_{ij}+2\sigma^{qh}_{xy\ j}(\tilde{x},\tilde{y},t)\sin\gamma_{ij}\cos\gamma_{ij}+\sigma^{qh}_{yy\ j}(\tilde{x},\tilde{y},t)\cos^2\gamma_{ij}
\end{aligned}
\tag{4.6}
$$

$$N_{ij}(\tilde{x},\tilde{y},t) = p_j^{\mathrm{ds}}(\tilde{x},\tilde{y},t)$$

$$O_{ij}(\tilde{x},\tilde{y},t) = p_j^{\mathrm{dn}}(\tilde{x},\tilde{y},t)$$

$$R_{ij}(\tilde{x},\tilde{y},t) = p_j^{\mathrm{qf}}(\tilde{x},\tilde{y},t)$$

$$R_{ij}(\tilde{x},\tilde{y},t) = p_j^{\mathrm{qh}}(\tilde{x},\tilde{y},t)$$

$$U_{ij}(\tilde{x},\tilde{y},t) = T_j^{\mathrm{qh}}(\tilde{x},\tilde{y},t)$$

where $\gamma_{ij}=\beta_i - \beta_j$, $\tilde{x}$ (= $x_i - x_j$) and $\tilde{y}$ (= $y_i - y_j$) are the distance between the midpoint of the influencing fracture segment j and the influenced fracture segment i in x- and y-direction, respectively.

4.2.2 Time Marching Scheme

Formulations of induced pressure, temperature, displacement and stress are only space-dependent (Eqs. 4.1-4.5). In practical applications, DDM solutions are also time-dependent as fluid and heat sources and displacement discontinuities change over time. In this case, a time marching scheme shown in Figure 4.3 is usually adopted and the influence of the entire previous source strengths' and discontinuities' increments are superimposed to the solution of the current time step as below:

$$
\begin{aligned}
\Delta\sigma_{\mathrm{s}\,i}^{\tau_n} &= \sum_{j=1}^{N} A_{ij}^{\tau_1}\Delta D_{\mathrm{s}\,j}^{\tau_1} + \sum_{j=1}^{N} B_{ij}^{\tau_1}\Delta D_{\mathrm{n}\,j}^{\tau_1} + \sum_{j=1}^{N} C_{ij}^{\tau_1}\Delta Q_{\mathrm{fs}\,j}^{\tau_1} + \sum_{j=1}^{N} E_{ij}^{\tau_1}\Delta Q_{\mathrm{hs}\,j}^{\tau_1} \\
&\quad + \sum_{tc=2}^{n}\sum_{j=1}^{N} A_{ij}^{\tau_{tc}}\Delta D_{\mathrm{s}\,j}^{\tau_{tc}} + \sum_{tc=2}^{n}\sum_{j=1}^{N} B_{ij}^{\tau_{tc}}\Delta D_{\mathrm{n}\,j}^{\tau_{tc}} + \sum_{tc=2}^{n}\sum_{j=1}^{N} C_{ij}^{\tau_{tc}}\Delta Q_{\mathrm{fs}\,j}^{\tau_{tc}} + \sum_{tc=2}^{n}\sum_{j=1}^{N} E_{ij}^{\tau_{tc}}\Delta Q_{\mathrm{hs}\,j}^{\tau_{tc}} \\
\Delta\sigma_{\mathrm{n}\,i}^{\tau_n} &= \sum_{j=1}^{N} F_{ij}^{\tau_1}\Delta D_{\mathrm{s}\,j}^{\tau_1} + \sum_{j=1}^{N} H_{ij}^{\tau_1}\Delta D_{\mathrm{n}\,j}^{\tau_1} + \sum_{j=1}^{N} L_{ij}^{\tau_1}\Delta Q_{\mathrm{fs}\,j}^{\tau_1} + \sum_{j=1}^{N} M_{ij}^{\tau_1}\Delta Q_{\mathrm{hs}\,j}^{\tau_1} \\
&\quad + \sum_{tc=2}^{n}\sum_{j=1}^{N} F_{ij}^{\tau_{tc}}\Delta D_{\mathrm{s}\,j}^{\tau_{tc}} + \sum_{tc=2}^{n}\sum_{j=1}^{N} H_{ij}^{\tau_{tc}}\Delta D_{\mathrm{n}\,j}^{\tau_{tc}} + \sum_{tc=2}^{n}\sum_{j=1}^{N} L_{ij}^{\tau_{tc}}\Delta Q_{\mathrm{fs}\,j}^{\tau_{tc}} + \sum_{tc=2}^{n}\sum_{j=1}^{N} M_{ij}^{\tau_{tc}}\Delta Q_{\mathrm{hs}\,j}^{\tau_{tc}} \qquad (4.7) \\
\Delta p_i^{\tau_n} &= \sum_{j=1}^{N} N_{ij}^{\tau_1}\Delta D_{\mathrm{s}\,j}^{\tau_1} + \sum_{j=1}^{N} O_{ij}^{\tau_1}\Delta D_{\mathrm{n}\,j}^{\tau_1} + \sum_{j=1}^{N} R_{ij}^{\tau_1}\Delta Q_{\mathrm{fs}\,j}^{\tau_1} + \sum_{j=1}^{N} S_{ij}^{\tau_1}\Delta Q_{\mathrm{hs}\,j}^{\tau_1} \\
&\quad + \sum_{tc=2}^{n}\sum_{j=1}^{N} N_{ij}^{\tau_{tc}}\Delta D_{\mathrm{s}\,j}^{\tau_{tc}} + \sum_{tc=2}^{n}\sum_{j=1}^{N} O_{ij}^{\tau_{tc}}\Delta D_{\mathrm{n}\,j}^{\tau_{tc}} + \sum_{tc=2}^{n}\sum_{j=1}^{N} R_{ij}^{\tau_{tc}}\Delta Q_{\mathrm{fs}\,j}^{\tau_{tc}} + \sum_{tc=2}^{n}\sum_{j=1}^{N} S_{ij}^{\tau_{tc}}\Delta Q_{\mathrm{hs}\,j}^{\tau_{tc}} \\
\Delta T_i^{\tau_n} &= \sum_{j=1}^{N} U_{ij}^{\tau_1}\Delta Q_{\mathrm{hs}\,j}^{\tau_1} + \sum_{tc=2}^{n}\sum_{j=1}^{N} U_{ij}^{\tau_{tc}}\Delta Q_{\mathrm{hs}\,j}^{\tau_{tc}}
\end{aligned}
$$

Here, n is the number of the current time step, N is the number of fracture segments, and tc is the time interval counter. The following conventions are adopted in this study to present the DDM formulations. The model starts from the initial time t_0 with constant or variable time steps. Thermal, hydraulic and geomechanical unknowns such as pressure, temperature, normal and shear stresses and fracture aperture are estimated at each specific time step (t_1, t_2, …, t_n). The displacement discontinuities, fluid and heat source strengths as well as pressure and temperature variation (Δp and ΔT) are assigned to different time intervals (τ_1, τ_2, …, τ_n). Based on Figure 4.3, the time duration τ_l, which is defined as t_n-t_{n-l}, is the accumulative time interval value for discontinuities and strengths calculation. In this study, the italicized subscript corresponds to the fracture segment number (spatial component), whereas the italicized superscript presents the time step number (temporal component), for example $\chi^{\tau 1}{}_i$ is the value of χ in i^{th} fracture segment during the last time interval t_n-t_{n-1}.

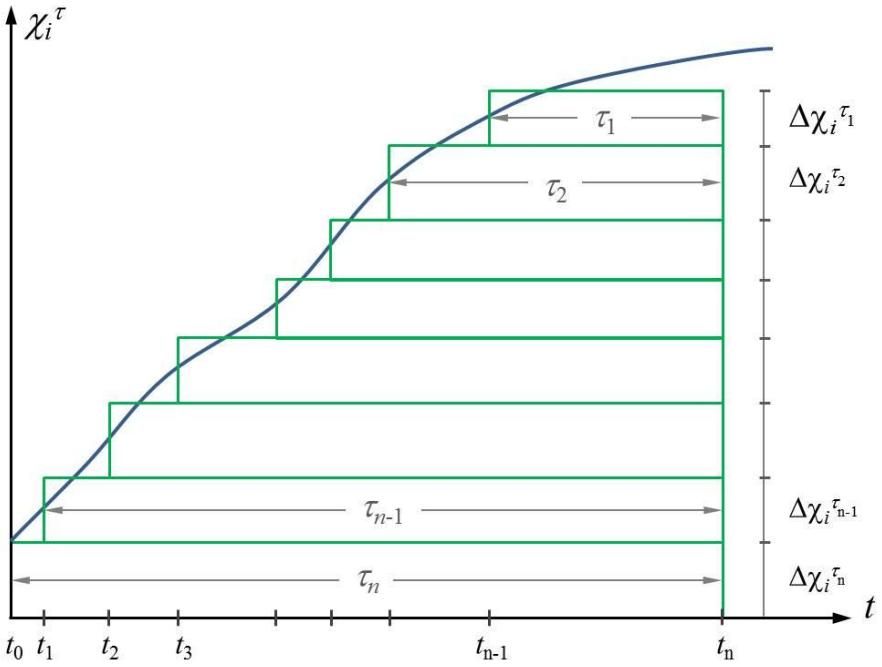

Figure 4.3. Time marching scheme for continuous fluid and heat sources and displacement discontinuities.

Based on Eq. 4.7, the induced pressure, temperature and stresses variation with respect to the initial value (based on $\tau_n=t_n-t_0$) can be calculated using the superposition of current and previous discontinuities and strengths variation during each time interval. Thus, Eq. 4.7 can be rearranged based on the known and unknown values as:

$$\sum_{j=1}^{N} A_{ij}^{\tau_1}\Delta D_{\mathrm{s}j}^{\tau_1} + \sum_{j=1}^{N} B_{ij}^{\tau_1}\Delta D_{\mathrm{n}j}^{\tau_1} + \sum_{j=1}^{N} C_{ij}^{\tau_1}\Delta Q_{\mathrm{fs}j}^{\tau_1} + \sum_{j=1}^{N} E_{ij}^{\tau_1}\Delta Q_{\mathrm{hs}j}^{\tau_1} - \Delta\sigma_{\mathrm{s}i}^{\tau_n}$$
$$= -\sum_{tc=2}^{n}\sum_{j=1}^{N} A_{ij}^{\tau_{tc}}\Delta D_{\mathrm{s}j}^{\tau_{tc}} - \sum_{tc=2}^{n}\sum_{j=1}^{N} B_{ij}^{\tau_{tc}}\Delta D_{\mathrm{n}j}^{\tau_{tc}} - \sum_{tc=2}^{n}\sum_{j=1}^{N} C_{ij}^{\tau_{tc}}\Delta Q_{\mathrm{fs}j}^{\tau_{tc}} - \sum_{tc=2}^{n}\sum_{j=1}^{N} E_{ij}^{\tau_{tc}}\Delta Q_{\mathrm{hs}j}^{\tau_{tc}}$$
$$\sum_{j=1}^{N} F_{ij}^{\tau_1}\Delta D_{\mathrm{s}j}^{\tau_1} + \sum_{j=1}^{N} H_{ij}^{\tau_1}\Delta D_{\mathrm{n}j}^{\tau_1} + \sum_{j=1}^{N} L_{ij}^{\tau_1}\Delta Q_{\mathrm{fs}j}^{\tau_1} + \sum_{j=1}^{N} M_{ij}^{\tau_1}\Delta Q_{\mathrm{hs}j}^{\tau_1} - \Delta\sigma_{\mathrm{n}i}^{\tau_n}$$
$$= -\sum_{tc=2}^{n}\sum_{j=1}^{N} F_{ij}^{\tau_{tc}}\Delta D_{\mathrm{s}j}^{\tau_{tc}} - \sum_{tc=2}^{n}\sum_{j=1}^{N} H_{ij}^{\tau_{tc}}\Delta D_{\mathrm{n}j}^{\tau_{tc}} - \sum_{tc=2}^{n}\sum_{j=1}^{N} L_{ij}^{\tau_{tc}}\Delta Q_{\mathrm{fs}j}^{\tau_{tc}} - \sum_{tc=2}^{n}\sum_{j=1}^{N} M_{ij}^{\tau_{tc}}\Delta Q_{\mathrm{hs}j}^{\tau_{tc}} \quad (4.8)$$
$$\sum_{j=1}^{N} N_{ij}^{\tau_1}\Delta D_{\mathrm{s}j}^{\tau_1} + \sum_{j=1}^{N} O_{ij}^{\tau_1}\Delta D_{\mathrm{n}j}^{\tau_1} + \sum_{j=1}^{N} R_{ij}^{\tau_1}\Delta Q_{\mathrm{fs}j}^{\tau_1} + \sum_{j=1}^{N} S_{ij}^{\tau_1}\Delta Q_{\mathrm{hs}j}^{\tau_1} - \Delta p_i^{\tau_n}$$
$$= -\sum_{tc=2}^{n}\sum_{j=1}^{N} N_{ij}^{\tau_{tc}}\Delta D_{\mathrm{s}j}^{\tau_{tc}} - \sum_{tc=2}^{n}\sum_{j=1}^{N} O_{ij}^{\tau_{tc}}\Delta D_{\mathrm{n}j}^{\tau_{tc}} - \sum_{tc=2}^{n}\sum_{j=1}^{N} R_{ij}^{\tau_{tc}}\Delta Q_{\mathrm{fs}j}^{\tau_{tc}} - \sum_{tc=2}^{n}\sum_{j=1}^{N} S_{ij}^{\tau_{tc}}\Delta Q_{\mathrm{hs}j}^{\tau_{tc}}$$
$$\sum_{j=1}^{N} U_{ij}^{\tau_1}\Delta Q_{\mathrm{hs}j}^{\tau_1} - \Delta T_i^{\tau_n} = \sum_{tc=2}^{n}\sum_{j=1}^{N} U_{ij}^{\tau_{tc}}\Delta Q_{\mathrm{hs}j}^{\tau_{tc}}$$

The left hand side of Eq. 4.8 represents the combination of unknown variables whereas the right hand side is known. As it can be seen, there exist 8*N* unknowns and 4*N* equations that can be converted into 6*N* unknowns and 6*N* equations by estimating the boundary conditions on the fracture wall, i.e. $\Delta\sigma_{\mathrm{n}}$, $\Delta\sigma_{\mathrm{s}}$, Δp, and ΔT.

4.3 Fracture Mechanics

The mechanical behavior of fractured rocks is complex and usually influenced by a variety of factors such as rock elastic properties (Young's modulus and Poisson's ratio), interface friction (un-weathered and weathered friction angle), surface adhesion (cohesion and UCS), surface roughness (JRC), and the presence of fluids and debris at interfaces.

Based on the stress state, three different types of fracture behavior are noted (Figure 4.4). *Mode I* describes a symmetric fracture opening (with respect to *x*-*z* plane) under a normal tensile stress.

Mode II corresponds to fracture slip (in *x*-direction normal to the fracture front) under in-plane (co-directional) shear stress. *Mode III* denotes the fracture tearing (in *z*-direction tangential to fracture front) as a result of out-of-plane shear stress.

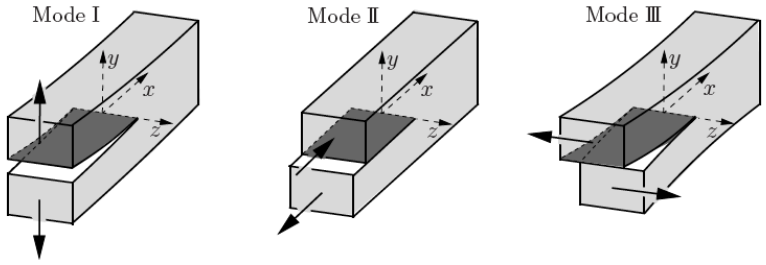

Figure 4.4. Three different fracture opening types [reproduced from Gross & Seelig, 2006].

4.3.1 Fracture Normal and Shear Stiffnesses

Various empirical relationships between normal and shear stress and displacements of the fracture plane have been proposed. Goodman (1976) proposed a hyperbolic relation between normal effective stress (σ'_{n}) and fracture closure (D_{n}):

$$\sigma'_{\mathrm{n}} = \sigma'_{\mathrm{n0}} + R\sigma'_{\mathrm{n0}}\left(\frac{D_{\mathrm{n}}}{D_{\mathrm{n\,max}} - D_{\mathrm{n}}}\right)^{t} \qquad D_{\mathrm{n}} < D_{\mathrm{n\,max}} \tag{4.9}$$

where σ'_{n0} is the initial effective normal stress, $D_{\mathrm{n\,max}}$ is the maximum closure and parameters R and t are experimentally determined. Bandis et al. (1983) proposed an alternative form of Eq. 4.10 for a small initial stress condition (Figure 4.5).

$$\sigma'_{\mathrm{n}} = \frac{D_{\mathrm{n}}}{a_{\mathrm{n}} - b_{\mathrm{n}} D_{\mathrm{n}}} \tag{4.10}$$

where σ_{n} is the effective stress, and a_{n} and b_{n} are constant parameters which are defined based on the limiting values of effective normal stress as below

$$\sigma'_{\mathrm{n}} \to \infty \Rightarrow \frac{a_{\mathrm{n}}}{b_{\mathrm{n}}} = \text{verical asymptote to the hyperbola} = D_{\mathrm{n\,max}}$$

$$\sigma'_{\mathrm{n}} \to 0 \Rightarrow D_{\mathrm{n}} \to 0 \Rightarrow K_{\mathrm{n}} = \frac{1}{a_{\mathrm{n}}} = K_{\mathrm{n0}}$$

Eq. 4.10 can be re-written based on maximum closure and initial normal stiffness:

$$\sigma'_{\mathrm{n}} = \frac{D_{\mathrm{n\,max}} . K_{\mathrm{n0}} . D_{\mathrm{n}}}{D_{\mathrm{n\,max}} - D_{\mathrm{n}}} \tag{4.11}$$

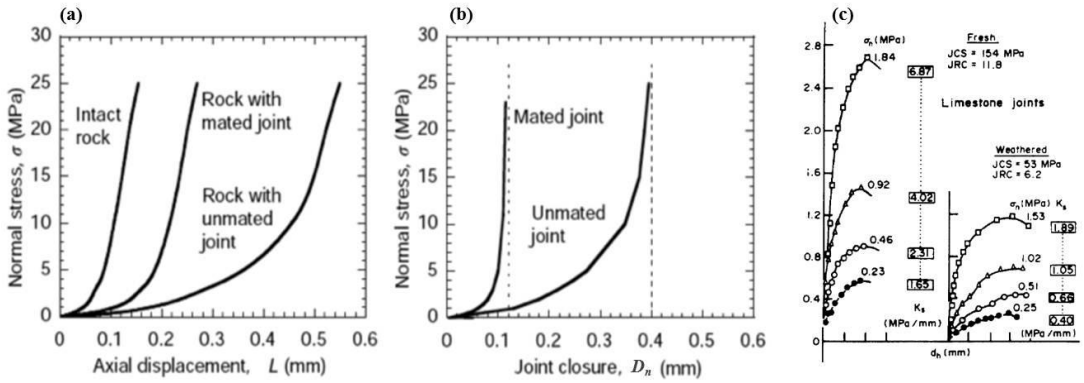

Figure 4.5. Normal and shear fracture deformation under normal and shear stress conditions. (a) axial displacement and (b) fracture closure under normal stress, (c) shear deformation vs. shear stress under different normal stresses [reproduced from Bandis et al., 1983]

The value of fracture normal stiffness can be estimated at any effective stress level of σ'_{n}, based on initial normal stiffness and maximum closure as below:

$$K_{\mathrm{n}} = \frac{\partial \sigma'_{\mathrm{n}}}{\partial D_{\mathrm{n}}} = \frac{K_{\mathrm{n0}}}{\left[1 - \sigma'_{\mathrm{n}} / (K_{\mathrm{n0}} D_{\mathrm{n\,max}} + \sigma'_{\mathrm{n}})\right]^2} \tag{4.12}$$

Based on the above empirical equation, an increase in the effective stress (*i.e.* fracture closure) is associated with a normal stiffness increment until it becomes infinity. In this case, the fracture behavior is dependent on the fracture aperture state and normal stiffness. On the other hand, when the effective stress decreases (*i.e.* fracture opening), fracture normal stiffness reduces until

it reaches zero. In this case, the fracture behavior is very sensitive to the elastic properties of the ambient rock mass [Rutqvist, 1995].

For shear displacement, non-linear behavior is usually expressed via hyperbolic functions. Kulhaway (1975) proposed the following relationship between shear stress (σ_s) and displacement (D_s) for the pre-peak range of the shearing phase:

$$\sigma_s = \frac{D_s}{a_s + b_s D_s} \tag{4.13}$$

where constants a_s and b_s are defined as below

$$D_s \to \infty \Rightarrow \frac{1}{b_s} = \text{horizontal asymptote to the hyperbola} = \sigma_{s\,max}$$

$$\sigma_s \to 0 \Rightarrow D_s \to 0 \Rightarrow K_s = \frac{1}{a_s} = K_{s0}$$

In the above formulation, $\sigma_{s\,max}$ is the peak shear stress and K_{si} is the initial shear stiffness of a fracture.

Barton et al. (1985) used the concept of mobilized roughness to describe the shear behavior of a fracture. To quantify shear stress, a mobilized roughness coefficient (JRC_{mob}) is used which is a function of fracture properties such as normal load, fracture length, current shear displacement and shear displacement history [UDEC Manual]. For the mobilized shear strength ($\sigma_{s\,mob}$) for any shear displacement they suggested:

$$\sigma_{s\,mob} = \sigma_n \tan\left[JRC_{mob} \log\left(JCS / \sigma_n \right) + \phi_r \right] \tag{4.14}$$

where JCS is the joint compressive strength and ϕ_r is the residual friction angle.

Clearly, the complexity of fracture displacement in real cases requires the acceptance of a great degree of empiricism, and calibration of real cases will always be necessary because of this complexity and the uncertainty of the geometrical disposition and individual properties of an array of fractures.

In this study, the modified Barton-Bandis model is implemented to estimate the fracture normal stiffness. In this manner the same formulation for fracture closure is used for the case of injection into the fracture network, which is associated with fracture opening. This behavior is associated with fracture normal stiffness decreasing until it approaches zero when the effective stress becomes zero (Figure 4.6). It should be noted that in this theory it is assumed that the tensile strength of the fracture is negligible and also the effect of fracture scale is not considered.

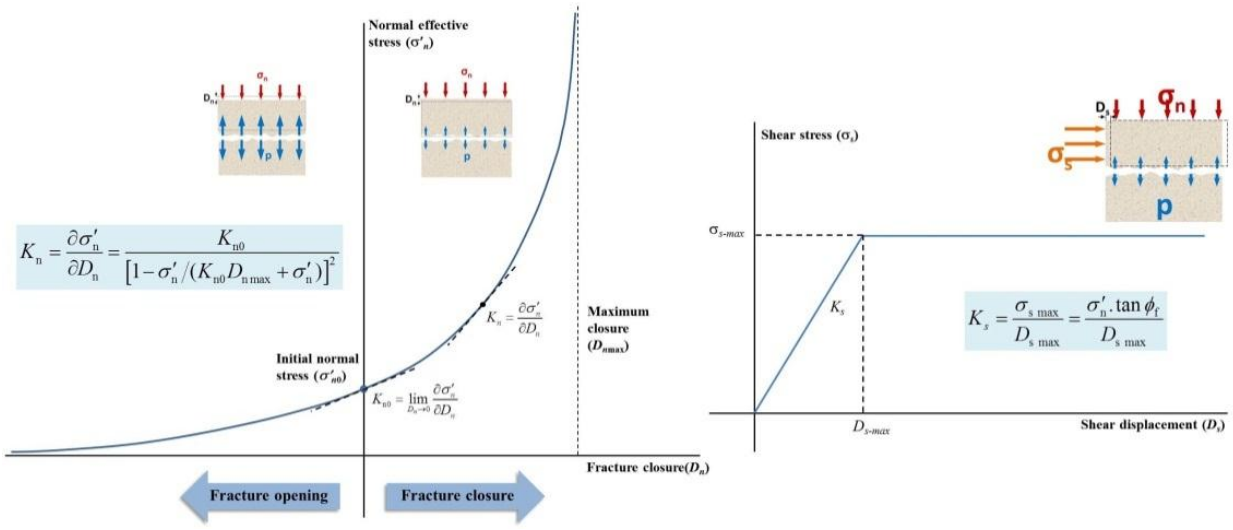

Figure 4.6. Normal and shear fracture stiffness variation under normal and shear stress changes.

A linear relationship between shear stress and shear deformation is considered prior to the peak shear stress that corresponds to constant fracture shear stiffness. The peak shear stress is estimated based on the Mohr-Coulomb criterion for cohesionless rocks (*i.e.* $\sigma_{s\,max} = \sigma'_n \tan\phi_f$).

Due to the complexity of the fracture behavior beyond the peak shear stress, zero fracture shear stiffness is assumed here (Figure 4.6).

4.3.2 Shear Dilation

Fractures are influenced by pore pressure and temperature variation especially under injection processes. In this situation, the dominant failure mechanism is slippage beyond a threshold pressure. The shear slippage is associated with fracture dilation normal to the fracture surface, which can occur at a pressure less than the minimum horizontal stress (Figure 4.7). This phenomenon is called shear dilation and is defined as the displacement normal to the fracture surface during shear slip along a non-planar fracture plane. Shear dilation is a low-effective-stress phenomenon more likely if there are high in situ differential stresses. Injection processes lead to the lowering of effective stresses, which essentially leads to a frictional strength reduction [Dusseault & Collins, 2008]. There are some required geomechanical properties for the occurrence of shear dilation such as high rock strength, high deviatoric stress, brittle rock with a tendency towards plastic deformation (i.e. low Poisson's ratio and high Young's modulus), low strength of rock fabric, and the existence of natural rock fractures.

During the shearing of a fracture, the asperities of the fracture surface slide over each other and cause the dilation normal to the fracture surfaces which is associated with the fracture aperture increment. Barton et al., (1985) quantified the shear dilation effect by introducing the relationship between shear displacement and normal displacement of the fracture as

$$D_{\text{n dilation}} = -D_{\text{s}} \tan\psi \tag{4.15}$$

$D_{\text{n dilation}}$ is the fracture deformation due to shear dilation and ψ is the dilation angle. The negative sign in Eq. 4.15 corresponds to fracture opening as a result of positive shear deformation. Dilation angle is negative in compression whereas it is positive in dilation. Barton et al. (1985) suggested an empirical relationship for shear dilation angle as a function of physical properties of fracture surface as below

$$\psi = \frac{1}{2} JRC \log\left(\frac{JCS}{\sigma'_{\text{n}}}\right) \tag{4.16}$$

In this study, only a constant and small dilation angle is implemented in the model because of the complexity of dilation behavior under different stress conditions.

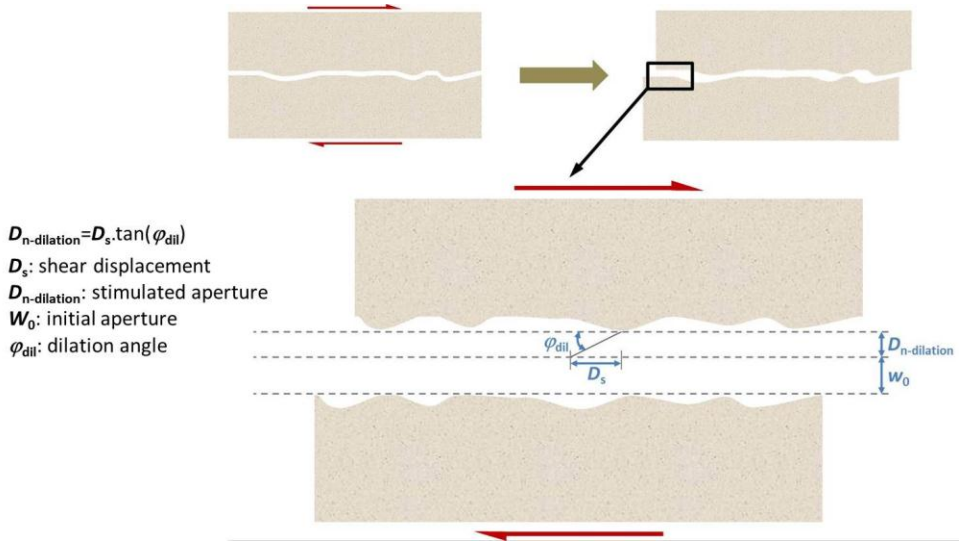

Figure 4.7. Fracture aperture variation caused by shear displacement [reproduced after Rahman et al., 2002]

4.4 Fluid Flow in the Fractures

Much work has been done to study fluid flow behavior in fractures including laboratory work on fluid flow in natural and induced fractures, in-situ fracture studies in the field, and numerical methods [Louis, 1969; Iwai, 1976; Detournay, 1980; Witherspoon et al., 1981; Elsworth, 1984].

Fluid flow in fractures can be modeled by considering fractures as parallel plates within which the volumetric flow rate is proportional to the pressure gradient [Asgian, 1988].

Consider a representative part of a single fracture with a constant elemental length of Δx, unit thickness, and constant aperture of w over the elemental length for a specific time. The pressure diffusion equation for the one-dimensional transient single phase fluid flow along the x-axis is derived based on the fluid mass conservation equation as below:

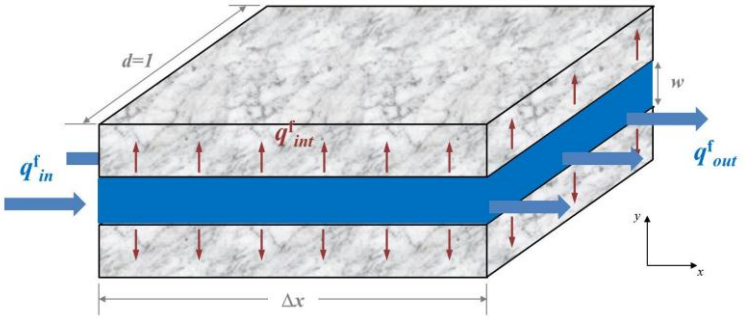

Figure 4.8. Single phase fluid flow in a representative fracture model

$$\frac{\partial(\rho_f w q_x^f)}{\partial x} = -\frac{\partial(\rho_f w)}{\partial t} \mp \rho_f q_s^f \tag{4.17}$$

where ρ_f is the fluid density, q^f_x is the Darcy velocity in the x-direction, q^f_s is the source/sink term with the dimension of volumetric flow rate per unit elemental length Δx and unit thickness. The first term in the left hand side represents the net flow passing through the elemental length of the fracture, the first term on the right hand side is the mass storage variation over time and the second term is the source/sink term. The negative sign in the last term corresponds to fluid withdrawal from the fracture, whereas a positive sign represents injection into the fracture.

Expanding the mass storage time derivative using the definition of isothermal fluid compressibility (c_f) and fluid thermal expansion coefficient (β_f) and considering a constant fluid density over the elemental length of the fracture, the above equation can be re-written as:

$$\frac{\partial(\rho_f w)}{\partial t} = w\frac{\partial \rho_f}{\partial t} + \rho_f \frac{\partial w}{\partial t} = w\left[\rho_f c_f \frac{\partial p}{\partial t} - \rho_f \beta_f \frac{\partial T}{\partial t}\right] + \rho_f \frac{\partial w}{\partial t} \tag{4.18}$$

$$\frac{\partial (w q_x^f)}{\partial x} = -w c_f \frac{\partial p}{\partial t} + w\beta_f \frac{\partial T}{\partial t} - \frac{\partial w}{\partial t} \mp q_s^f \tag{4.19}$$

Based on the assumption of laminar flow (small Reynolds number), the fracture intrinsic conductivity could be defined using the cubic law [Witherspoon et al., 1980] which implies that the Darcy velocity be described as

$$q_x^f = -\frac{w^2}{12\mu}\frac{\partial p}{\partial x} \tag{4.20}$$

The source/sink term in the pressure diffusion equation consists of two terms; one of them is natural and the other one is induced. The natural source/sink term is the fluid leak-off from the fracture into the surrounding rocks when the fracture pressure is more than the matrix pressure and flow will be in the other direction when the fracture is under depletion. The induced part of the source/sink term occurs due to fluid production or injection into the fracture. In this formulation, a fluid injection process is assumed, so the source/sink term has the following components:

$$q_s^f = q_{int}^f - q_{inj}^f$$

where $q^{\mathrm{f}}_{\mathrm{int}}$ is the interface flow rate between fracture and matrix per elemental fracture length and unit thickness and $q^{\mathrm{f}}_{\mathrm{inj}}$ is the injection flow rate per elemental length and unit thickness. Substituting the above equations into Eq. 4.19 results in

$$\frac{w^3}{12\mu}\frac{\partial^2 p}{\partial x^2} = wc_{\mathrm{f}}\frac{\partial p}{\partial t} - w\beta_{\mathrm{f}}\frac{\partial T}{\partial t} + \frac{\partial w}{\partial t} + q^{\mathrm{f}}_{\mathrm{int}} - q^{\mathrm{f}}_{\mathrm{inj}} \tag{4.21}$$

This equation is the general form of the one-dimensional fluid diffusion equation in a fracture. The left hand side shows the net flow rate in the fracture, the first term on the right hand side is the fluid volume variation due to compression or expansion, the second term represents the fluid volume changes as a result of temperature variation, the third term is the fluid volume changes due to fracture deformation, the fourth term is the interface flow rate into the surrounding rocks, and the last term is the fluid injection rate per fracture elemental length and unit thickness.

It can be assumed that aperture changes are equal to the normal displacement discontinuity variations. In this case the displacement discontinuities form of the pressure diffusion equation has the following form:

$$\frac{w^3}{12\mu}\frac{\partial^2 p}{\partial x^2} = wc_{\mathrm{f}}\frac{\partial p}{\partial t} - w\beta_{\mathrm{f}}\frac{\partial T}{\partial t} - \frac{\partial D_{\mathrm{n}}}{\partial t} + q^{\mathrm{f}}_{\mathrm{int}} - q^{\mathrm{f}}_{\mathrm{inj}} \tag{4.22}$$

4.5 Heat Flow in Fractures

Most studies on heat transfer in porous media and fractures have been done in enhanced geothermal systems where water is circulated in the natural and man-made fractures in low permeability igneous and metamorphic hot rocks to extract geothermal energy [Hayashi et al., 1999; Ghassemi et al., 2005].

Heat transport in a fracture and its interaction with surrounding rocks can be studied using the energy conservation equation for the fluid and rock in the representative fracture segment. Again, consider the same control volume as for fluid flow. The heat transfer equation for one-dimensional transient heat flow along the *x*-axis is derived based on the heat conservation equation:

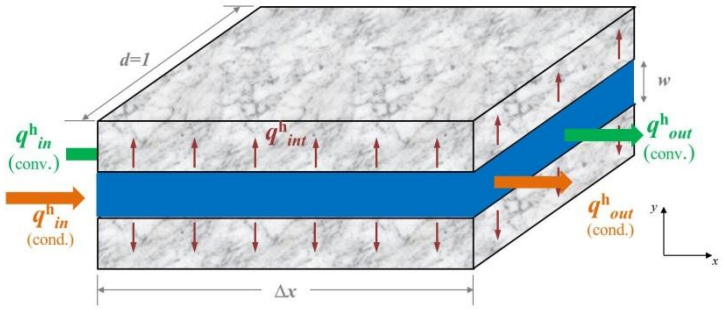

Figure 4.9. Heat flow in a representative fracture model

$$(Q^{\mathrm{h}}_{\mathrm{in}} - Q^{\mathrm{h}}_{\mathrm{out}})_{\mathrm{cond}} + (Q^{\mathrm{h}}_{\mathrm{in}} - Q^{\mathrm{h}}_{\mathrm{out}})_{\mathrm{conv}} = \frac{\partial(\rho_{\mathrm{f}} V_{\mathrm{f}} C_{\mathrm{f}} T)}{\partial t} \pm Q^{\mathrm{h}}_{\mathrm{s}} \tag{4.23}$$

where Q^{h} is the heat flow rate, V_{f} is the fluid volume, C_{f} is the specific heat of fluid and $Q^{\mathrm{h}}{}_{s}$ is the heat source/sink term. Subscripts "cond" and "conv" correspond to conduction and convection heat transfer, respectively.

In Eq. 4.23, the first term on the right hand side is the net conductive heat flow (transferred energy by heat flux) and the second term is the net convective heat flow (transferred energy by mass flux). The first term on the right hand side is the variation of fluid energy over time and the second term is the source/sink term. It should be noted that heat radiation is assumed to be negligible. Applying the definitions of heat conduction and convection and dividing the equation

by the elemental fracture length Δx for a unit thickness fracture, the heat transfer equation can be written as

$$k_{\mathrm{T}} w \frac{\partial^2 T}{\partial x^2} - \rho_{\mathrm{f}} C_{\mathrm{f}} q_x^{\mathrm{f}} w \frac{\partial T}{\partial x} = \frac{\partial (\rho_{\mathrm{f}} C_{\mathrm{f}} w T)}{\partial t} \pm q_{\mathrm{s}}^{\mathrm{h}} \tag{4.24}$$

where k_{T} is the thermal conductivity, q^{f}_x is the Darcy velocity in the x-direction and q^{h}_s is the heat source/sink term per unit thickness and elemental length Δx. In this formulation, thermal conductivity, Darcy velocity, and fluid specific heat are assumed to be constant over time. Expanding the fluid energy time derivative using the definition of isothermal fluid compressibility (c_{f}) and fluid thermal expansion coefficient (β_{f}) and considering a constant fluid density over the elemental length of the fracture, the above equation can be re-written as:

$$\begin{aligned}
&\frac{\partial \left(\rho_{\mathrm{f}} C_{\mathrm{f}} w T\right)}{\partial t} = C_{\mathrm{f}} w T \frac{\partial \rho_{\mathrm{f}}}{\partial t} + \rho_{\mathrm{f}} C_{\mathrm{f}} T \frac{\partial w}{\partial t} + \rho_{\mathrm{f}} C_{\mathrm{f}} w \frac{\partial T}{\partial t} = C_{\mathrm{f}} w T \left[\rho_{\mathrm{f}} c_{\mathrm{f}} \frac{\partial p}{\partial t} - \rho_{\mathrm{f}} \beta_{\mathrm{f}} \frac{\partial T}{\partial t} \right] \\
&+ \rho_{\mathrm{f}} C_{\mathrm{f}} T \frac{\partial w}{\partial t} + \rho_{\mathrm{f}} C_{\mathrm{f}} w \frac{\partial T}{\partial t} = \left[\rho_{\mathrm{f}} C_{\mathrm{f}} w - \rho_{\mathrm{f}} C_{\mathrm{f}} w \beta_{\mathrm{f}} T\right] \frac{\partial T}{\partial t} + \left[\rho_{\mathrm{f}} C_{\mathrm{f}} w c_{\mathrm{f}} T\right] \frac{\partial p}{\partial t} + \left[\rho_{\mathrm{f}} C_{\mathrm{f}} T\right] \frac{\partial w}{\partial t} \\
&k_{\mathrm{T}} w \frac{\partial^2 T}{\partial x^2} - \rho_{\mathrm{f}} C_{\mathrm{f}} q_x^{\mathrm{f}} w \frac{\partial T}{\partial x} = \left[\rho_{\mathrm{f}} C_{\mathrm{f}} w - \rho_{\mathrm{f}} C_{\mathrm{f}} w \beta_{\mathrm{f}} T\right] \frac{\partial T}{\partial t} + \left[\rho_{\mathrm{f}} C_{\mathrm{f}} w c_{\mathrm{f}} T\right] \frac{\partial p}{\partial t} - \left[\rho_{\mathrm{f}} C_{\mathrm{f}} T\right] \frac{\partial D_{\mathrm{n}}}{\partial t} + q_{\mathrm{int}}^{\mathrm{h}} - q_{\mathrm{s}}^{\mathrm{h}}
\end{aligned} \tag{4.25}$$

This equation is the general form of one-dimensional heat transfer equation in a fracture. The first term on the left hand side term shows the heat conduction and the second term is the heat convection, the first term on the right hand side is the internal energy variation due to temperature changes, the second term represents the internal energy changes due to compression or expansion, the third term is the internal energy changes as a result of fracture deformation (normal displacement discontinuity), the fourth term is the interface heat flow rate into the

surrounding rocks and the last term is the heat source rate per fracture elemental length and unit thickness.

Assuming a constant fracture aperture and fluid density over time results in the conventional one-dimensional heat transfer equation in the following form:

$$k_{\mathrm{T}} \frac{\partial^2 T}{\partial x^2} - \rho_{\mathrm{f}} C_{\mathrm{f}} q_x^{\mathrm{f}} \frac{\partial T}{\partial x} = \rho_{\mathrm{f}} C_{\mathrm{f}} \frac{\partial T}{\partial t} + q_{\mathrm{int}}^{\mathrm{h}} - q_{\mathrm{s}}^{\mathrm{h}} \tag{4.26}$$

4.6 Fully Coupled Finite Difference - Displacement Discontinuity Model

Based on the discussion in Section 4.3, the normal and shear displacement discontinuities are related to the normal and shear stresses on the fracture plane through the fracture normal and shear stiffnesses as below:

$$\begin{aligned} \Delta\sigma'^{\tau_n}_{\mathrm{n}\,i} &= \Delta\sigma^{\tau_n}_{\mathrm{n}\,i} - \Delta p_i^{\tau_n} = -\sum_{tc=1}^{n} K_{\mathrm{n}\,i}^{t_{n-tc+1}} (\Delta D_{\mathrm{n}\,i}^{\tau_{tc}} + \tan\psi . \Delta D_{\mathrm{s}\,i}^{\tau_{tc}}) \\ \Delta\sigma_{\mathrm{s}\,i}^{\tau_n} &= \sum_{tc=1}^{n} K_{\mathrm{s}\,i}^{\tau_{tc}} \Delta D_{\mathrm{s}\,i}^{\tau_{tc}} \end{aligned} \tag{4.27}$$

In Eq. 4.27, it is assumed that the fracture is at an equilibrium state under the in-situ stress prior to the injection/production process. This implies that the in-situ stresses do not change the fracture's aperture at the initial time step. Normal and shear stresses in Eq. 4.8 can be replaced by the expressions in Eq. 4.27, to reduce the problem to 2*N* unknowns:

$$\begin{aligned} &\sum_{j=1}^{N} A_{ij}^{\tau_1} \Delta D_{\mathrm{s}\,j}^{\tau_1} + \sum_{j=1}^{N} B_{ij}^{\tau_1} \Delta D_{\mathrm{n}\,j}^{\tau_1} + \sum_{j=1}^{N} C_{ij}^{\tau_1} \Delta Q_{\mathrm{fs}\,j}^{\tau_1} + \sum_{j=1}^{N} E_{ij}^{\tau_1} \Delta Q_{\mathrm{hs}\,j}^{\tau_1} - K_{\mathrm{s}\,i}^{t_n} \Delta D_{\mathrm{s}\,i}^{\tau_1} \\ &= -\sum_{tc=2}^{n} \sum_{j=1}^{N} A_{ij}^{\tau_{tc}} \Delta D_{\mathrm{s}\,j}^{\tau_{tc}} - \sum_{tc=2}^{n} \sum_{j=1}^{N} B_{ij}^{\tau_{tc}} \Delta D_{\mathrm{n}\,j}^{\tau_{tc}} - \sum_{tc=2}^{n} \sum_{j=1}^{N} C_{ij}^{\tau_{tc}} \Delta Q_{\mathrm{fs}\,j}^{\tau_{tc}} - \sum_{tc=2}^{n} \sum_{j=1}^{N} E_{ij}^{\tau_{tc}} \Delta Q_{\mathrm{hs}\,j}^{\tau_{tc}} + \sum_{tc=2}^{n} K_{\mathrm{s}\,i}^{t_{n-tc+1}} \Delta D_{\mathrm{s}\,i}^{\tau_{tc}} \end{aligned}$$

$$
\begin{aligned}
&p_i^{t_n} + \sum_{j=1}^{N} F_{ij}^{\tau_1} \Delta D_{\mathrm{s}\,j}^{\tau_1} + \sum_{j=1}^{N} H_{ij}^{\tau_1} \Delta D_{\mathrm{n}\,j}^{\tau_1} + \sum_{j=1}^{N} L_{ij}^{\tau_1} \Delta Q_{\mathrm{fs}\,j}^{\tau_1} + \sum_{j=1}^{N} M_{ij}^{\tau_1} \Delta Q_{\mathrm{hs}\,j}^{\tau_1} + K_{\mathrm{n}\,i}^{t_n} \left[\Delta D_{\mathrm{n}\,i}^{\tau_1} + \tan\psi \Delta D_{\mathrm{s}\,i}^{\tau_1} \right] \\
&= -\sum_{tc=2}^{n} \sum_{j=1}^{N} F_{ij}^{\tau_{tc}} \Delta D_{\mathrm{s}\,j}^{\tau_{tc}} - \sum_{tc=2}^{n} \sum_{j=1}^{N} H_{ij}^{\tau_{tc}} \Delta D_{\mathrm{n}\,j}^{\tau_{tc}} - \sum_{tc=2}^{n} \sum_{j=1}^{N} L_{ij}^{\tau_{tc}} \Delta Q_{\mathrm{fs}\,j}^{\tau_{tc}} - \sum_{tc=2}^{n} \sum_{j=1}^{N} M_{ij}^{\tau_{tc}} \Delta Q_{\mathrm{hs}\,j}^{\tau_{tc}} \\
&- \sum_{tc=2}^{n} K_{\mathrm{n}\,i}^{t_{n-tc+1}} \left[\Delta D_{\mathrm{n}\,i}^{\tau_{tc}} + \tan\psi \Delta D_{\mathrm{s}\,i}^{\tau_{tc}} \right] + p_i^{t_0}
\end{aligned}
\tag{4.28}
$$

$$
\begin{aligned}
&\sum_{j=1}^{N} N_{ij}^{\tau_1} \Delta D_{\mathrm{s}\,j}^{\tau_1} + \sum_{j=1}^{N} O_{ij}^{\tau_1} \Delta D_{\mathrm{n}\,j}^{\tau_1} + \sum_{j=1}^{N} R_{ij}^{\tau_1} \Delta Q_{\mathrm{fs}\,j}^{\tau_1} + \sum_{j=1}^{N} S_{ij}^{\tau_1} \Delta Q_{\mathrm{hs}\,j}^{\tau_1} - p_i^{t_n} \\
&= -\sum_{tc=2}^{n} \sum_{j=1}^{N} N_{ij}^{\tau_{tc}} \Delta D_{\mathrm{s}\,j}^{\tau_{tc}} - \sum_{tc=2}^{n} \sum_{j=1}^{N} O_{ij}^{\tau_{tc}} \Delta D_{\mathrm{n}\,j}^{\tau_{tc}} - \sum_{tc=2}^{n} \sum_{j=1}^{N} R_{ij}^{\tau_{tc}} \Delta Q_{\mathrm{fs}\,j}^{\tau_{tc}} - \sum_{tc=2}^{n} \sum_{j=1}^{N} S_{ij}^{\tau_{tc}} \Delta Q_{\mathrm{hs}\,j}^{\tau_{tc}} - p_i^{t_0}
\end{aligned}
$$

$$
\sum_{j=1}^{N} U_{ij}^{\tau_1} \Delta Q_{\mathrm{hs}\,j}^{\tau_1} - T_i^{t_n} = \sum_{tc=2}^{n} \sum_{j=1}^{N} U_{ij}^{\tau_{tc}} \Delta Q_{\mathrm{hs}\,j}^{\tau_{tc}} - T_i^{t_0}
$$

In Eq. 4.28, p_i^{t0} and T_i^{t0} are the pressure and temperature at time step zero which are the initial pressure and temperature in the rock.

The modified version of pressure and temperature diffusion equations (Eq. 4.22 and 4.25) can also be added to Eq. 4.28 (refer to Appendix F), to come up with 6*N* equation and 6*N* unknowns, which are pressure, temperature, fluid and heat source strengths, and normal and shear displacement discontinuities in each fracture segment:

$$
\begin{aligned}
&\sum_{j=1}^{N} A_{ij}^{\tau_1} \Delta D_{\mathrm{s}\,j}^{\tau_1} + \sum_{j=1}^{N} B_{ij}^{\tau_1} \Delta D_{\mathrm{n}\,j}^{\tau_1} + \sum_{j=1}^{N} C_{ij}^{\tau_1} \Delta Q_{\mathrm{fs}\,j}^{\tau_1} + \sum_{j=1}^{N} E_{ij}^{\tau_1} \Delta Q_{\mathrm{hs}\,j}^{\tau_1} - K_{\mathrm{s}\,i}^{t_n} \Delta D_{\mathrm{s}\,i}^{\tau_1} \\
&= -\sum_{tc=2}^{n} \sum_{j=1}^{N} A_{ij}^{\tau_{tc}} \Delta D_{\mathrm{s}\,j}^{\tau_{tc}} - \sum_{tc=2}^{n} \sum_{j=1}^{N} B_{ij}^{\tau_{tc}} \Delta D_{\mathrm{n}\,j}^{\tau_{tc}} - \sum_{tc=2}^{n} \sum_{j=1}^{N} C_{ij}^{\tau_{tc}} \Delta Q_{\mathrm{fs}\,j}^{\tau_{tc}} - \sum_{tc=2}^{n} \sum_{j=1}^{N} E_{ij}^{\tau_{tc}} \Delta Q_{\mathrm{hs}\,j}^{\tau_{tc}} + \sum_{tc=2}^{n} K_{\mathrm{s}\,i}^{t_{n-tc+1}} \Delta D_{\mathrm{s}\,i}^{\tau_{tc}}
\end{aligned}
$$

$$
\begin{aligned}
&p_i^{t_n} + \sum_{j=1}^{N} F_{ij}^{\tau_1} \Delta D_{\mathrm{s}\,j}^{\tau_1} + \sum_{j=1}^{N} H_{ij}^{\tau_1} \Delta D_{\mathrm{n}\,j}^{\tau_1} + \sum_{j=1}^{N} L_{ij}^{\tau_1} \Delta Q_{\mathrm{fs}\,j}^{\tau_1} + \sum_{j=1}^{N} M_{ij}^{\tau_1} \Delta Q_{\mathrm{hs}\,j}^{\tau_1} + K_{\mathrm{n}\,i}^{t_n} \left[\Delta D_{\mathrm{n}\,i}^{\tau_1} + \tan\psi \Delta D_{\mathrm{s}\,i}^{\tau_1} \right] \\
&= -\sum_{tc=2}^{n} \sum_{j=1}^{N} F_{ij}^{\tau_{tc}} \Delta D_{\mathrm{s}\,j}^{\tau_{tc}} - \sum_{tc=2}^{n} \sum_{j=1}^{N} H_{ij}^{\tau_{tc}} \Delta D_{\mathrm{n}\,j}^{\tau_{tc}} - \sum_{tc=2}^{n} \sum_{j=1}^{N} L_{ij}^{\tau_{tc}} \Delta Q_{\mathrm{fs}\,j}^{\tau_{tc}} - \sum_{tc=2}^{n} \sum_{j=1}^{N} M_{ij}^{\tau_{tc}} \Delta Q_{\mathrm{hs}\,j}^{\tau_{tc}} \\
&- \sum_{tc=2}^{n} K_{\mathrm{n}\,i}^{t_{n-tc+1}} \left[\Delta D_{\mathrm{n}\,i}^{\tau_{tc}} + \tan\psi \Delta D_{\mathrm{s}\,i}^{\tau_{tc}} \right] + p_i^{t_0}
\end{aligned}
$$

$$
\begin{aligned}
&\sum_{j=1}^{N} N_{ij}^{\tau_1} \Delta D_{\mathrm{s}\,j}^{\tau_1} + \sum_{j=1}^{N} O_{ij}^{\tau_1} \Delta D_{\mathrm{n}\,j}^{\tau_1} + \sum_{j=1}^{N} R_{ij}^{\tau_1} \Delta Q_{\mathrm{fs}\,j}^{\tau_1} + \sum_{j=1}^{N} S_{ij}^{\tau_1} \Delta Q_{\mathrm{hs}\,j}^{\tau_1} - p_i^{t_n} \\
&= -\sum_{tc=2}^{n} \sum_{j=1}^{N} N_{ij}^{\tau_{tc}} \Delta D_{\mathrm{s}\,j}^{\tau_{tc}} - \sum_{tc=2}^{n} \sum_{j=1}^{N} O_{ij}^{\tau_{tc}} \Delta D_{\mathrm{n}\,j}^{\tau_{tc}} - \sum_{tc=2}^{n} \sum_{j=1}^{N} R_{ij}^{\tau_{tc}} \Delta Q_{\mathrm{fs}\,j}^{\tau_{tc}} - \sum_{tc=2}^{n} \sum_{j=1}^{N} S_{ij}^{\tau_{tc}} \Delta Q_{\mathrm{hs}\,j}^{\tau_{tc}} - p_i^{t_0}
\end{aligned}
\qquad (4.29)
$$

$$
\sum_{j=1}^{N} U_{ij}^{\tau_1} \Delta Q_{\mathrm{hs}\,j}^{\tau_1} - T_i^{t_n} = \sum_{tc=2}^{n} \sum_{j=1}^{N} U_{ij}^{\tau_{tc}} \Delta Q_{\mathrm{hs}\,j}^{\tau_{tc}} - T_i^{t_0}
$$

$$
\sum_{l=1}^{nc} \Gamma_{i-jl}^{\mathrm{f}} \tau_1 p_{jl}^{t_n} - \left[\sum_{l=1}^{nc} \Gamma_{i-jl}^{\mathrm{f}} \tau_1 + 2a_i \, w_i^{t_n} c_{\mathrm{f}} \right] p_i^{t_n} + 2a_i \, \Delta D_{\mathrm{n}\,i}^{\tau_1} - 2a_i \, \tau_1 \Delta Q_{\mathrm{fs}\,i}^{\tau_1} = -2a_i \, w_i^{t_n} c_{\mathrm{f}} \, p_i^{t_{n-1}} - \tau_1 . q_{\mathrm{inj}}^{\mathrm{f}}
$$

$$
\begin{aligned}
&\sum_{l=1}^{nc} \left[\Gamma_{i-jl}^{\mathrm{h}} \tau_1 - \rho_{\mathrm{f}} q_x^{\mathrm{f}\,t_n} C_{\mathrm{f}} \Omega_{i-jl}^{\mathrm{h}} \tau_1 \right] T_{jl}^{t_n} - \sum_{l=1}^{nc} \left\{ \Gamma_{i-jl}^{\mathrm{h}} \tau_1 + \rho_{\mathrm{f}} C_{\mathrm{f}} \left[q_x^{\mathrm{f}\,t_n} \Omega_{i-jl}^{\mathrm{h}} \tau_1 + 2a_i w_i^{t_n} \right] \right\} T_i^{t_n} - 2a_i \tau_1 \Delta Q_{\mathrm{hs}\,i}^{\tau_1} \\
&= -2a_i \rho_{\mathrm{f}} C_{\mathrm{f}} w_i^{t_n} T_i^{t_{n-1}} - \tau_1 . q_{\mathrm{inj}}^{\mathrm{h}}
\end{aligned}
$$

Eq. 4.29 is the final form of the governing equation for a two-dimensional hybrid finite difference-displacement discontinuity method in a thermo-poroelastic medium. The displacement discontinuity equations (first four equations) are linear, whereas the heat and fluid diffusion equations are non-linear, i.e. aperture and Darcy velocity, which are unknown in the new time step, also appear in the coefficients of the pressure and temperature terms.

This non-linearity can be handled using different methods such as a simple iteration method, a direct iteration method, and the Newton-Raphson method. In the simple iteration method, the aperture and Darcy velocity (iteration's unknowns) from the previous time step are used in the

current time step. In the direct iteration method, the iterations' unknowns are calculated iteratively until the difference between two successive values is less than a specific tolerance; in this method the values from the previous time step are used as the initial guesses for the unknowns. The Newton-Raphson method to estimate the iteration's unknown uses a tangent approach similar to the direct method, but with faster convergence. In this study, both simple iteration and direct iteration methods are applied to Eq. 4.29 to estimate the fracture's unknowns. The simple iteration form of Eq. 4.29 has the following form:

$$
\begin{aligned}
&\sum_{j=1}^{N} A_{ij}^{\tau_1}\Delta D_{\mathrm{s}\,j}^{\tau_1}+\sum_{j=1}^{N} B_{ij}^{\tau_1}\Delta D_{\mathrm{n}\,j}^{\tau_1}+\sum_{j=1}^{N} C_{ij}^{\tau_1}\Delta Q_{\mathrm{fs}\,j}^{\tau_1}+\sum_{j=1}^{N} E_{ij}^{\tau_1}\Delta Q_{\mathrm{hs}\,j}^{\tau_1}-K_{\mathrm{s}\,i}^{t_n}\Delta D_{\mathrm{s}\,i}^{\tau_1}\\
&=-\sum_{tc=2}^{n}\sum_{j=1}^{N} A_{ij}^{\tau_{tc}}\Delta D_{\mathrm{s}\,j}^{\tau_{tc}}-\sum_{tc=2}^{n}\sum_{j=1}^{N} B_{ij}^{\tau_{tc}}\Delta D_{\mathrm{n}\,j}^{\tau_{tc}}-\sum_{tc=2}^{n}\sum_{j=1}^{N} C_{ij}^{\tau_{tc}}\Delta Q_{\mathrm{fs}\,j}^{\tau_{tc}}-\sum_{tc=2}^{n}\sum_{j=1}^{N} E_{ij}^{\tau_{tc}}\Delta Q_{\mathrm{hs}\,j}^{\tau_{tc}}+\sum_{tc=2}^{n} K_{\mathrm{s}\,i}^{t_{n-tc+1}}\Delta D_{\mathrm{s}\,i}^{\tau_{tc}}
\end{aligned}
$$

$$
\begin{aligned}
&p_i^{t_n}+\sum_{j=1}^{N} F_{ij}^{\tau_1}\Delta D_{\mathrm{s}\,j}^{\tau_1}+\sum_{j=1}^{N} H_{ij}^{\tau_1}\Delta D_{\mathrm{n}\,j}^{\tau_1}+\sum_{j=1}^{N} L_{ij}^{\tau_1}\Delta Q_{\mathrm{fs}\,j}^{\tau_1}+\sum_{j=1}^{N} M_{ij}^{\tau_1}\Delta Q_{\mathrm{hs}\,j}^{\tau_1}+K_{\mathrm{n}\,i}^{t_n}\left[\Delta D_{\mathrm{n}\,i}^{\tau_1}+\tan\psi\Delta D_{\mathrm{s}\,i}^{\tau_1}\right]\\
&=-\sum_{tc=2}^{n}\sum_{j=1}^{N} F_{ij}^{\tau_{tc}}\Delta D_{\mathrm{s}\,j}^{\tau_{tc}}-\sum_{tc=2}^{n}\sum_{j=1}^{N} H_{ij}^{\tau_{tc}}\Delta D_{\mathrm{n}\,j}^{\tau_{tc}}-\sum_{tc=2}^{n}\sum_{j=1}^{N} L_{ij}^{\tau_{tc}}\Delta Q_{\mathrm{fs}\,j}^{\tau_{tc}}-\sum_{tc=2}^{n}\sum_{j=1}^{N} M_{ij}^{\tau_{tc}}\Delta Q_{\mathrm{hs}\,j}^{\tau_{tc}}\\
&-\sum_{tc=2}^{n} K_{\mathrm{n}\,i}^{t_{n-tc+1}}\left[\Delta D_{\mathrm{n}\,i}^{\tau_{tc}}+\tan\psi\Delta D_{\mathrm{s}\,i}^{\tau_{tc}}\right]+p_i^{t_0}
\end{aligned}
$$

$$
\begin{aligned}
&\sum_{j=1}^{N} N_{ij}^{\tau_1}\Delta D_{\mathrm{s}\,j}^{\tau_1}+\sum_{j=1}^{N} O_{ij}^{\tau_1}\Delta D_{\mathrm{n}\,j}^{\tau_1}+\sum_{j=1}^{N} R_{ij}^{\tau_1}\Delta Q_{\mathrm{fs}\,j}^{\tau_1}+\sum_{j=1}^{N} S_{ij}^{\tau_1}\Delta Q_{\mathrm{hs}\,j}^{\tau_1}-p_i^{t_n}\\
&=-\sum_{tc=2}^{n}\sum_{j=1}^{N} N_{ij}^{\tau_{tc}}\Delta D_{\mathrm{s}\,j}^{\tau_{tc}}-\sum_{tc=2}^{n}\sum_{j=1}^{N} O_{ij}^{\tau_{tc}}\Delta D_{\mathrm{n}\,j}^{\tau_{tc}}-\sum_{tc=2}^{n}\sum_{j=1}^{N} R_{ij}^{\tau_{tc}}\Delta Q_{\mathrm{fs}\,j}^{\tau_{tc}}-\sum_{tc=2}^{n}\sum_{j=1}^{N} S_{ij}^{\tau_{tc}}\Delta Q_{\mathrm{hs}\,j}^{\tau_{tc}}-p_i^{t_0}
\end{aligned}
\qquad (4.30)
$$

$$
\sum_{j=1}^{N} U_{ij}^{\tau_1}\Delta Q_{\mathrm{hs}\,j}^{\tau_1}-T_i^{t_n}=\sum_{tc=2}^{n}\sum_{j=1}^{N} U_{ij}^{\tau_{tc}}\Delta Q_{\mathrm{hs}\,j}^{\tau_{tc}}-T_i^{t_0}
$$

$$
\sum_{l=1}^{nc}\Gamma_{i-jl}^{\mathrm{f}}\tau_1 p_{jl}^{t_n}-\left[\sum_{l=1}^{nc}\Gamma_{i-jl}^{\mathrm{f}}\tau_1+2a_i\, w_i^{t_{n-1}}c_{\mathrm{f}}\right]p_i^{t_n}+2a_i\,\Delta D_{\mathrm{n}\,i}^{\tau_1}-2a_i\,\tau_1\Delta Q_{\mathrm{fs}\,i}^{\tau_1}=-2a_i\, w_i^{t_{n-1}}c_{\mathrm{f}}\, p_i^{t_{n-1}}-\tau_1.q_{\mathrm{inj}}^{\mathrm{f}}
$$

$$\sum_{l=1}^{nc}\left[\Gamma^{\mathrm{h}}_{i-jl}\tau_1-\rho_{\mathrm{f}}q_x^{\mathrm{f}\,t_{n-1}}C_{\mathrm{f}}\Omega^{\mathrm{h}}_{i-jl}\tau_1\right]T_{jl}^{t_n}-\sum_{l=1}^{nc}\left\{\Gamma^{\mathrm{h}}_{i-jl}\tau_1+\rho_{\mathrm{f}}C_{\mathrm{f}}\left[q_x^{\mathrm{f}\,t_{n-1}}\Omega^{\mathrm{h}}_{i-jl}\tau_1+2a_i w_i^{t_{n-1}}\right]\right\}T_i^{t_n}-2a_i\tau_1\Delta Q^{\tau_1}_{\mathrm{hs}\,i}$$
$$=-2a_i\rho_{\mathrm{f}}C_{\mathrm{f}}w_i^{t_{n-1}}T_i^{t_{n-1}}-\tau_1.q^{\mathrm{h}}_{\mathrm{inj}}$$

where w_i^{tn} and $q^{\mathrm{f}}{}_x^{tn}$ have been substituted by w_i^{tn-1} and $q^{\mathrm{f}}{}_x^{tn-1}$. The left hand side of Eq. 4.30 contains the unknowns whereas all the parameters on the right hand side are known. Integrating all these equations together results in a 6*N* linear system of equations that can be solved for the unknowns using common solution methods such as Gaussian elimination. A 6×6 part of the whole matrix for the fracture segment *i* is shown in Eq. 4.31:

$$\begin{bmatrix}
\ddots & \vdots & \vdots & \vdots & \vdots & \vdots & \vdots & \iddots \\
\cdots & COF_{\mathrm{p}\,i} & -2\tau_1 a_i & 0 & 0 & 0 & 2a_i & \cdots \\
\cdots & -1 & R_{ij} & 0 & S_{ij} & N_{ij} & O_{ij} & \cdots \\
\cdots & 0 & 0 & COF_{\mathrm{T}\,i} & -2\tau_1 a_i/\rho_{\mathrm{f}}C_{\mathrm{f}} & 0 & 0 & \cdots \\
\cdots & 0 & 0 & -1 & U_{ij} & 0 & 0 & \cdots \\
\cdots & 0 & C_{ij} & 0 & E_{ij} & A_{ij}-K_{\mathrm{s}\,i} & B_{ij} & \cdots \\
\cdots & +1 & L_{ij} & 0 & M_{ij} & F_{ij}+K_{\mathrm{n}\,i}\tan\psi & G_{ij}+K_{\mathrm{n}\,i} & \cdots \\
\iddots & \vdots & \vdots & \vdots & \vdots & \vdots & \vdots & \ddots
\end{bmatrix}
\begin{bmatrix} \vdots \\ p_i \\ \Delta Q_{\mathrm{fs}\,i} \\ T_i \\ \Delta Q_{\mathrm{hs}\,i} \\ \Delta D_{\mathrm{s}\,i} \\ \Delta D_{\mathrm{n}\,i} \\ \vdots \end{bmatrix}
=
\begin{bmatrix} \vdots \\ bp_i \\ bQ_{\mathrm{fs}\,i} \\ bT_i \\ bQ_{\mathrm{hs}\,i} \\ bD_{\mathrm{s}\,i} \\ bD_{\mathrm{n}\,i} \\ \vdots \end{bmatrix} \tag{4.31}$$

where COF_{p} and COF_{T} are the pressure and temperature coefficients that were presented in Eq. 4.30.

Solving Eq. 4.30 will give an estimate of the unknowns for each fracture segment. Using this estimation, it is possible to estimate displacement, stress, pressure and temperature on the fracture plane and the surrounding rock using Eq. 4.7. Both pressure and temperature can be estimated using the diffusion equations as well as fluid and heat source equations that should be identical as all these equations are solved simultaneously.

The following assumptions are considered in the FDM-DDM hybrid solution:

- Linear elastic, isotropic and homogenous porous medium;
- Quasi-static condition with no inertial forces;
- Plane strain condition;
- Single phase transient fluid flow under a Darcian flow condition without any gravitational forces;
- No chemical reaction during the fluid and heat flow;
- No viscous dissipation, radiative effect and work (energy loss) due to pressure change;
- Thermal local equilibrium between solid and liquid phase;
- Constant porosity, thermal expansion coefficient, thermal conductivity, fluid density, and fluid viscosity;
- Heat conduction is the only heat transfer mechanism in the rock where heat convection is also considered to model the heat propagation in the fracture network;
- Effect of volumetric strain on temperature variation is negligible;
- Modified Barton-Bandis is implemented to estimate the fracture normal stiffness. Tensile strength of the fracture is negligible and the effect of fracture scale is not considered;
- Constant fracture shear stiffness is considered prior to peak shear stress. Beyond the peak shear stress, zero fracture shear stiffness is assumed;
- Constant dilation angle due to the complexity of dilation behavior under different stress conditions.

4.7 Chapter Summary

In this chapter the structure of the hybrid FDM-DDM model was presented. For this purpose, the equations for displacement discontinuities as well as fluid and heat source strengths were presented using the fundamental solutions described in Chapter 3. The behavior of fractures was quantified using the fracture parameters such as normal and shear fracture stiffness and shear dilation angle. The implicit finite difference form of the fluid and heat governing equation in the fracture network was also presented in this chapter. In order to have a fully coupled approach, all the displacement discontinuities equations and finite difference governing equations were put together to construct a matrix with size $6N$ by $6N$ where N is the number of fracture segments in the problem.

Chapter 5
Model Verification

Analytical or semi-analytical solutions are the preferred initial approach in any engineering analysis. Analytical solutions permit direct physical insight of problems and quick estimation of unknowns. Although there are some closed-form solutions for coupled stress-flow problems in the literature, THM coupled problems cannot be evaluated properly using analytical or semi-analytical solutions. Dusseault (2008) summarized some of the drawbacks of analytical or semi-analytical solutions of coupled problems as below:

- These type of solutions can only consider a limited degree of coupling (e.g. Wang and Dusseault (2003) coupled solution for tangential stress calculation around a wellbore),
- A linear constitutive law is usually implemented (e.g. elasticity),
- Simple loading behavior is used (e.g. uniform pressure changes, single well),
- Simple geometry (e.g. plane strain, plane stress, axisymmetric),
- Homogeneous and isotropic,
- Constant boundary conditions (e.g. constant far field stresses, constant flux or pressure at wellbore face).

Closed form solutions are usually a good benchmark for numerical solutions and can be used for model verification. Based on this, several analytical solutions has been chosen to verify the existing FDM/DDM model. At the beginning of this chapter, four closed form solutions for the elastic, poroelastic and thermoelastic medium are implemented to validate the displacement

discontinuity part of the existing model. It follows then by a simple comparison between poroelastic, thermoelastic and thermoporoelastic model for a single horizontal fracture that one may understand the behavior of the fracture under all these conditions.

5.1 Uniform Pressurization of a Single Fracture in an Elastic Medium

Sneddon (1951) proposed an analytical solution for the opening of a single fracture under a uniform fluid pressure in an elastic medium. In the derivation, he assumed the plane-strain condition which can be implemented to estimate the fracture aperture in a horizontal plane perpendicular to the vertical axis of the fracture. Based on his formulation, the fracture under a uniform pressure will have an elliptical cross-section which is given by the formula,

$$D_{\mathrm{n}}(x) = u_{\mathrm{y}}(x,0^{-}) - u_{\mathrm{y}}(x,0^{+}) = -\frac{2P(1-\nu)}{G}\sqrt{a^2 - x^2} \tag{5-1}$$

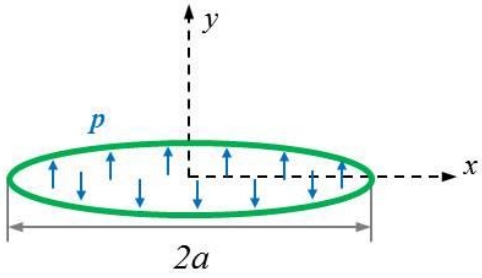

Figure 5.1. Uniformly pressurized fracture

where D_{n} is the normal displacement discontinuity (amount of fracture closure) and P is the uniform fracture pressure.

A constant pressure of 1 MPa is applied to a fracture with a length of 10 meters and the amount of fracture opening along the fracture is plotted in Figure 5.2 in a dimensionless form. In this example, DDM results are shown for three different fracture segment sizes: 0.5 m (20 segments), 0.25 m (40 segments), and 0.125 m (80 segments). As it can be seen, a good match is obtained between numerical and analytical solutions, even though there is an overestimation for all three numerical results close to fracture tips. Also, increasing the number of segments moves the numerical results toward the analytical solution [as shown by Crouch, 1976].

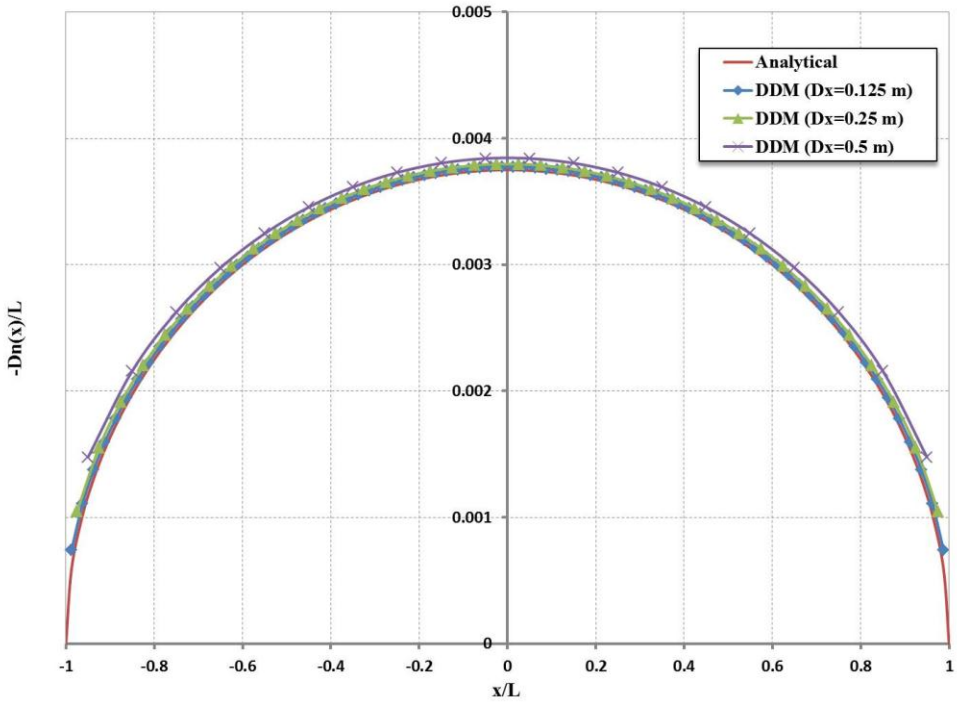

Figure 5.2. Numerical and analytical solutions of the fracture opening under a uniform pressurization in an elastic medium ($\nu = 0.25$, $P/G = 0.0025$).

5.2 Uniform Pressurization of a Single Fracture in a Poroelastic Medium

5.2.1 Load Decomposition Solution

Detournay and Cheng (1991) decomposed the behavior of a uniformly pressurized fracture in a poroelastic medium with fluid leak-off between fracture and surrounding rocks into two boundary conditions, one for the stress loading (mode I) and the other for pressure loading (mode II). The transient behavior of the fracture under these two loading conditions can be summarized as below:

Mode I loading

Mode I corresponds to the stress loading by applying a constant normal stress to the fracture plane. The boundary conditions of the fracture under this loading can be written as

$$\sigma_{\mathrm{n}}(x,t) = -P\mathrm{H}(t) \qquad p(x,t) = 0 \tag{5-2}$$

where σ_{n} and p are the normal stress and pressure on the fracture plane and H(t) is the Heaviside step function. The initial conditions for the both loading type are zero stress and pore pressure everywhere.

At early time, right after applying the normal stress inside the fracture, an undrained elastic behavior becomes dominant. The fracture opening can be estimated using Sneddon's elastic solution with an undrained Poisson's ratio. This undrained behavior reverts to drained behavior over time as the fracture opens and the loading induced pressure gradually disappears. Sneddon's solution with the drained Poisson's ratio describes the amount of fracture opening as the long-term solution.

Short - term: *Long - term*:

$$D_n(x) = -\frac{2P(1-\nu_u)}{G}\sqrt{a^2 - x^2} \qquad D_n(x) = -\frac{2P(1-\nu)}{G}\sqrt{a^2 - x^2} \tag{5-3}$$

Based on Eq. 5-3, the long term aperture is greater than the short-term aperture, which is one of the characteristic of poroelastic materials as they become softer when drained [Detournay and Cheng, 1991].

To verify the DDM model, a 10-meter horizontal fracture (Figure 5.1) is an anisotropic medium without any in-situ stresses is uniformly pressurized with 1 MPa. The amount of fracture opening over the fracture length is depicted in Figure 5.3 in terms of normalized length and normal displacement discontinuities with respect to the fracture half length.

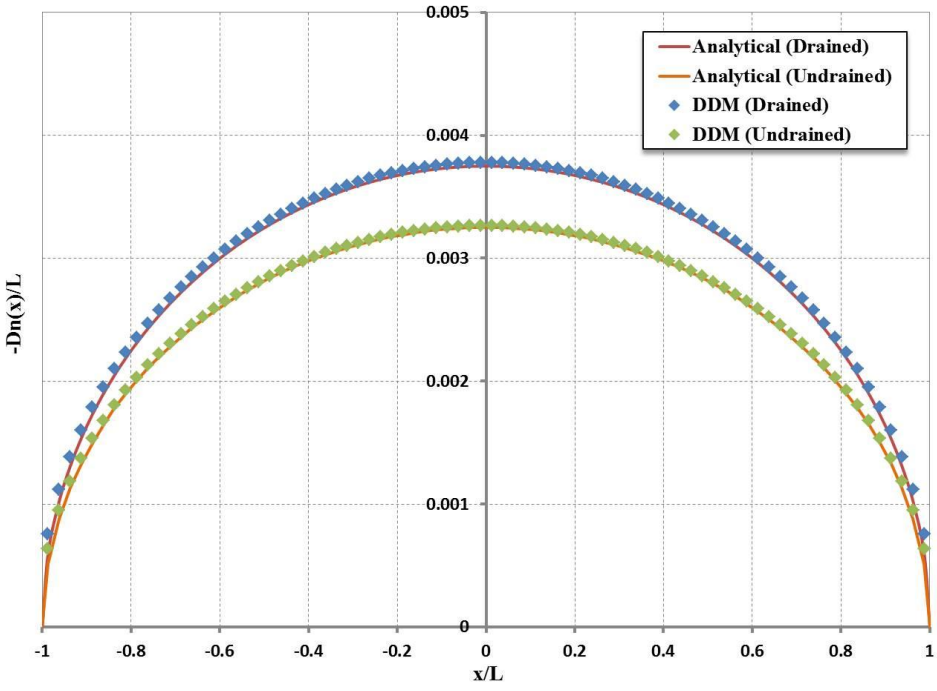

Figure 5.3. Numerical and analytical solutions of the fracture opening for the stress loading mode along the fracture length ($\nu = 0.25$, $\nu_u = 0.35$, $P/G = 0.0025$).

A good correspondence between the analytical solution for drained and undrained conditions and the DDM model is obtained. As was observed also in Figure 5.2, the DDM solution overestimates the amount of fracture opening as one moves toward the fracture tips.

The evolution of fracture aperture over time (for a one year period) at the center of the fracture (x=0), which also corresponds to the maximum opening in Eq. 5-3, is drawn in Figure 5.4. In this figure, a normalized time based on the hydraulic diffusivity is adopted. As the poroelastic medium becomes softer over time, the fracture aperture increases from the undrained asymptotic value at early time to the drained one. The overestimation of the numerical solution in comparison with Sneddon's solution is apparent in this figure; it is less than five per cent.

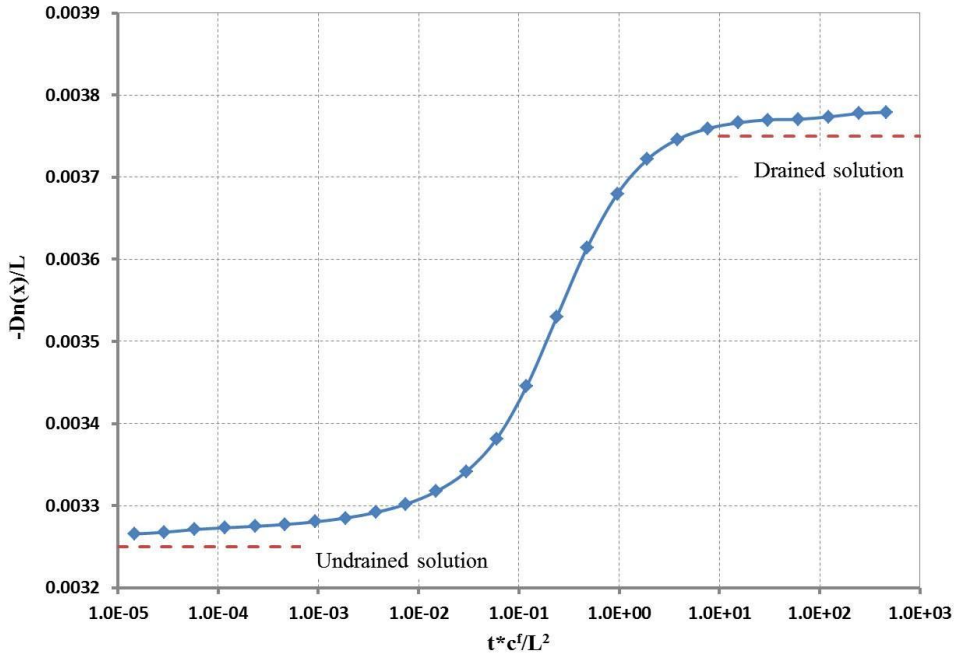

Figure 5.4. Fracture aperture opening over time in the middle of a single fracture under the stress loading mode ($\nu = 0.25$, $\nu_u = 0.35$, $P/G = 0.0025$).

Mode II loading

At early time, exactly after application of pressure in the fracture, the pressure starts to propagate into the surrounding rocks under a one-dimensional flow mechanism perpendicular to the fracture walls. The step pressure does not induce any aperture changes at early time. With time increments, the fracture starts to close as the fracture pressure propagates into the surrounding rocks and results in the poroelastic dilation of the rocks around the fracture.

Short - term: $D_n(x) = 0$

Long - term: $$D_n(x) = \frac{3P(\nu_u - \nu)}{BG(1+\nu_u)}\sqrt{a^2 - x^2} \tag{5.4}$$

The fracture closure profile along the fracture length and fracture closure profile over time in the middle of the fracture under pressure loading is shown in Figure 5.5 and Figure 5.6, respectively.

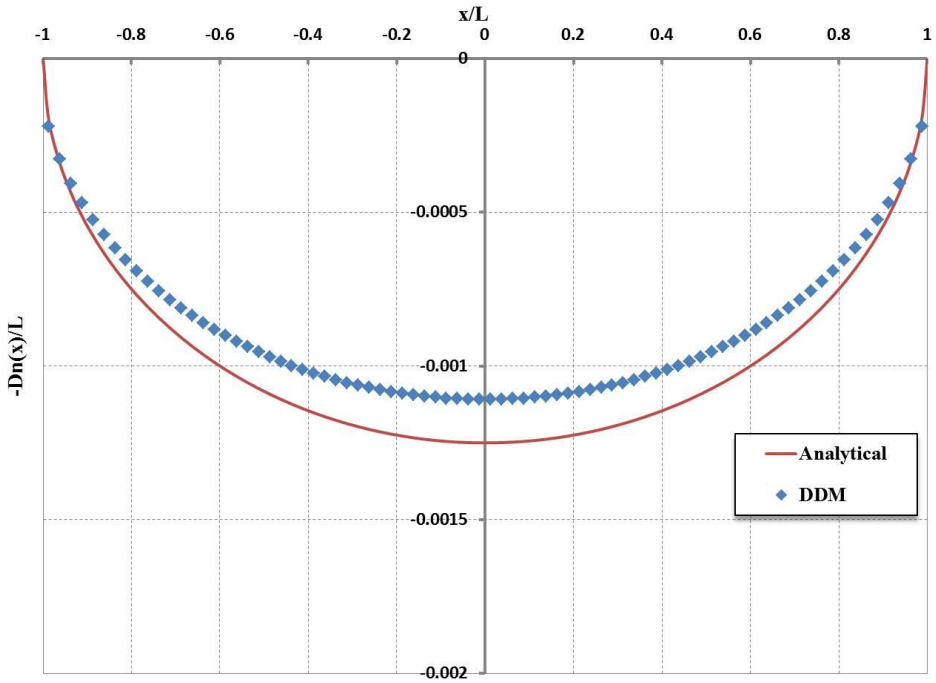

Figure 5.5. Numerical and analytical solutions of the fracture opening for the pressure loading mode along the fracture length ($\nu = 0.25$, $\nu_u = 0.35$, $P/G = 0.0025$).

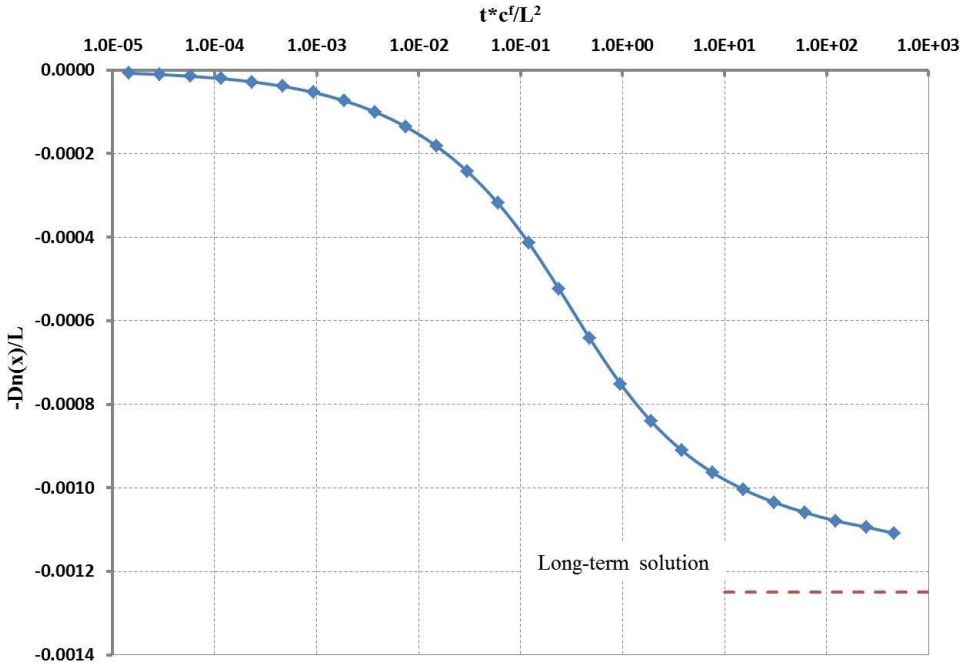

Figure 5.6. Fracture aperture closure over time in the middle of a single fracture under the pressure loading mode (ν=0.25, ν_u=0.35, P/G=0.0025).

There is a noticeable difference between the long-term numerical and analytical solutions for the fracture closure under pressure loading. This difference happens as the elastic coupling between pore pressure and stress is assumed to be negligible for the derivation of the analytical solution of the pressure loading mode [Detournay and Cheng, 1993] and represents the complete drainage of pore pressure in the infinite medium at infinite time. This error has been observed in similar works such as Vandamme *et al.* (1989) and Zhang (2004).

Mode I and II can be combined together to understand the behavior of an elastic fracture in a poroelastic medium (Figure 5.7and Figure 5.8).

Based on Figure 5.7 and Figure 5.8, the fracture aperture increases when a constant pressure is applied in the fracture. At early time, an instantaneous fracture opening occurs as a result of undrained behaviour of the poroelastic medium that is reduced over time until it reaches a

drained behavior with eventual complete equilibration of the pore pressure in the surrounding rocks. The difference between analytical and numerical solution for long term behavior can also be seen here.

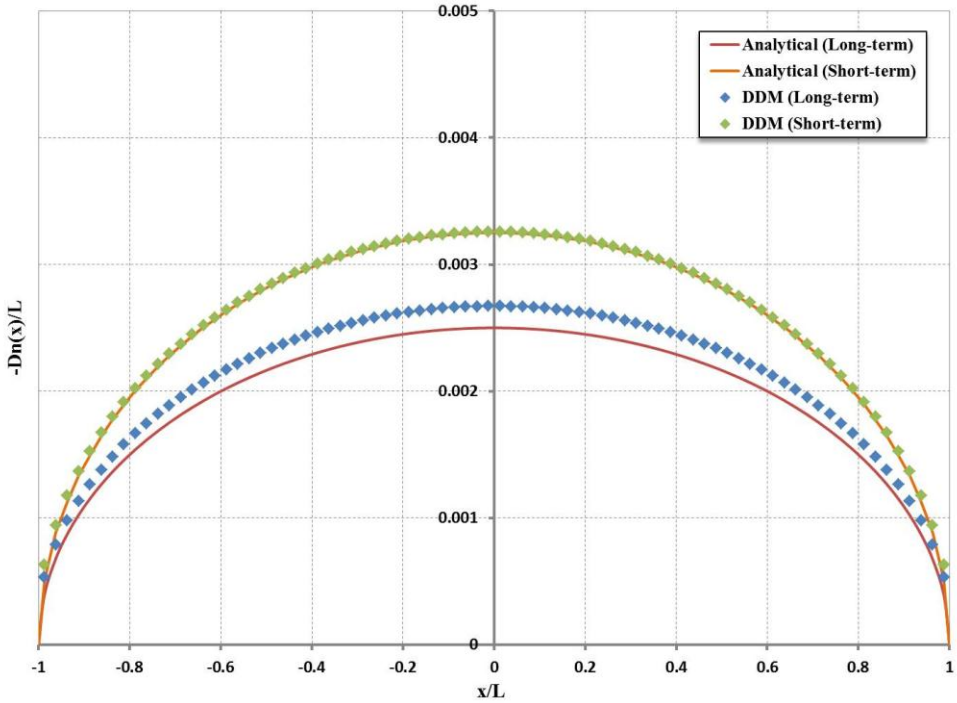

Figure 5.7. Numerical and analytical solutions of the fracture opening for mode I+II loading along the fracture length ($\nu = 0.25$, $\nu_u = 0.35$, $P/G = 0.0025$).

5.2.2 Haimson's Solution

Haimson (1968) modified Sneddon's solution for the fracture aperture estimation in a poroelastic medium by adding the normal induced displacement as a result of fluid leak-off into the surrounding rocks. He used the analogy between thermoelasticity and poroelasticity to derive the leak-off induced displacement from the thermoelastic displacement solution suggested by Olesiak and Sneddon (1959) in an infinite elastic medium as

$$D_n(x) = -\frac{2P}{G}\left[(1-\nu) - \frac{2(1-2\nu)}{9}\alpha\right]\sqrt{a^2 - x^2} \tag{5.5}$$

where the second term in the bracket represents the fracture aperture reduction due to the fluid leak-off into the rock mass adjacent to the fracture. It was assumed that fluid flow into the rock is steady-state, which is equivalent to the long-term solution of Detournay and Cheng's mode I+II. A comparison between the amounts of fracture opening along the fracture length calculated using the Haimson's formulation, Detournay and Cheng's solution (Mode I+II) and the DDM model developed herein is presented in Figure 5.9.

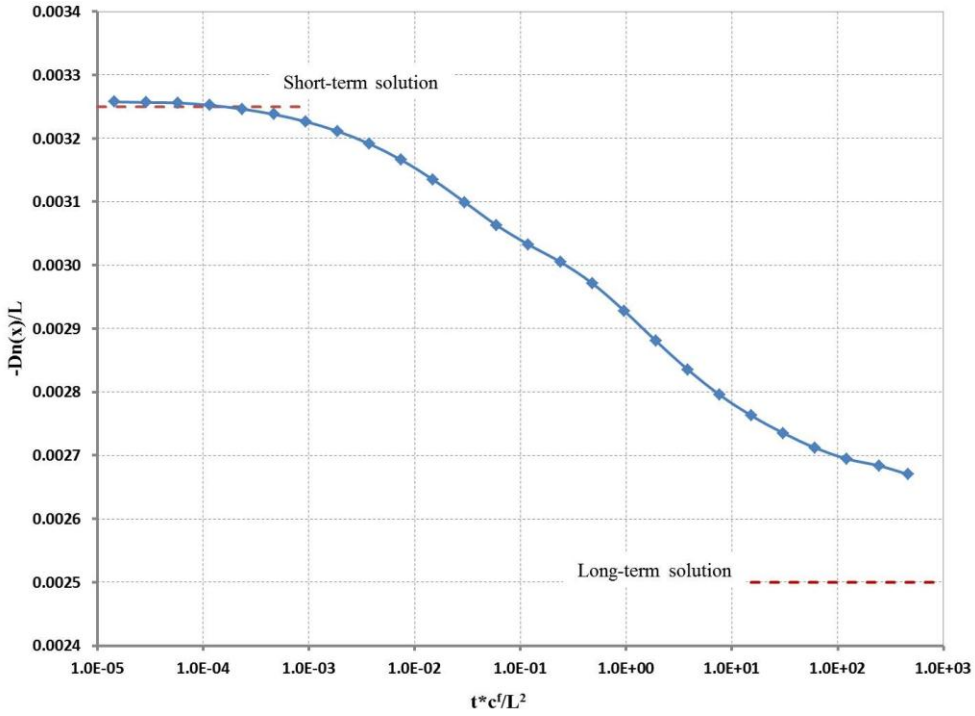

Figure 5.8. Fracture aperture variation over time in the middle of a single fracture under the mode I+II loading ($\nu = 0.25$, $\nu_u = 0.35$, $P/G = 0.0025$).

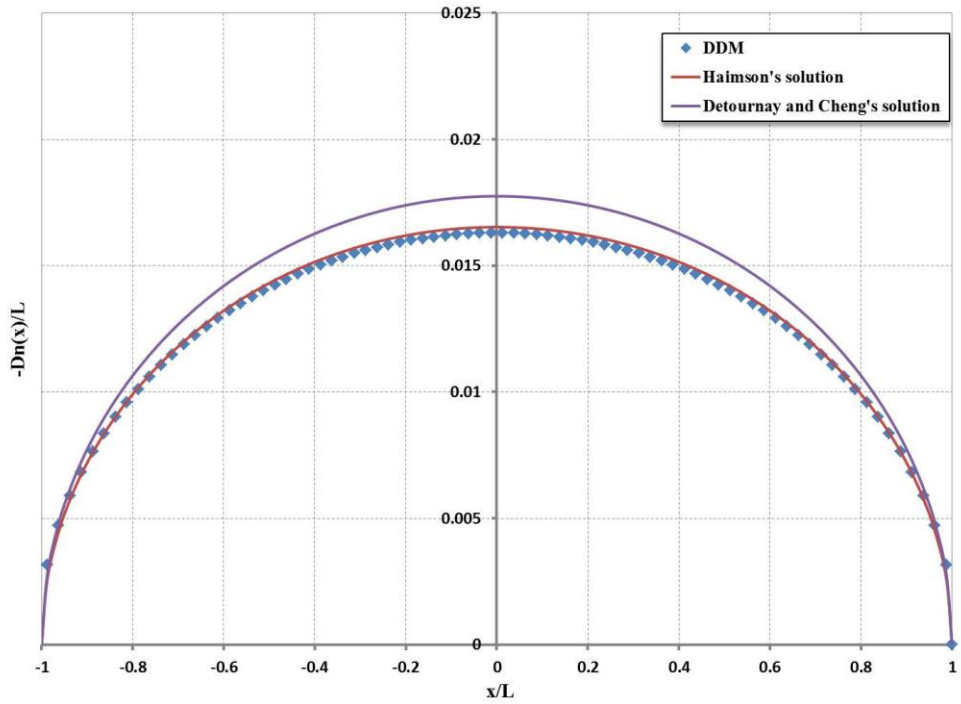

Figure 5.9. Numerical and analytical solutions of the fracture opening using the Haimson and Detournay& Cheng's solution along the fracture length ($\nu = 0.25$, $\nu_u = 0.35$, $P/G = 0.0125$, $\alpha = 0.8$).

As seen in this figure, a good correspondence between Haimson's solution and the DDM results is obtained. The previously mentioned difference between the DDM results and Detournay and Cheng's solution is visible again in Figure 5.9.

5.3 Uniform Cooling of a Single Fracture in a Thermoelastic Medium

In this section, the effect of uniform cooling of a fracture on the fracture opening in a thermoelastic medium is considered (Figure 5.10). For this purpose, it is assumed that the initial temperature of a 400-meter fracture is 80°C colder than the surrounding rocks. Zhang (2004) proposed the following formulation for the long-term maximum fracture opening as a result of a constant ΔT temperature changes:

$$D_{\text{n max}} = -\frac{2\beta_s L(1-\nu)}{3}\Delta T \tag{5.6}$$

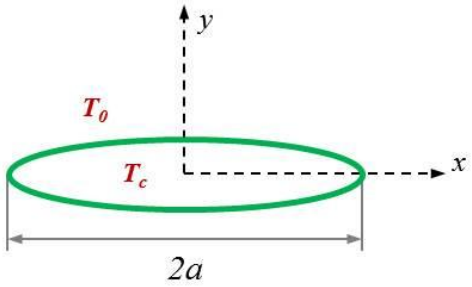

Figure 5.10. Uniform cooling of fracture

Figure 5.11 indicates that the fracture starts to open as soon as the cold temperature is applied, and at late time (one year in this example) it is approaching an asymptotic value which is shown by the red dashed line (Zhang's solution). The difference between the analytical and numerical solution is about 7 percent at this time increment, and the numerical solution is continuing to converge to the asymptotic value. The same result would be obtained using a thermoporoelastic approach as the cooling effect induces a pressure reduction in the surrounding rocks, not the fracture surface [Zhang, 2004].

5.4 Single Fracture Behavior under Different Cases

The FDM/DDM model is implemented in this section to simulate the behavior of a single fracture and the adjacent rock for three different cases:

- A poroelastic case where an isothermal fluid in injected in the middle of a fracture at a constant rate.

- A thermoelastic case in which a constant temperature source is applied in the middle of the fracture.
- A thermo-poroelastic case which is a combination of the poroelastic and thermoelastic cases, i.e. a cold fluid is injected at a constant rate in the middle of the fracture.

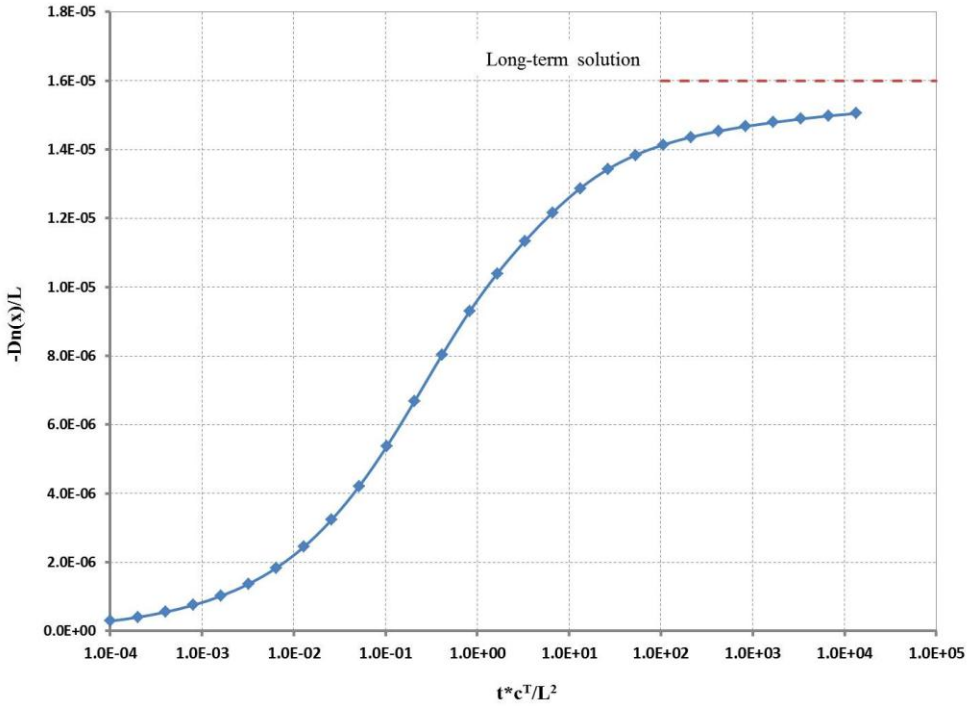

Figure 5.11. Fracture aperture variation over time in the middle of a single fracture under the uniform cooling (ν = 0.25, ΔT = -80°C, β_s = 2.4×10^{-7}1/°C, G =400 MPa).

Thermal, hydraulic and geomechanical parameters are assumed to be identical in all the cases analyzed (Table 5.1), and a comparison between different cases is done in the last section, presenting the effect of pressure, temperature and their combination on the fracture and surrounding rocks. It should be mentioned here that large rock porosity (25%) has been used in the examples in this study, which is more than the typical porosity of the carbonate rocks (5-10%). The only purpose to choose this high value was to present the physical behavior of

fractures that could be representative of massive produced water disposal in highly porous carbonate rocks dominated by fracture flow.

5.4.1 Poroelastic case

In this section, an isothermal viscous fluid is injected in the middle of a 40-meter vertical fracture at a constant rate of 2×10^{-6} m^3/s for 10 hours. In this case, it is reasonable to model the problem with a plane strain assumption in the horizontal plane perpendicular to the injection well axis.

Table 5.1. Thermal, hydraulic and geomechanical properties of the single fracture and adjacent rock for three different cases: poroelastic, thermoelastic and thermo-poroelastic.

Drained Poisson's ratio (ν)	0.25	Undrained Poisson's ratio (ν_u)	0.35
Young's modulus (E)	10 GPa	in-situ horizontal stress (σ_{xx})	30 MPa
in-situ vertical stress (σ_{yy})	20 MPa	in-situ shear stress (σ_{xy})	0
Initial pressure (p_0)	10 MPa	Initial temperature (T_0)	80°C
Initial fracture aperture (w_0)	0.1 mm	Fracture maximum closure (w_{res})	50 μm
Fracture normal stiffness (K_n)	100 GPa/m	Fracture shear stiffness (K_s)	100 GPa/m
Fluid compressibility (c_f)	7×10^{-10} 1/Pa	Fluid dynamic viscosity (μ)	1 cP
Fluid thermal conductivity (k_{Tf})	0.6 J/m°Ks	Fluid density (ρ_f)	1000 kg/m^3
Fluid specific heat (C_f)	4200 J/kg°K	Rock heat diffusivity (c^T)	5×10^{-5} m^2/s
Matrix permeability (k_m)	1 mD	Matrix porosity (ϕ_m)	0.25
Fluid thermal expansion (β_f)	2.4×10^{-5} 1/°K	Rock thermal expansion (β_s)	2.1×10^{-5} 1/°K
Biot's coefficient (α)	0.8	Dilation angle (ψ)	0
Cohesion (σ_c)	0	Friction angle (ϕ)	30
Injection fluid rate (Q_{inj})	2×10^{-6} m^3/s	Injection temperature (T_{inj})	50°C

In-situ stresses are anisotropic, with the minimum horizontal stress (σ_{yy}) equal to 20 MPa and perpendicular to the fracture plane and the maximum horizontal stress (σ_{xx}) equal to 30 MPa along the fracture plane. For simplicity, σ_{xx} and σ_{yy} will be referred to as horizontal and vertical stresses in the two-dimensional plane strain model. Fracture pressure and fracture aperture profiles along the fracture, as well as a pore pressure propagation map after 10 hours fluid

injection, are shown in Figure 5.12. As time increases, the fluid starts to propagate in the fracture faster than the rock as a result of the higher fluid conductivity of the fracture. This transient pressure propagation is converted to a steady state flow in the fracture and an isobaric regime becomes dominant along the fracture as the pressure front reaches the fracture tips rapidly. This behavior explains the fracture pressure profile with a maximum of 11.36 MPa at the injection point (x=0). This pressure increment increases the fracture aperture to a maximum value of 0.178 mm, which is equivalent to 2700 Darcy. The fracture aperture decreases toward the fracture tips.

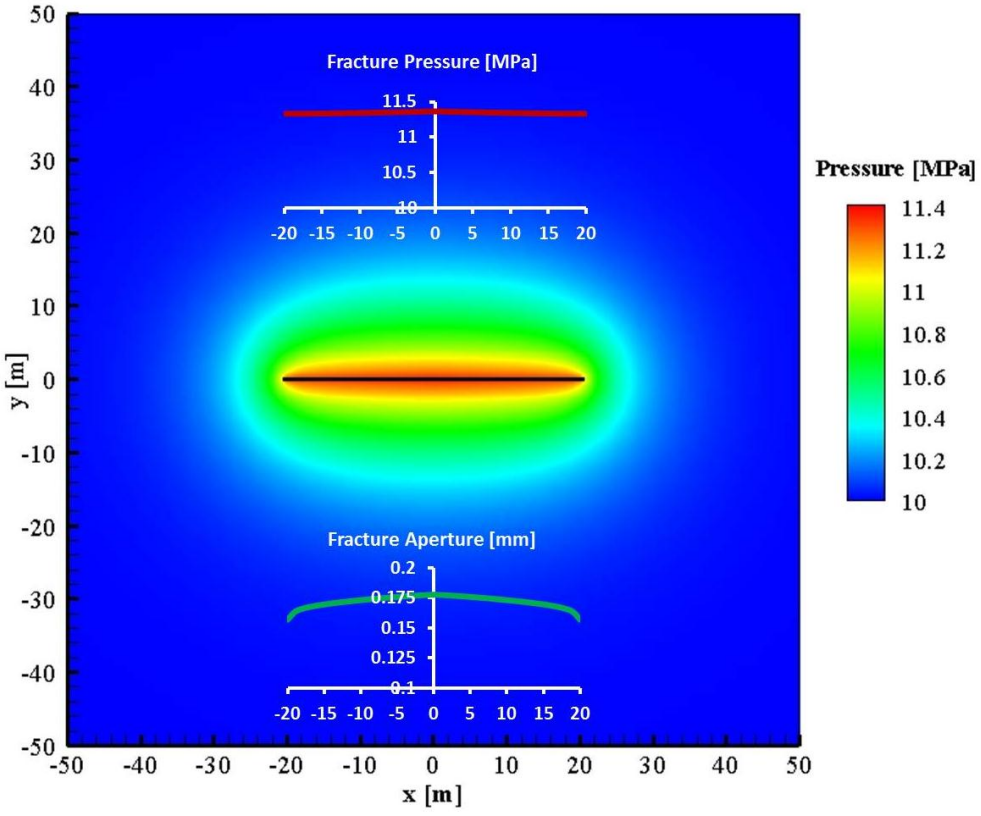

Figure 5.12. Fracture pressure profile (red line), fracture aperture profile (green line), and pore pressure in the surrounding poroelastic medium after 10 hours of fluid injection.

Pore pressure in the permeable rock around the fracture increases and the isobars will have an approximately elliptical shape elongated along the fracture length as a result of the isotropic and homogeneous rock properties.

In-situ effective stresses as well as shear stresses and displacements after 10 hours of fluid injection are depicted in Figure 5.13. As the fracture opens, it pushes the surrounding rock away, which causes a positive displacement above and in the right hand side of the fracture and a negative displacement on the bottom left hand side. Horizontal and vertical displacements are symmetrical with respect to vertical and horizontal straight lines passing through the injection point. The shape of horizontal displacement is almost circular, whereas the vertical displacement spreads along the fracture and the maximum values occur close to the injection point.

Vertical and horizontal effective stresses around the injection point decrease as the pore pressure increases in the surrounding rock, even though the total stresses increase slightly as a result of rock compression. Because of conservation of momentum (conservation of stress for equilibrium), this stress reduction is compensated by an increase of stress moving away from the center of fracture. For the effective horizontal stress (σ'_{xx}), this increment mostly occurs above and under the fracture, whereas for the vertical effective stress (σ'_{yy}), it occurs at the sides of fracture. The rate of stress reduction for vertical effective stress is more than for horizontal effective stress, which is the driving mechanism for propagation along the fracture as soon as the vertical effective stress exceeds the tensile strength of the fracture tips. Most of the shear stresses occur above and under the fracture tips as the difference between horizontal and vertical stresses reaches a maximum in that region.

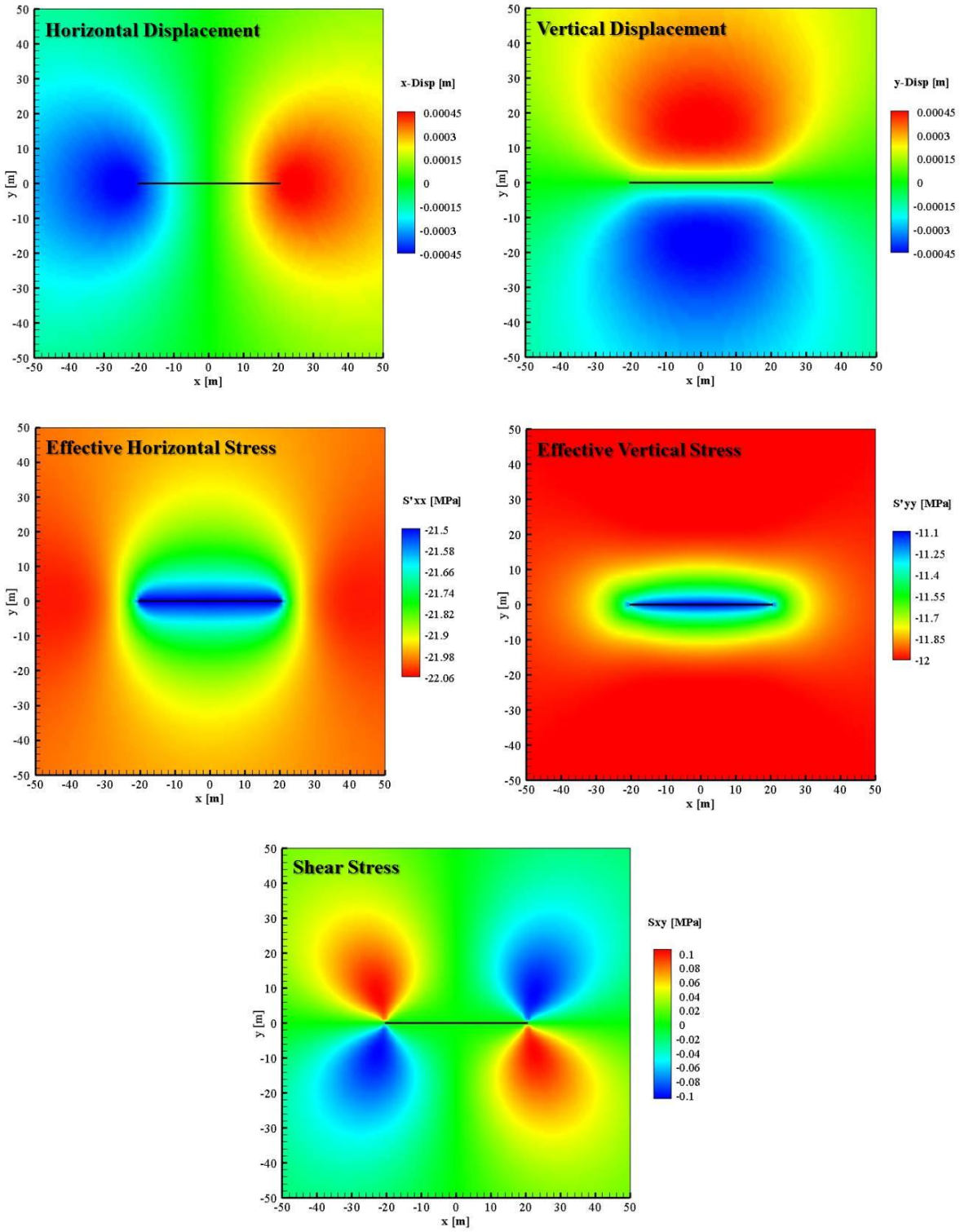

Figure 5.13. Horizontal and vertical displacements and effective stresses as well as shear stress maps around a pressurized fracture in a poroelastic medium.

5.4.2 Thermoelastic case

In this case, a heat source is applied in the middle of the single fracture with a temperature of 30°C which is 50°C colder than the initial temperature of the fracture wall and its surrounding rock. It is assumed that there is no fluid flow in the fracture and no fluid leak-off from the fracture into the rock. Based on this assumption, the only heat transfer mechanism in the medium is heat conduction, which is a slower mechanism in comparison to heat convention. The other model properties are identical with the previous case (Table 5.1).

As expected, the cold front propagates slowly and it only affects the area adjacent to the heat source in 10 hours of cold injection (Figure 5.14). As the result, only the fracture aperture near the injection point is affected, showing an abrupt increase of 0.41 mm (14000 mD). The influenced cold area around the fracture is almost circular as a constant value for heat diffusion in all directions was assumed for this problem. The radius of the influenced area is almost one meter with a minimum temperature of 45°C. The cold temperature will propagate over time symmetrically in both the fracture and the rock over time and the existence of the fracture will not affect the heat propagation speed in the rock.

Figure 5.15 depicts the induced displacements and stresses as a result of cooling the injection point in the middle of the single fracture. Cooling is usually associated with rock shrinkage and stress reduction in the influenced medium. These effects can be seen in horizontal and vertical displacements. As we expect, the rock starts to shrink toward the injection point and shows a symmetric but reverse displacement with the smaller influenced zone in comparison with the poroelastic case. The displacement contours are almost circular without any influence from the fracture pattern as a result of the isotropy and homogeneity of the thermoelastic medium.

The horizontal and vertical effective stresses are reduced in the cold area from their initial values of 22 MPa and 12 MPa, respectively (the green area in the effective stress maps in Figure 5.15). The stress compensation occurs at the top and bottom of the cold region for the horizontal effective stress and at the sides for the vertical effective stress. The shear stresses also develop mainly at the sides of injection area as the temperature changes has not reached to the fracture tips. It should be noticed here that the sign of shear stresses is different than the poroelastic case. Here the rock shrinks in the cold region whereas in the poroelastic case the rock compresses as a result of fracture opening and pore pressure increases in the region adjacent to the fracture.

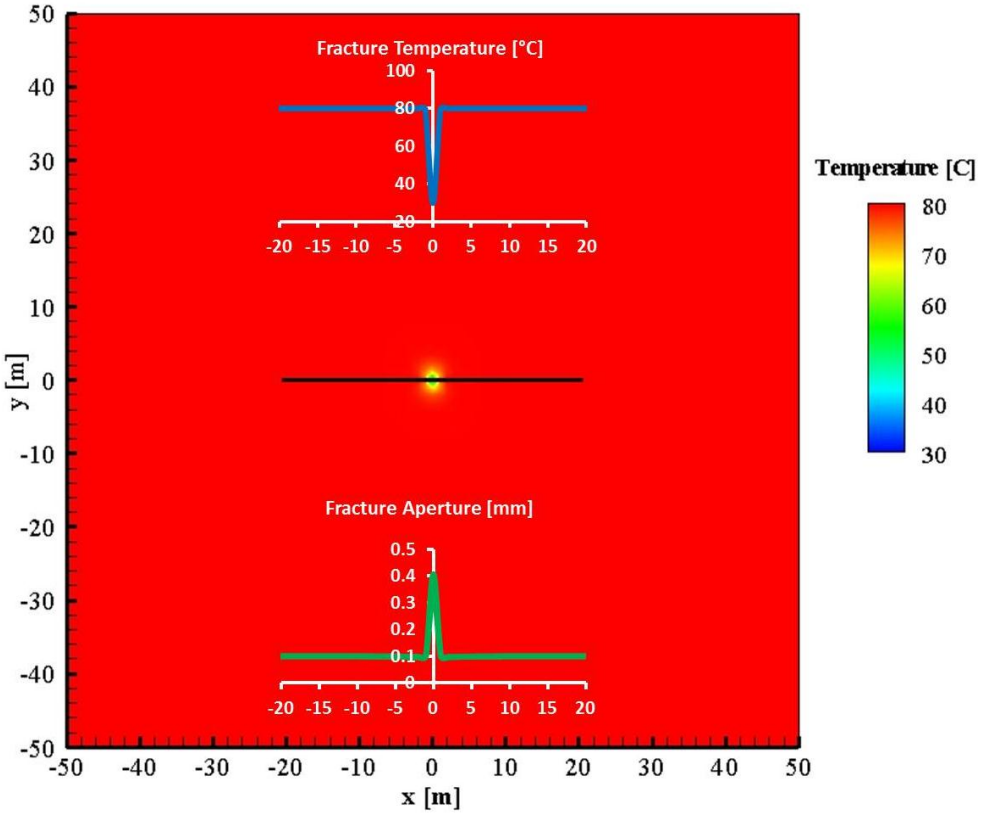

Figure 5.14. Fracture temperature profile (blue line), fracture aperture profile (green line), and temperature map in the surrounding thermoelastic rock after 10 hours of cold fluid injection.

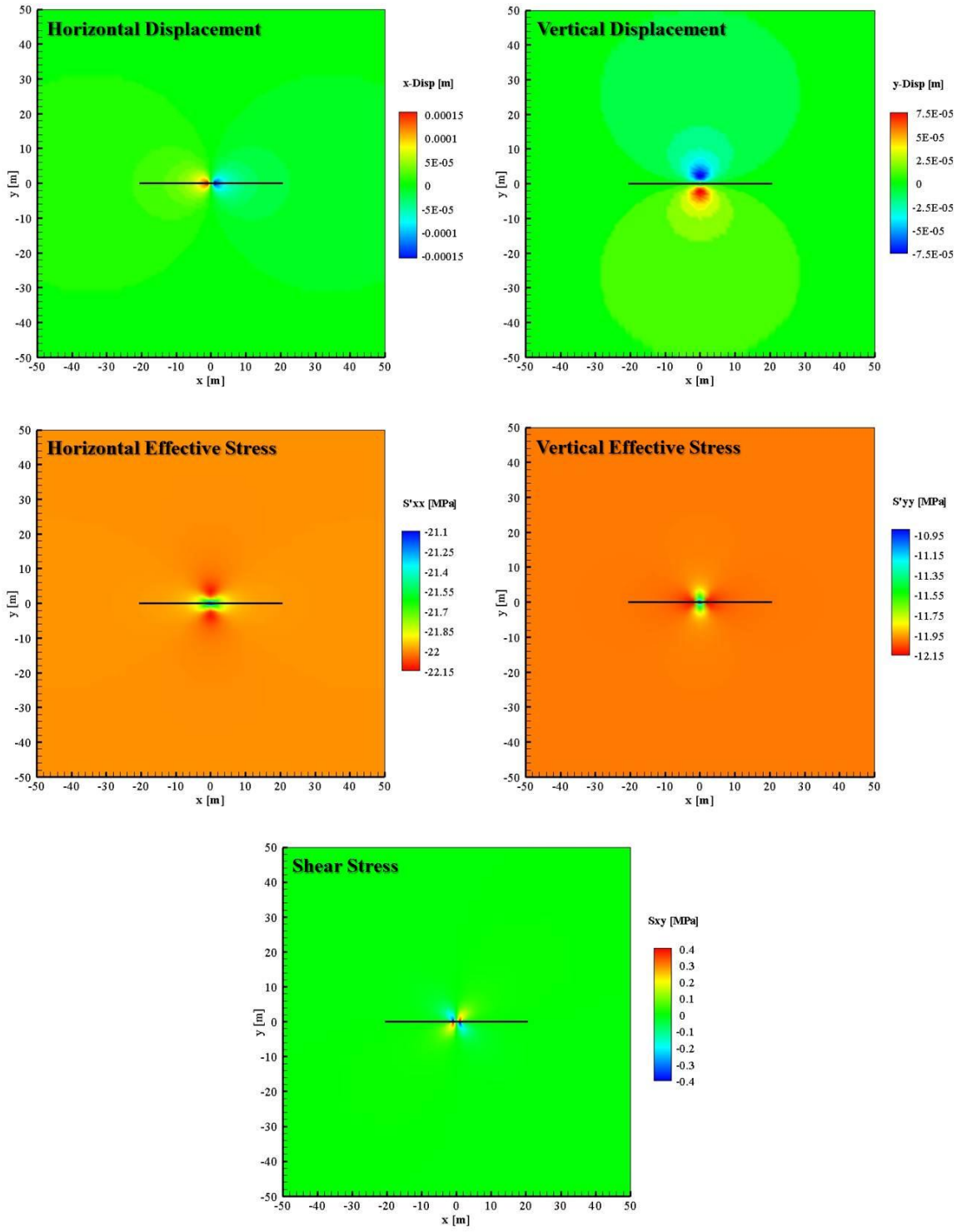

Figure 5.15. Horizontal and vertical displacements and effective stresses as well as shear stress maps around a fracture with a heat source (colder than the surrounding rock) in a thermoelastic medium.

5.4.3 Thermo-poroelastic case

In this part a combination of both poroelastic and thermoelastic cases is considered to study the behavior of fracture and rock under cold fluid injection in the middle of fracture at a constant rate. As there is fluid flow in the fracture, convection is also assists conduction to transfer heat in the fracture. Heat conduction is still the only thermal propagation driving force in the rock. The thermal, hydraulic and mechanical properties of the model were shown in Table 5.1.

Based on Figure 5.16, pressure increases in the fracture and its surrounding rocks in amanner similar to the poroelastic problem. The maximum pressure in the fracture is 11.26 MPa which is 0.1 MPa less than the pressure at the injection point in the poroelastic model. This difference occurs as a result of cooling the fracture and increasing the fracture aperture with a magnitude of 0.317 mm (8500 Darcy) in comaprison with the fracture aperture at injection point in the poroelastic case which was 0.178 mm (2700 Darcy).

As heat convection assists the heat conduction process, temperature propagates much faster in the fracture in comparison with the thermoelastic problem. As can be seen in Figure 5.16, the fracture temperature reduces to the injection temperature for a distance of 6.5 meters away from injection point. This temperature reduction increases the fracture aperture more than the poroelastic case whereas it is possible to recognize the cold part of fracture from the aperture profile where shows more fracture opening from the temperature effect than the pressure effect. As the convective heat propagates faster in the thermoporoelastic case than the thermoelastic one, more rock around the fracture cools down as this cold region spreads along the fracture, giving a different shape than the thermoelastic problem.

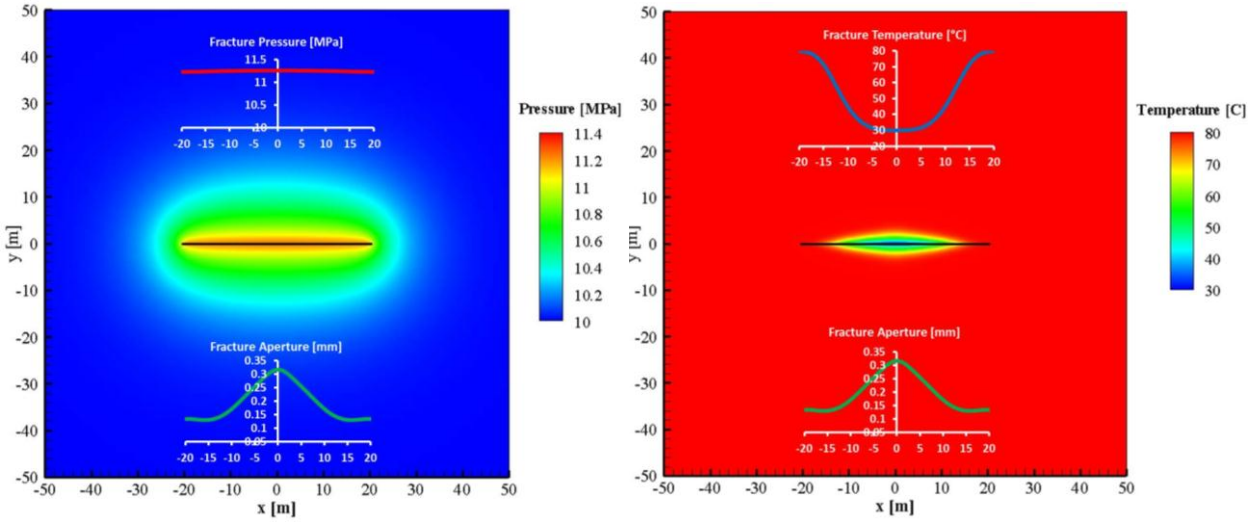

Figure 5.16. Fracture pressure profile (red line), fracture temperature profile (blue line), fracture aperture profile (green line), pore pressure map (left) and temperature map (right) in the surrounding rock after 10 hours of cold fluid injection in a thermo-poroelastic medium.

Horizontal and vertical displacements are responding as a combination of both cases, i.e. the rocks close to the cold region are shrinking (thermal effect) whereas the rocks far away from the cold area are pushing away from the fracture (hydraulic effect). The magnitude of thermally induced displacements is more than the hydraulic one and over time as the heat front moves from the injection point toward the fracture tips, the thermal displacements move toward the hydraulic displacements. This is in agreement with the fact that a pressure front usually moves faster than a heat front, so the induced effect of each process is also time dependent, i.e. the hydraulic effect can be considered as the early time effect, whereas the thermal effect usually becomes dominant at a later time. As the direction of thermal and hydraulic displacements are opposite to each other in this problem, a zero displacement contour can be recognized in each time step between the thermal and hydraulic induced displacements. This contour expands over time and its shape is controlled mostly by the isothermal contours.

Horizontal and vertical effective stresses reduction in Figure 5.17 mostly occurs as a result of cold fluid injection. It was mentioned for the poroelastic case that the rate of stress reduction for vertical effective stress is more than horizontal effective stress, which is the driving mechanism for fracture propagation along the fracture as soon as the vertical effective stress reaches the tensile strength of the fracture tips. This is not the scenario for the thermoporoelastic case, as the thermal effects mask the hydraulic effect (mostly for horizontal effective stress) and as can be noted in Figure 5.17, the reduction rate of horizontal effective stress is more than for the vertical effective stress. This could lead to generation of secondary fractures perpendicular to the main fracture, increasing the surface area for heat exchange, which will affect the heat exchange and hydraulic response behavior prediction of the fractured medium.

The effect mentioned above is visible in Figure 5.18, which shows the horizontal and vertical stress map. The maximum reduction rate for horizontal and vertical stresses is 3.56 MPa and 0.34 MPa, respectively.

Returning to Figure 5.17, shear stresses occur at the cold fluid front in the rock and their direction shows that the thermal effect is the dominant mechanism. It is worthwhile to mention that even the shape of induced shear stress by pressure and temperature propagation is different. Poroelastic induced shear stresses are more spread out than for the thermoelastic case.

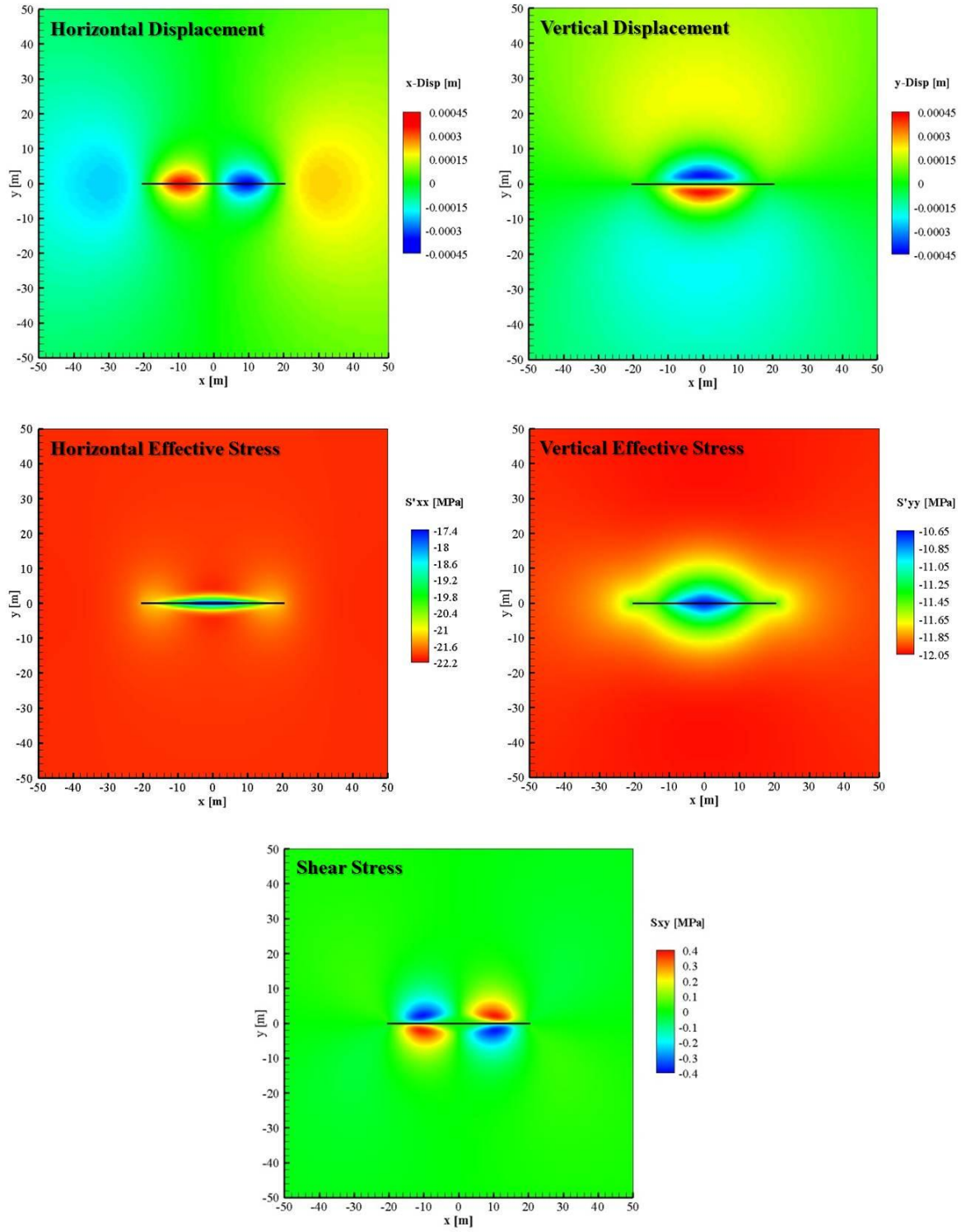

Figure 5.17. Horizontal and vertical displacements and effective stresses as well as shear stress maps around a cold pressurized fracture in a thermo-poroelastic medium.

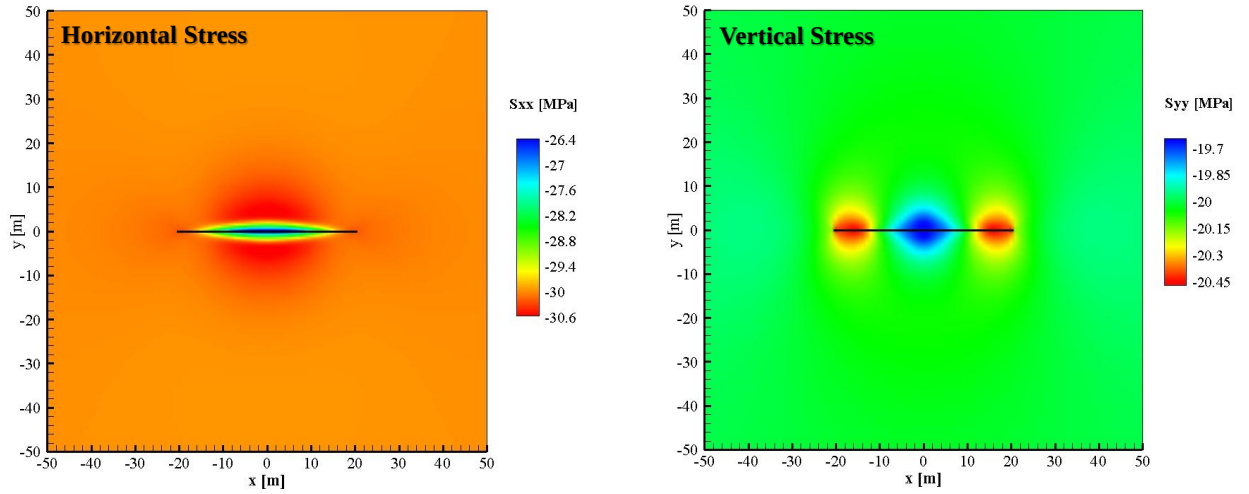

Figure 5.18. Horizontal and vertical stresses as well around a cold pressurized fracture in a thermo-poroelastic medium.

5.4.4 Comparison of poroelastic, thermoelastic and thermo-poroelastic models

Three different cases were studied in the previous sections and the pressure, temperature, displacements, and effective stress maps were shown. It was also noted that the thermoporoelastic case is a combination of both poroelastic and thermoelastic cases but considering also the effect of thermal convection in the formulation, which is not considered in the thermoelastic problems. In this section, a comparison of these three cases is attempted using different profiles for the parameters of interest. For this purpose, a 200-meter horizontal profile two meters above the fracture is considered because the horizontal profile can show more parameters changes above a horizontal fracture in a plane strain cross-section.

The pressure profile does not contain the thermoelastic case as it was assumed that no fluid flow took place into the rock matrix in that model. Also, the poroelastic profile does not exist in the temperature representation as it was assumed to be isothermal (Figure 5.19).

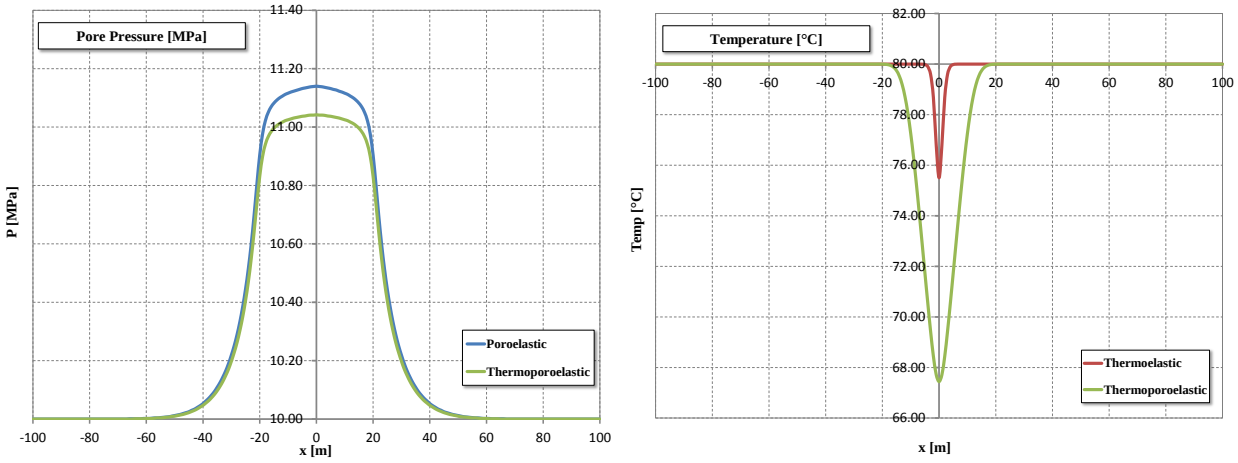

Figure 5.19. Pore pressure and temperature profiles along a 200-meter horizontal line located 2 meters above the fracture for 3 different cases, i.e. poroelastic (blue line), thermoelastic (red line), and thermoporoelastic (green line).

As mentioned for the thermoporoelastic case, the amount of pressure increase is less than for the poroelastic case, and this is visible in Figure 5.19. The maximum difference occurs above the injection point, about 0.1 MPa.

The thermoporoelastic case also shows more heat propagation than the thermoelastic one, even though heat conduction is the only heat transfer mechanism in the rock. This difference in heat propagation (about 8°C for the point above the injection point in the profile) occurs as the fracture cools down faster in the presence of heat convection and the superposition of all heat source strengths affects the surrounding rock more than the case without any convective terms.

In the case of displacements, hydraulic fracture opening moves the rock away from the fracture which is shown by positive values for u_x for the positive x and negative values for u_x for the negative x (Figure 5.20). This behavior is opposite for the thermal fracture opening as a result of rock contraction in the heat influenced region. The poroelastic profile for u_x shows a combination of both processes with amplification of the thermal effect as a result of heat

convection. The same behavior with a different pattern can be seen for the vertical displacement (u_y), i.e. a positive value for the pressure effect and a negative value for the temperature effect.

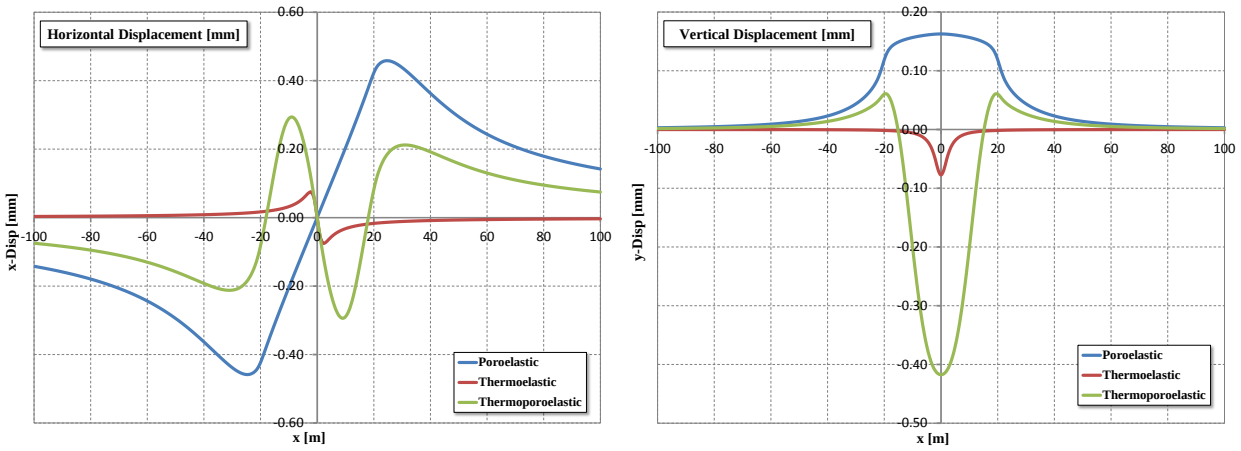

Figure 5.20. Displacement profiles along a 200-meter horizontal line located 2 meters above the fracture for 3 different cases, i.e. poroelastic (blue line), thermoelastic (red line), and thermoporoelastic (green line).

Figure 5.21 presents the vertical and horizontal effective stresses as well as shear stress profiles for the three different cases. Effective stress decreases when the pressure increases, which is the case for the poroelastic profiles, even though total horizontal and vertical stresses increase slightly as a result of fracture opening and compression of the surrounding rocks. For the thermoelastic case, in the absence of pore pressure, vertical effective stress decreases as the rock shrinks more vertically (*y*-direction referred to Figure 5.20), which is associated with a small increase in the horizontal effective stress. Vertical effective stress shows the combination of both other cases where the mechanism's transient zone is apparent with a change in the slope of the effective vertical stress (green line at fracture tips in the vertical effective stress profile).

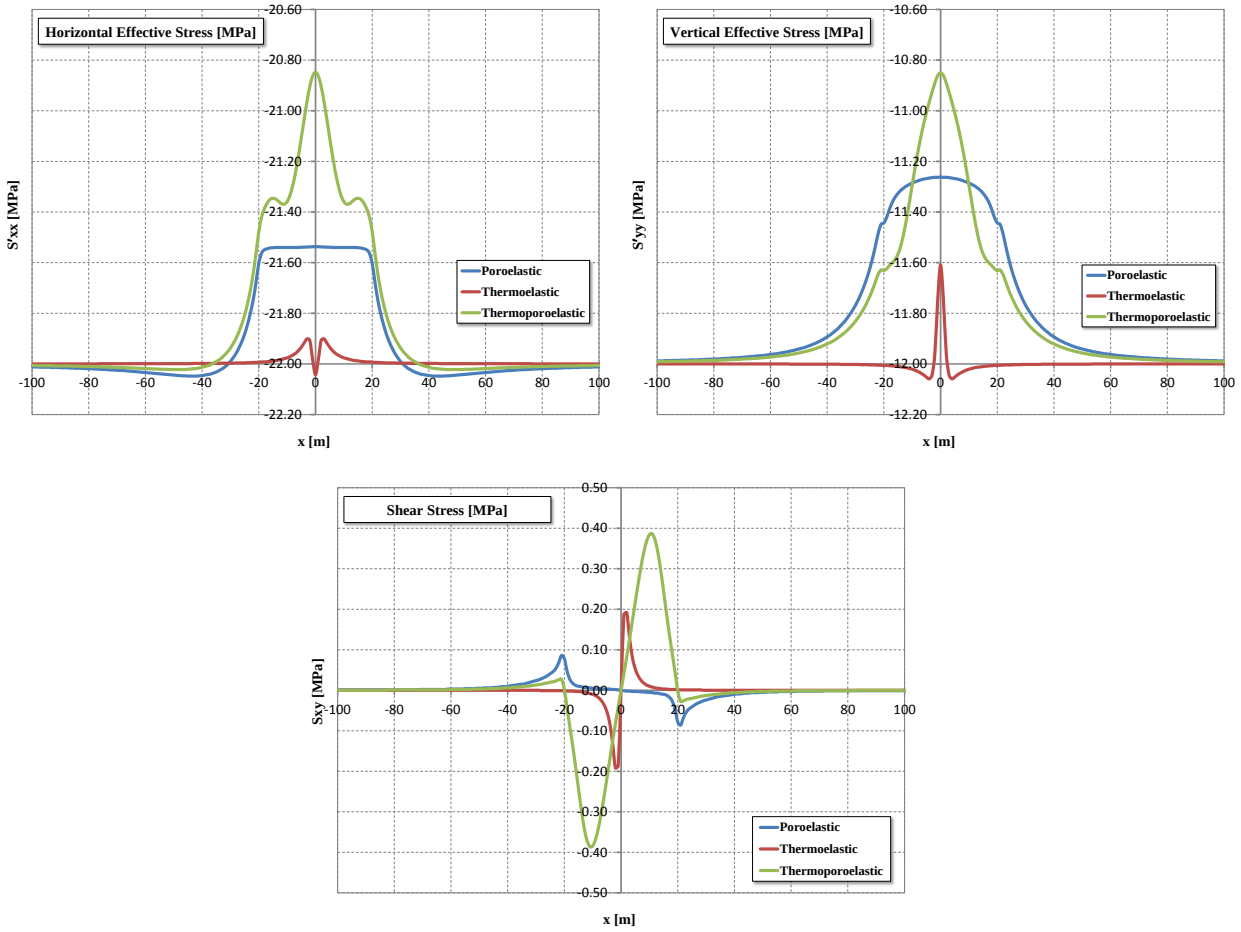

Figure 5.21. Stress profiles along a 200-meter horizontal line located 2 meters above the fracture for 3 different cases, i.e. poroelastic (blue line), thermoelastic (red line), and thermoporoelastic (green line).

The behavior of horizontal effective stresses for the thermoporoelastic case is a bit different. It expects that above the injection point the effective stress increases (similar to the thermoelastic problem), but due to the fact that the profile is so close to the fracture, the two positive peaks are added together and this shape is constructed. To check this explanation, the horizontal effective stress along five different profiles with various elevations are estimated and compared together in Figure 5.22.

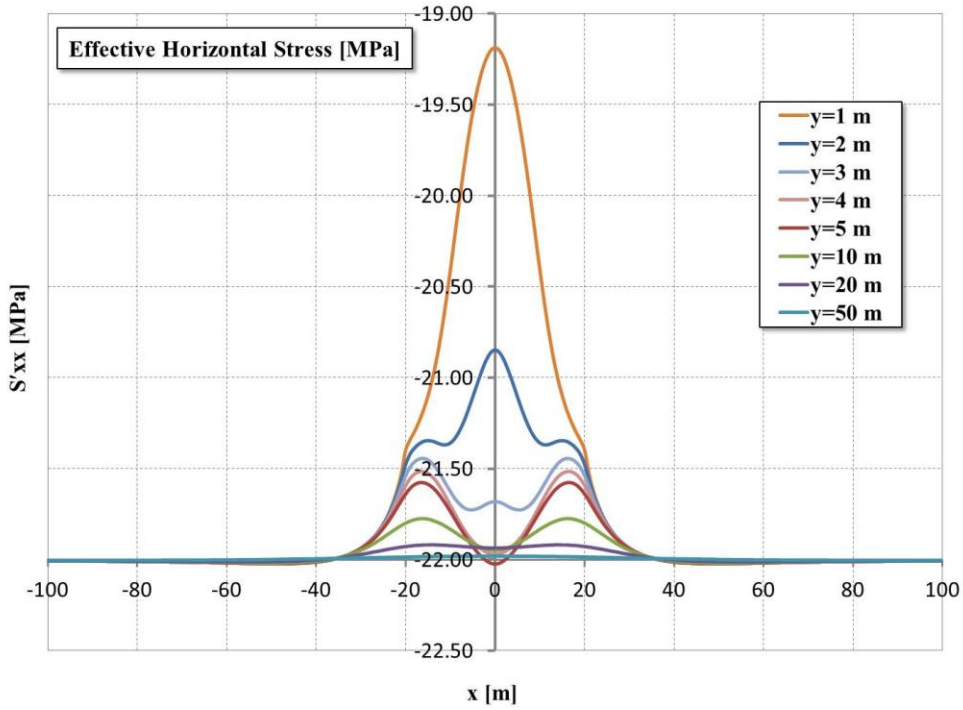

Figure 5.22. Effective horizontal stress profiles along a 200-meter horizontal profile with different elevations above a single fracture in a thermoporoelastic medium.

Shear stress profiles with different cases show different behaviors as well, i.e. poroelastic shear stresses occur at the fracture tips whereas when temperature differences are introduced into the model, higher shear stress with different directions at the heat front are induced with respect to the poroelastic case.

5.5 Chapter Summary

In this chapter, the hybrid FDM-DDM model was verified with some existing analytical solutions such as Sneddon's solution and Detournay and Cheng's solution. It was shown that there is a good correspondence between numerical and analytical solutions. Also the behavior of a single fracture in anisotropic in-situ stress conditions for different scenarios, i.e. poroelastic, thermoelastic and thermo-poroelastic, was studied and the pore pressure, temperature,

deformation and stresses were compared. As a result of cold fluid injection, fracture aperture increases as a consequence of two mechanisms: pore pressure increment reduces the effective stress acting at fracture planes that is associated with an increment in fracture normal displacement discontinuity and rock shrinkage as a result of cooling the rock. Based on the results, the pore pressure effect is dominant at early time after injection initiation, whereas the temperature effect becomes dominant at later time as the temperature propagation is slower than pressure propagation in the rock.

Chapter 6
Model Application

The FDM-DDM hybrid model is implemented in this chapter to study the behavior of a thermo-poroelastic medium under injection/production processes with different fracture network configurations. At the end of this chapter, a sensitivity analysis is done to describe the response of the medium to the variation of some thermal, hydraulic and geomechanical properties of the fracture and rock.

6.1 Isothermal Fluid Injection into an Orthogonal Fracture Network

The FDM/DDM model is used in this section to model the behavior of an orthogonal fracture network under the isothermal injection of a compressible fluid for two different cases: isotropic in-situ stress and anisotropic in-situ stress. This comparison is done to show that fluid tends to flow perpendicular to the minimum in-situ stress as it is easier to open the fracture in this direction. For this purpose, 11 fractures in the *x*-direction and 10 fractures in the *y*-direction are assumed with an identical fracture spacing of 20 meters (Figure 6.1). For the isotropic case, both horizontal and vertical stresses are identical to 30 MPa, whereas for the anisotropic case, the horizontal stress and vertical stress are 50 MPa and 30 MPa, respectively. The hydraulic and geomechanical properties of these models can be found in Table 6.1. All the properties are identical for both models, except the fracture normal stiffness in the anisotropic model which is 60 GPa/m for the fractures in the x-direction and 100 GPa/m for the y-direction fractures as a result of the anisotropy of the in-situ stresses. This assumption is in agreement with the definition of fracture normal stiffness [Goodman, 1974]. An isothermal fluid with a constant

compressibility ($c_f = 7\times10^{-4}$ MPa^{-1}) and dynamic viscosity (μ = 1 cP) is injected at a constant rate ($q_{inj} = 10^{-4}$ m^3/sec) for 30 hours.

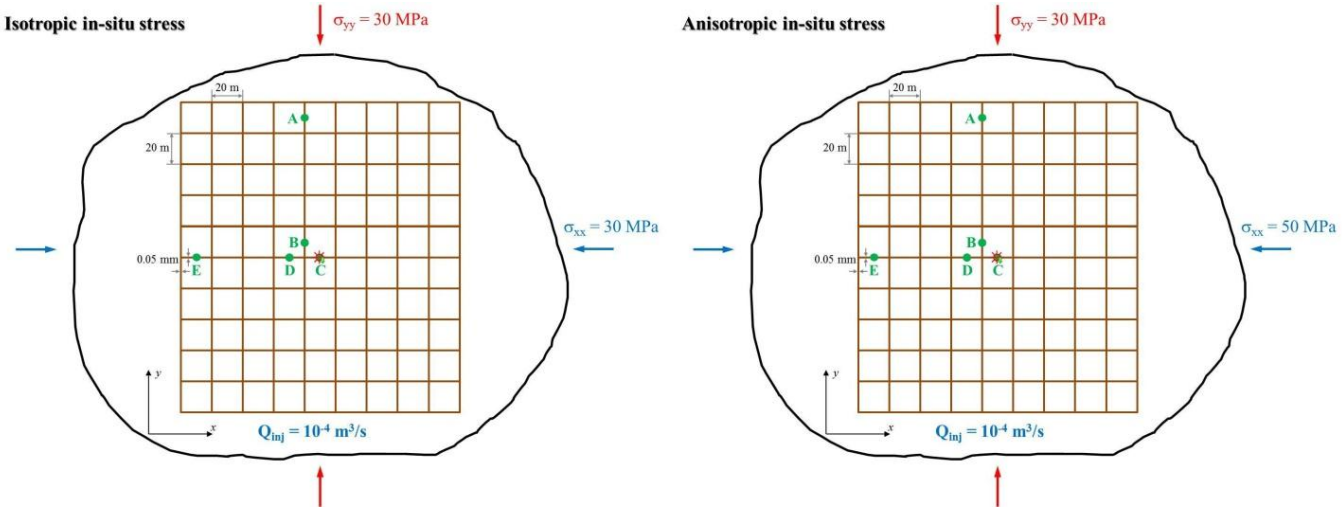

Figure 6.1. 180 by 200 m^2 fracture network with an injection source in the middle of fracture network under the isotropic (left) and anisotropic (right) in-situ stress conditions

Table 6.1. Geomechanical and hydraulic properties of the orthogonal fracture network and surrounding rock

Drained Poisson's ratio (ν)	0.25	Undrained Poisson's ratio (ν_u)	0.35
Young's modulus (E)	20 GPa	Initial pressure (p_0)	15 MPa
Initial fracture aperture (w_0)	50 μm	Fracture maximum closure ($D_{n\,max}$)	25 μm
Fracture normal stiffness (K_{n0})*	60, 100 GPa/m	Fracture shear stiffness (K_{s0})	50 GPa/m
Fluid compressibility (c_f)	7×10^{-10} 1/Pa	Fluid dynamic viscosity (μ)	1 cP
Biot's coefficient (α)	0.8	Fluid density (ρ_f)	1000 kg/m^3
Matrix permeability (k_m)	0.1 mD	Matrix porosity (ϕ_m)	0.25
Friction angle (ϕ)	30°	Cohesion (σ_c)	0
Injection fluid rate (Q_{inj})	10^{-4} m^3/s	Dilation angle (ψ)	0

*Different initial fracture normal stiffness is assumed for horizontal and vertical fractures.

First the isotropic stress model is considered in this section, followed by the anisotropic one. Figure 6.2 depicts the fluid and fracture aperture variation in the fracture network after 30 hours of fluid injection into the middle of the model (point C in Figure 6.1). The width of fracture elements is chosen based on the fracture aperture after 30 hours of injection. As expected,

pressure propagates symmetrically around the injection point with a maximum value of 16.16 MPa that increases the fracture aperture at the injection point to 0.128 mm (1400 Darcy). These numbers indicate the high sensitivity of fracture aperture on pressure in the fractures, as only 1.16 MPa increase in pressure is associated with seven times increment in fracture conductivity from the initial condition (w_0=0.05 m, k_{f0}=200 Darcy).

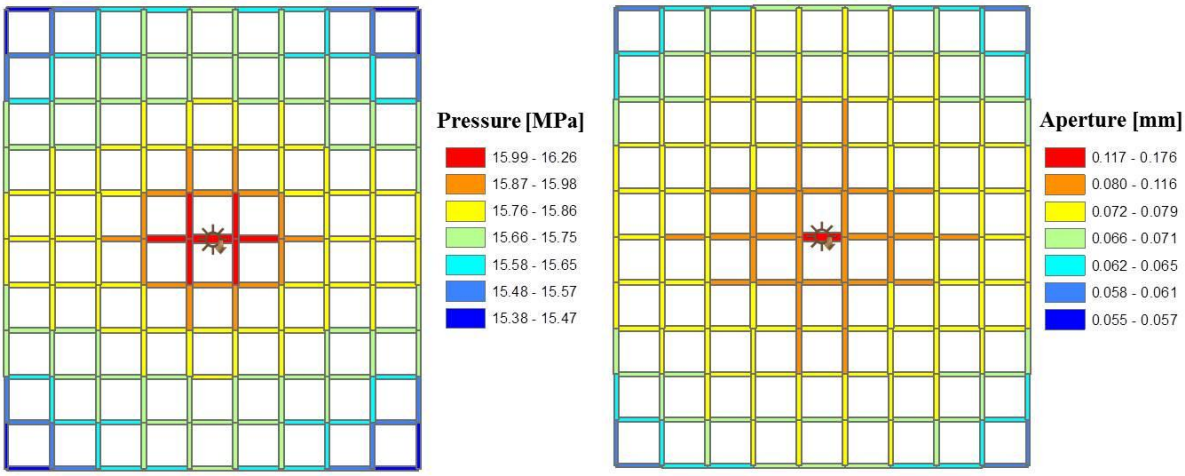

Figure 6.2. Fracture fluid pressure (left) and fracture aperture (right) variation after 30 hours of fluid injection under isotropic in-situ stress condition

As a result of fluid injection into the fractures, the pore pressure in the rock also increases, following the pattern of fracture network. The amount of pressure increment in the rock is much less than the fracture network as a result of the large conductivity difference between them. This behavior is shown in Figure 6.3 that depicts the pore pressure map after 12 and 30 hours of the initiation of fluid injection into the medium.

The symmetry of pressure propagation in the rock is visible in this figure. It is also found that the pressure has not affected all the rock blocks between the fracture sets after 12 hours. After

30 hours all the blocks are affected by the injection well, expect the middle of the blocks at the corners of the fracture network which does not show any pressure increment.

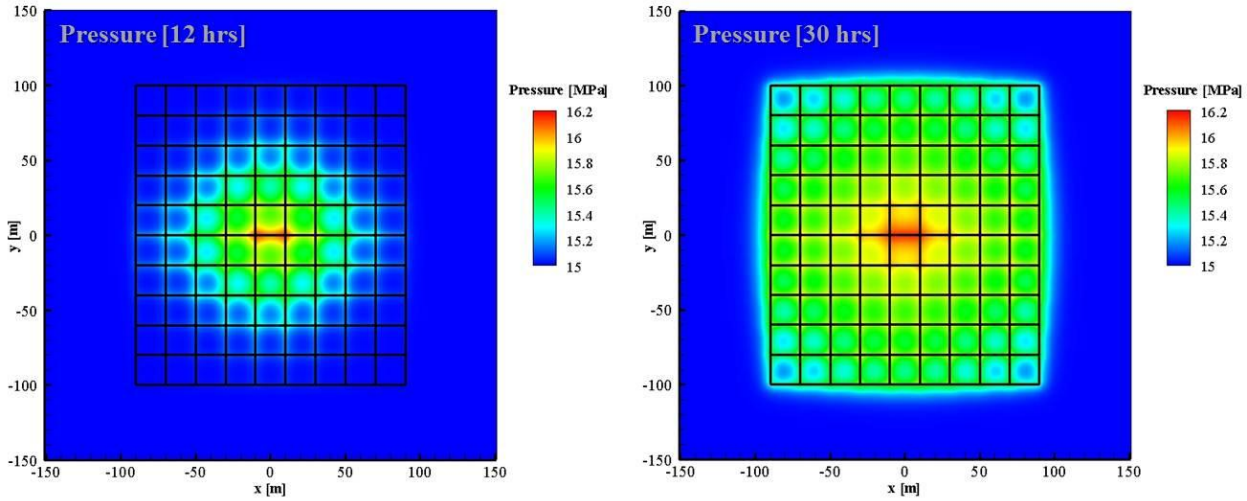

Figure 6.3. Pore pressure variation after 12 (left) and 30 (right) hours of fluid injection under isotropic in-situ stress condition

Fluid injection also disturbs the rock stresses around the fractures, especially effective stresses. Horizontal and vertical effective stresses and shear stress in the rock are shown in Figure 6.4. Both horizontal and vertical effective stresses decrease in the medium as the pore pressure increases, even though there is a slight increment in the rock stresses as a result of fracture opening and rock hardening. The affected area of horizontal effective stress is more than the vertical one in the middle of the fracture network; the same behaviour was seen in the case of the single fracture problem in a poroelastic medium (Figure 5.13). Shear stresses are mostly developing at the corner of the fracture network as a result of pore pressure increases and the forces pushing the rock outward. In this case, the upper left corner is displaced counter-clockwise (positive shear stress) whereas the right upper corner is rotated clockwise (negative).

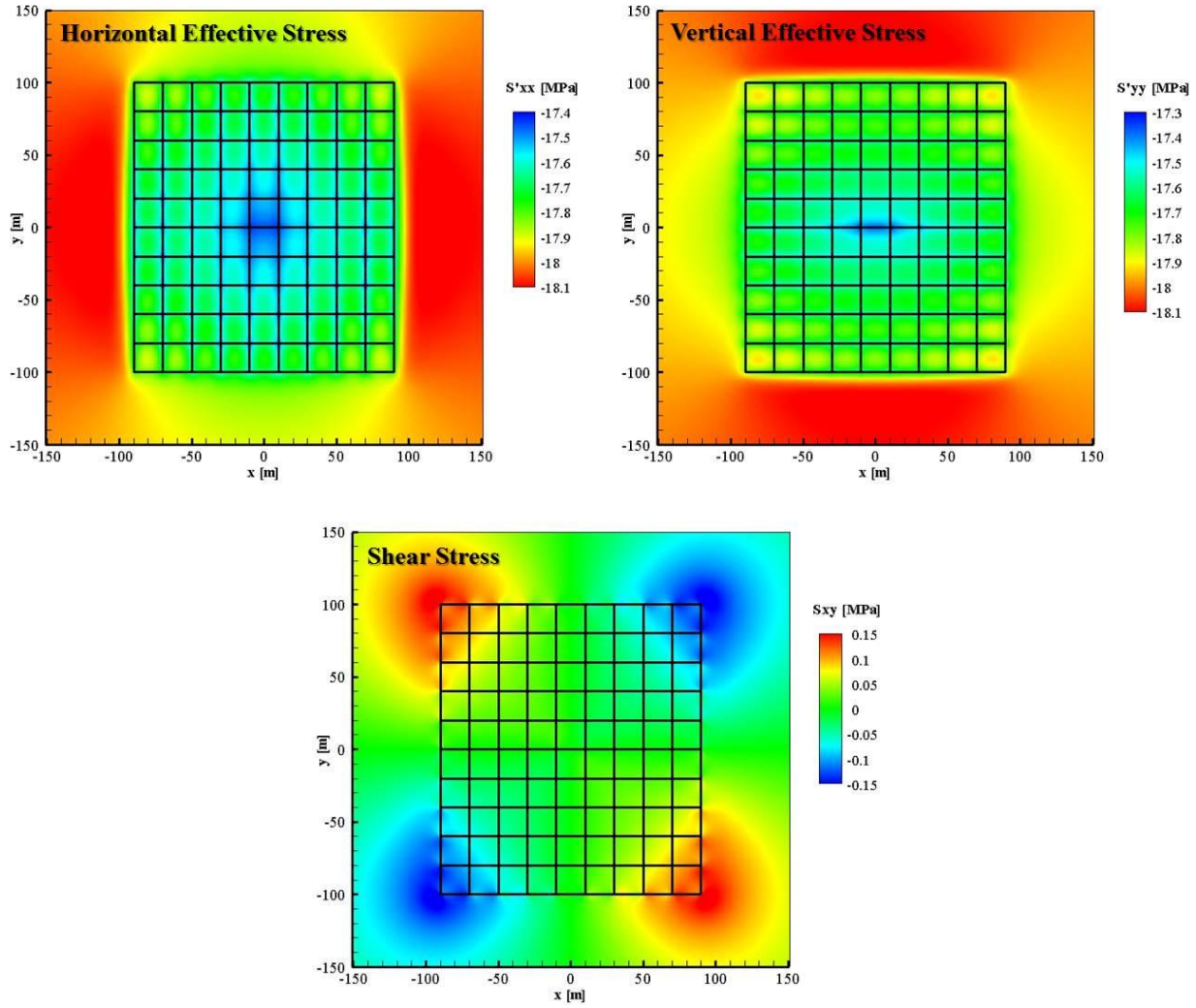

Figure 6.4. Horizontal and vertical effective stress as well as shear stress maps in the surrounding rock of a cubical fracture network after 30 hours of fluid injection under isotropic in-situ stress condition

In the case of anisotropic in-situ stress, fluid propagates horizontally faster as the minimum in-situ stress is vertical and opens up the horizontal fractures more than the vertical ones (Figure 6.5). Fracture aperture at the injection point after 30 hours of injection is estimated to be equal to 0.18 mm (2600 Darcy which is more than tenfold increase with respect to the initial fracture conductivity 200 Darcy) where the fracture fluid pressure is 16.26 MPa.

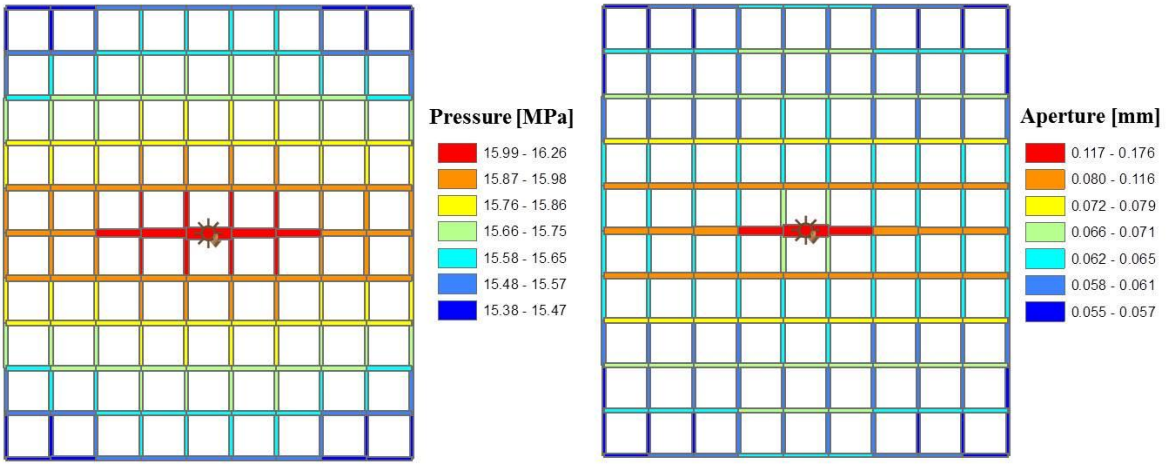

Figure 6.5. Fracture fluid pressure (left) and fracture aperture (right) variation after 30 hours of fluid injection under anisotropic in-situ stress condition

The highest fracture opening in the vertical fractures occurs in the fractures ambient to the injection point (point B in Figure 6.1) where the fracture pressure and aperture are equal to 16.08 MPa and 0.066 mm (360 Darcy), respectively. The maximum aperture in the *x*-direction except for the injection point is equal to 0.14 mm (1600 Darcy) for a pressure increase of 1.15 MPa at point D in Figure 6.1. These values show that the existence of anisotropy in in-situ stresses and fracture normal stiffnesses affects the fluid propagation and fracture aperture significantly.

Pore pressure propagation in the surrounding rock is also affected by in-situ stress anisotropy, especially after 30 hours of the injection initiation based on the Figure 6.6. The anisotropic behavior of pore pressure is not that significant in the pressure map at 12 hours as the pressure has not reached the fracture boundaries.

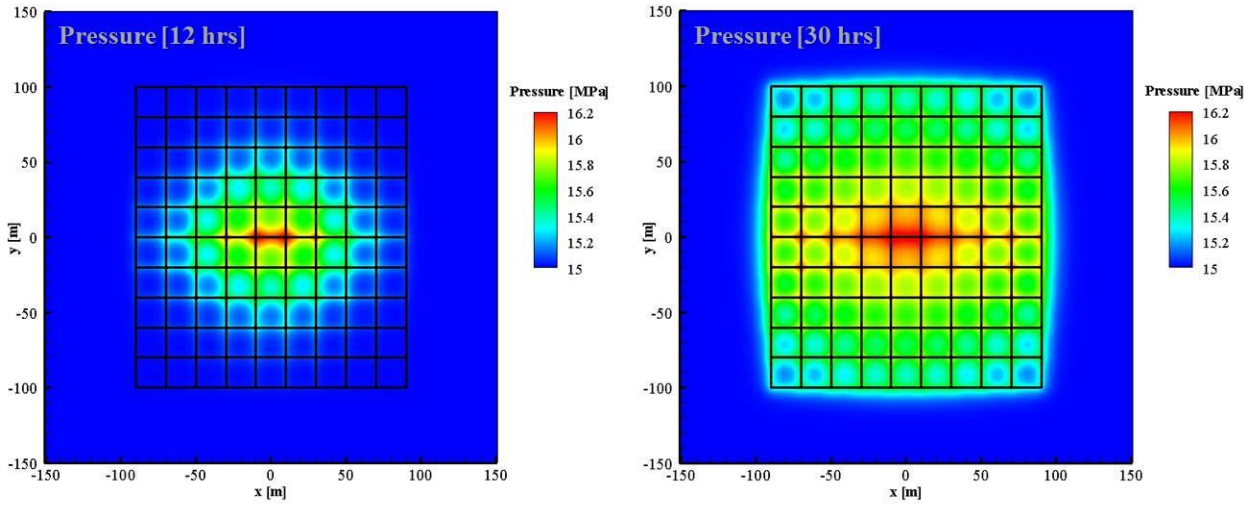

Figure 6.6. Pore pressure variation after 12 (left) and 30 (right) hours of fluid injection under isotropic in-situ stress condition

The same plot as Figure 6.4 is shown in Figure 6.7 for the stresses at 30 hours. The effective stresses are more elongated in the *x*-direction as the pressure increment rate is higher in this direction. Also, the shear stresses are extended slightly away from the injection point along the *y*-axis as the horizontal fractures open more in the anisotropic case in comparison with the isotropic one.

Five points are selected here and their fracture pressure and aperture evolution over time for both isotropic and anisotropic cases are compared. These five points are specified by A-E in Figure 6.1 where point C is the injection point. The pressure variation over time for these points is depicted in Figure 6.8. A seven-hour time lag is observed for the pressure rise in point A and E as they are located 90.55 and 80 meter away from the injection point C. For the isotropic case, the pressure evolution at points B and D are identical as they are located in the same fracture distance (cumulative length of fractures) from point C.

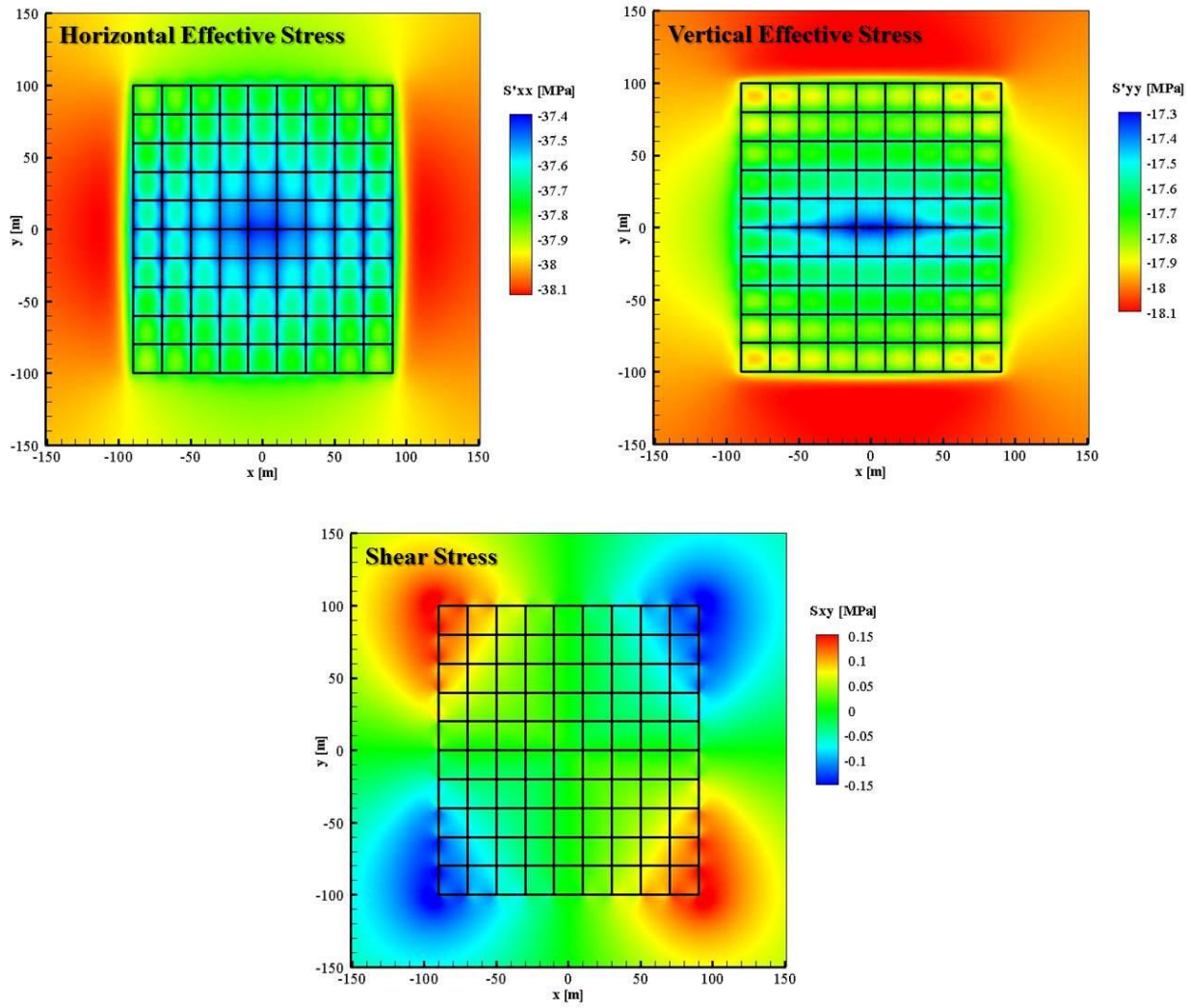

Figure 6.7. Horizontal and vertical effective stress as well as shear stress maps in the surrounding rock of a cubical fracture network after 30 hours of fluid injection under isotropic in-situ stress condition

The pressure increment in the anisotropic stress condition is more than for the isotropic case for all the points except point A which is located in the vertical fracture far away from the injection point. This pressure difference between the two cases occurs as the amount of total energy for opening fractures for the anisotropic stress condition in this problem is more than for the

isotropic case as one of the in-situ stresses was increased to apply the stress anisotropy to the model.

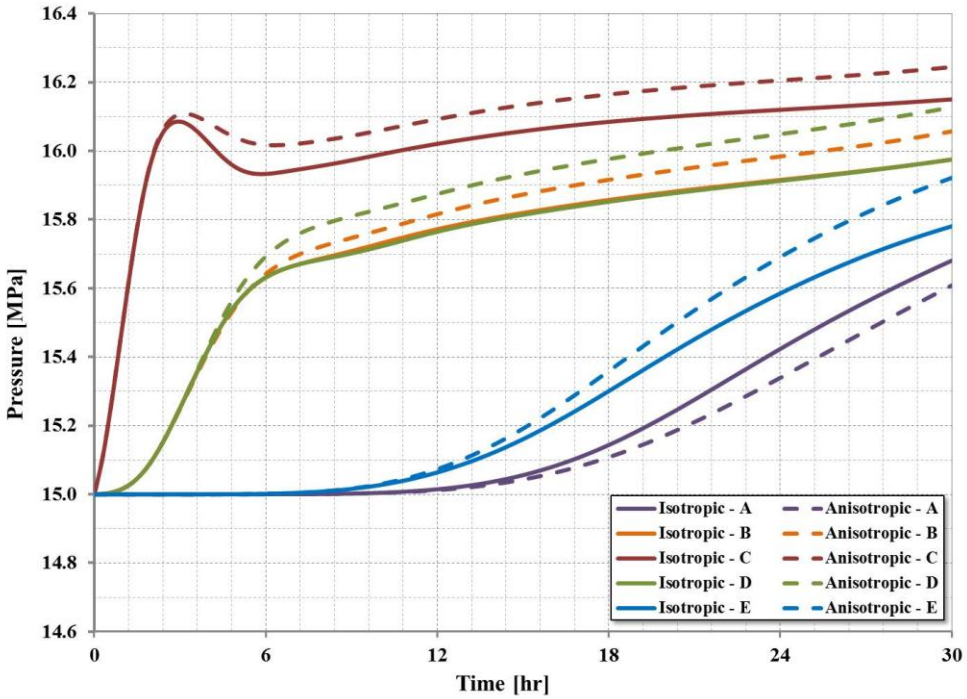

Figure 6.8. Fracture pressure evolution over time for five specified point in the fracture network for two in-situ stress conditions: isotropic and anisotropic.

These pressure changes induce similar fracture opening behavior to the considered points as shown in Figure 6.9. The only discrepancy in the behavior of pressure and aperture happens in point B. Fracture aperture at this point for both cases is less than point D, which has the identical pressure as for the isotropic case. This phenomenon occurs as the fracture aperture increment at the injection point increases the stress locally in the surrounding blocks, especially the upper block which is also the adjacent block to point B. The normal stress difference between points B and D is about 0.04 MPa after 30 hours of injection.

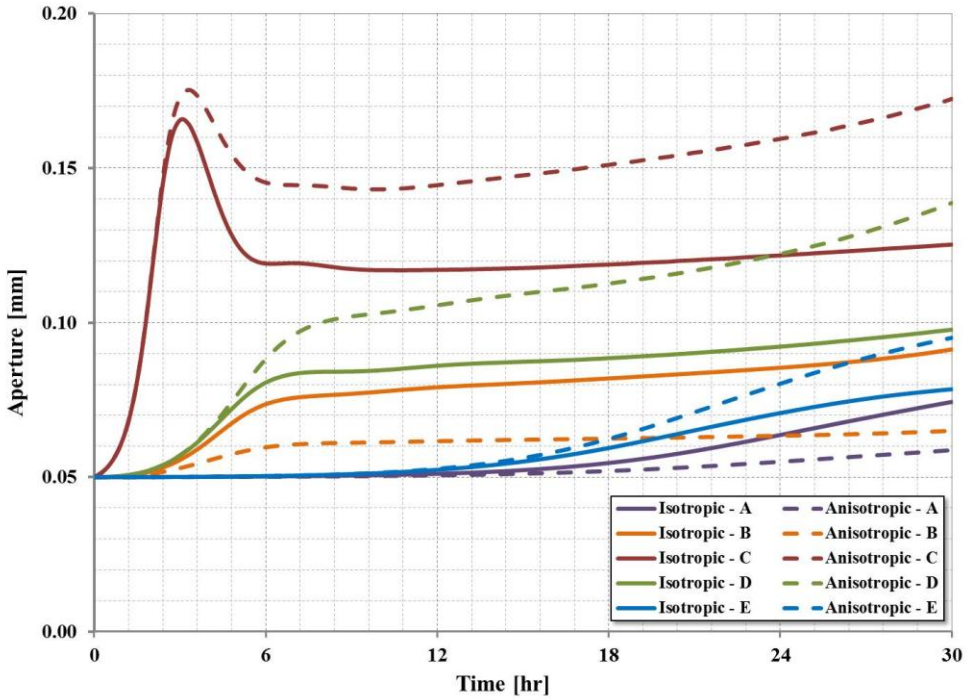

Figure 6.9. Fracture aperture evolution over time for five specified point in the fracture network for two in-situ stress conditions: isotropic and anisotropic.

A local peak pressure at point C after 3.5 hours of injection initiation can be observed in Figure 6.8 which is associated with an abrupt fracture aperture increment. This phenomenon demonstrates a transient flow from the fracture into the rock. Before this peak, most of the fluid flow occurs in the fracture network and after reaching the peak, fluid penetration occurs into the matrix at the injection point, which is followed by a local pressure decrement. To prove this claim, the pressure growth in the injection point (point C) over time for different matrix permeabilities is shown in Figure 6.10. The abrupt pressure increase at early time disappears when the matrix permeability increases, showing that the fluid leak-off occurs gradually for the high permeability rock (10 mD in the case of Figure 6.10).

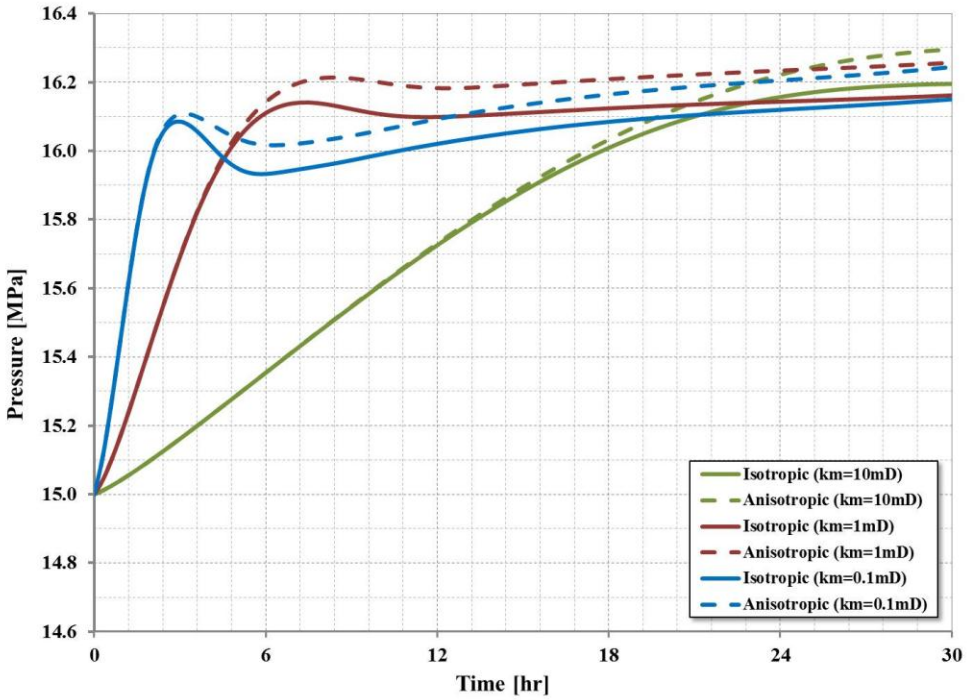

Figure 6.10. Fracture pressure evolution over time at the injection well for different rock permeabilities.

6.2 Thermal Fluid Injection into an Orthogonal Fracture Network

In this section, a viscous fluid with a temperature of 50°C colder than the initial temperature in the fracture network and rock (T_0 = 80°C) is injected to the fracture network in Figure 6.1 with an anisotropic in-situ stress condition. Hydraulic and geomechanical properties for this example are the same as section 6.1 (Table 6.1) and the thermal properties of the fluid and rock are shown in Table 6.2. Fracture pressure, aperture and temperature in the fracture network after 30 hours of cold fluid injection are presented in Figure 6.11.

Table 6.2. Thermal properties of the orthogonal fracture network and surrounding rock

Fluid specific heat (C_f)	4200 J/kg°K	Rock heat diffusivity (c^T)	5×10^{-5} m^2/s
Fluid thermal expansion (β_f)	2.4×10^{-5} 1/°K	Rock thermal expansion (β_s)	2.1×10^{-5} 1/°K
Fluid thermal conductivity (k_{Tf})	0.6 J/m°Ks		

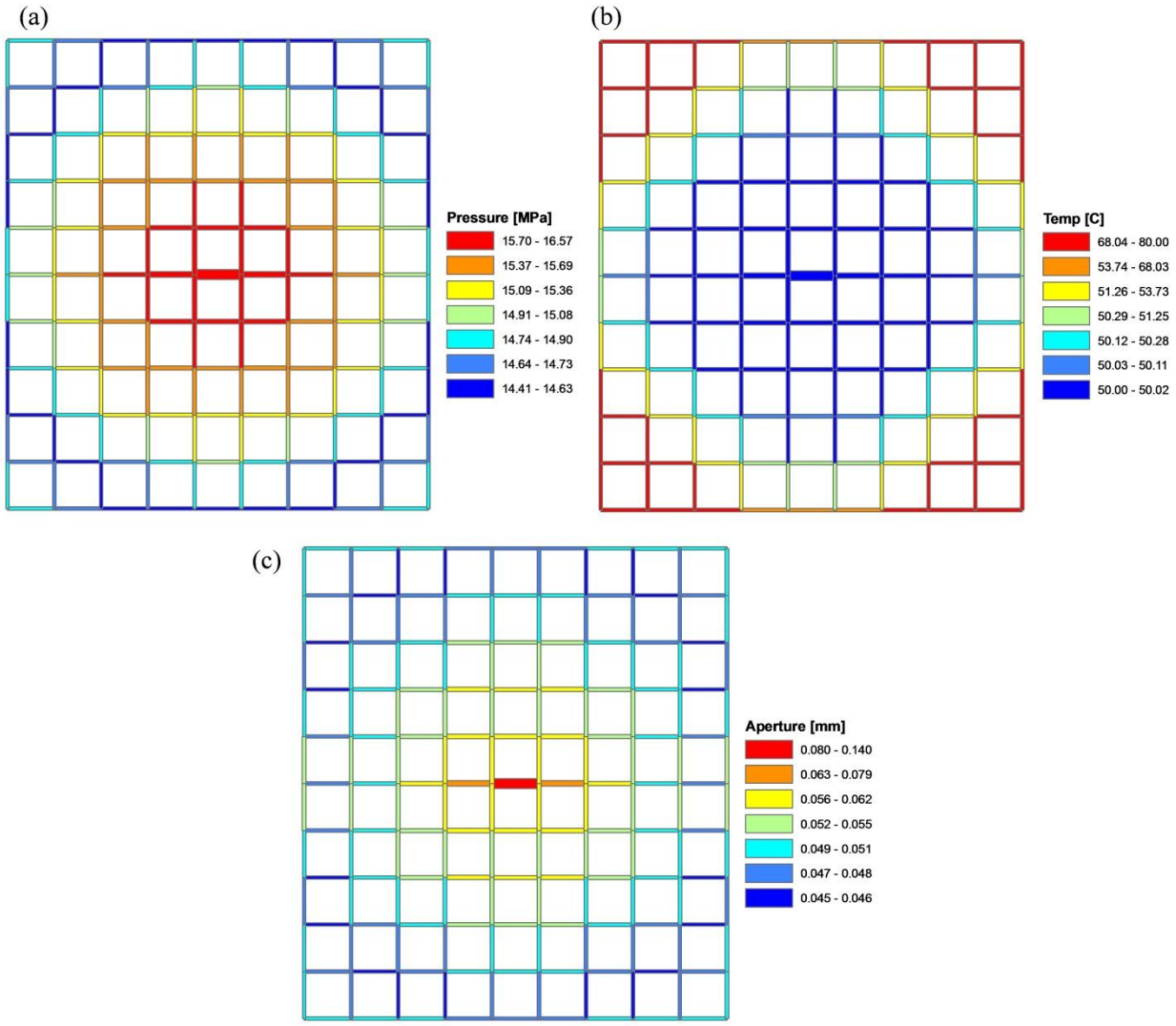

Figure 6.11. Pressure (a), temperature (b) and aperture (c) maps of fracture network after 30 hours of cold fluid injection

The pressure starts to propagate in the fractures as soon as injection starts and as can be seen in Figure 6.11.a, it tends to propagate in the *x*-direction more than the *y*-direction as it is easier for the pressure to open the fracture in the *x*-direction because of the lesser perpendicular stress ($\sigma_{yy}<\sigma_{xx}$) and normal fracture stiffness in comparison with the vertical fractures. The same behavior is visible also for heat flow in the fracture network. As heat convection is much faster than heat conduction and is controlled by the fluid velocity in the fracture network, the injection

fluid cools down the fracture network and its surrounding rock in the *x*-direction more than in the *y*-direction. The change in temperature (-30°C) affects almost the whole fracture network except for the four corners of the network, which are not also affected much by the fluid injection process, but they nonetheless show a pressure reduction as the result of thermoelastic rock shrinkage. This effect is more visible in the displacement maps of the rock mass. An abrupt fracture aperture increment occurs at the injection fracture segment as a result of both pressure increase and temperature reduction (rock shrinkage). The fracture aperture in segments with the yellow color in the temperature map has a slight reduction as well as in the fracture pressure that represents the temperature front in the fracture network.

In order to see the effect of injection on the fracture network rock blocks, pressure, temperature, displacement and stress are calculated using the displacement discontinuity method (Figure 6.12 and Figure 6.13).

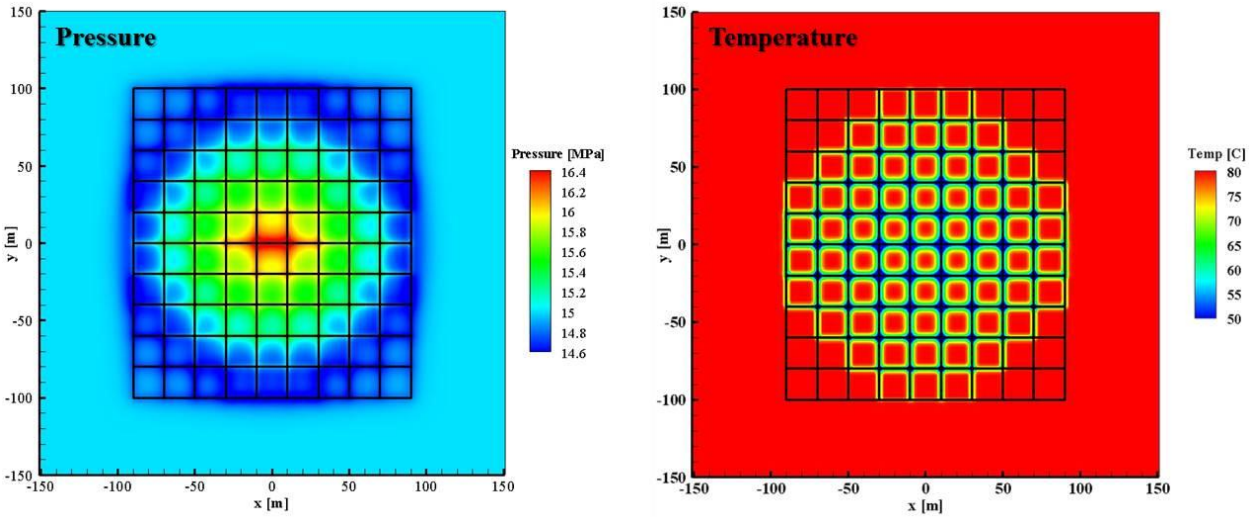

Figure 6.12. Pressure and temperature propagation maps in the rock around the fracture network after 30 hours of cold fluid injection.

Pressure propagates almost symmetrically in the whole mass with a small tendency to flow more in the *x*-direction rather than vertically, as this is the more favorable path for flow in the fractures (Figure 6.12). The pressure front in the rock is visible (light blue), followed by a pressure reduction in the rock as the result of rock shrinkage. Temperature propagates much more slowly in the rock than within the fractures as heat conduction is the only heat transfer mechanism within the rock blocks. In Figure 6.12, the cooling effect has not yet reached the middle of any rock blocks. The amount of temperature reduction at the intersection of fractures is more than in the rock close to the injection point. This happens because of the methodology used in the displacement discontinuity method, i.e. temperature is estimated as the superposition of all influenced segments based on their distance, leads to a greater effect at the intersections. This spurious artifact could be empirically corrected in future realizations of this coding.

Figure 6.13 shows the displacements, effective stresses and shear stresses in the rock around the fracture network. As a result of cooling, the rock blocks should start to shrink, and the data in the horizontal (*x*-direction) and vertical (*y*-direction) displacement maps confirm this. This thermal effect is dominant in the cold region and compensates the pressure effect that pushes the rock away from the fracture network. In the injection area, as the pore pressure increases, both horizontal and vertical effective stresses diminish from their initial values (σ'_{xx} = -38 MPa, σ'_{yy} = -18 MPa), however this effect is suppressed by the temperature effect that reduces (more than fivefold with respect to pressure effect) the horizontal and vertical stresses (both total and effective) adjacent to the horizontal and vertical fractures, respectively.

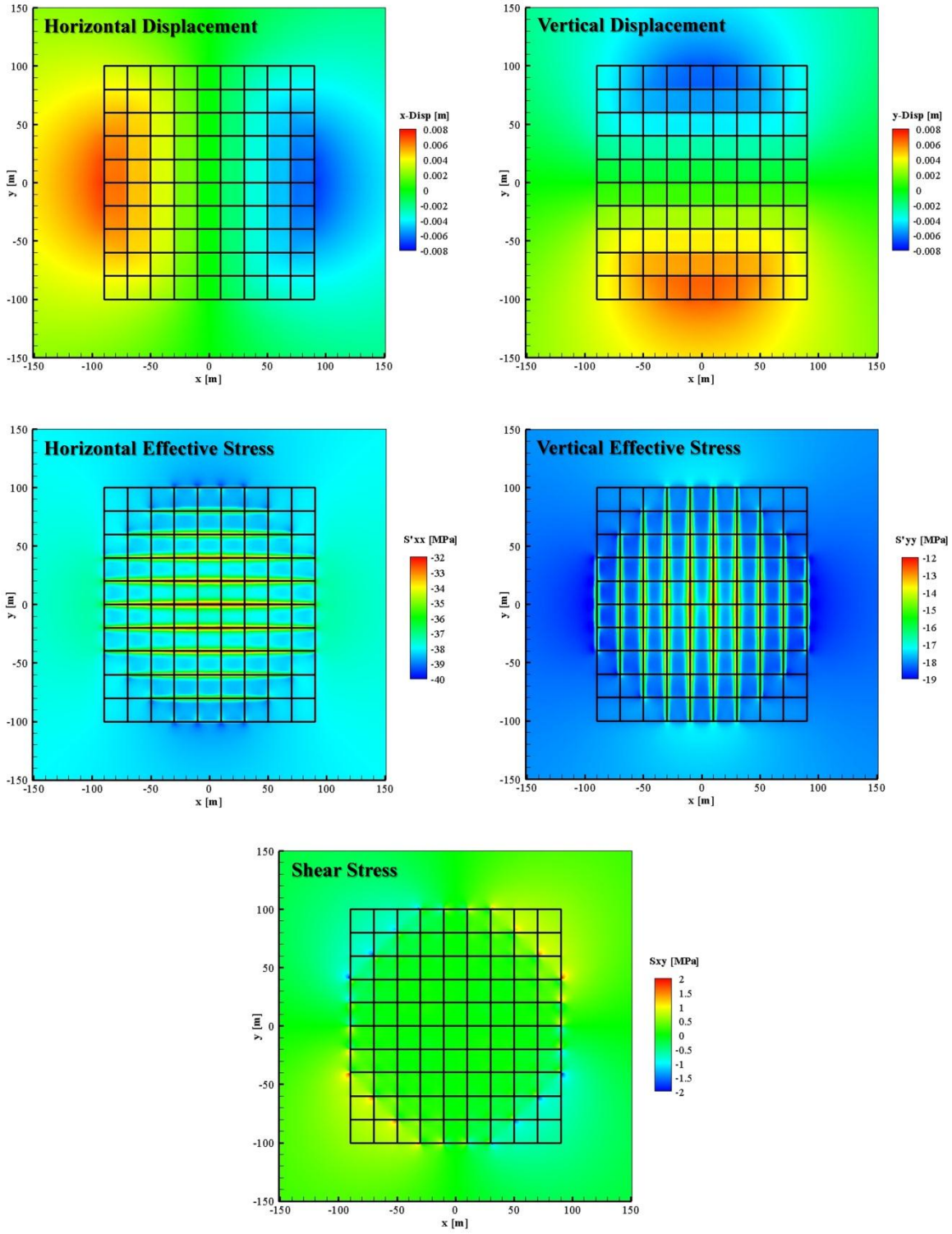

Figure 6.13. Displacements, effective stresses and shear stress maps in the rock around the fracture network after 30 hours of cold fluid injection.

This effect was reported by Perkins and Gonzalez (1985) and is sketched in Figure 6.14. Based on their work, cold fluid injection into a reservoir that is almost impermeable is accompanied by the development of hydraulically induced fracturing perpendicular to the minimum horizontal stress [Hubbert and Willis, 1957], arising from the cooling of the rock surrounding the fracture (Case 1). If the injection process is continued with a high flow rate, the fracture extends to a greater distance and changes the shape of the cooled region to an ellipse with the long axis lying parallel to the fracture orientation. This elongation affects the thermal stress variation by reducing the stress parallel to the fracture plane more than the stress perpendicular to the fracture surface (i.e. $\Delta\sigma_2 > \Delta\sigma_1$ in Case 2). In this case, the difference between the principal stresses around the fracture drops until all stresses approach the same value. More injection into this fracture causes the stress parallel to the fracture to diminish less than the perpendicular one, i.e. secondary fractures perpendicular to the primary fracture will initiate as the effective stresses parallel to the fracture near the central injection point drop well below the injection pressure (Case 3). In Case 3, for a homogeneous case, the dominant fracture will propagate from the injection point where the pressures are the highest, but depending on the geometry, the fracture toughness and the pressure losses within the fracture, other secondary fractures will propagate at other locations along the cooled fracture [Perkins and Gonzalez, 1985].

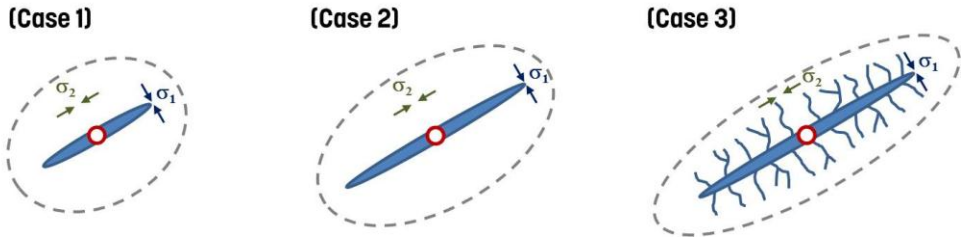

Figure 6.14. Schematic plan view of cooled region around a vertical fracture for three different injection conditions [reproduced after Perkins and Gonzalez, 1985]

Returning to Figure 6.13, shear stresses are the largest at the thermal front where an abrupt displacement occurs as a result of rock shrinkage.

6.3 Thermal Fluid Injection and Extraction from a Brick-Shaped Fracture Network

In this section, a combination of injection and production fluid sources is considered in a brick-shaped fracture network. It is assumed that a cold fluid (20˚C) is injected with a constant rate of 10^{-4} m^3/s in the upper left part of the network (point I in Figure 6.15) for four days with an initial temperature of (70˚C) and fluid is extracted with half the rate of fluid withdrawal (i.e. 5×10^{-5} m^3/s) from point P. The initial fracture aperture and maximum fracture closure are assumed to be 0.1 mm and 50 μm, respectively. Other hydraulic, thermal and geomechanical properties are identical with Table 6.1 and Table 6.2.

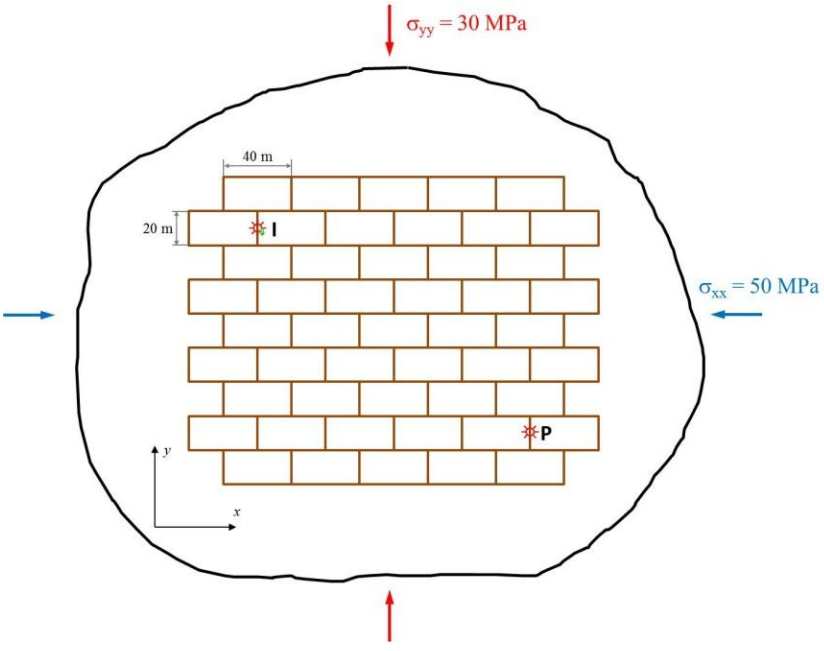

Figure 6.15. Schematic representation of the brick-shaped fracture network model

Injection causes an increase in the fracture pressure and in the surrounding rock, whereas the fluid production reduces the pressure. In this example, at early time the difference of pressure between injection and production points is high; however, this difference decreases over time as the injection rate is twice the production rate and the total pressure in the fracture and rock increases. This effect is depicted for both the fracture network and the surrounding rock in Figure 6.16 and Figure 6.17.

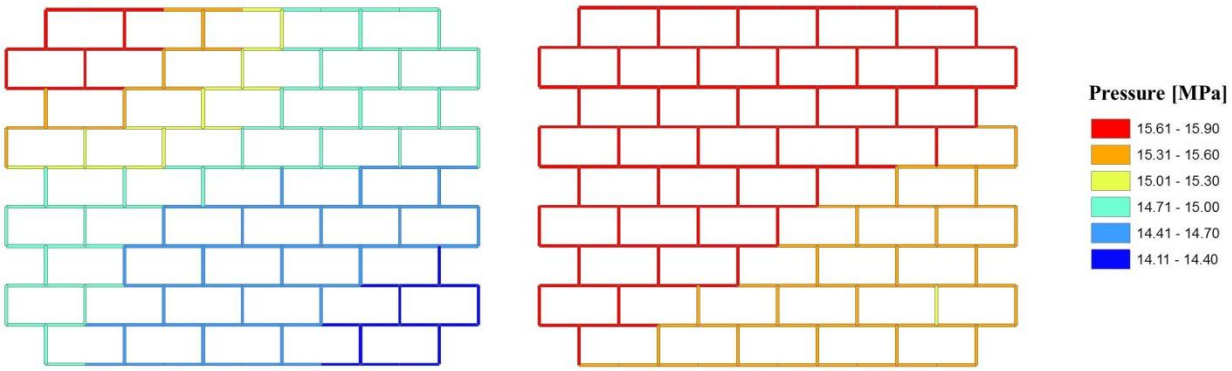

Figure 6.16. Pressure propagation in the fractures after 1 day (left) and 4 days (right) of cold fluid injection and extraction from a brick-shaped fracture network.

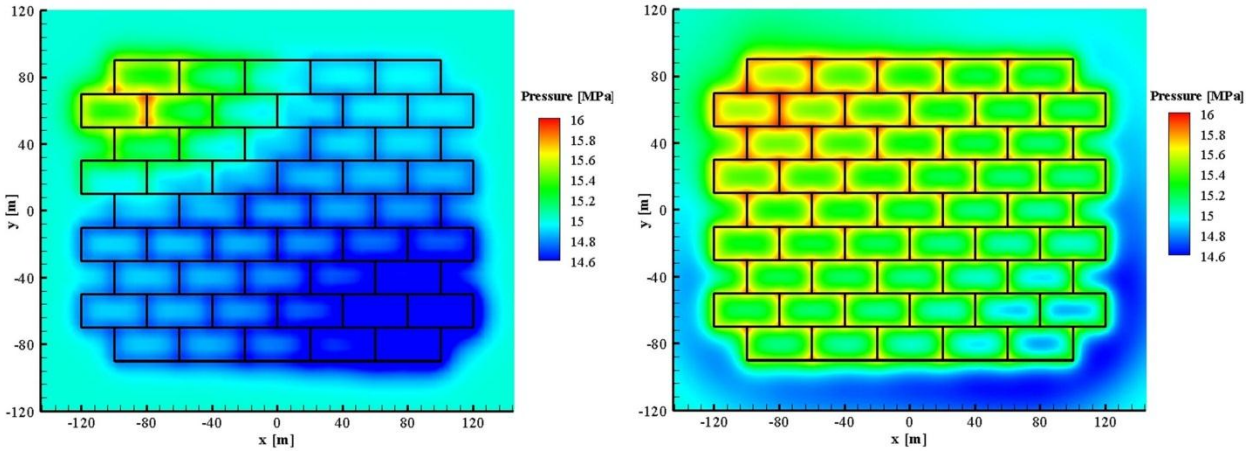

Figure 6.17. Pressure propagation in the rock after 1 day (left) and 4 days (right) of cold fluid injection and extraction from a brick-shaped fracture network.

After 4 days of fluid injection, the minimum fracture pressure is equal to 15.28 MPa whereas the rock at the lower right part of the fracture network in Figure 6.17 has a pressure less than the initial pore pressure in the model (< 15 MPa). This pressure reduction occurs as a result of fluid extraction prior to the pressure front reaching the production point. After that, the pressure reduction is compensated from the fractures rather than the surrounding rock as it is more convenient for the fluid to transfer through the fracture network. As the average fracture pressure is increasing over time, it will compensate for the rock pressure reduction.

The pressure influenced area around the injection point is smaller than that around the production source, even though the injection rate is double the production rate. This phenomenon happens as a result of cold fluid injection and rock cooling around the injection source changing the fracture aperture (Figure 6.18 and Figure 6.19). After 4 days, the injected fluid cools down the entire fracture network and the thermally induced stress changes in the fracture network attenuate.

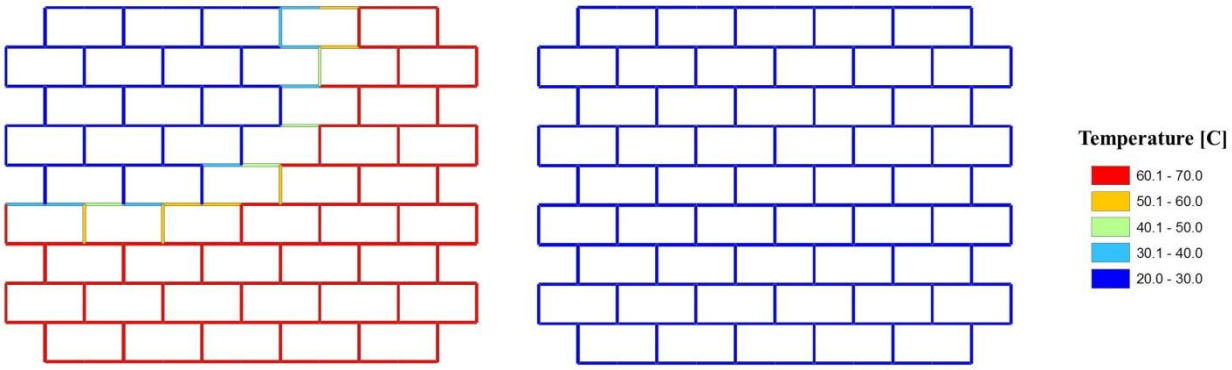

Figure 6.18. Temperature propagation in the fractures after 1 day (left) and 4 days (right) of cold fluid injection and extraction from a brick-shaped fracture network.

The production processes affect the fracture aperture in the manner shown in Figure 6.20. Fracture aperture increases in the cold and injection influence area and drops in the production influence regions. In Figure 6.20, it is also shown that at the end of each fracture set, an abrupt increase in the fracture aperture occurs as the rock outside of the fracture network starts to cool down and the amount of rock shrinkage in more than the small blocks among the fracture sets.

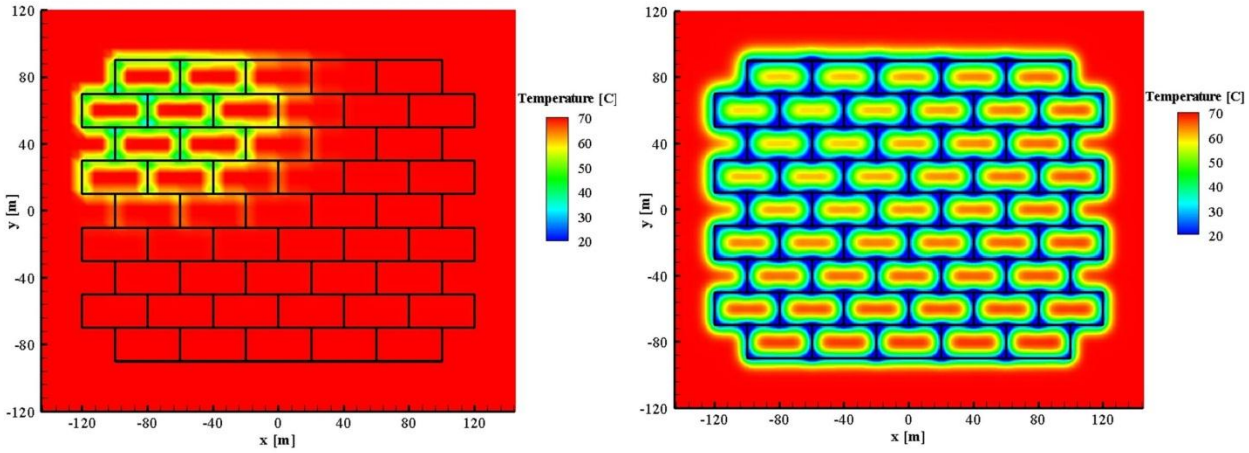

Figure 6.19. Temperature propagation in the rock after 1 day (left) and 4 days (right) of cold fluid injection and extraction from a brick-shaped fracture network.

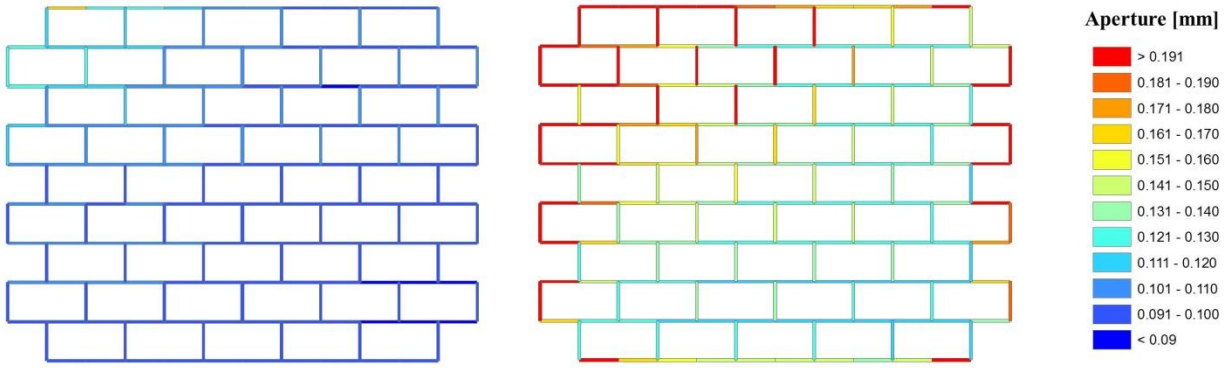

Figure 6.20. Aperture propagation in the fractures after 1 day (left) and 4 days (right) of cold fluid injection and extraction from a brick-shaped fracture network.

In all of the simulation results, a gentle tendency for pressure and temperature to flow horizontally can be seen as a result of lowered in-situ stress and fracture normal stiffness in the vertical direction.

6.4 Fluid Extraction from a non-Orthogonal Fracture Network

To study the effect of shear dilation on fracture behavior, a non-orthogonal fracture network is considered in this section. Two fracture sets intersecting at 53° are assumed in a poroelastic medium with a production source in the middle of model. An anisotropic in-situ stress condition is considered with two different combinations (Figure 6.21); case 1 where the acute angle is oriented in the direction of minimum stress (i.e. $\sigma_{yy}=\sigma_{min}$) and case 2 where the acute angle is oriented in the direction of maximum stress (i.e. $\sigma_{yy}=\sigma_{max}$).

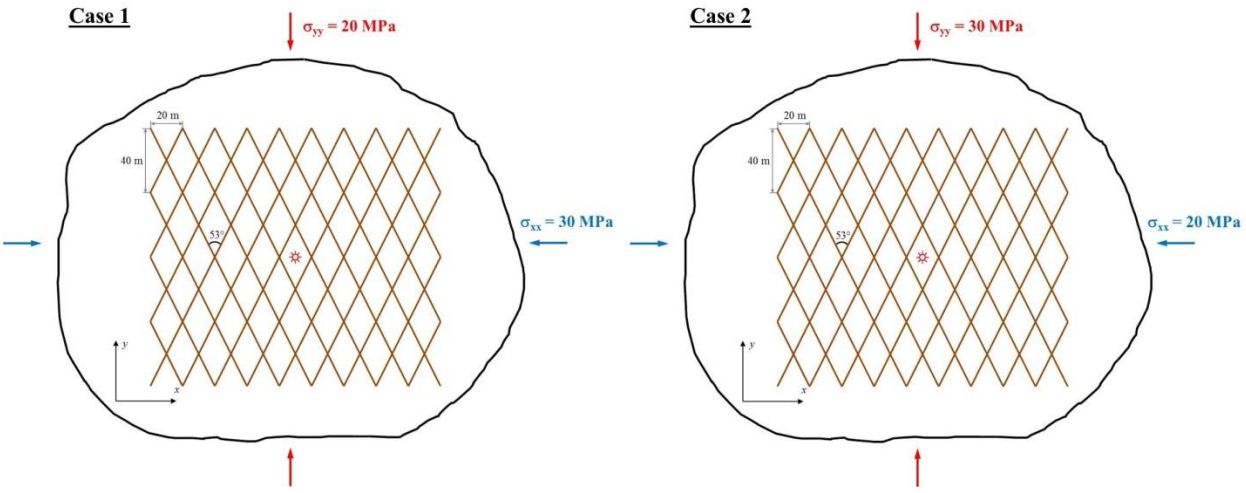

Figure 6.21. Schematic representation of an inclined fracture network with a production source in the middle for two different in-situ stress configurations.

Fluid is produced at a constant rate of 10^{-5} m^3/s for five days from the poroelastic medium; other model properties are listed in Table 6.3.

The normal stresses on the fracture segments for case 1 and 2 are 28 MPa and 22 MPa, respectively. The absolute value of shear stress for both cases is identical to 4 MPa (refer to Appendix E). Considering the initial pressure (16 MPa), the fracture segments in case 1 have not reached the Mohr-Coulomb criterion, whereas all the fracture segments in case 2 have already passed the yield criterion and are yielded. Based on Section 4.3.1, the shear stiffness for fractures in case 2 is zero as the fractures are already yielded and it is easier for the fractures to move laterally and increase the shear displacement discontinuities as well as the fracture aperture.

Table 6.3. Geomechanical and hydraulic properties of the non-orthogonal fracture network and surrounding rock

Drained Poisson's ratio (ν)	0.25	Undrained Poisson's ratio (ν_u)	0.35
Young's modulus (E)	20 GPa	Initial pressure (p_0)	16 MPa
Initial fracture aperture (w_0)	0.1 mm	Fracture maximum closure (w_{res})	50 μm
Fracture normal stiffness (K_n)*	10 GPa/m	Fracture shear stiffness (K_s)	10 GPa/m
Fluid compressibility (c_f)	7×10^{-10} 1/Pa	Fluid dynamic viscosity (μ)	1 cP
Production fluid rate (Q_{prod})	10^{-5} m^3/s	Fluid density (ρ_f)	1000 kg/m^3
Matrix permeability (k_m)	0.05 mD	Matrix porosity (ϕ_m)	0.25
Biot's coefficient (α)	0.8	Dilation angle (ψ)	5
Cohesion (σ_c)	0	Friction angle (ϕ)	30

For case 1, fluid extraction reduces the fracture pressure identically in the fracture network as the fracture conductivity is five orders more than the rock permeability and fracture network is the main fluid source in the system (Figure 6.22). This pressure reduction also affects the fracture apertures, reducing them mostly in the fracture segments inclined away from the production point (Figure 6.22.b). As the fracture segments have not reached the yield point in case 1, fracture shear stiffness controls the shear displacement discontinuities and the contribution of shear dilation to fracture opening is negligible (Figure 6.23). A non-zero shear displacement

discontinuity occurs in the fracture segments inclined toward the production point as a result of fluid extraction and increases the fracture aperture slightly in comparison with the fracture segments inclined away from the fracture network's center.

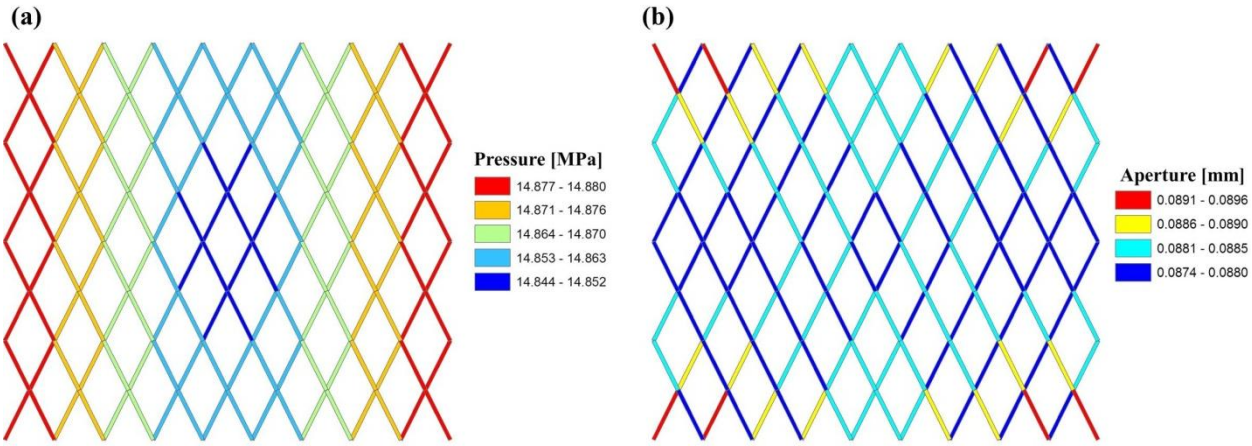

Figure 6.22. Fracture's pressure (a) and aperture (b) maps of the inclined fracture network after 5 days of fluid extraction for in-situ stress configuration of case 1.

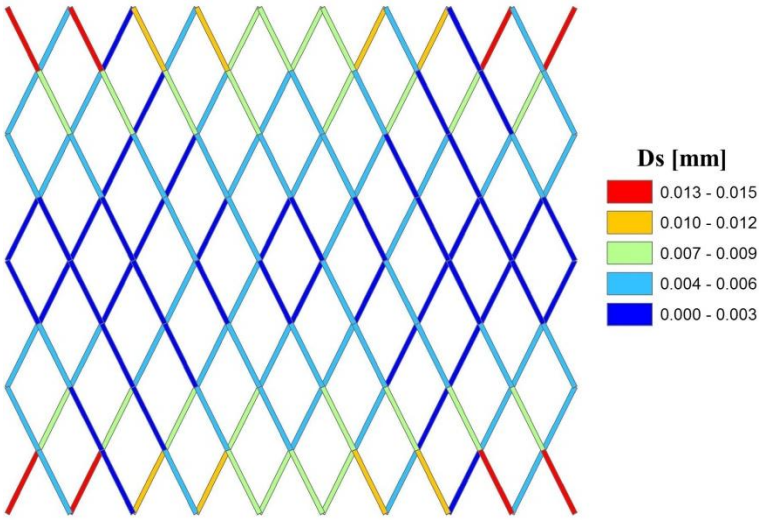

Figure 6.23. Shear displacement discontinuities of the inclined fracture network after 5 days of fluid extraction for in-situ stress configuration of case 1.

Considering case 2 with a maximum in-situ stress in the vertical direction, the average fracture pressure is slightly smaller than the case 1, as a result of shear dilation effects that increase the

aperture in the yielded fracture segments (Figure 6.24). Based on the direction of fracture planes' movement, the matrix blocks tend to move toward the production point. In this situation, most of the displacement occurs at the corner of the fracture network that shows the maximum amount of fracture opening.

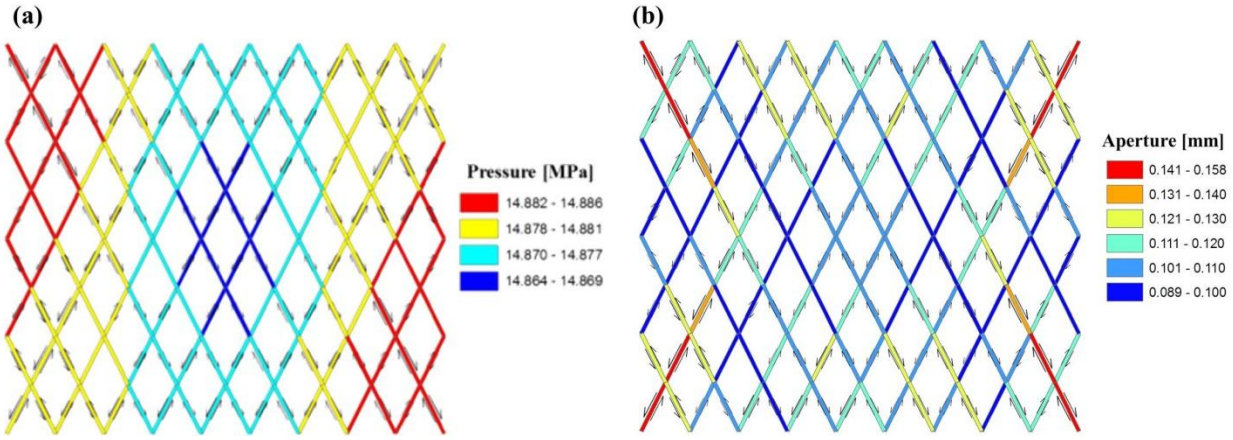

Figure 6.24. Fracture's pressure (a) and aperture (b) maps of the inclined fracture network after 5 days of fluid extraction for in-situ stress configuration of case 2.

The magnitude of shear displacement discontinuities for case 2 is more than ten-fold the value of D_s for case 1 as a result of fracture yielding (Figure 6.25).

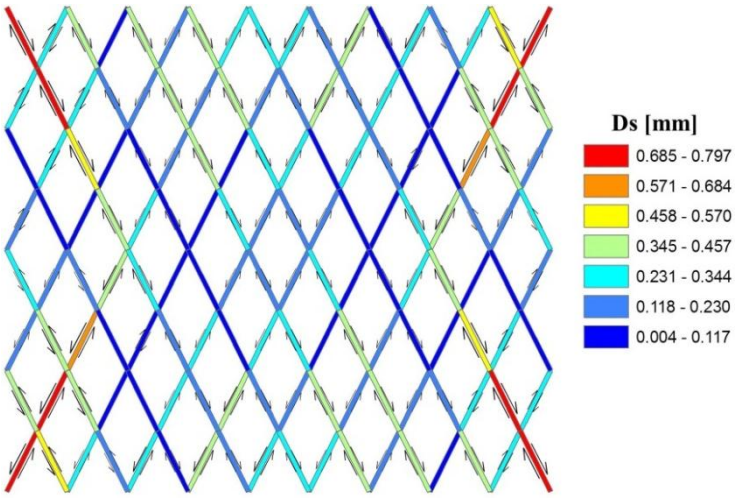

Figure 6.25. Shear displacement discontinuities of the inclined fracture network after 5 days of fluid extraction for in-situ stress configuration of case 2.

6.5 Sensitivity Analysis

It is worthwhile to investigate the effect of thermal, hydraulic and geomechanical properties on the thermo-hydro-mechanical behavior of fractures. In this case, a 40-meter single fracture (similar to section 5.4) is assumed and the sensitivity of the fracture response on the variation of some influenced parameters under a constant rate of cold fluid injection is analyzed. The properties of the fracture and surrounding rock are presented in Table 6.4.

Table 6.4. Geomechanical and hydraulic properties of the fracture network and surrounding rock

Drained Poisson's ratio (ν)	0.2	Undrained Poisson's ratio (ν_u)	0.3
Young's modulus (E)	10 GPa	in-situ horizontal stress (σ_{xx})	30 MPa
in-situ vertical stress (σ_{yy})	25 MPa	in-situ shear stress (σ_{xy})	0
Initial pressure (p_0)	10 MPa	Initial temperature (T_0)	80°C
Initial fracture aperture (w_0)	0.1 mm	Fracture maximum closure (w_{res})	50 μm
Fracture normal stiffness (K_n)	100 GPa/m	Fracture shear stiffness (K_s)	100 GPa/m
Fluid compressibility (c_f)	7×10^{-10} 1/Pa	Fluid dynamic viscosity (μ)	1 cP
Fluid thermal conductivity (k_{Tf})	0.6 J/m°Ks	Fluid density (ρ_f)	1000 kg/m^3
Fluid specific heat (C_f)	4200 J/kg°K	Rock heat diffusivity (c^T)	5×10^{-5} m^2/s
Matrix permeability (k_m)	1 mD	Matrix porosity (ϕ_m)	0.25
Fluid thermal expansion (β_f)	2.4×10^{-5} 1/°K	Rock thermal expansion (β_s)	2.1×10^{-5} 1/°K
Biot's coefficient (α)	0.8	Dilation angle (ψ)	0
Cohesion (σ_c)	0	Friction angle (ϕ)	30
Injection fluid rate (Q_{inj})	2×10^{-6} m^3/s	Injection temperature (T_{inj})	50°C

6.5.1 Fracture Aperture

The default initial fracture aperture in the model (0.1 mm) is compared with four other fracture apertures to study the effect of initial fracture aperture on the fracture's pressure, temperature, and aperture variation under cold fluid injection. The results are depicted in Figure 6.26. In the case of fracture pressure, increasing the initial fracture aperture increases the fracture pressure, but decreases the fracture pressure variation along the fracture, i.e. the fracture's pressure for the case of w=0.5 mm along the fracture's length is identical. This effect reduces the velocity of

fluid in the fracture, causing a reduction in thermal convection process. This effect can be seen in the temperature profile, as the cold fluid propagates faster when the initial fracture aperture decreases. The rate of fracture aperture increment decreases by increasing the initial fracture aperture. To see this effect, the relative fracture aperture with respect to the initial fracture aperture is shown in Figure 6.26. The amount of maximum fracture opening with respect to the initial fracture aperture increases dramatically by decreasing the initial fracture aperture.

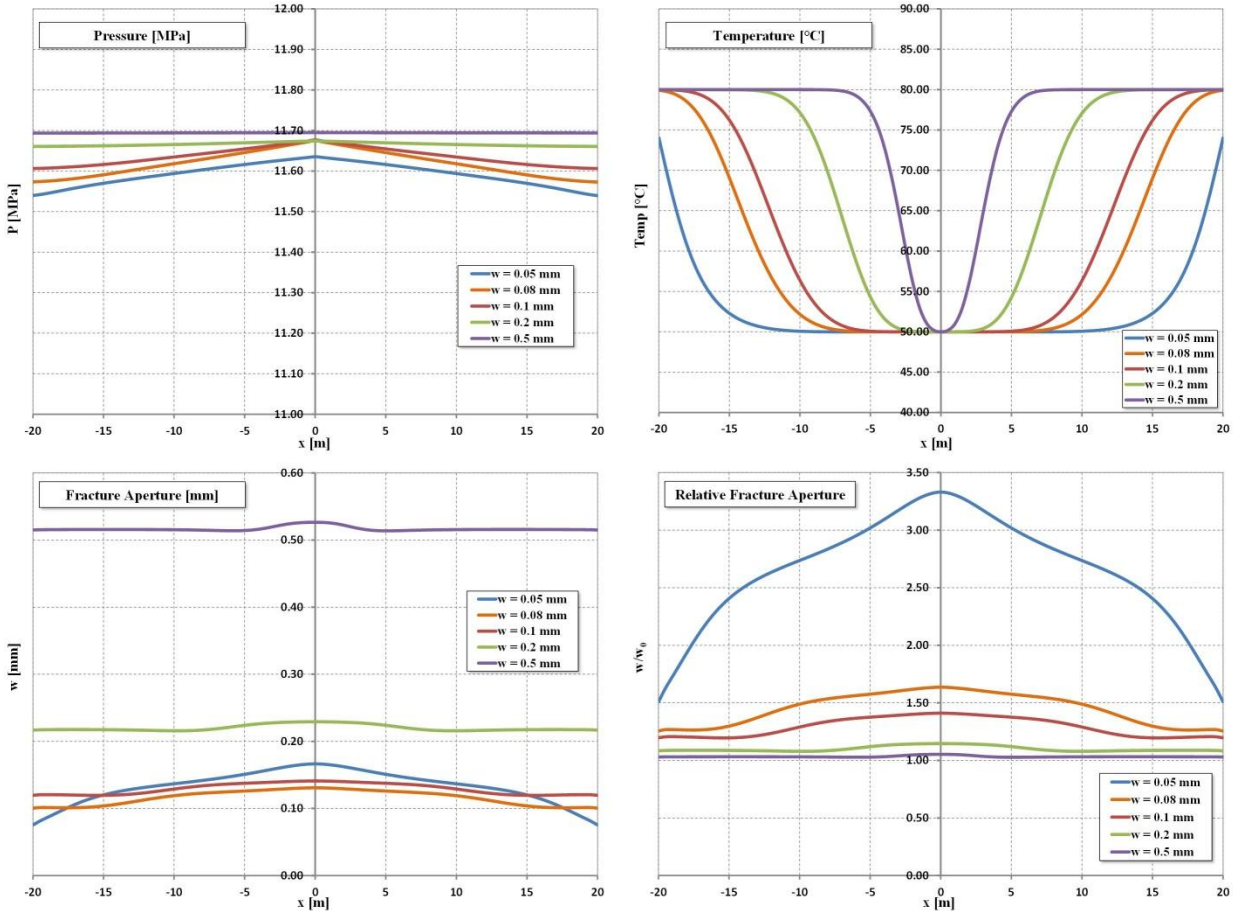

Figure 6.26. Fracture pressure, temperature, and aperture after 10 hours of injection for different initial fracture aperture.

6.5.2 Fracture Normal Stiffness

As mentioned in Section 4.3.1, a hyperbolic relationship based on the Barton-Bandis approach is adopted in this study. In this section, the effect of different initial fracture normal stiffness for the single fracture case is shown in Figure 6.27. As expected, increasing the fracture normal stiffness induces more constraint against opening of the fracture planes, and this increases the fracture pressure, especially at the injection point. This fracture pressure increment accelerates the thermal convection process; it can be seen in Figure 6.27 that the thermal front for the highest initial fracture normal stiffness is slightly ahead of the other thermal fronts.

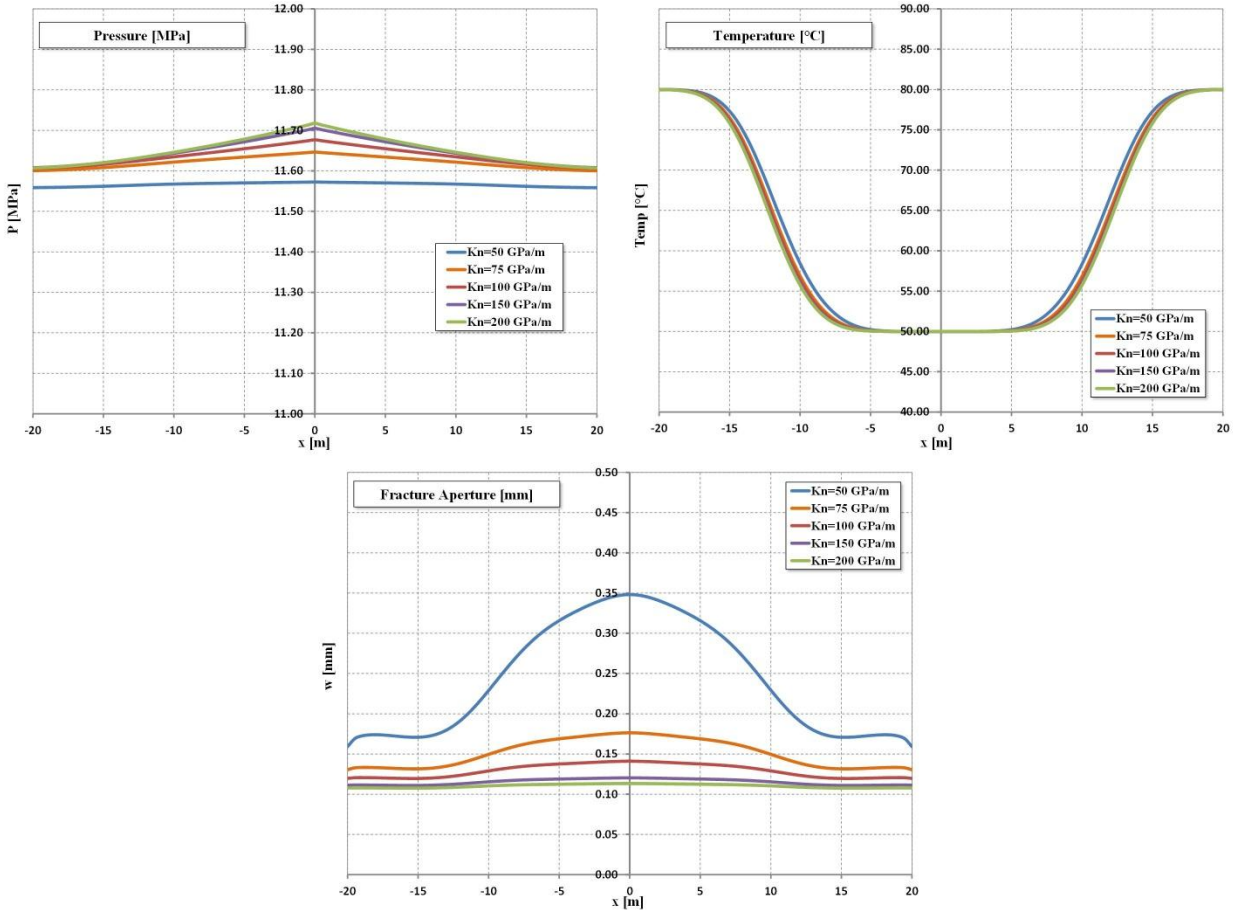

Figure 6.27. Fracture pressure, temperature, and aperture after 10 hours of injection for different fracture normal stiffness.

6.5.3 Fluid Compressibility

It seems that fluid compressibility does not have a significant effect on the thermo-hydro-mechanical behavior of the fracture model considered (Figure 6.28). A subtle change in fracture pressure using different fluid compressibilities is visible, but temperature and fracture aperture are not influenced by the variation of fluid compressibilities in the range of values considered.

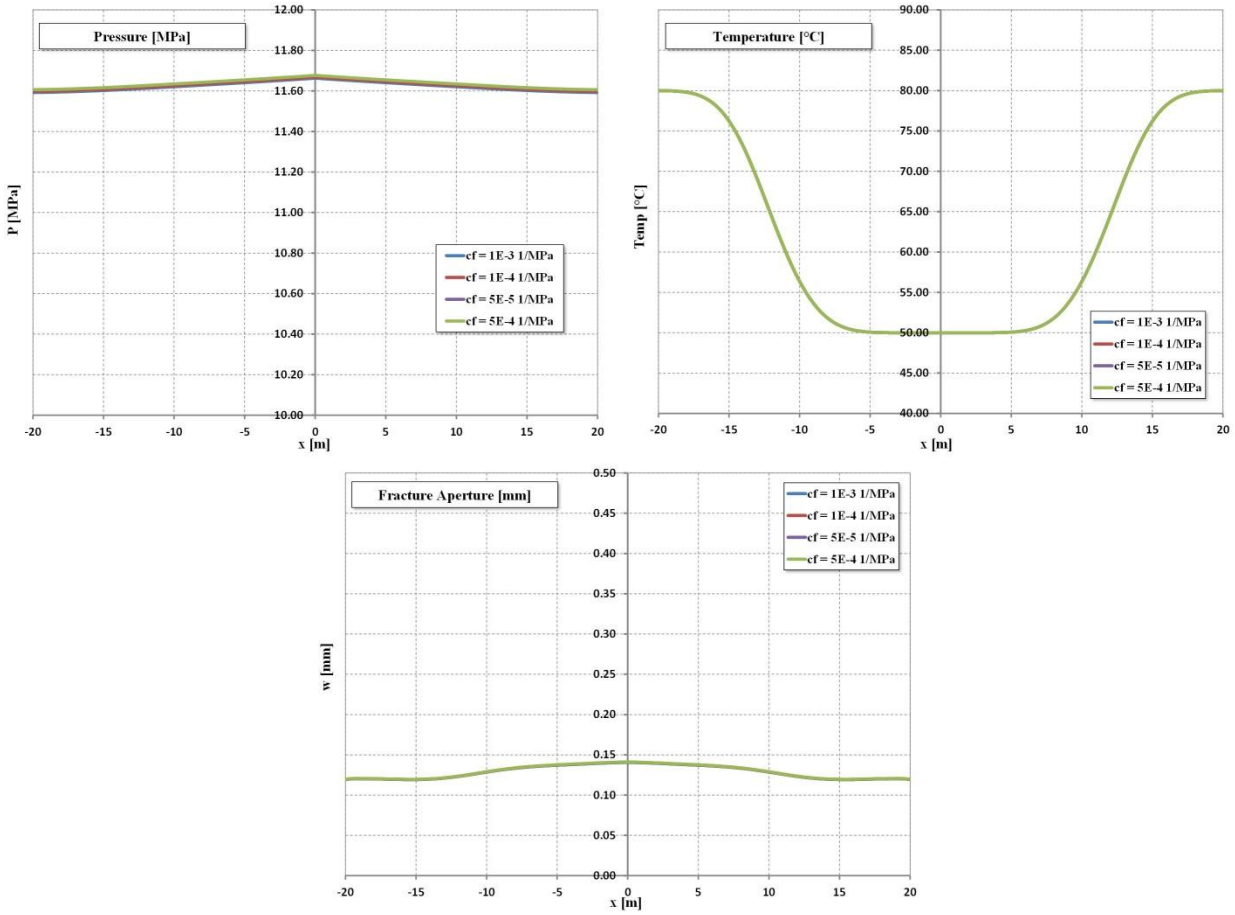

Figure 6.28. Fracture pressure, temperature, and aperture after 10 hours of injection for different fluid compressibility.

6.5.4 Fluid Viscosity

Fluid viscosity has a major contribution to the fracture's behavior, especially on pressure and aperture. Based on Figure 6.29, fracture pressure increases as the fracture viscosity goes up, associated with fracture opening. The influence of viscosity on fracture aperture is significant, and increasing the fluid viscosity reduces the mobility of fluid in the fracture, which affects the fluid velocity and slows down the thermal convection process in the fracture.

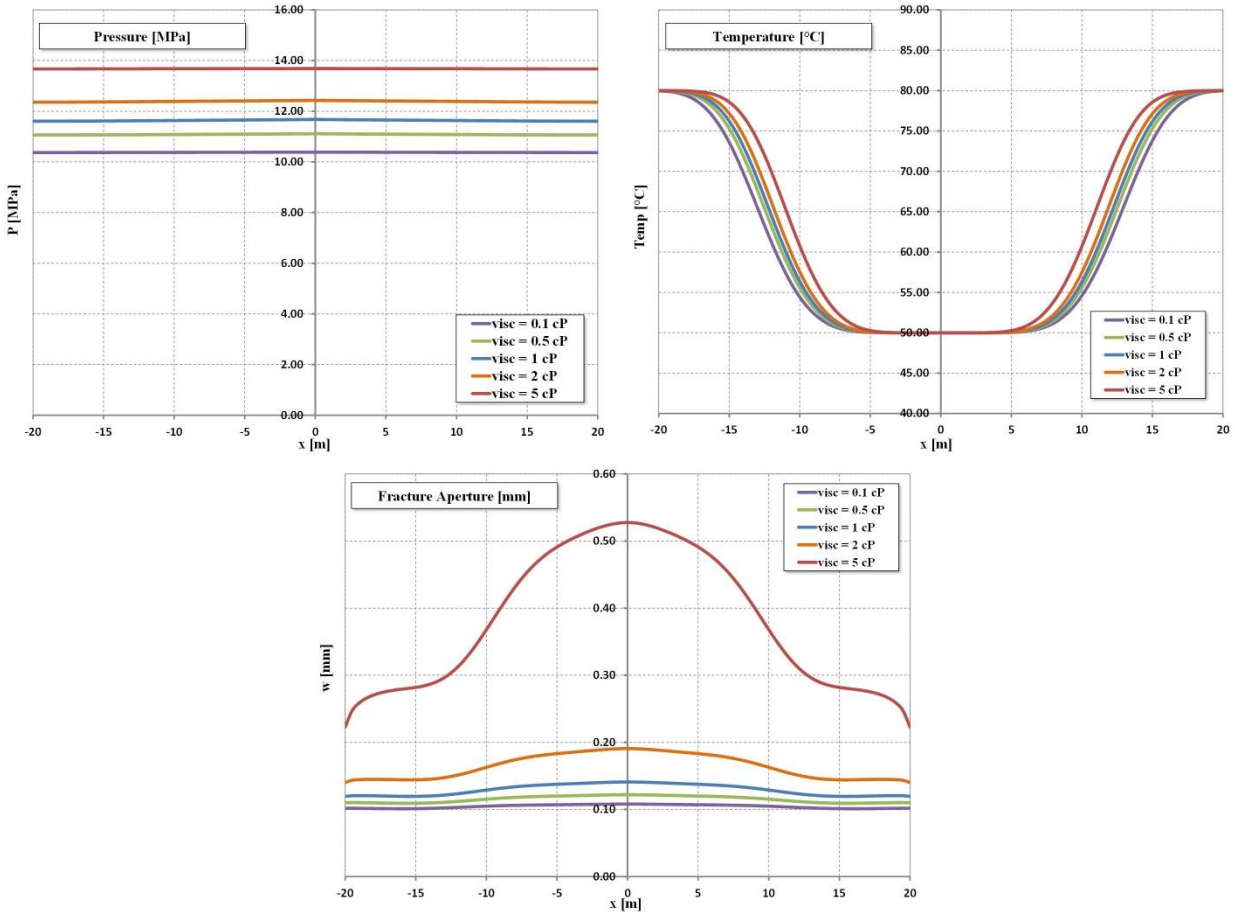

Figure 6.29. Fracture pressure, temperature, and aperture after 10 hours of injection for different fluid viscosity.

6.5.5 Matrix Permeability

Matrix permeability controls the rate of fluid penetration from the fracture into the rock matrix. Low fracture conductivity corresponds to a lesser amount of fluid transfer between fracture and matrix, and this increases the fracture pressure and temperature. Increasing the matrix permeability reduces the fracture pressure and aperture. Based on Figure 6.30, a high transfer rate between fracture and matrix reduces the fluid velocity in the fracture, and that induces a reduction in the rate of cooling of the fracture by thermal convection.

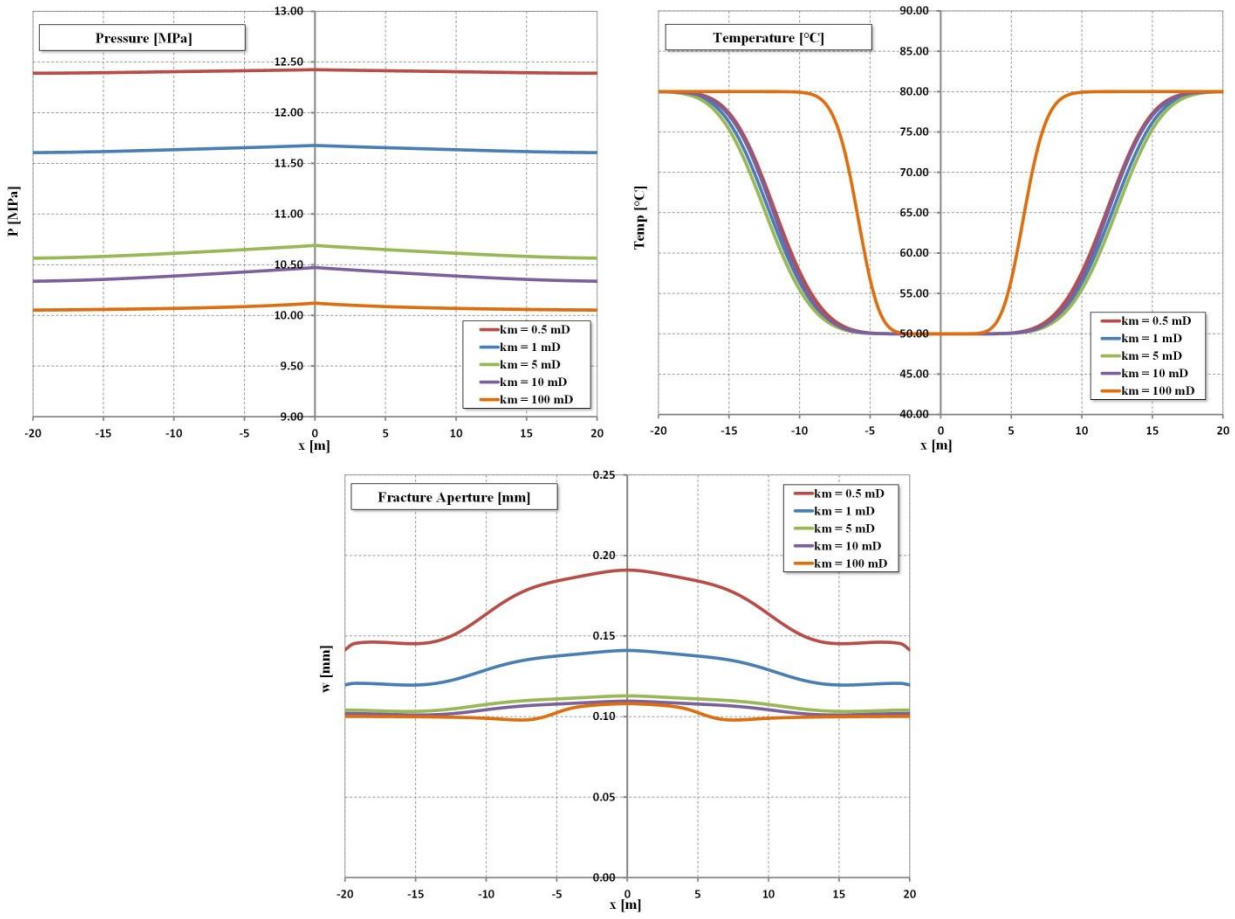

Figure 6.30. Fracture pressure, temperature, and aperture after 10 hours of injection for different matrix permeability.

6.5.6 Thermal Conductivity

The thermal conductivity of the rock surrounding the fracture also affects the fracture's pressure, temperature and aperture. Based on Figure 6.31, an increase in thermal conductivity reduces the fracture pressure. This behavior is expected as increasing the rock's thermal conductivity cools down a larger area around the fracture and increases the fracture aperture and reduces the fracture aperture. It also increases the thermal front propagation slightly.

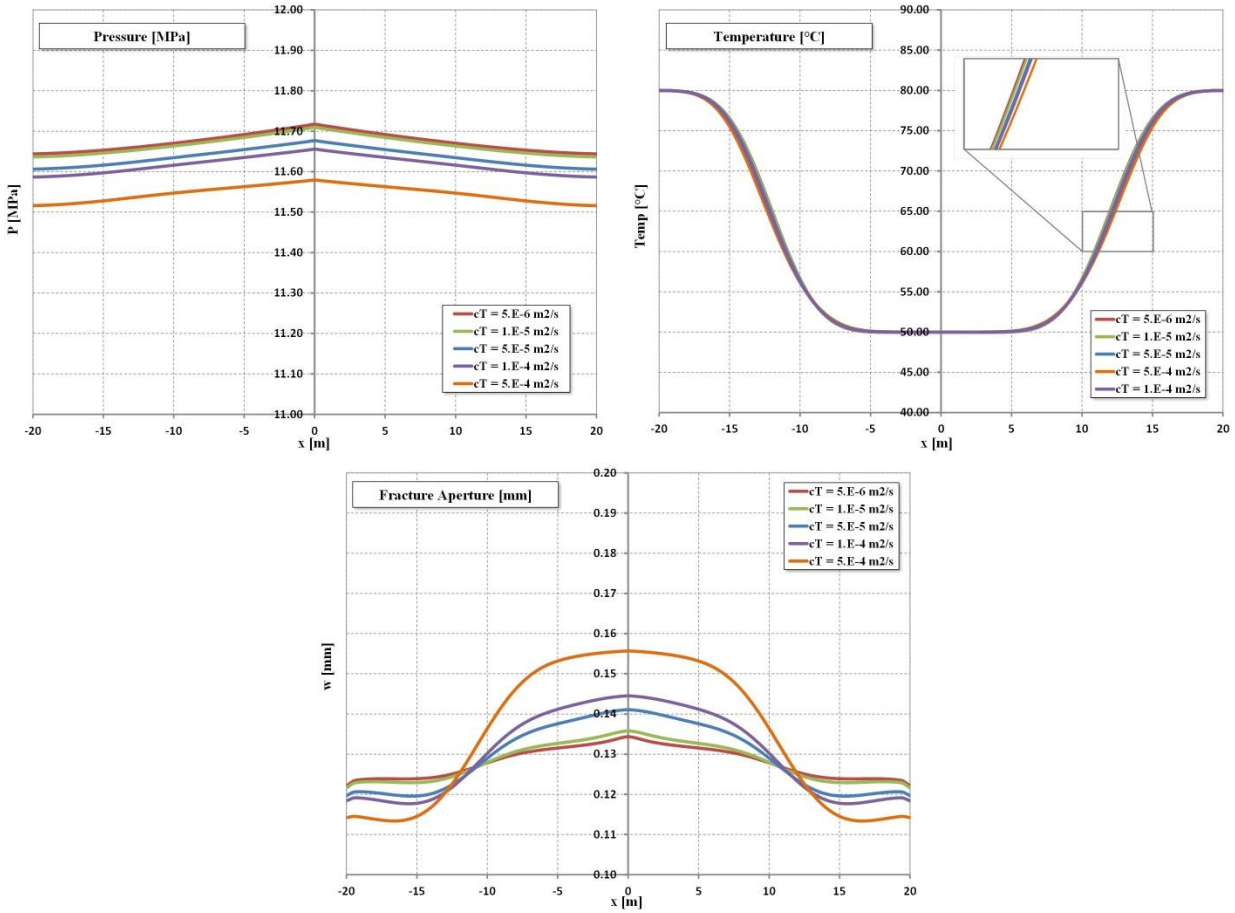

Figure 6.31. Fracture pressure, temperature, and aperture after 10 hours of injection for different rock's thermal conductivity.

6.5.7 Injection Temperature

In this comparison, the effect of injection temperature on the behavior of the fracture is considered. The fracture undergoes isothermal, hot and cold temperature injection with respect to the initial temperature in the fracture and rock (Figure 6.32). Cooling down the fracture increases the rock aperture as a result of rock shrinkage that induces a pressure reduction in the fracture. On the other hand, hot fluid injection reduces the fracture aperture in association with a pressure increase.

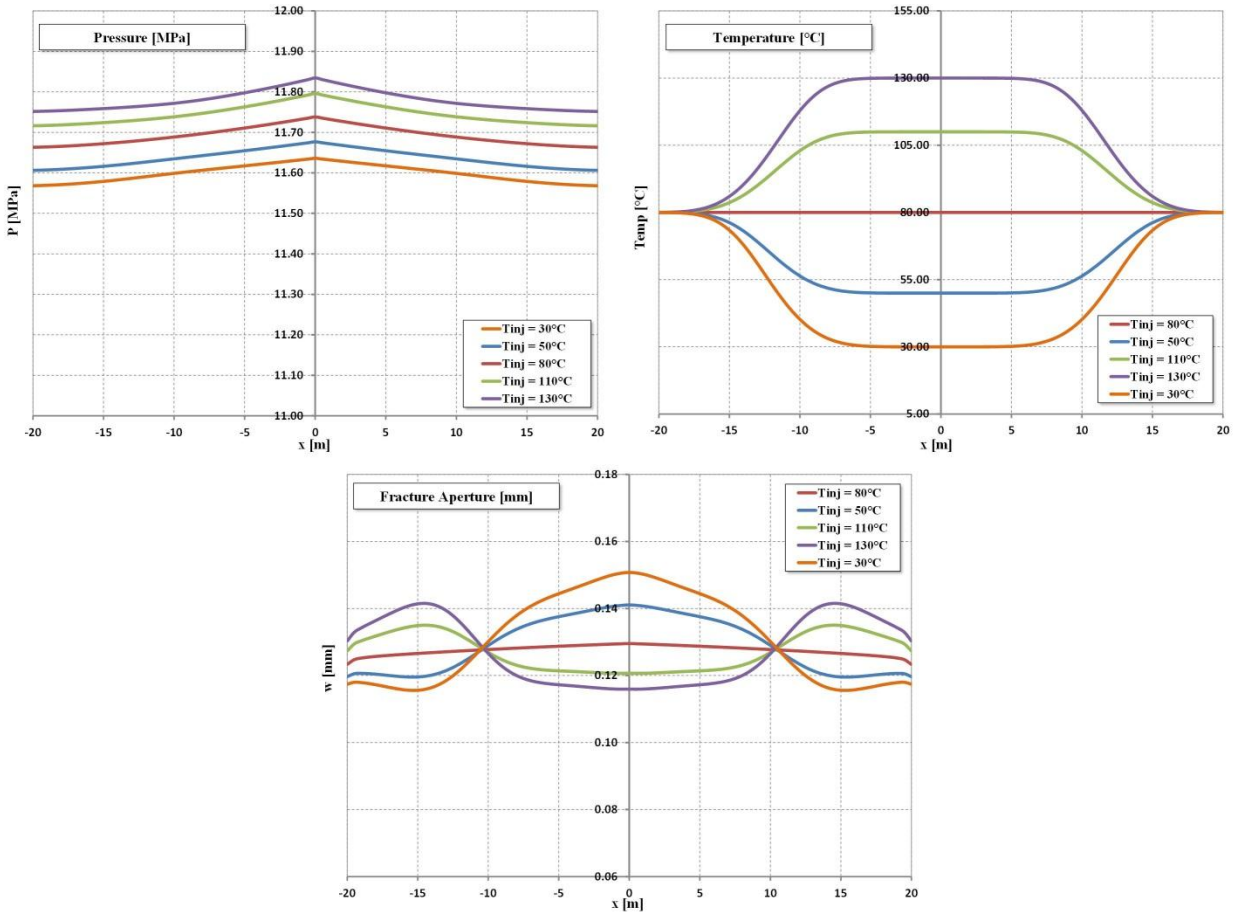

Figure 6.32. Fracture pressure, temperature, and aperture after 10 hours of injection for different injection's temperature.

The amount of fracture closure and opening for a constant cold and hot temperature is not constant as a Barton-Bandis model is adopted in this simulation, i.e. the fracture normal stiffness

The amount of fracture closure and opening for a constant cold and hot temperature is not constant as a Barton-Bandis model is adopted in this simulation, i.e. the fracture normal stiffness increases as the normal stress on the rock goes up and the fracture aperture reduces. This effect can be seen in Figure 6.32 for fracture aperture variation. Also, the stress transfer mechanism along the fracture is shown in this figure.

6.6 Chapter Summary

This chapter presented the response of fracture networks under different situations using the hybrid FDM-DDM model. The effect of in-situ stress on fluid propagation in the fracture network was studied and it was shown that fluid tends to open the fractures perpendicular to the minimum in-situ stress direction.

When a cold fluid is injected into the fracture network, the effect of cooling becomes dominant over time in the near field. This cooling is associated with stress reduction, especially in the horizontal and vertical direction for the horizontal and vertical fractures, respectively. This behavior is in a good agreement with the work of Perkins and Gonzalez (1985).

Moreover, the effect of shear dilation on fracture opening during the fluid extraction was presented. Under the fracture's yield condition, the fracture shear stiffness becomes zero and a shear displacement is induced in the fractures. This shear displacement is converted to a normal

displacement (fracture opening) using the dilation angle which is calculated based on the fracture surface properties.

At the end, a sensitivity analysis on some hydraulic, thermal and geomechanical properties was presented and the effect of all these properties on the fracture's pressure, temperature and aperture was compared.

Chapter 7
Conclusions and Recommendations

7.1 Conclusions

Geomechanics has become a major consideration for scientists and engineers in different fields such as oil and gas, geothermal, and nuclear waste disposal during the last two decades because of stress changes and displacements that can lead to induced seismicity, enhanced permeability, thermally induced fracturing, changes in fracture network properties, and so on. In the oil and gas industry, the coupled stress-flow-displacement considerations become significant in the simulation of stress-sensitive reservoirs such as poorly compacted rocks (e.g. North Sea chalk and high porosity oil sands) and naturally fractured reservoirs (e.g. fractured carbonates, shale gas and shale oil deposits).

The behavior of naturally fractured reservoirs (NFRs) during production processes is completely different than conventional reservoirs because of the dominant effects of fractures on fluid flux, with attendant issues of fracturefabric complexity and lithological heterogeneity. Most unconventional simulators cannot handle the geomechanical effects in the reservoir and surrounding rock mass properly as they usually consider pore compressibility as the only geomechanical parameter for the reservoir simulation, and may not even calculate the stresses arising from the reaction of the surrounding rock mass to the volume changes taking place in the reservoir. In this case the necessity of a coupled approach between the thermal, hydraulic and geomechanical mechanisms in order to realistically estimate the behavior of the medium to the injection is crucial.

To achieve a suitable level of coupling, a thermo-hydro-mechanical coupling approach was introduced in this study implementing the finite difference method and displacement discontinuity method together. The model is then verified with some analytical solutions that estimate the amount of fracture opening under elastic, poroelastic and thermoelastic conditions.

The key contribution of this work is to develop and enable a fully coupled THM model for some of the complexities of a fracture network, using the concepts listed below:

- A modified Barton-Bandis fracture stiffness model is applied in the model, especially for the case of fluid injection that is associated with normal stress reduction at fracture planes.
- The effect of shear dilation is introduced to the model and the results for a non-orthogonal fracture model clearly demonstrated the importance of this effect on fracture aperture, especially for the yielded fractures. A constant dilation angle was introduced to the model, but it is possible to use a non-constant value as a function of normal effective stress as well as fracture properties such as JCS and JRC.
- The finite difference discretization for fluid and heat flow was adjusted to accommodate the displacement discontinuity method as the dimensions of their solutions are different., i.e. for this study, the DDM solution is one dimensional where FDM solution is two dimensional.
- The results of the numerical solution demonstrated that in the case of an anisotropic in-situ stress condition, pressure and temperature tend to flow perpendicular to the minimum in-situ stress, as it is easier to open the fracture in this direction.

- Time dependency of THM effects were observed in this study. Due to the fact that the pressure front always moves faster than the heat front in fracture flow, the induced effect of each production process is also time dependent, i.e. hydraulic effects can be considered as the early time effect in fracture flow, whereas the thermal effect usually becomes dominant at later time.
- It was also shown that the effect of cooling suppresses the fluid injection effect in the near field especially in the case of displacements. Both horizontal and vertical effective stresses are reduced as a result of cold fluid injection; however, the reduction rate of horizontal and vertical stresses in the rocks adjacent to the horizontal and vertical fractures are more than in other places, which is in agreement with Perkins and Gonzalez (1985).

The results of this work clearly show the importance of rate, aspect ratio (i.e. geometry) and the coupling effects among fracture flow rate, aperture changes arising from coupled stress, pressure and temperature changes. When a problem becomes this complex (and this problem is relatively regular, homogeneous and isotropic in terms of fracture fabric and rock mass parameters), details of rock mass behavior may evade intuition and this means that the results of modeling must be scrutinized extremely carefully to make sure the results are reasonable. The effects of fracture dilation from cooling and pressure in an anisotropic stress field can easily lead to large concentrations of shear stress and different locations in the rock mass reaching the hydraulic fracture condition ($p_{inj} > \sigma_3 + F$, where F is a scale-dependent fracture toughness factor), or exceeding the slip condition in natural fractures, leading to shear, dilation, and permanent increases in permeability (self-propping) [Dusseault et al., 2011]. These results have a direct

bearing on hydraulic injection for induced fracturing and promoting of shearing, such as hydraulic fracturing of shale gas or shale oil reservoirs using liquid N_2 or CO_2, or even just the long-term injection of cooler flood water into a fractured carbonate to increase oil recovery. Furthermore, these results should be able to lead to a better understanding of induced seismicity in injection projects of all kinds, whether it is for waste water disposal, or for the extraction of geothermal energy.

7.2 Recommendations

Possible future work for the further study is as follows:

- It is possible to extend the current model into a three dimensional model that increases the number of degrees of freedom by one.
- Fracture propagation can be added to the current model using the implementation of a combination of quadratic and square root elements for displacement discontinuities and source strengths.
- The amount of energy release as a result of fracture propagation and fracture rupture can be calculated for induced seismicity investigation as a result of fluid injection/extraction from the fractures.
- Two-phase or three-phase fluid flow can be added to consider the behavior of fractured reservoirs accurately in the case of water flooding, CO_2 injection and so on.
- Fluid flow in the fracture network can be improved considering the fluid volume balance at fractures' intersection by estimating the pressure at nodal values.

- Due to the presence of intersecting fractures in the model, an equivalent porous medium considering the fracture network and the surrounding rock can be considered to be a better estimation for the fluid pressure in the matrix block.
- A non-constant porosity, fluid viscosity, fluid density and rock thermal conductivity can be added to the model to consider the dependency of these parameters to stress, pressure and temperature.
- The effect of secondary mineralization can be introduced to the fluid and heat conservation equations by considering a contact porosity that is defined as the open fracture surface area over the total fracture area

References

Aktan, T. and Farouq-Ali, S. (1978). Finite Element Analysis of Temperature and Thermal Stresses Induced by Hot Water Injection. Old SPE Journal. 18(6): 457-469.

Asgian, M. (1988). A Numerical Study of Fluid Flow in Deformable, Naturally Fractured Reservoirs. PhD thesis. University of Minnesota. Minneapolis, MN, United States.

Aziz, K. and Settari, A. (1979). Petroleum Reservoir Simulation. Elsevier, London.

Bandis, S.C., Lumsden, A.C. and Barton, N.R. (1983). Fundamentals of Rock Joint Deformation. International Journal of Rock Mechanics and Mining Sciences & Geomechanics Abstracts. 20 (6): 249-268.

Barton, N., Bandis, S. and Bakhtar, K. (1985). Strength, Deformation and Conductivity Coupling of Rock Joints. International Journal of Rock Mechanics and Mining Sciences & Geomechanics Abstracts. 22 (3): 121-140

Bear, J. (1988). Dynamics of Fluids in Porous Media. Environmental Science Series. American Elsevier Pub. Co., New York.

Bejan, A. and Kraus, A.D. (2003). Heat Transfer Handbook. Wiley, New Jersey, USA.

Berchenko I. (1998). Thermal Loading of Saturated Rock Mass: Field Experiment and Modeling using Thermoporoelastic Singular Solutions. PhD thesis, University of Minnesota. Minneapolis, MN, United States.

Biot, M. (1941). General Theory of Three Dimentional Consolidation. Journal of Applied Physics. 12(2): 155-164.

Booker, J.R. and Savvidou, C. (1985). Consolidation around a Point Heat Source. International Journal for Numerical and Analytical Methods in Geomechanics. 9(2): 173-184.

Buczkowski, R. and Kleiber, M. (1997). Elasto-plastic Interface Model for 3D Frictional Orthotropic Contact Problems. International Journal for Numerical Methods in Engineering. 40: 599–619.

Caillabet, Y., Fabrie, P., Landerau, P., Noetinger, B. and Quintard, M. (2000). Implementation of a Finite-Volume Method for the Determination of Effective parameters in fissured porous media. Numerical Methods of Partial Differential Equations. 16: 237–263.

Carvalho, J.L. 1990. Poroelastic Effects and Influence of Material Interfaces on Hydraulic Fracturing. PhD thesis, University of Toronto, Toronto, ON, Canada.

Castelletto N. (2010). Thermoporoelastic Modelling of Deep Aquifer Injection and Pumping by Mixed Finite Elements and Finite Volumes. PhD thesis, University of Padova. Padova, Italy.

Coussy, O. (2004). Poromechanics. Wiley, London.

Crouch, S.L. (1976). Solution of Plane Elasticity Problems by the Displacement Discontinuity Method. International Journal for Numerical Methods in Engineering. 10(2): 301-343.

Crouch, S.L. and Starfield, A.M. (1983). Boundary Element Methods in Solid Mechanics. Allen and Unwin, London.

Cundall, P.A., & Hart, R.D. (1989). Numerical Modelling of Discontinua. 1st U.S. Conference on Discrete Element Methods. Golden, Colorado. 1-17.

Davies, J.P. and Davies, D.K. (2001). Stress-dependent Permeability: Characterization and Modeling. SPE Journal. 6(2): 224-235.

Desai, C.S., Zamman, M.M., Lightner, J.G. and Siriwardane, H.J. (1984). Thin Layer Element for Interfaces and Joints. International Journal for Numerical and Analytical Methods in Geomechanics. 8: 19-43.

Detournay E. (1980). Hydraulic Conductivity of Closed Rock Fracture: An Experimental and Analytical Study. 13th Canadian Rock Mechanics Symposium. CIM Special Volume 22: 168-173.

Detournay E. and Cheng A.H.-D. (1991). Plane Strain Analysis of a Stationary Hydraulic Fracture in a Poroelastic Medium. International Journal of Solids and Structures. 27(13): 1645-1662.

Detournay E. and Cheng A.H.-D. (1993). Fundamentals of Poroelasticity. in J.A. Hudson (ed) Comprehensive Rock Engineering: Principles, Practices, and Projects. 2: 113-171.

Dusseault, M.B. (2008). Coupling Geomechanics and Transport in Petroleum Engineering. Keynote paper, Proceedings of the 1st Southern Hemisphere International Rock Mechanics Symposium. Perth, Western Australia.

Dusseault, M. and Collins, P. (2008). Geomechanics Effects in Thermal Processes for Heavy Oil Exploitation. Canadian Society of Exploration Geophysicists Recorder. 20-23.

Elsworth, D. (1984). Laminar and Turbulent Flow in Rock Fissures and Fissure Networks. PhD thesis, University of California. Berkeley, CA, United States.

Geertsma, J. (1957). The Effect of Pressure Decline on Volumetric Changes of Porous Rocks. Trans. AIME. 210(1): 331-340.

Geertsma, J. (1966). Problems of Rock Mechanics in Petroleum Production Engineering. 1st Congress on International Society of Rock Mechanics. Lisbon, Portugal. 585-594.

Ghaboussi, J. and Wilson, E.L. (1973). Flow of Compressible Fluid in Porous Elastic Media. International Journal for Numerical Methods in Engineering. 5(3): 419-442.

Ghassemi, A. and Zhang Q. (2004). A Transient Fictitious Stress Boundary Element Method for Porothermoelastic Media. Engineering Analysis with Boundary Elements. 28: 1363-1373.

Ghassemi, A., Tarasovs, S. and Cheng, A.H.-D. (2005). Integral Equation Solution of Heat Extraction-induced Thermal Stress in Enhanced Geothermal Reservoirs. International Journal for Numerical and Analytical Methods in Geomechanics. 29: 829-844.

Goodman, R.E., Taylor, R.L. and Brekke, T.L. (1968). A Model for the Mechanics of Jointed Rock. Journal of the Soil Mechanics and Foundations Division, ASCE 94. SM3: 637–659.

Goodman, R.E. (1974). The Mechanical Properties of Joints. 3rd Congress of International Society of Rock Mechanics. Denver, Colorado. 127-140.

Goodman, R.E. (1976). Methods of Geological Engineering in Discontinuous Rock. New York. 472 p.

Goodman, R.E. and Shi, G.H. (1985). Block Theory and Its Application to Rock Engineering. Prentice Hall, New Jersey.

Granet, S., Fabrie, P., Lemonnier, P. and Quintard, M. (2001). A Two-Phase Flow Simulation of a Fractured Reservoir Using a New Fissure Element Method. Journal of Petroleum Science and Engineering. 32 (1): 35–52.

Gross, J. and Seelig, T. (2006). Fracture Mechanics with an Introduction to Micromechanics. Springer, the Netherlands.

Hahn, J.K. (1988). Realistic Animation of Rigid Bodies. Computer Graphics. 24 (4): 299-308.

Haimson B. (1968). Hydraulic Fracturing in Porous and Nonporous Rock and its Potential for Determining in-situ Stresses at Great Depth. PhD thesis, University of Minnesota. Minneapolis, MN, United States.

Hayashi K, Willis-Richards, J., Hopkirk, R.J. and Niibori, Y. (1999). Numerical Models of HDR Geothermal Reservoirs - A Review of Current Thinking and Progress. Geothermics. 28:507–518.

Hocking, G., Mustoe, G.G.W. and Williams, J.R. (1985). CICE Discrete Element Code - Theoretical Manual. Applied Mechanics Inc. Lakewood, Colorado.

Hojka, K., Dusseault, M.B. and Bogobowicz, A. (1993). Analytical Solutions for Transient Thermoelastic Stress Fields around a Borehole during Fluid Injection into Permeable Media. Journal of Canadian Petroleum Technology. 32(4): 49-57.

Hubbert, M.K. and Willis, D.G. (1957). Mechanics of hydraulic fracturing. Transactions of the American Institute of Mining Engineers. 210: 153-168.

Iwai, K. (1976). Fundamental Studies of Fluid Flow through a Single Fracture. PhD thesis, University of California. Berkeley, CA, United States.

Jalali, M.R. and Dusseault. M.B. (2011) .Coupling Geomechanics and Transport in Petroleum Engineering. 4th Iranian Rock Mechanics Conference. Tehran, Iran.

Jing, L. (2003). A Review of Techniques, Advances and Outstanding Issues in Numerical Modelling for Rock Mechanics and Rock Engineering. International Journal of Rock Mechanics & Mining Sciences. 40: 283-353.

Knaap, W. van der (1959). Nonlinear Behavior of Elastic Porous Media. Petroleum Transactions AIME. 216: 179-187.

Kulhaway, F.H. (1975). Stress-deformation Properties of Rock and Rock Discontinuities. Engineering Geology. 8: 327-350.

Lanru, J. and Xiating, F. (2003). Numerical Modeling for Coupled Thermo-Hydro-Mechanical and Chemical Processes (THMC) of Geological Media – International and Chinese Experiences. Chinese Journal of Rock Mechanics and Engineering. 22(10): 1704-1715.

Louis, C. (1969). A Study of Groundwater Flow in Jointed Rock and its Influence on the Stability of Rock Masses. Rock Mechanics Research Report No. 10. Imperial College, University of London. London, UK.

MacGillivray, D., Davidson, B. and Dusseault, M.B. (1996). One-dimensional Thermal Conductivity Measurements in Quartz-Illite and Smectitic Shales. Eurock 96, ISRM International Symposium, Turin, Italy. 107-113.

McTigue D.F. (1986). Thermoelastic Response of Fluid-saturated Porous Rock. Journal of Geophysical Research. 91(B9): 9533–9542.

Narr, W., Schechter, D.W. and Thompson, L.B. (2006). Naturally Fractured Reservoir Characterization. Textbook Series, SPE, Richardson, Texas.

Nelson, R.A. (2001). Geologic Analysis of Naturally Fractured Reservoirs. 2nd ed. Gulf Professional Publishing.

Nur, A. and Byerlee, J.D. (1971). An Exact Effective Stress Law for Elastic Deformation of Rock with Fluid. Journal of Geophysical Research. 76(26): 6414-6418.

Olesiak, Z. and Sneddon, I.N. (1959). The Distribution of Thermal Stress in an Infinite Elastic Solid Containing a Penny-shaped Crack. Archives for Rational Mechanics. 238 pages.

Palciauskas V.V. and Domenico P.A. (1982). Characterization of drained and undrained response of thermally loaded repository rocks. Water Resources Research. 18(2): 281–290.

Perkins, T.K. and Gonzalez, J.A. (1985). The Effect of Thermoelastic Stresses on Injection Well Fracturing. SPE Journal. 25(1): 78-88.

Rahman, M.K., Hossain, M.M. and Rahman S.S. (2002). A Shear-dilation Based Model for Evaluation of Hydraulically Stimulated Naturally Fractured Reservoirs. International Journal for Numerical and Analytical Methods in Geomechanics. 26(5): 469-497.

Rice, J.R. and Cleary, M.P. (1976). Some Basic Stress-diffusion Solutions for Fluid Saturated Elastic Porous Media with Compressible Constituents. Reviews of Geophysics and Space Physics. 14(2): 227-241.

Rutqvist J. (1995). A Method to Determine Stress-Transmissivity Relationship of Joints from Hydraulic Field Testing. 8th ISRM Congress. Tokyo, Japan.

Salamon, M.D.G. (1963). Elastic Analysis of Displacements and Stresses Induced by the Mining of Seam or Reef Deposits. Journal of the South African Institute of Mining and Metallurgy. 64: 128-149.

Salamon, M.D.G. (1968). Two-dimensional Treatment of Problems Arising from Mining Tabular Deposits in Isotropic or Transversely Isotropic Ground. International Journal of Rock Mechanics and Mining Sciences & Geomechanics Abstracts. 5(2): 159-185.

Schiffman, R.L. (1971). A Thermoelastic Theory of Consolidation. Environmental and Geophysical Heat Transfer, ASCE. 4: 78-84.

Settari, A. and Walters, D. (2001). Advances in Coupled Geomechanical and Reservoir Modeling with Applications to Reservoir Compaction. SPE Journal. 6(3): 334-342.

Settari, A., Walters, D. and Behie, G. (2001). Use of coupled reservoir and geomechanical modelling for integrated reservoir analysis and management. Journal of Canadian Petroleum Technology. 40(12): 55-61.

Shi, G.H. (1989). Discontinuous Deformation Analysis - A New Numerical Model for the Statics and Dynamics of Block Systems. Lawrence Berkeley Laboratory. Report to DOE OWTD, Contract AC03-76SF0098.

Skempton, A.W. (1954). The Pore Pressure Coefficients A and B. Geotechnique. 4: 143-147.

Sneddon, I.N. (1951). Fourier Transforms. McGraw-Hill, New York.

Terzaghi, K. (1925). Principles of Soil Mechanics. Engineering News Record. 95(8).

Tao, Q., Ghassemi, A. and Ehlig-Economides, C.A. (2011). A Fully Coupled Method to Model Fracture Permeability Change in Naturally Fractured Reservoirs. International Journal of Rock Mechanics & Mining Sciences. 48(2): 259-268.

Tran, D., Settari, A. and Nghiem, L. (2002). New Iterative Coupling between a Reservoir Simulator and a Geomechanics Module. SPE Journal. 9(3): 362-369.

Universal Distinct Element Code (UDEC) Manual, ITASCA Consulting Group, Inc. 2006, www.itascacg.com.

Vandamme, L., Detournay, E. and Cheng A.H.-D. (1989). A Two-dimensional Poroelastic Displacement Discontinuity Method for Hydraulic Fracture Simulation. International Journal for Numerical and Analytical Methods in Geomechanics. 13: 215-224.

Wang, Y. and Dusseault, M.B. (2003). A Coupled Conductive-Convective Thermo-poroelastic Solution and Implications for Wellbore Stability. Journal of Petroleum Science and Engineering. 38(3): 187-198.

Walton, O.R. (1980). Particle Dynamic Modeling of Geological Materials. Lawrence Livermore National Laboratory. Report UCRL-52915.

Warburton, P.M. (1981). Vector Stability Analysis of an Arbitrary Polyhedral Rock Block with any Number of Free Faces. International Journal of Rock Mechanics and Mining Science & Geomechanics Abstracts. 18: 415-427.

Witherspoon, P.A., Wang, J.S.Y., Iwai, K. and Gale, J.E. (1980). Validity of Cubic Law for Fluid Flow in a Deformable Rock Fracture. Water Resources Research. 16(6): 1016-1024.

Witherspoon, P.A., Tsang, Y.W., Long, J.C.S. and Noorishad, J. (1981). New Approaches to Problems of Fluid Flow in Fractured Rock Masses. 22nd U.S. Symposium on Rock Mechanics (USRMS). Cambridge, MA, United State.

Zhang, Q. (2004). A Boundary Element Method for Thermo-poroelasticity with Applications in Rock Mechanics. MSc thesis, University of North Dakota. Grand Forks, ND, United States.

Zienkiewicz, O.C., Best, B., Dullage, C. and Stagg, K. (1970). Analysis of Nonlinear Problems in Rock Mechanics with Particular Reference to Jointed Rock Systems. 2nd International Congress on Rock Mechanics. Belgrade, Serbia.

Appendix A

Fundamental Solution for a Unit Continuous Displacement Discontinuity in an Elastic Medium

Considering a fracture segment with a length of *2a* elongated in the *x*-direction (Figure A-1), the fundamental solutions for stress and displacement in the influenced point (*x*,*y*) can be written as a function of distance from influencing point (*x*′,0) and geomechanical properties of rocks as below [Crouch and Starfield, 1983]:

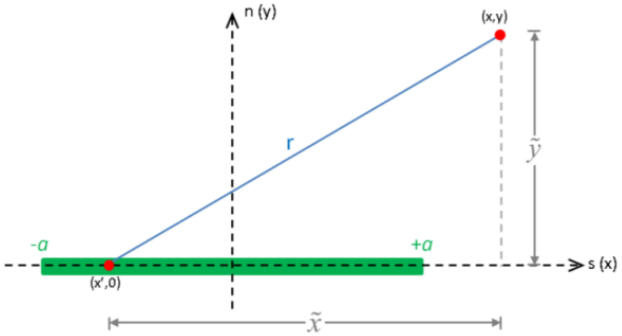

Figure A-1. Schematic representation of a single fracture for displacement discontinuity formulations

$$r^2 = \tilde{x}^2 + \tilde{y}^2 = (x - x')^2 + y^2 \qquad -a \le x' \le +a \tag{A-1}$$

<u>Induced displacement for normal displacement discontinuity</u>

$$u_x^{dn} = -\frac{1}{4\pi(1-\nu)}\left[(1-2\nu)\ln|r| + \frac{\tilde{y}^2}{r^2}\right]\Bigg|_{x'=-a}^{x'=+a} \tag{A-2}$$

$$u_y^{dn} = -\frac{1}{4\pi(1-\nu)}\left[-2(1-\nu)\arctan\left(\frac{\tilde{x}}{\tilde{y}}\right) - \frac{\tilde{x}\tilde{y}}{r^2}\right]\Bigg|_{x'=-a}^{x'=+a} \tag{A-3}$$

Induced stress for normal displacement discontinuity

$$\sigma_{xx}^{dn} = -\frac{G}{2\pi(1-\nu)}\left[\frac{\tilde{x}^3 - \tilde{x}\tilde{y}^2}{r^4}\right]_{x'=-a}^{x'=+a} \tag{A-4}$$

$$\sigma_{yy}^{dn} = -\frac{G}{2\pi(1-\nu)}\left[\frac{\tilde{x}^3 + 3\tilde{x}\tilde{y}^2}{r^4}\right]_{x'=-a}^{x'=+a} \tag{A-5}$$

$$\sigma_{xy}^{dn} = -\frac{G}{2\pi(1-\nu)}\left[\frac{\tilde{x}^2\tilde{y} - \tilde{y}^3}{r^4}\right]_{x'=-a}^{x'=+a} \tag{A-6}$$

Induced displacement for shear displacement discontinuity

$$u_x^{ds} = -\frac{1}{4\pi(1-\nu)}\left[-2(1-\nu)\arctan\left(\frac{\tilde{x}}{\tilde{y}}\right) + \frac{\tilde{x}\tilde{y}}{r^2}\right]_{x'=-a}^{x'=+a} \tag{A-7}$$

$$u_y^{dn} = -\frac{1}{4\pi(1-\nu)}\left[-(1-2\nu)\ln|r| + \frac{\tilde{y}^2}{r^2}\right]_{x'=-a}^{x'=+a} \tag{A-8}$$

Induced stress for shear displacement discontinuity

$$\sigma_{xx}^{ds} = -\frac{G}{2\pi(1-\nu)}\left[-\frac{3\tilde{x}^2\tilde{y} + \tilde{y}^3}{r^4}\right]_{x'=-a}^{x'=+a} \tag{A-9}$$

$$\sigma_{yy}^{ds} = -\frac{G}{2\pi(1-\nu)}\left[\frac{\tilde{x}^2\tilde{y} - \tilde{y}^3}{r^4}\right]_{x'=-a}^{x'=+a} \tag{A-10}$$

$$\sigma_{xy}^{ds} = -\frac{G}{2\pi(1-\nu)}\left[\frac{\tilde{x}^3 - \tilde{x}\tilde{y}^2}{r^4}\right]_{x'=-a}^{x'=+a} \tag{A-11}$$

Appendix B

Fundamental Solution for a Unit Continuous Displacement Discontinuity in a Porous Medium

The fundamental solutions for pressure, stress and displacement in the influenced point (x,y) can be written as a function of distance from influencing point (x',0) and geomechanical and hydraulic properties of rocks as below [Vandamme *et al.*, 1989; Carvalho, 1990]:

$$r^2 = \tilde{x}^2 + \tilde{y}^2 = (x - x')^2 + y^2 \quad -a \le x' \le +a$$

$$\xi^2 = \frac{r^2}{4c^{\mathrm{f}}t} \tag{B-1}$$

$$\mathrm{E}_1(x) = \int_x^{\infty} \frac{e^{-u}}{u}\, du \tag{B-2}$$

Induced pore pressure for normal displacement discontinuity

$$p^{\mathrm{dn}} = -\frac{G(\nu_{\mathrm{u}} - \nu)}{2\pi\alpha(1-2\nu)(1-\nu_{\mathrm{u}})}\left[-\frac{2\tilde{x}}{r^2}\left(1 - e^{-\xi^2}\right)\right]\Bigg|_{x'=-a}^{x'=+a} \tag{B-3}$$

Induced displacement for normal displacement discontinuity

$$u_{\mathrm{x}}^{\mathrm{dn}} = -\frac{1}{4\pi(1-\nu)}\left\{(1-2\nu)\ln|r| - \left(\frac{\nu_{\mathrm{u}} - \nu}{1-\nu_{\mathrm{u}}}\right)\left[\frac{\ln r^2 + \mathrm{E}_1(\xi^2)}{2} - \frac{1 - e^{-\xi^2}}{2\xi^2}\right]\right.$$
$$\left. + \frac{\tilde{y}^2}{r^2}\left[1 + \left(\frac{\nu_{\mathrm{u}} - \nu}{1-\nu_{\mathrm{u}}}\right)\left[1 - \frac{1 - e^{-\xi^2}}{\xi^2}\right]\right]\right\}\Bigg|_{x'=-a}^{x'=+a} \tag{B-4}$$

$$u_{\mathrm{y}}^{\mathrm{dn}} = -\frac{1}{4\pi(1-\nu)}\left\{-2(1-\nu)\arctan\left(\frac{\tilde{x}}{\tilde{y}}\right) - \frac{\tilde{x}\tilde{y}}{r^2}\left[1+\left(\frac{\nu_{\mathrm{u}}-\nu}{1-\nu_{\mathrm{u}}}\right)\left[1-\frac{1-e^{-\xi^2}}{\xi^2}\right]\right]\right\}\Bigg|_{x'=-a}^{x'=+a} \tag{B-5}$$

Induced stress for normal displacement discontinuity

$$\sigma_{\mathrm{xx}}^{\mathrm{dn}} = -\frac{G}{2\pi(1-\nu)}\left\{\frac{\tilde{x}^3-\tilde{x}\tilde{y}^2}{r^4}+\left(\frac{\nu_{\mathrm{u}}-\nu}{1-\nu_{\mathrm{u}}}\right)\left[\frac{\tilde{x}^3-\tilde{x}\tilde{y}^2}{r^4}+\frac{3\tilde{x}\tilde{y}^2-\tilde{x}^3}{r^4}\frac{1-e^{-\xi^2}}{\xi^2}-\frac{2\tilde{x}\tilde{y}^2}{r^4}e^{-\xi^2}\right]\right\}\Bigg|_{x'=-a}^{x'=+a} \tag{B-6}$$

$$\sigma_{\mathrm{yy}}^{\mathrm{dn}} = -\frac{G}{2\pi(1-\nu)}\left\{\frac{\tilde{x}^3+3\tilde{x}\tilde{y}^2}{r^4}+\left(\frac{\nu_{\mathrm{u}}-\nu}{1-\nu_{\mathrm{u}}}\right)\left[\frac{\tilde{x}^3+3\tilde{x}\tilde{y}^2}{r^4}+\frac{\tilde{x}^3-3\tilde{x}\tilde{y}^2}{r^4}\frac{1-e^{-\xi^2}}{\xi^2}-\frac{2\tilde{x}^3}{r^4}e^{-\xi^2}\right]\right\}\Bigg|_{x'=-a}^{x'=+a} \tag{B-7}$$

$$\sigma_{\mathrm{xy}}^{\mathrm{dn}} = -\frac{G}{2\pi(1-\nu)}\left\{\frac{\tilde{x}^2\tilde{y}-\tilde{y}^3}{r^4}+\left(\frac{\nu_{\mathrm{u}}-\nu}{1-\nu_{\mathrm{u}}}\right)\left[\frac{\tilde{x}^2\tilde{y}-\tilde{y}^3}{r^4}-\frac{3\tilde{x}^2\tilde{y}-\tilde{y}^3}{r^4}\frac{1-e^{-\xi^2}}{\xi^2}+\frac{2\tilde{x}^2\tilde{y}}{r^4}e^{-\xi^2}\right]\right\}\Bigg|_{x'=-a}^{x'=+a} \tag{B-8}$$

Induced pore pressure for shear displacement discontinuity

$$p^{\mathrm{ds}} = -\frac{G(\nu_{\mathrm{u}}-\nu)}{2\pi\alpha(1-2\nu)(1-\nu_{\mathrm{u}})}\left[\frac{2\tilde{y}}{r^2}\left(1-e^{-\xi^2}\right)\right]\Bigg|_{x'=-a}^{x'=+a} \tag{B-9}$$

Induced displacement for shear displacement discontinuity

$$u_{\mathrm{x}}^{\mathrm{ds}} = -\frac{1}{4\pi(1-\nu)}\left\{-2(1-\nu)\arctan\left(\frac{\tilde{x}}{\tilde{y}}\right)+\frac{\tilde{x}\tilde{y}}{r^2}\left[1+\left(\frac{\nu_{\mathrm{u}}-\nu}{1-\nu_{\mathrm{u}}}\right)\left[1-\frac{1-e^{\xi^2}}{\xi^2}\right]\right]\right\}\Bigg|_{x'=-a}^{x'=+a} \tag{B-10}$$

$$u_{\mathrm{y}}^{\mathrm{dn}} = -\frac{1}{4\pi(1-\nu)}\left\{-(1-2\nu)\ln|r|+\left(\frac{\nu_{\mathrm{u}}-\nu}{1-\nu_{\mathrm{u}}}\right)\left[\frac{\ln r^2+\mathrm{E}_1(\xi^2)}{2}+\frac{1-e^{\xi^2}}{2\xi^2}\right]\right.$$
$$\left.+\frac{\tilde{y}^2}{r^2}\left[1+\left(\frac{\nu_{\mathrm{u}}-\nu}{1-\nu_{\mathrm{u}}}\right)\left[1-\frac{1-e^{\xi^2}}{\xi^2}\right]\right]\right\}\Bigg|_{x'=-a}^{x'=+a} \tag{B-11}$$

Induced stress for shear displacement discontinuity

$$\sigma_{xx}^{ds} = -\frac{G}{2\pi(1-\nu)}\left\{\frac{-3\tilde{x}^2\tilde{y}-\tilde{y}^3}{r^4}+\left(\frac{\nu_u-\nu}{1-\nu_u}\right)\left[\frac{-3\tilde{x}^2\tilde{y}-\tilde{y}^3}{r^4}+\frac{3\tilde{x}^2\tilde{y}-\tilde{y}^3}{r^4}\frac{1-e^{-\xi^2}}{\xi^2}+\frac{2\tilde{y}^3}{r^4}e^{-\xi^2}\right]\right\}\Bigg|_{x'=-a}^{x'=+a} \tag{B-12}$$

$$\sigma_{yy}^{ds} = -\frac{G}{2\pi(1-\nu)}\left\{\frac{\tilde{x}^2\tilde{y}-\tilde{y}^3}{r^4}+\left(\frac{\nu_u-\nu}{1-\nu_u}\right)\left[\frac{\tilde{x}^2\tilde{y}-\tilde{y}^3}{r^4}-\frac{3\tilde{x}^2\tilde{y}-\tilde{y}^3}{r^4}\frac{1-e^{-\xi^2}}{\xi^2}+\frac{2\tilde{x}^2\tilde{y}}{r^4}e^{-\xi^2}\right]\right\}\Bigg|_{x'=-a}^{x'=+a} \tag{B-13}$$

$$\sigma_{xy}^{ds} = -\frac{G}{2\pi(1-\nu)}\left\{\frac{\tilde{x}^3-\tilde{x}\tilde{y}^2}{r^4}+\left(\frac{\nu_u-\nu}{1-\nu_u}\right)\left[\frac{\tilde{x}^3-\tilde{x}\tilde{y}^2}{r^4}+\frac{3\tilde{x}\tilde{y}^2-\tilde{x}^3}{r^4}\frac{1-e^{-\xi^2}}{\xi^2}-\frac{2\tilde{x}\tilde{y}^2}{r^4}e^{-\xi^2}\right]\right\}\Bigg|_{x'=-a}^{x'=+a} \tag{B-14}$$

where

Hydraulic diffusivity [L^2T^{-1}]: $$c^f = \frac{\kappa_f}{S} = \frac{k}{\mu}\frac{M(1-\nu)(1-2\nu_u)}{(1-\nu_u)(1-2\nu)} \tag{B-15}$$

Biot's modulus [$ML^{-1}T^{-2}$]: $$M = \frac{2G(\nu_u-\nu)}{\alpha^2(1-2\nu)(1-2\nu_u)} \tag{B-16}$$

Storage coefficient [$M^{-1}LT^2$]: $$S = \frac{(1-\nu_u)(1-2\nu)}{M(1-\nu)(1-2\nu_u)} \tag{B-17}$$

Biot's coefficient [-]: $$\alpha = \frac{3(\nu_u-\nu)}{B(1-2\nu)(1+\nu_u)} \tag{B-18}$$

Appendix C

Fundamental Solution for a Unit Continuous Fluid Source in a Porous Medium

The fundamental solutions for pressure, stress and displacement in the influenced point (x,y) can be written as a function of distance from influencing point (x',0) and geomechanical and hydraulic properties of rocks as below [Vandamme *et al.*, 1989; Carvalho, 1990]:

$$r^2 = \tilde{x}^2 + \tilde{y}^2 = (x - x')^2 + y^2 \quad -a \le x' \le +a$$

$$\xi^2 = \frac{r^2}{4c^{\mathrm{f}}t}$$

$$\mathrm{E}_1(x) = \int_x^{\infty} \frac{e^{-u}}{u} du$$

Induced pore pressure for fluid source

$$p^{\mathrm{qf}} = \frac{\mu}{4\pi k} \int_{-a}^{+a} \mathrm{E}_1(\xi^2) dx' \tag{C-1}$$

Induced displacement for fluid source

$$u_{\mathrm{x}}^{\mathrm{qf}} = \frac{\alpha\mu(1-2\nu)}{16\pi kG(1-\nu)} \left[2c^{\mathrm{f}} t e^{-\xi^2} - \frac{r^2}{2} \mathrm{E}_1(\xi^2) - 2c^{\mathrm{f}} t \left(\ln r^2 + \mathrm{E}_1(\xi^2) \right) \right]_{x'=-a}^{x'=+a} \tag{C-2}$$

$$u_{\mathrm{y}}^{\mathrm{qf}} = \frac{\alpha\mu(1-2\nu)}{16\pi kG(1-\nu)} \left\{ \left[-4c^{\mathrm{f}} t \arctan\left(\frac{\tilde{x}}{\tilde{y}} \right) \right]_{x'=-a}^{x'=+a} + \tilde{y} \int_{-a}^{+a} \mathrm{E}_1(\xi^2) dx' - 4c^{\mathrm{f}} t \tilde{y} \int_{-a}^{+a} \frac{e^{-\xi^2}}{r^2} dx' \right\} \tag{C-3}$$

Induced stress for fluid source

$$\sigma_{xx}^{qf} = \frac{\alpha\mu(1-2\nu)}{8\pi k(1-\nu)}\left\{\left[-\tilde{x}\left(\frac{1}{\xi^2}-\frac{e^{-\xi^2}}{\xi^2}+\mathrm{E}_1\left(\xi^2\right)\right)\right]\Bigg|_{x'=-a}^{x'=+a} - 2\int_{-a}^{+a}\mathrm{E}_1\left(\xi^2\right)dx'\right\} \tag{C-4}$$

$$\sigma_{yy}^{qf} = \frac{\alpha k(1-2\nu)}{8\pi\mu(1-\nu)}\left[\tilde{x}\left(\frac{1}{\xi^2}-\frac{e^{-\xi^2}}{\xi^2}+\mathrm{E}_1\left(\xi^2\right)\right)\right]\Bigg|_{x'=-a}^{x'=+a} \tag{C-5}$$

$$\sigma_{xy}^{qf} = \frac{\alpha\mu(1-2\nu)}{8\pi k(1-\nu)}\left[-\tilde{y}\left(\frac{1}{\xi^2}-\frac{e^{-\xi^2}}{\xi^2}+\mathrm{E}_1\left(\xi^2\right)\right)\right]\Bigg|_{x'=-a}^{x'=+a} \tag{C-6}$$

Appendix D

Fundamental Solution for a Unit Heat Source in a Porous Medium

The fundamental solutions for temperature, pressure, stress and displacement in the influenced point (x,y) can be written as a function of distance from influencing point (x',0) and thermal, geomechanical and hydraulic properties of rocks as below [Berchenko, 1998; Zhang, 2004]:

$$r^2 = \tilde{x}^2 + \tilde{y}^2 = (x - x')^2 + y^2 \quad -a \le x' \le +a$$

$$\xi^2 = \frac{r^2}{4c^{\mathrm{f}}t} \qquad \text{and} \qquad \zeta^2 = \frac{r^2}{4c^{\mathrm{T}}t} \tag{D-1}$$

$$\mathrm{E}_1(x) = \int_x^{\infty} \frac{e^{-u}}{u}\, du$$

Induced temperature for heat source

$$T^{\mathrm{qh}} = \frac{1}{4\pi k_{\mathrm{T}}} \int_{-a}^{+a} \mathrm{E}_1(\zeta^2)\, dx' \tag{D-2}$$

Induced pore pressure for heat source

$$p^{dh} = \frac{c'}{4\pi k_{\mathrm{T}}} \left[\int_{-a}^{+a} e^{-\zeta^2}\, dx' \right] \qquad \text{for } c^{\mathrm{f}} = c^{\mathrm{T}} \tag{D-3}$$

$$p^{dh} = \frac{c'}{4\pi k_{\mathrm{T}}(1-\omega^2)} \left[\int_{-a}^{+a} \mathrm{E}_1(\zeta^2)\, dx' - \int_{-a}^{+a} \mathrm{E}_1(\xi^2)\, dx' \right] \qquad \text{for } c^{\mathrm{f}} \neq c^{\mathrm{T}} \tag{D-4}$$

Induced displacement for heat source

For $c^{\mathrm{f}}=c^{\mathrm{T}}$

$$u_{\mathrm{x}}^{\mathrm{qh}}=\frac{\eta\Upsilon}{8\pi k_{\mathrm{T}}G}\left\{(\lambda_1-1)\left[2c^{\mathrm{T}}te^{-\zeta^2}-\frac{r^2}{2}\mathrm{E}_1(\zeta^2)-2c^{\mathrm{T}}t\left(\ln r^2+\mathrm{E}_1(\zeta^2)\right)\right]\right\|_{x'=-a}^{x'=+a}+\int_{-a}^{+a}\tilde{x}\mathrm{E}_1(\zeta^2)dx'\Bigg\} \quad \text{(D-5)}$$

$$u_{\mathrm{y}}^{\mathrm{qh}}=\frac{\eta\Upsilon}{8\pi k_{\mathrm{T}}G}\left\{(\lambda_1+1)\left[\left[-4c^{\mathrm{T}}t\arctan\left(\frac{\tilde{x}}{\tilde{y}}\right)\right]\right\|_{x'=-a}^{x'=+a}-4c^{\mathrm{T}}t\tilde{y}\int_{-a}^{+a}\frac{e^{-\zeta^2}}{r^2}dx'\right]+(\lambda_1+2)\tilde{y}\int_{-a}^{+a}\mathrm{E}_1(\zeta^2)dx'\right\} \quad \text{(D-6)}$$

For $c^{\mathrm{f}}\neq c^{\mathrm{T}}$

$$\begin{aligned}u_{\mathrm{x}}^{\mathrm{qh}}=\frac{\eta\Upsilon}{8\pi k_{\mathrm{T}}G(1-\omega^2)}\Bigg\{&\lambda_2\left[2c^{\mathrm{T}}te^{-\zeta^2}-\frac{r^2}{2}\mathrm{E}_1(\zeta^2)-2c^{\mathrm{T}}t\left(\ln r^2+\mathrm{E}_1(\zeta^2)\right)\right]\Bigg\|_{x'=-a}^{x'=+a}\\&-\left[2c^{\mathrm{f}}te^{-\xi^2}-\frac{r^2}{2}\mathrm{E}_1(\xi^2)-2c^{\mathrm{f}}t\left(\ln r^2+\mathrm{E}_1(\xi^2)\right)\right]\Bigg\|_{x'=-a}^{x'=+a}\Bigg\}\end{aligned} \quad \text{(D-7)}$$

$$\begin{aligned}u_{\mathrm{y}}^{\mathrm{qh}}=\frac{\eta\Upsilon}{8\pi k_{\mathrm{T}}G(1-\omega^2)}\Bigg\{&\lambda_2\left[-4c^{\mathrm{T}}t\arctan\left(\frac{\tilde{x}}{\tilde{y}}\right)\right]\Bigg\|_{x'=-a}^{x'=+a}+\lambda_2\tilde{y}\int_{-a}^{+a}\mathrm{E}_1(\zeta^2)dx'-4c^{\mathrm{T}}\lambda_2t\tilde{y}\int_{-a}^{+a}\frac{e^{-\zeta^2}}{r^2}dx'\\&+\left[4c^{\mathrm{f}}t\arctan\left(\frac{\tilde{x}}{\tilde{y}}\right)\right]\Bigg\|_{x'=-a}^{x'=+a}-\tilde{y}\int_{-a}^{+a}\mathrm{E}_1(\xi^2)dx'+4c^{\mathrm{f}}t\tilde{y}\int_{-a}^{+a}\frac{e^{-\xi^2}}{r^2}dx'\Bigg\}\end{aligned} \quad \text{(D-8)}$$

Induced stress for heat source

For $c^{\mathrm{f}}=c^{\mathrm{T}}$

$$\sigma_{\mathrm{xx}}^{\mathrm{qh}}=\frac{\eta\Upsilon}{4\pi k_{\mathrm{T}}}\left\{\left[-\tilde{x}(\lambda_1+1)\left(\frac{1}{\zeta^2}-\frac{e^{-\zeta^2}}{\zeta^2}+\mathrm{E}_1\left(\zeta^2\right)\right)\right]\Bigg\|_{x'=-a}^{x'=+a}-(2\lambda_1+1)\int_{-a}^{+a}\mathrm{E}_1\left(\zeta^2\right)dx'-2\tilde{y}^2\int_{-a}^{+a}\frac{e^{-\zeta^2}}{r^2}dx'\right\} \quad \text{(D-9)}$$

$$\sigma_{\mathrm{yy}}^{\mathrm{qh}}=\frac{\eta\Upsilon}{4\pi k_{\mathrm{T}}}\left\{\left[\tilde{x}(\lambda_1+1)\left(\frac{1}{\zeta^2}-\frac{e^{-\zeta^2}}{\zeta^2}+\mathrm{E}_1\left(\zeta^2\right)\right)\right]\Bigg\|_{x'=-a}^{x'=+a}+\int_{-a}^{+a}\mathrm{E}_1\left(\zeta^2\right)dx'-2\int_{-a}^{+a}\frac{\tilde{x}^2e^{-\zeta^2}}{r^2}dx'\right\} \quad \text{(D-10)}$$

$$\sigma_{xy}^{qh}=\frac{\eta\Upsilon}{4\pi k_T}\left\{\left[-\tilde{y}(\lambda_1+1)\left(\frac{1}{\zeta^2}-\frac{e^{-\zeta^2}}{\zeta^2}+\mathrm{E}_1\left(\zeta^2\right)\right)\right]\Bigg|_{x'=-a}^{x'=+a}+2\tilde{y}\int_{-a}^{+a}\frac{\tilde{x}e^{-\zeta^2}}{r^2}dx'\right\} \tag{D-11}$$

For $c^f \neq c^T$

$$\begin{aligned}\sigma_{xx}^{qh}=&\frac{\eta\Upsilon}{4\pi k_T(1-\omega^2)}\left\{\left[-\lambda_2\tilde{x}\left(\frac{1}{\zeta^2}-\frac{e^{-\zeta^2}}{\zeta^2}+\mathrm{E}_1\left(\zeta^2\right)\right)\right]\Bigg|_{x'=-a}^{x'=+a}-2\lambda_2\int_{-a}^{+a}\mathrm{E}_1\left(\zeta^2\right)dx'\right.\\&\left.+\left[\tilde{x}\left(\frac{1}{\xi^2}-\frac{e^{-\xi^2}}{\xi^2}+\mathrm{E}_1\left(\xi^2\right)\right)\right]\Bigg|_{x'=-a}^{x'=+a}+2\int_{-a}^{+a}\mathrm{E}_1\left(\xi^2\right)dx'\right\}\end{aligned} \tag{D-12}$$

$$\sigma_{yy}^{qh}=\frac{\eta\Upsilon}{4\pi k_T(1-\omega^2)}\left\{\left[\lambda_2\tilde{x}\left(\frac{1}{\zeta^2}-\frac{e^{-\zeta^2}}{\zeta^2}+\mathrm{E}_1\left(\zeta^2\right)\right)\right]\Bigg|_{x'=-a}^{x'=+a}-\left[\tilde{x}\left(\frac{1}{\xi^2}-\frac{e^{-\xi^2}}{\xi^2}+\mathrm{E}_1\left(\xi^2\right)\right)\right]\Bigg|_{x'=-a}^{x'=+a}\right\} \tag{D-13}$$

$$\sigma_{xy}^{qh}=\frac{\eta\Upsilon}{4\pi k_T(1-\omega^2)}\left\{\left[-\lambda_2\tilde{y}\left(\frac{1}{\zeta^2}-\frac{e^{-\zeta^2}}{\zeta^2}+\mathrm{E}_1\left(\zeta^2\right)\right)\right]\Bigg|_{x'=-a}^{x'=+a}+\left[\tilde{y}\left(\frac{1}{\xi^2}-\frac{e^{-\xi^2}}{\xi^2}+\mathrm{E}_1\left(\xi^2\right)\right)\right]\Bigg|_{x'=-a}^{x'=+a}\right\} \tag{D-14}$$

where

Thermal conductivity [$MLT^{-3}\theta^{-1}$] $$k_T=(1-\phi)k_{Ts}+\phi k_{Tf} \tag{D-15}$$

Thermal diffusivity [L^2T^{-1}] $$c^T=\frac{k_T}{\rho C} \tag{D-16}$$

Hydro-thermal coupling coefficient [$ML^{-1}T^{-2}\theta^{-1}$] $$\Upsilon=\frac{\beta_o}{S} \tag{D-17}$$

Hydro-thermal coupling coefficient [θ^{-1}] $$\beta_o=\beta_m-\frac{2\eta\beta_s(1+\nu)}{3(1-2\nu)} \tag{D-18}$$

Hydro-thermal coupling coefficient [θ^{-1}] $$\beta_m = \alpha\beta_s + \phi_o(\beta_f - \beta_s)$$ (D-19)

Hydro-mechanical coefficient [-] $$\eta = \frac{\alpha(1-2\nu)}{2(1-\nu)}$$ (D-20)

Thermo-mechanical coefficient [-] $$\lambda_1 = \frac{K\beta_s}{\alpha\Upsilon}$$ (D-21)

Thermo-mechanical coefficient [-] $$\lambda_2 = 1 + (1-\omega^2)\lambda_1$$ (D-22)

Hydro-thermal coefficient [-] $$\omega^2 = \frac{c^{\mathrm{f}}}{c^{\mathrm{T}}}$$ (D-23)

Appendix E
Coordinate Transformation

In displacement discontinuity method, we are dealing with pore pressure, temperature, displacement and stress in different coordinate systems i.e. fracture local Cartesian coordinates as well as global Cartesian coordinates. As the pore pressure and temperature are scalars, the orientation of coordinate systems does not change their value. However, coordinate transformation is required for the displacement and stress. In the following the coordinate transformation between local and global Cartesian systems are described.

Displacement transformation

Based on Figure E-1, the local displacements ($u_{\bar{x}}$,$u_{\bar{y}}$) can be transformed to the global displacements (u_x,u_y) using the following relationships:

$$\begin{aligned} u_x &= u_{\bar{x}} \cos\beta - u_{\bar{y}} \sin\beta \\ u_y &= u_{\bar{x}} \sin\beta + u_{\bar{y}} \cos\beta \end{aligned} \qquad \text{(E-1)}$$

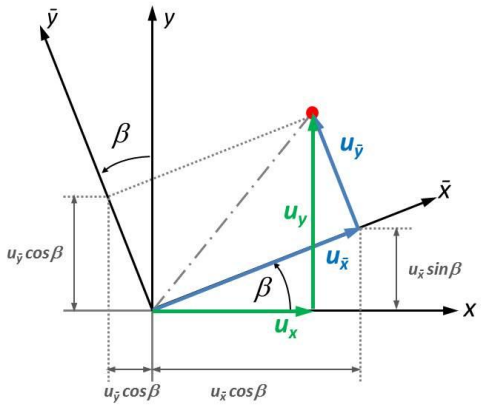

Figure E-1. Transformation of displacements

The inverse transformation (i.e. global to local coordinate systems) is

$$\begin{aligned} u_{\bar{x}} &= u_x \cos\beta + u_y \sin\beta \\ u_{\bar{y}} &= -u_x \sin\beta + u_y \cos\beta \end{aligned} \qquad \text{(E-2)}$$

The general form of the mentioned displacement transformation from local coordinate system (x_j,y_j) with the directional angle β_j to the local coordinate system (x_i,y_i) with the directional angle β_i has the following form:

$$\begin{aligned} u_{x_i} &= u_{x_j} \cos\gamma_{ij} + u_{y_j} \sin\gamma_{ij} \\ u_{y_i} &= -u_{x_j} \sin\gamma_{ij} + u_{y_j} \cos\gamma_{ij} \end{aligned} \qquad \text{(E-3)}$$

where $\gamma_{ij} = \beta_i - \beta_j$.

Stress transformation

Stress transformation can be calculated using the normal and shear stress on a plane that its outward normal makes the angle α with the local ȳ-axis. The normal and shear stress in Figure E-2 can be written using the local stresses as below:

$$\begin{aligned} \sigma_n &= \sigma_{\bar{x}\bar{x}} \sin^2\alpha - 2\sigma_{\bar{x}\bar{y}} \sin\alpha\cos\alpha + \sigma_{\bar{y}\bar{y}} \cos^2\alpha \\ \sigma_s &= (\sigma_{\bar{y}\bar{y}} - \sigma_{\bar{x}\bar{x}}) \sin\alpha\cos\alpha + \sigma_{\bar{x}\bar{y}} (\cos^2\alpha - \sin^2\alpha) \end{aligned} \qquad \text{(E-4)}$$

Using this definition, local stresses can be transformed to the global stresses by considering different values for angle α as below:

$$\begin{aligned} &\alpha = -\beta \Rightarrow (\sigma_n)_{\alpha=-\beta} = +\sigma_{yy} \quad \text{and} \quad (\sigma_s)_{\alpha=-\beta} = +\sigma_{yx} \\ &\alpha = \frac{\pi}{2} - \beta \Rightarrow (\sigma_n)_{\alpha=\frac{\pi}{2}-\beta} = +\sigma_{xx} \quad \text{and} \quad (\sigma_s)_{\alpha=\frac{\pi}{2}-\beta} = -\sigma_{xy} \end{aligned} \qquad \text{(E-5)}$$

Here is the stress transformation from local Cartesian coordinate system to the global Cartesian coordinate system:

$$\begin{aligned}
\sigma_{xx} &= \sigma_{\bar{x}\bar{x}} \cos^2\beta - 2\sigma_{\bar{x}\bar{y}} \sin\beta\cos\beta + \sigma_{\bar{y}\bar{y}} \sin^2\beta \\
\sigma_{yy} &= \sigma_{\bar{x}\bar{x}} \sin^2\beta + 2\sigma_{\bar{x}\bar{y}} \sin\beta\cos\beta + \sigma_{\bar{y}\bar{y}} \cos^2\beta \\
\sigma_{xy} &= \sigma_{yx} = (\sigma_{\bar{x}\bar{x}} - \sigma_{\bar{y}\bar{y}}) \sin\beta\cos\beta + \sigma_{\bar{x}\bar{y}} (\cos^2\beta - \sin^2\beta)
\end{aligned} \tag{E-6}$$

The inverse transformation (i.e. global to local coordinate systems) has the following form:

$$\begin{aligned}
\sigma_{\bar{x}\bar{x}} &= \sigma_{xx} \cos^2\beta + 2\sigma_{xy} \sin\beta\cos\beta + \sigma_{yy} \sin^2\beta \\
\sigma_{\bar{y}\bar{y}} &= \sigma_{xx} \sin^2\beta - 2\sigma_{xy} \sin\beta\cos\beta + \sigma_{yy} \cos^2\beta \\
\sigma_{\bar{x}\bar{y}} &= \sigma_{\bar{y}\bar{x}} = (\sigma_{yy} - \sigma_{xx}) \sin\beta\cos\beta + \sigma_{xy} (\cos^2\beta - \sin^2\beta)
\end{aligned} \tag{E-7}$$

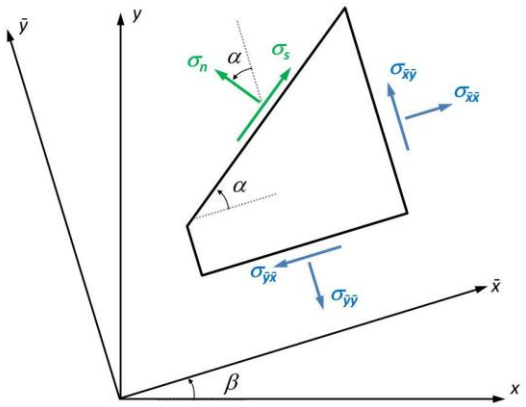

Figure E-2. Transformation of stresses

The general form of the stress transformation from local coordinate system (x_j,y_j) with the directional angle β_j to the local coordinate system (x_i,y_i) with the directional angle β_i has the following form:

$$\begin{aligned}
\sigma_{x_i x_i} &= \sigma_{x_j x_j} \cos^2\gamma_{ij} + 2\sigma_{x_j y_j} \sin\gamma_{ij}\cos\gamma_{ij} + \sigma_{y_j y_j} \sin^2\gamma_{ij} \\
\sigma_{y_i y_i} &= \sigma_{x_j x_j} \sin^2\gamma_{ij} - 2\sigma_{x_j y_j} \sin\gamma_{ij}\cos\gamma_{ij} + \sigma_{y_j y_j} \cos^2\gamma_{ij} \\
\sigma_{x_i y_i} &= \sigma_{y_i x_i} = (\sigma_{y_j y_j} - \sigma_{x_j x_j}) \sin\gamma_{ij}\cos\gamma_{ij} + \sigma_{x_j y_j} (\cos^2\gamma_{ij} - \sin^2\gamma_{ij})
\end{aligned} \tag{E-8}$$

where $\gamma_{ij} = \beta_i - \beta_j$.

In displacement discontinuity method, it is required to transform the local stresses in a local coordinate (x_j,y_j) with a directional angle β_j into the normal and shear stresses in another local coordinate (x_i,y_i) with directional angle β_i. This transformation can be done using the following formulation:

$$\sigma_{n_i} = \sigma_{x_j x_j} \sin^2 \gamma_{ij} - 2\sigma_{x_j y_j} \sin \gamma_{ij} \cos \gamma_{ij} + \sigma_{y_j y_j} \cos^2 \gamma_{ij}$$
$$\sigma_{s_i} = (\sigma_{y_j y_j} - \sigma_{x_j x_j}) \sin \gamma_{ij} \cos \gamma_{ij} + \sigma_{x_j y_j} (\cos^2 \gamma_{ij} - \sin^2 \gamma_{ij})$$

Appendix F

Fluid and Heat Flow Discretization in Fracture Network

Single Phase Fluid Flow in Fracture Network

The one-dimensional fluid diffusion equation (Eq. 4.22) can be solved numerically via different techniques such as finite difference method. The discretization of this equation requires three points for one dimensional solution. In the case of the fracture network showed in Figure F-1, each fracture element is connected with six fracture elements and using the conventional finite difference discretization for this setup is not feasible. For this case, mass conservation equation is implemented again and the discretization is done for a specific time step as below:

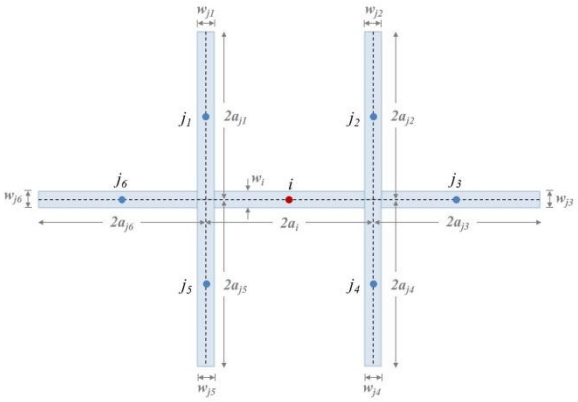

Figure F-1. Fracture segments location in the considered fracture network

$$\sum_{l=1}^{6} \rho_{\mathrm{f}} A_{i-jl} q_{i-jl}^{\mathrm{f}} = \Delta M + \rho_{\mathrm{f}} q_{\mathrm{s}}^{\mathrm{f}} \tag{F-1}$$

where $A_{i\text{-}jl}$ is the cross sectional area between element i and jl, $q^{\mathrm{f}}_{i\text{-}jl}$ is the Darcy velocity of flow between element i and jl and ΔM is the fluid mass changes of element i.

In order to calculate the flow rate between two fracture elements with different elemental size and aperture, an averaging concept should be implemented on transmissibility and cross sectional area based on the transmissibility averaging concept introduced by Aziz and Settari (1979). In this case, let's assume two adjacent fracture elements (*i* and *j*) with different aperture and elemental length (Figure F-2). The flow rate between *i* and *j* is

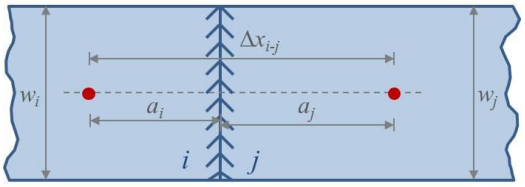

Figure F-2. Averaging of transmissibility [modified after Aziz and Settari, 1979]

$$Q_{i-j}^{\mathrm{f}} = -\frac{w_i^2}{12\mu} A_i \frac{(p_{\mathrm{i}} - p_{\mathrm{int}})}{a_i} = -\frac{w_j^2}{12\mu} A_j \frac{(p_{\mathrm{int}} - p_j)}{a_j} \tag{F-2}$$

where A_i and A_j are the cross sectional area of the elements *i* and *j*, respectively, which are not identical due to different fracture aperture and p_{int} is the pressure at the interface. Applying a unit width in this equation:

$$Q_{i-j}^{\mathrm{f}} = -\frac{w_i^3}{12\mu} \frac{(p_{\mathrm{i}} - p_{\mathrm{int}})}{a_i} = -\frac{w_j^3}{12\mu} \frac{(p_{\mathrm{int}} - p_j)}{a_j} = \Gamma_i^{\mathrm{f}} (p_{\mathrm{int}} - p_i) = \Gamma_j^{\mathrm{f}} (p_j - p_{\mathrm{int}}) \tag{F-3}$$

The flow rate between these two elements can be written as the pressure difference of two elements by elimination of interface pressure and introducing a mean value for Γ^{f}:

$$Q_{i-j}^{\mathrm{f}} = \Gamma_{i-j}^{\mathrm{f}} (p_j - p_i)$$

Comparing Eqs. F-2 and F-3, results

$$\Gamma^{\mathrm{f}}_{i-j} = \frac{1}{12\mu}\left[\frac{a_i}{w_i^3} + \frac{a_j}{w_j^3}\right]^{-1} \tag{F-4}$$

Therefore, $\Gamma^{\mathrm{f}}_{i\text{-}j}$ is the harmonic mean value of Γ^{f}_{i} and Γ^{f}_{j}.

Based on the harmonic value for transmissibility between two fracture elements, Eq. 4.21 for a unit fracture thickness and a specific time step t can be written as:

$$\sum_{l=1}^{6} \Gamma^{\mathrm{f}}_{i-jl}\left[\, p_{jl}^{t_n} - p_i^{t_n} \,\right]\tau_1 = 2a_i \Delta w_i^{\tau_1} + 2a_i w_i^{t_n} c_{\mathrm{f}} \Delta p_i^{\tau_1} - 2a_i w_i^{t_n} \beta_{\mathrm{f}} \Delta T_i^{\tau_1} + 2a_i \tau_1 \Delta Q_{\mathrm{fs}\,i}^{\tau_1} - \tau_1 q_{\mathrm{inj}}^{\mathrm{f}} \tag{F-5}$$

where p_i^{tn} represents the fracture pressure of element i at time step n, τ_1 is the time duration between last time step and current time step (last time step). The temperature effect of pressure propagation (third term on the right hand side of Eq. F-5) can be neglected as its value is almost negligible in comparison with the other terms. Substituting aperture changes with normal displacement discontinuities of the last time step, Eq. F-5 can be written as

$$\sum_{l=1}^{nc} \Gamma^{\mathrm{f}}_{i-jl}\tau_1 p_{jl}^{t_n} - \left[\sum_{l=1}^{nc} \Gamma^{\mathrm{f}}_{i-jl}\tau_1 + 2a_i\, w_i^{t_n} c_{\mathrm{f}}\right] p_i^{t_n} + 2a_i\, \Delta D_{\mathrm{n}\,i}^{\tau_1} - 2a_i\, \tau_1 \Delta Q_{\mathrm{fs}\,i}^{\tau_1} = -2a_i\, w_i^{t_n} c_{\mathrm{f}}\, p_i^{t_{n-1}} - \tau_1 . q_{\mathrm{inj}}^{\mathrm{f}} \tag{F-6}$$

The left hand side of Eq. F-6 represents the pressure of i^{th} and jl^{th} fracture segment, normal displacement discontinuity changes and interface flow rate from fracture into the surrounding rock, all at the current time step which are unknowns. The right hand side of the equation contains known parameters that include the pressure of the i^{th} fracture segment form the previous time step and the volume of injected fluid during the last time step.

Heat Flow in Fracture Network

The same procedure for the fluid flow in the considered seven-point fracture network model is applied for the heat transfer via implementation of energy conservation equation for the specific time step:

$$\sum_{l=1}^{6}\left[A_{i-jl} q^{\mathrm{h}}_{i-jl} + \rho_f q^{\mathrm{f}}_x A_{i-jl} C_f \left(T_i - T_{jl} \right) \right] = \Delta\left(M C_f T_i \right) + Q^{\mathrm{h}}_s \tag{F-7}$$

where M is the fluid mass in the considered control volume. Applying harmonic heat transmissibility (Γ^{h}) and an arithmetic cross-sectional average for a unit thickness fracture segment:

$$\sum_{l=1}^{6}\left[\Gamma^{\mathrm{h}}_{i-jl} \left(T_{jl} - T_i \right) + \rho_f q^{\mathrm{f}}_x C_f \Omega^{\mathrm{h}}_{i-jl} \left(T_i - T_{jl} \right) \right] = \Delta\left(2 a_i \rho_f w_i C_f T_i \right) + Q^{\mathrm{h}}_s \tag{F-8}$$

where:

Harmonic heat transmissibility: $$\Gamma^{\mathrm{h}}_{i-jl} = \frac{1}{k_{\mathrm{T}}}\left[\frac{a_i}{w_i} + \frac{a_{jl}}{w_{jl}} \right]^{-1}$$

Arithmetic cross-sectional mean: $$\Omega^{\mathrm{h}}_{i-jl} = \frac{w_i + w_{jl}}{2}$$

Expanding the right hand side of the heat conservation equation will result in

$$\begin{aligned}&\sum_{l=1}^{6} \Gamma^{\mathrm{h}}_{i-jl} \tau_1 \left[T^{t_n}_{jl} - T^{t_n}_i \right] + \rho_{\mathrm{f}} q^{\mathrm{f}\,t_n}_x C_{\mathrm{f}} \Omega^{\mathrm{h}}_{i-jl} \tau_1 \left[T^{t_n}_{jl} - T^{t_n}_i \right] = 2 a_i \rho_{\mathrm{f}} C_{\mathrm{f}} w^{t_n}_i \Delta T^{\tau_1}_i + 2 a_i \rho_{\mathrm{f}} C_{\mathrm{f}} T^{t_0}_i \Delta w^{\tau_1}_i \\ &+2 a_i C_{\mathrm{f}} w^{t_n}_i T^{t_0}_i \left[\rho_{\mathrm{f}} c_{\mathrm{f}} \Delta p^{\tau_1}_i - \rho_{\mathrm{f}} \beta_{\mathrm{f}} \Delta T^{\tau_1}_i \right] + 2 a_i \tau_1 \Delta Q^{\tau_1}_{\mathrm{hs}\,i} - \tau_1 . q^{\mathrm{h}}_{\mathrm{inj}}\end{aligned} \tag{F-9}$$

Substituting aperture changes with normal displacement discontinuities of the last time step, the Eq. F-9 can be re-written as

$$\begin{aligned}&\sum_{l=1}^{6}\left[\Gamma^{\mathrm{h}}_{i-jl}\tau_1-\rho_{\mathrm{f}}q_x^{\mathrm{f}\,t_n}C_{\mathrm{f}}\Omega^{\mathrm{h}}_{i-jl}\tau_1\right]T_{jl}^{t_n}-\sum_{l=1}^{6}\left\{\Gamma^{\mathrm{h}}_{i-jl}\tau_1+\rho_{\mathrm{f}}C_{\mathrm{f}}\left[q_x^{\mathrm{f}\,t_n}\Omega^{\mathrm{h}}_{i-jl}\tau_1+2a_i w_i^{t_n}-2a_i\beta_{\mathrm{f}}w_i^{t_n}T_i^{t_0}\right]\right\}T_i^{t_n}\\&-\left[2a_i\rho_{\mathrm{f}}C_{\mathrm{f}}w_i^{t_n}T_i^{t_0}c_{\mathrm{f}}\right]p_i^{t_n}+2a_i\rho_{\mathrm{f}}C_{\mathrm{f}}T_i^{t_0}\Delta D_{\mathrm{n}\,i}^{\tau_1}-2a_i\tau_1\Delta Q_{\mathrm{hs}\,i}^{\tau_1}\\&=-2a_i\rho_{\mathrm{f}}C_{\mathrm{f}}w_i^{t_n}\left[\left(1-\beta_{\mathrm{f}}T_i^{t_0}\right)T_i^{t_{n-1}}+c_{\mathrm{f}}T_i^{t_0}p_i^{t_{n-1}}\right]-\tau_1.q_{\mathrm{inj}}^{\mathrm{h}}\end{aligned}\qquad\text{(F-10)}$$

The left hand side of Eq. F-10 represents the temperature of i^{th} and jl^{th} fracture segment, pressure of the i^{th} fracture segment, normal displacement discontinuity changes and interface heat flow rate from fracture into the surrounding rock, all at the current time step which are unknowns. The right hand side of the equation contains known parameters that include the pressure and temperature of the i^{th} fracture segment form the previous time step and the amount of heat injected fluid during the last time step.

Based on the above formulation, the effect of density and normal displacement discontinuity changes over time are negligible, so Eq. F-10 can be simplified as

$$\begin{aligned}&\sum_{l=1}^{6}\left[\Gamma^{\mathrm{h}}_{i-jl}\tau_1-\rho_{\mathrm{f}}q_x^{\mathrm{f}\,t_n}C_{\mathrm{f}}\Omega^{\mathrm{h}}_{i-jl}\tau_1\right]T_{jl}^{t_n}-\sum_{l=1}^{6}\left\{\Gamma^{\mathrm{h}}_{i-jl}\tau_1+\rho_{\mathrm{f}}C_{\mathrm{f}}\left[q_x^{\mathrm{f}\,t_n}\Omega^{\mathrm{h}}_{i-jl}\tau_1+2a_i w_i^{t_n}\right]\right\}T_i^{t_n}-2a_i\tau_1\Delta Q_{\mathrm{hs}\,i}^{\tau_1}\\&=-2a_i\rho_{\mathrm{f}}C_{\mathrm{f}}w_i^{t_n}T_i^{t_{n-1}}-\tau_1.q_{\mathrm{inj}}^{\mathrm{h}}\end{aligned}\qquad\text{(F-11)}$$